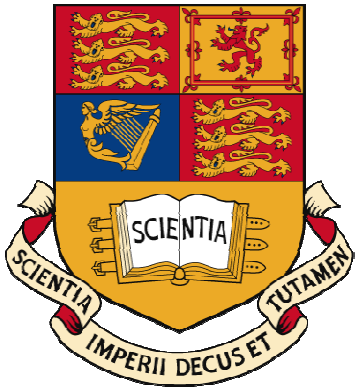
Piezoelectric actuators for delamination control in composite plates subjected to low velocity impact

by

Mohamed Sultan Ibrahim Shaik Dawood



Thesis submitted for the degree of Doctor of Philosophy of the Imperial College London

Department of Aeronautics
Imperial college London
2010

Abstract

The potential of *MFC* actuator as a tool for reducing low velocity impact induced delamination has been investigated using *LS-DYNA* explicit code. For this purpose, three different piezoelectric actuation models were implemented through its user defined material subroutine, namely, the linear strain model, electric field dependent model and induced strain model. The induced strain model was found to provide the best match with experimental results for actuation strain prediction, hence used in impact investigations.

In predicting the delamination, a newly formulated damage model was used as it was found that the existing damage models in *LS-DYNA* are simplistic and rate sensitive. An independent three-dimensional piezoelectric finite element code was developed and used to study the effects of design and actuation parameters on the actuation characteristics of the *MFC*. The parametric study was meant to determine a laminate-actuator system that would allow sufficient presence of the piezoelectric effects in it. A selected laminate-actuator system was later used to investigate the effects of piezoelectric control actions on the impact force and displacement for purely elastic impact cases. For simply supported laminate it was found that the peak impact force and displacement could be reduced by applying a counter moment to the incoming impact load, whereas for clamped laminate the same was achieved by regulating the laminate stiffness at the impact point.

The technique of impact force reduction confirmed that delamination could be reduced. However, this concept could not be experimentally verified as the design requirements could not be practically implemented. The actuator required voltages beyond its operating range to reduce delamination even in the case of very low energy impact. This is something not achievable with the existing piezoelectric materials. Assuming powerful piezoelectric actuators are not impossible in near future, this study could provide useful information for an attempt to validate this concept.

Table of Contents

ABSTRACT 2

DECLARATION OF ORIGINALITY 8

ACKNOWLEDGEMENT 9

NOMENCLATURE 10

LIST OF FIGURES 15

LIST OF TABLES 24

CHAPTER 1: INTRODUCTION 25

1.1 MOTIVATION, SCOPE, OBJECTIVE AND CONTRIBUTION 25

1.2 OUTLINE OF THESIS 28

1.3 CONTRIBUTIONS 30

1.4 PUBLICATIONS 33

CHAPTER 2: LOW VELOCITY IMPACT ON COMPOSITES – A REVIEW 34

2.1 CHAPTER INTRODUCTION 34

2.2 COMPOSITE MATERIALS 34

2.3 CLASSIFICATIONS OF COMPOSITE MATERIALS 35

2.3.1 Particulate composite 35

2.3.2 Fibre reinforced composite 36

2.3.3 Laminated composite material 37

2.4 IMPACT ON COMPOSITE MATERIALS 40

2.5 IMPACT DYNAMICS 41

2.6 DAMAGE EVOLUTION DUE TO LOW VELOCITY IMPACT 43

2.6.1 Matrix cracking 43

2.6.2 Delamination 45
2.6.3 Fibre failure 45
2.7 FAILURE ANALYSIS 46
2.7.1 Stress based failure models 46
2.7.2 Fracture mechanics approach 49
2.7.3 Damage mechanics 52
2.7.4 Delamination threshold force 56
2.8 METHODS OF IMPROVING THE IMPACT TOLERANCE OF COMPOSITE LAMINATES 58
2.8.1 Woven fabrics 58
2.8.2 Stitching 59
2.8.3 Z-pinning 59
2.8.4 Piezoelectric actuators 59
2.9 FINITE ELEMENT ANALYSIS OF LOW VELOCITY IMPACT 60
2.10 DELAMINATION MODELLING USING LS-DYNA 61
2.11 CHAPTER SUMMARY 62
CHAPTER 3: PIEZOELECTRIC MATERIALS – A REVIEW 64
3.1 CHAPTER INTRODUCTION 64
3.2 SMART MATERIALS 64
3.2.1 Shape memory alloys 65
3.2.2 Magneto- and electrostrictive materials 66
3.2.3 Electro- and magnetorheological fluids 66
3.2.4 Piezoelectric materials 67
3.3 PIEZOELECTRIC MATERIALS 67
3.3.1 Poling and depoling of piezoelectric materials 68
3.3.2 Hysteresis in piezoelectric materials 69
3.3.3 Piezoelectric electromechanical response 70
3.4 TYPES OF PIEZOELECTRIC MATERIALS 72
3.4.1 Piezopolymer and piezoceramic actuators 72
3.4.2 AFC and MFC actuators 74
3.5 PIEZOELECTRIC APPLICATIONS 75
3.5.1 Vibration control 76
3.5.2 Shape control 76
3.5.3 Buckling control 77

3.5.4 Bi-stable structures 77
3.5.5 Structural health monitoring 78
3.5.6 Structural damage control 78
3.6 ANALYSIS OF SMART STRUCTURES 79
3.7 PIEZOELECTRIC CONSTITUTIVE RELATION 81
3.8 PIEZOELECTRIC STRAIN MODELS 85
3.9 EFFECT OF PIEZOELECTRIC ACTUATION ON BENDING DEFORMATION 86
3.10 SELECTION OF A SUITABLE ACTUATION MODEL 88
3.11 CHAPTER SUMMARY 89
CHAPTER 4: PIEZOELECTRIC CONSTITUTIVE MODEL 90
4.1 CHAPTER INTRODUCTION 90
4.2 PIEZOELECTRIC LINEAR CONSTITUTIVE EQUATION 90
4.3 PIEZOELECTRIC NONLINEAR CONSTITUTIVE RELATION 96
4.4 A SIMPLIFIED THREE-DIMENSIONAL NONLINEAR PIEZOELECTRIC CONSTITUTIVE MODEL 99
4.5 CHAPTER SUMMARY 105
CHAPTER 5: FINITE ELEMENT FORMULATION OF STATIC SHAPE CONTROL CODES 107
5.1 CHAPTER INTRODUCTION 107
5.2 FINITE ELEMENT FORMULATION 107
5.2.1 Strain-displacement relationship 108
5.2.2 Electric field-voltage relationship 111
5.2.3 System potential energy 114
5.3 STATIC SHAPE CONTROL 121
5.3.1 Inverse shape control 121
5.3.2 Active shape control 123
5.3.3 Voltage based shape control 124
5.4 CHAPTER SUMMARY 124
CHAPTER 6: VALIDATION OF THE FINITE ELEMENT CODES 129
6.1 CHAPTER INTRODUCTION 129
6.2 LINEAR PIEZOELECTRIC MATERIAL MODEL 129
6.2.1 Free strain test 130

6.2.2 Piezoelectric bimorph beam 134
6.3 NONLINEAR PIEZOELECTRIC MATERIAL MODEL 136
6.4 BISTABLE COMPOSITE 139
6.5 CHAPTER SUMMARY 143
CHAPTER 7: EFFECTS OF PIEZOELECTRIC ACTUATIONS ON STRUCTURAL DEFORMATION: A PARAMETRIC STUDY 145
7.1 CHAPTER INTRODUCTION 145
7.2 SETUPS FOR NUMERICAL SIMULATION 146
7.3 EFFECTS OF BOUNDARY CONDITIONS 151
7.3.1 Simply supported laminate 151
7.3.2 Clamped laminate 156
7.3.3 Simply supported versus clamped laminates 161
7.4 EFFECTS OF MATERIAL PROPERTIES 163
7.5 EFFECTS OF LAMINATE THICKNESS 168
7.6 EFFECTS OF ACTUATOR PLACEMENTS 170
7.7 EFFECTS OF ACTUATOR TYPE 184
7.8 CHAPTER SUMMARY 187
CHAPTER 8: INTERFACE ELEMENT FORMULATION AND VALIDATION 189
8.1 CHAPTER INTRODUCTION 189
8.2 CONSTITUTIVE MODEL 190
8.3 MIXED MODE FORMULATION 195
8.4 SINGLE ELEMENT VALIDATION – MODE I 196
8.5 SINGLE ELEMENT VALIDATION – MODE II 197
8.6 DOUBLE CANTILEVER BEAM TEST (DCB) 198
8.7 END NOTCHED FLEXURE TEST (ENF) 201
8.8 LOW VELOCITY IMPACT VALIDATION 203
8.8.1 Symmetric cross-ply laminate – thick plate 204
8.8.2 Symmetric cross-ply laminate – thin plate 208
8.9 CHAPTER SUMMARY 213
CHAPTER 9: EFFECTS OF PIEZOELECTRIC ACTUATIONS ON THE ELASTIC LOW VELOCITY IMPACT RESPONSE OF COMPOSITE LAMINATE 215
9.1 CHAPTER OVERVIEW 215

9.2 NUMERICAL MODEL 216
9.3 IMPACT RESPONSE OF SIMPLY SUPPORTED CROSS-PLY LAMINATE 218
9.3.1 Effects of different impact energy levels 218
9.3.2 Effects piezoelectric actuations – 2.0J impact 220
9.3.3 Effects piezoelectric actuations – 2.5J impact 224
9.3.4 Effects of electrical loading rates on peak impact force and displacement 227
9.4 IMPACT RESPONSE OF CLAMPED CROSS-PLY LAMINATE 232
9.4.1 Effects of different impact energy levels 232
9.4.2 Effects piezoelectric actuations – 1.0J impact 234
9.4.3 Effects of piezoelectric actuations – 2.5J impact 237
9.5 CHAPTER SUMMARY 239

CHAPTER 10: EFFECTS OF PIEZOELECTRIC ACTUATIONS ON DELAMINATION DUE TO LOW VELOCITY IMPACT 241

10.1 CHAPTER OVERVIEW 241
10.2 NUMERICAL MODEL 242
10.3 EFFECTS OF PIEZOELECTRIC ACTUATIONS ON DELAMINATION - 1.0J IMPACT CASE 243
10.4 EFFECTS OF PIEZOELECTRIC ACTUATIONS ON DELAMINATION - 2.0J IMPACT CASE 248
10.5 CHAPTER SUMMARY 251

CHAPTER 11: SUMMARY, CONCLUSIONS AND FUTURE WORK 253

11.1 SUMMARY 253
11.2 CONCLUSIONS AND FUTURE WORK 256
APPENDIX A 259
APPENDIX B 264
APPENDIX C 266
APPENDIX D 268
APPENDIX E 269
BIBLIOGRAPHY 271

Declaration of originality

I confirm that the work presented in this thesis is the personal work of the author and all else is appropriately referenced.

Acknowledgement

I would like to thank and acknowledge the International Islamic University Malaysia for sponsoring my studies at Imperial College London.

I am heartily thankful and greatly indebted to my supervisors Dr. Lorenzo Iannucci, Dr. Emile Greenhalgh and Dr. Ahmad Kamal Arrifin for their guidance and dedication on the supervision of my PhD. I am very thankful to Dr. Iannucci for his patience and tolerance to my ignorance and his continuous support during my difficult times.

I would also like to thank Mr. Simon Burbidge from the High Performance Computing centre at Imperial College London who helped me with my extensive computational needs. My special thanks to Dr. Viet who helped me a lot during the initial stage of my PhD. I would also like to thank my friends Oliver, Joseba, Robert, Fabian, Dr. Lucio, Dr. Baiz and Dr. Xiyong for their help and laughter.

I would like to express my deepest gratitude to my father Dr. Shaik Dawood and my mother Fareetha Beevi for their undivided love, guidance and support and to whom I owe my success. I would also like to thank my wife Anis Parveen and my daughters Nur Asma and Safia Zahara for their love and patience in helping me to achieve my success.

Lastly, I offer my regards to all of those who supported me in any respect during the completion of this PhD.

Nomenclature

A_1	Strain constant along direction *1*
A_2	Strain constant along direction *2*
A_3	Strain constant along direction *3*
A_a	Surface area of charge density
A_t	Surface area of surface traction
B_1	Electrostrictive constant along direction *1*
B_2	Electrostrictive constant along direction *2*
B_p	Voltage gradient operator
B_u	Strain displacement operator
D^*	Effective bending stiffness of orthotropic plate
D_{k}	Electric displacement
E_D	Young's modulus of isotropic material
E_a	Actuator modulus
E_{ij}	Young's modulus of orthotropic material
$E_{n,}\, E_k$	Electric field
E_s	Substrate modulus
E_v^B	Electric field of bottom actuator
E_v^T	Electric field of top actuator
F_{cr}	Critical delamination threshold force for circular plate
F_e	Global electrical load
F_m	Global external mechanical load
G_{12}, G_{23}, G_{13}	Shear modulus
$G_{\mathrm{I}}, G_{\mathrm{II}}, G_{\mathrm{III}}$	Mode I, II and III strain energy release rates

$G_{\mathrm{CI}}, G_{\mathrm{CII}}, G_{\mathrm{CIII}}$	Mode I, II and III critical strain energy release rates
H_E	Electrical potential energy
H_M	Mechanical potential energy
K_{aa}	Global actuator electrical stiffness
K_{ss}	Global sensor electrical stiffness
K_{ua}	Global structure-actuator coupling stiffness
K_{us}	Global structure-sensor coupling stiffness
K_{uu}	Global stiffness
M_u	Global mass
M_ε	Electrically induced moment
N_i	Interpolation function
P_{cr}	Critical delamination threshold force
R_{ux}	Weighting function w.r.t to displacement along *x*
R_{uy}	Weighting function w.r.t to displacement along *y*
R_{uz}	Weighting function w.r.t to displacement along *z*
S_{23}, S_{31}	Out of plane through thickness transverse shear strengths
S_{ijlm}^E	Elastic compliance
T_{min}	Response time to achieve nominal actuation
$\ddot{X}$	Global nodal acceleration
Y_i	Damage energy release rate
Z_T	Out of plane through thickness normal strength
d_e^n	Effective damage parameter for mixed mode
d_{i}	Effective damage parameter for single loading
d_0	Strain constant
$d_{\mathrm{I}}, d_{\mathrm{II}}, d_{\mathrm{III}}$	Damage scalar variables
d_{ijn}	Piezoelectric strain coefficients
d_{ijnr}	Electrostrictive coefficients
d_ε	Induced strain dependent strain coefficient
d_E	Electric field dependent strain coefficient
e_d	Failure index for delamination
e_y	Error function
f_e	Element electrical load
f_m	Element external mechanical load

f_o	Resonant frequency
$k_{\mathrm{I}}, k_{\mathrm{II}}, k_{\mathrm{III}}$	Interface stiffnesses
k_{aa}	Element actuator electrical stiffness
k_{ss}	Element sensor electrical stiffness
k_{ua}	Element structure-actuator coupling stiffness
k_{us}	Element structure-sensor coupling stiffness
k_{uu}	Element stiffness
n_a	Total number of actuator elements
n_d	Number of delaminations
n_e	Total number of elements applied with electrical load
n_m	Total number of elements applied with mechanical load
n_s	Total number of sensor elements
n_u	Total number of structural elements
s^E_{ijlmpq}	Nonlinear elastic compliances
t_3	Electrode spacing for conventional actuators
t_{IDE}	*IDE* spacing
t_a	Thickness of actuator
t_c	Thickness of interface layer
t_s	Thickness of substrate
$\ddot{u}$	Element nodal acceleration
$u_{\mathrm{I}}, u_{\mathrm{II}}, u_{\mathrm{III}}$	Local displacement
$u_{max,i}$	Ultimate failure displacement
$u_{o,i}$	Damage onset displacement
u_x	Total displacement along *x*
u_{xi}	Nodal displacement along *x*
u_y	Total displacement along *y*
u_{yi}	Nodal displacement along *y*
u_z	Total displacement along *z*
u_{zi}	Nodal displacement along *z*
v_a	Element actuator voltage
v_s	Element sensor voltage
x_j	Direction of electric field
y_c	Actuated shape

y_d	Desired shape
$\mathcal{V}_a$	Global actuator voltage
$\mathcal{V}_s$	Global sensor voltage
α_e	Dimensionless parameter
β_e^n,	Dimensionless parameter
ε_1	Actual strain in direction *1*
ε_2	Actual strain in direction *2*
ε_f	Curvature
ε_{ij}	Strain components
ε_{knr}	Nonlinear dielectric permittivity coefficients
$\varepsilon_{kn}^{\sigma}$	Dielectric permittivity coefficients
ε_o	Mid-plane strain
ε_{p1}	Actuation strain in direction *1*
ε_{p2}	Actuation strain in direction *2*
ε_{p3}	Actuation strain in direction *3*
κ_{ijlmn}	Elastostrictive coefficients
ν_{ij}	Poisson's ratio
$\sigma_{\mathrm{I}}, \sigma_{\mathrm{II}}, \sigma_{\mathrm{III}}$	Local stresses
σ_{ij}	Stress components
$\sigma_{o,i}$	Damage onset peak stress
A	Extensional stiffness coefficient
B	Extension-bending coupling stiffness coefficients
D	Bending stiffness coefficient
G	Gibbs free energy function
H	Potential energy
K	Kinetic energy
M	Moment resultant
N	Force resultant
P	Pressure
Q	Surface charge density
R	Weighting matrix
S	Entropy

T	Absolute temperature
U	Internal energy
V	Volume
W	Work
X	Global nodal displacement
m	Element mass
q	Surface traction
t	Thickness
u	Element nodal displacement
v	Nodal voltage
ρ	Mass density

List of Figures

Figure 2.1: Types of composite materials 35

Figure 2.2: Specific strength and stiffness properties 37

Figure 2.3: Eurofighter - material distributions 37

Figure 2.4: Characteristics of a unidirectional fibrous composite 38

Figure 2.5: Laminated composite 38

Figure 2.6: Impact induced damages in composites 43

Figure 2.7: Types of matrix cracks 44

Figure 2.8: Predicted delamination in composite plate at 6.5J impact 47

Figure 2.9: Stresses inducing delamination 49

Figure 2.10: Fracture modes 50

Figure 2.11: Sublaminate with delamination 51

Figure 2.12: Mixed mode bilinear damage curve 52

Figure 2.13: Traction-displacement laws 53

Figure 3.1: Piezoelectric effects 68

Figure 3.2: Piezoelectric domains 69

Figure 3.3: Hysteresis effect in piezoceramic 70

Figure 3.4: Schematic illustration of an *IDE* circuit 72

Figure 3.5: Actuation mode of *PVDF* and *PZT* actuators 74

Figure 3.6: Geometric configurations of *AFC* actuator 75

Figure 3.7: Geometric configurations of *MFC* actuator 75

Figure 3.8: Strain-electric field plot of unconstrained *MFC* 82

Figure 3.9: Induced strain models 86

Figure 5.1: Eight-node solid hexahedron element 108

Figure 5.2: *MFC* actuator - planar actuation directions 114

Figure 5.3: Flowchart - *3DSHAPE-I* code 126

Figure 5.4: Flowchart - *3DSHAPE-A* code 127

Figure 5.5: Flowchart - *3DSHAPE-V* code 128

Figure 6.1: Unconstrained *G1195* piezoceramic 131

Figure 6.2: Strain in *x* direction obtained from *umat50* (T_{min}=30 μs) 131

Figure 6.3: Strain in *z* direction obtained from *umat50* (T_{min}=30 μs) 132

Figure 6.4: Strain in *x* direction obtained from *umat50* (T_{min}=0.5ms) 133

Figure 6.5: Strain in *z* direction obtained from *umat50* (T_{min}=0.5ms) 133

Figure 6.6: Experimental configuration of piezoelectric bimorph beam 134

Figure 6.7: Finite element model used in the bimorph analysis 135

Figure 6.8: Piezoelectric sandwich structure 137

Figure 6.9: Bistable state of (0/90) composite 140

Figure 6.10: *FEA* model of the bistable (0_{MFC}/0/90) composite 141

Figure 6.11: Bistable State B of (0_{MFC}/0/90) laminate 141

Figure 6.12: z_d values measured at different actuation voltages 143

Figure 7.1: Clamped and simply supported boundary conditions 148

Figure 7.2: Actuator placements for quarter model 150

Figure 7.3: Displacements about *y* of *SS* 1mm *P0* laminate 152

Figure 7.4: Displacements about *x* of *SS* 1mm *P0* laminate 152

Figure 7.5: Displacements of *SS* 1mm *P0* laminate at 1000V/-1000V 153

Figure 7.6: Displacements about *y* of *SS* 1mm *P90* laminate 154

Figure 7.7: Displacements about *x* of *SS* 1mm *P90* laminate 154

Figure 7.8: Displacements of *SS* 1mm *P90* laminate at 1000V/-1000V 155

Figure 7.9: Displacements about *y* of *SS* 1mm *P0* and *P90* laminates at ±1000V 156

Figure 7.10: Displacements about *x* of *SS* 1mm *P0* and *P90* laminates at ±1000V 156

Figure 7.11: Displacements about *y* of *CC* 1mm *P0* laminate 157

Figure 7.12: Displacements about *x* of *CC* 1mm *P0* laminate 158

Figure 7.13: Displacements of *CC* 1mm *P0* laminate at ±1000V 158

Figure 7.14: Displacement about *y* of *CC* 1 mm *P90* laminate 159

Figure 7.15: Displacement about *x* of *CC* 1mm *P90* laminate 159

Figure 7.16: Displacement of *CC* 1mm *P90* laminate at ±1000V 160

Figure 7.17: Displacements about *y* of *CC* 1mm *P0* and *P90* laminates at ±1000V 161

Figure 7.18: Displacements about *x* of *CC* 1mm *P0* and *P90* laminates at ±1000V 161

Figure 7.19: Displacements about *y* of *CC* and *SS* 1mm *P0* laminate at ±1000V 162

Figure 7.20: Displacements about *x* of *CC* and *SS* 1mm *P0* laminate at ±1000V 162

Figure 7.21: Displacements about *y* of *CC* and *SS* 1mm *P90* laminate at ±1000V 163

Figure 7.22: Displacements about *x* of *CC* and *SS* 1mm *P90* laminate at ±1000V 163

Figure 7.23: Displacements about *y* of *SS* 1mm *P0* laminate 164

Figure 7.24: Displacements about *y* of *CC* 1mm *P0* laminate 165

Figure 7.25: Displacements about *y* of *SS* 1mm *P90* laminate 165

Figure 7.26: Displacements about *y* of *CC* 1mm *P90* laminate 166

Figure 7.27: Displacements about *y* of *SS* and *CC* 1mm *P0* laminate at ±1000V 166

Figure 7.28: Displacements about *y* of *SS* and *CC* 1mm *P90* laminate at ±1000V 167

Figure 7.29: Displacements about *y* of *SS* 1mm *P0* laminate at ±1000V 167

Figure 7.30: Displacements about *y* of *CC* 1mm *P0* laminate at ±1000V 168

Figure 7.31: Displacements about *y* of *SS P0* laminate at ±1000V..... 169

Figure 7.32: Displacements about *y* of *CC P0* laminate at ±1000V 169

Figure 7.33: Displacements about *y* of 2mm *P0* laminate at ±1000V 170

Figure 7.34: Displacements about *y* of *SS* 1mm *P0* laminate at ±1000V 171

Figure 7.35: Displacements about *x* of *SS* 1mm *P0* laminate at ±1000V 172

Figure 7.36: Displacements about *y* of *CC* 1mm *P0* laminate at ±1000V 172

Figure 7.37: Displacements about *x* of *CC* 1mm *P0* laminate at ±1000V 173

Figure 7.38: Surface plot of *SS* 1mm *P0* laminate at ±1000V - Type *A* & *B*..... 174

Figure 7.39: Surface plot of *SS* 1mm *P0* laminate at ±1000V - Type *C* & *D* 175

Figure 7.40: Surface plot of *SS* 1mm *P0* laminate at ±1000V - Type *E* & *F*..... 176

Figure 7.41: Surface plot of *SS* 1mm *P0* laminate at ±1000V - Type *G* & *H*..... 177

Figure 7.42: Surface plot of *SS* 1mm *P0* laminate at ±1000V - Type *I* & *J* 178

Figure 7.43: Surface plot of *CC* 1mm *P0* laminate at ±1000V - Type *A* & *B* 179

Figure 7.44: Surface plot of *CC* 1mm *P0* laminate at ±1000V - Type *C* & *D*..... 180

Figure 7.45: Surface plot of *CC* 1mm *P0* laminate at ±1000V - Type *E* & *F* 181

Figure 7.46: Surface plot of *CC* 1mm *P0* laminate at ±1000V - Type *G* & *H* 182

Figure 7.47: Surface plot of *CC* 1mm *P0* laminate at ±1000V - Type *I* & *J* 183

Figure 7.48: Displacement about *y* of *SS* 1mm *P0* laminate using different actuator materials at ±1000V 185

Figure 7.49: Displacement about *y* of *CC* 1mm *P0* laminate using different actuator materials at ±1000V 185

Figure 7.50: Blocking force-free displacement plot at 1500V..... 186

Figure 7.51: Optimized working points for different fibre materials..... 187

Figure 8.1: Interface element coordinate system 190

Figure 8.2: Bilinear relationship for mode I delamination 191

Figure 8.3: Bilinear relationship for mode II delamination 191

Figure 8.4: Bilinear relationship for mixed mode delamination 192

Figure 8.5: Mode I single element validation 197

Figure 8.6: Mode II single element validation 198

Figure 8.7: *DCB* test specimen 198

Figure 8.8: Finite element model of *DCB* specimen 199

Figure 8.9: Boundary and loading conditions used in *DCB* simulation 200

Figure 8.10: Force-relative displacement - *DCB* simulation 201

Figure 8.11: *ENF* test specimen 201

Figure 8.12: Finite element model of *ENF* specimen 202

Figure 8.13: Boundary and loading conditions used in *ENF* simulation 203

Figure 8.14: Force-relative displacement - *ENF* simulation 203

Figure 8.15: Finite element model of $(0_2/c/90_2/90_2/c/0_2)$ impact test 205

Figure 8.16: Predicted delamination at (90/0) interface 206

Figure 8.17: Kinetic energy-time plot for 2.1J impact case 207

Figure 8.18: Impact force-time plot for 2.1J impact case 208

Figure 8.19: Displacement-time plot for 2.1J impact case 208

Figure 8.20: Finite element model of impact test specimen – top view 209

Figure 8.21: Finite element model of impact test specimen – detail view 210

Figure 8.22: Delamination at 90/0 interface –7.2J impact 210

Figure 8.23: Delamination at 0/90 interface –7.2J impact 210

Figure 8.24: Delamination at 90/0 interface –1.0J impact 211

Figure 8.25: Energy vs. time for *MAT 138* – 7.2J impact 212

Figure 8.26: Energy vs. time for *umat41v* – 7.2J impact 212

Figure 8.27: Delamination using *MAT 138* – 7.2J impact, time scale factor of 0.2 213
Figure 9.1: Finite element model of elastic impact test specimen 217
Figure 9.2: Force-time plot for *SS* cross-ply laminate – zero actuation 219
Figure 9.3: Displacement-time plot for *SS* cross-ply laminate – zero actuation 220
Figure 9.4: Force-time plot for *SS* cross-ply laminate: 2.0J impact – in-phase actuation 222
Figure 9.5: Force-time plot for *SS* cross-ply laminate: 2.0J impact – out-of-phase actuation 223
Figure 9.6: Displacement-time plot for *SS* cross-ply laminate: 2.0J impact – in-phase actuation 223
Figure 9.7: Displacement-time plot for *SS* cross-ply laminate: 2.0J impact – out-of-phase actuation 224
Figure 9.8: Force-time plot for *SS* cross-ply laminate: 2.5J impact – in-phase actuation 225
Figure 9.9: Force-time plot for *SS* cross-ply laminate: 2.5J impact – out-of-phase actuation 226
Figure 9.10: Displacement-time plot for *SS* cross-ply laminate: 2.5J impact – in-phase actuation 226
Figure 9.11: Displacement-time plot for *SS* cross-ply laminate: 2.5J impact – out-of-phase actuation 227
Figure 9.12: Force-impact energy plot for *SS* cross-ply laminate - negative bending actuation, 1ms loading rate 228
Figure 9.13: Displacement-impact energy plot for *SS* cross-ply laminate - negative bending actuation, 1ms loading rate 228
Figure 9.14: Impact force-impact energy plot for *SS* cross-ply laminate - negative bending actuation, 4ms loading rate 229
Figure 9.15: Displacement-impact energy plot for *SS* cross-ply laminate - negative bending actuation, 4ms loading rate 230

Figure 9.16: Close view of displacement-time plot for *SS* cross-ply laminate - negative bending actuation - 2.0J impact 231
Figure 9.17: Close view of displacement-time plot for *SS* cross-ply laminate - negative bending actuation - 2.5J impact 231
Figure 9.18: Impact force-time plot for *SS* cross-ply laminate - negative bending actuation 232
Figure 9.19: Force-time plot for *CC* cross-ply laminate – zero actuation 233
Figure 9.20: Displacement-time plot for *CC* cross-ply laminate – zero actuation 234
Figure 9.21: Impact force-time plot for *CC* cross-ply laminate: 1.0J impact – negative in-phase and negative bending actuations 235
Figure 9.22: Force-time plot for *CC* cross-ply laminate: 1.0J impact – positive in-phase and positive bending actuations 235
Figure 9.23: Displacement-time plot for *CC* cross-ply laminate: 1.0J impact – negative in-phase and negative bending actuations 236
Figure 9.24: Displacement-time plot for *CC* cross-ply laminate: 1.0J impact – positive in-phase and positive bending actuations 236
Figure 9.25: Force-time plot for *CC* cross-ply laminate: 2.5J impact – negative in-phase and negative bending actuations 237
Figure 9.26: Impact force-time plot for *CC* cross-ply laminate: 2.5J impact – positive in-phase and positive bending actuations 238
Figure 9.27: Displacement-time plot for *CC* cross-ply laminate: 2.5J impact – negative in-phase and negative bending actuations 238
Figure 9.28: Displacement-time plot for *CC* cross-ply laminate: 2.5J impact – positive in-phase and positive bending actuations 239
Figure 10.1: Finite element model of impact test specimen – top view 243
Figure 10.2: Finite element model of impact test specimen – detail view 243

Figure 10.3: Delamination at 90/0 interface for 1.0J impact case..... 244

Figure 10.4: Force-actuation voltage plot – 1.0J impact..... 245

Figure 10.5: Peak displacement-actuation voltage plot – 1.0J impact..... 246

Figure 10.6: Delamination threshold force-actuation voltage plot – 1.0J impact..... 247

Figure 10.7: Force-actuation voltage plot – 1.0J impact..... 247

Figure 10.8: Delamination at 90/0 interface for 2.0J impact..... 249

Figure 10.9: Force-actuation voltage plot – 2.0J impact..... 250

Figure 10.10: Displacement-actuation voltage plot – 2.0J impact..... 250

Figure 10.11: Force-actuation voltage plot – 2.0J impact..... 251

Figure A.1: Impact force-time plot for simply supported cross-ply laminate - 2.0J impact case.....259

Figure A.2: Displacement-time plot for simply supported cross-ply laminate: 2.0J impact case.....260

Figure A.3: Impact force-time plot for simply supported cross-ply laminate - 2.5J impact case.....260

Figure A.4: Displacement-time plot for simply supported cross-ply laminate: 2.5J impact case.....261

Figure A.5: Peak resultant impact force-time plot for clamped cross-ply laminate: 1.0J impact case.....261

Figure A.6: Displacement-time plot for clamped cross-ply laminate: 1.0J impact case.....262

Figure A.7: Peak resultant impact force-time plot for clamped cross-ply laminate: 2.5J impact case..... 262

Figure A.8: Displacement-time plot for clamped cross-ply laminate: 2.5J impact case.....263

Figure C.1: Simplified model of a quasi-isotropic laminate with internal delamination case.....267

Figure E.1: The smallest six modes of the elastic impact specimen.....269

Figure E.2: Displacement time plot for *SS* cross-ply laminate: 2.0J impact.....270

List of Tables

Table 3.1: Properties of *PVDF* and *PZT* actuators 73

Table 6.1: Material properties of *PZT-G1195* piezoceramic 130

Table 6.2: Free strain 131

Table 6.3: Material properties of *PVDF* polymers 135

Table 6.4: Deflection along the length of the bimorph *PVDF* beam 136

Table 6.5: Material properties of the sandwich specimen 137

Table 6.6: Strain prediction in piezoelectric sandwich structure 138

Table 6.7: Material properties used in the bistable simulation 142

Table 7.1: Material properties of composite laminates 149

Table 7.2: Material properties of piezoelectric actuators 150

Table 8.1: Material and interface properties of *DCB* test 199

Table 8.2: Material and interface properties of *ENF* test specimen 202

Table 8.3: Material properties of impact test specimen 205

Table C.1: Finite element details of numerical simulations 268

Chapter 1

Introduction

1.1 Motivation, scope, objective and contribution

Fibre reinforced composite laminates are widely used in the aerospace industry owing to their excellent strength-to-weight and stiffness-to-weight ratios compared to light alloys. However, a major setback with the use of composite laminates is their poor impact performance. Composite laminates have complex failure mechanisms which are normally displayed in the form of damage such as matrix cracking, delamination and fibre breakage (Abrate, 1998). In the case of low velocity impact delamination is detrimental to structural integrity and performance as it results in a severe reduction in the post impact compressive strength (Richardson and Wisheart, 1996). Hence there is a need to reduce delamination in laminated composite materials.

Methods in use to reduce delamination include techniques such as z-pinning and stitching (Greenhalgh and Hiley, 2003). However, these are passive methods. Piezoelectric materials have been used as sensors and actuators to actively control and enhance structural performances (Benjeddou, 2000). Several studies have demonstrated the capabilities of piezoelectric materials as damage controlling devices (Saravanos and Christoforou, 2002a). With advanced simulation tools, failures in composites could be studied with greater accuracy and at reduced cost compared to costly and lengthy experimentation.

The scope of this research is to numerically investigate the possible use of *Macro Fibre Composite* (*MFC*) actuator as a tool to reduce delamination due to low velocity impact in

fibre reinforced composite laminates. Among the numerical simulation tools available for the said purpose include *Abaqus* and *LS-DYNA*. *Abaqus* has the piezoelectric actuation module that could be readily used to achieve the objective of this research. However, in this software the electromechanical behaviour of the piezoelectric material is described using the linear piezoelectric actuation model (*Abaqus* Analysis User Manual-version 6.8).

Studies conducted in Chapters 9 and 10 have found that high electric fields were required to actuate the actuator in order to produce appreciable deformation to the host structure. In Chapter 6 it was also observed that the level of actuation was affected by the material orthotropy of the host structure. Hence, the inclusions of the electrostrictive and elastostrictive effects under combined loading conditions become necessary. The linear law is restricted to applications with low operating requirements and does not include, both, the electrostrictive and elastostrictive effects (Joshi, 1992).

Furthermore, the piezoelectric material module available in *Abaqus* is restricted to implicit or implicit dynamics analysis only (*Abaqus* Analysis User Manual-version 6.8). In the present investigation impact will be addressed using the explicit time integration method and the use of *Abaqus* will be inadequate for the purpose of the present work. *Ansys* is another numerical tool that offers piezoelectric capability but again the analysis is restricted to the use of linear actuation model. On the other hand, *LS-DYNA* lacks the piezoelectric material module and the closest substitute to simulate the piezoelectric effect is *MAT-ORTHOTROPIC-THERMAL* which is based on linear thermal strain-temperature relationship. This again would not account for the electrostrictive and elastostrictive effects under combined loading conditions.

The damage models that are currently available in *LS-DYNA* are simplistic for accurate damage prediction. The most commonly used damage model to predict delamination in composite laminates is based on the failure criteria approach. Cohesive based damage models have been made available in *LS-DYNA* and the one that is based on bilinear formulation is *MAT-COHESIVE-MIXED-MODE* (*LS-DYNA* Theory Manual, 2006). However, a series of impact test conducted in Chapter 8 found that this model to be numerically unstable at high impact loads. Iannucci (2006) has implemented a cohesive based damage model for predicting delamination in composite laminates in *LS-DYNA* through its user defined material subroutine. This model has been verified through a series of fracture tests but it lacks detail verification with respect to impact investigation.

As the overall objective of this research is to numerically investigate the use of piezoelectric actuator as a damage controlling device in the event of low velocity impact in composite laminates, the detail objectives are outlined as follows:

1. To include the damage code developed by Iannucci (2006) into the existing *LS-DYNA* user defined material subroutine and verify it for the prediction of low velocity impact induced delamination. This damage model has been tested through a series of fracture tests. However, with respect to impact, detailed verifications on its damage predictive capabilities are very limited. The model has only been verified using a simplified quasi-isotropic *Boeing* impact test coupon with delamination assumed to take place only at the centre of the laminate where the transverse shear stresses are the highest (Iannucci, 2006). In another investigation the damage model was tested with *CRAG* impact test specimen using a similar damage modelling approach (Iannucci and Willows, 2006). This was done as it is computationally demanding to include interface layers in between every plies. This approach would only give a representative damage envelope and not the actual damage scenario. In the present work, investigation will be carried out using a simple (0/90/0) cross ply laminate as cohesive layers need to be introduced only at the 0/90 and 90/0 interfaces and also due to the availability of large quantities of experimental results for the purpose of verification.
2. To implement three different piezoelectric actuation models into the *LS-DYNA* explicit finite element code through its user defined material subroutine. These are the linear, electric field dependent and induced strain dependent actuation models. The piezoelectric actuation model available in *Ansys* and *Abaqus* is based on the linear strain theory, which is inadequate for accurate actuation strain estimation at high fields and under combined loading conditions. It is also important to be mentioned that the current piezoelectric implementation into *LS-DYNA* would allow investigations to be carried out explicitly unlike in *Abaqus* where the analysis is restricted to implicit or implicit dynamics method only.
3. To numerically validate the implemented piezoelectric actuation models. The three different piezoelectric actuation models implemented into *LS-DYNA* will be validated using a number of test results extracted from the literature. The validation is intended to be based on both numerical and experimental results in order to reach a high level of confidence with the implemented models.
4. To develop an independent three-dimensional static piezoelectric finite element code based on the linear piezoelectric actuation model and conduct a parametric study to investigate the effects of design parameters such as boundary condition, stacking sequence, laminate thickness, material property, actuator placement and actuator type on the piezoelectric control actions. This is to numerically characterize the

electromechanical behaviour of the *MFC* actuator in order to determine a suitable laminate-actuator system for subsequent impact investigation. Unless this investigation will be conducted, it would be difficult to determine a suitable laminate-actuator configuration with appreciable presence of the piezoelectric effects.

5. To conduct a parametric study and investigate the effects of design and actuation parameters on the low velocity impact response of composite laminate-actuator system. This is to numerically characterize the effects of simple actuation techniques such as extension, compression and bending on the displacement and impact force histories of the laminate-actuator system. Since it has been suggested that there exists a critical load for delamination to initiate (Davies and Zhang, 1995), this step is intended to identify a suitable actuation technique that could be used to reduce the impact load for a given laminate-actuator configuration. This step is also intended to propose an appropriate impact condition to be used to validate the concept of impact induced delamination control using piezoelectric actuators.
6. To investigate the effects of piezoelectric actuation on impact induced delamination. The investigation will be limited to demonstrate the effects of piezoelectric actuation on laminate-actuator system subjected to low velocity impact based on the outcomes of objectives 4 and 5. The findings will be used to numerically demonstrate if impact induced delamination could be either prevented or reduced.

1.2 Outline of thesis

This thesis is organized into 11 chapters. Chapter 1 highlights the motivations, scopes, objectives, thesis outline and original contributions of this research work. Chapter 2 provides an overview on the low velocity impact analysis of composite materials. The discussions include brief classifications on the different types of composite materials, their applications and related advantages and disadvantages as well as review on some of the commonly used failure models in *LS-DYNA* to predict delamination in laminated composite. The chapter highlights the deficiencies in the existing damage models used in *LS-DYNA* and identifies a suitable damage model to be used to predict delamination in composite laminates subjected to low velocity impact.

Chapter 3 provides an overview on the applications and modelling techniques of smart materials in the field of structural engineering. The discussions include brief classifications on

the different types of smart materials, their applications and related advantages and disadvantages. The chapter focuses on the fundamentals, applications and modelling of piezoelectric materials relevant to the current research. The chapter highlights the inadequacy of the existing piezoelectric constitutive models available in finite element codes such as *Abaqus* and *Ansys* and outlines the need for a refined higher order actuation model that is accurate and physically based.

Chapter 4 presents the derivations of the linear and nonlinear piezoelectric constitutive models based on the *Gibbs* free energy function which is referenced to the work of Joshi (1992). The chapter also discusses other simplified nonlinear models that are currently in use. The formulation and implementation of the three-dimensional linear and nonlinear piezoelectric material models into the *LS-DYNA* finite element code through its user defined material subroutine are detailed in this chapter.

Chapter 5 presents three-dimensional finite element formulation and code development for plates integrated with piezoelectric actuators based on the linear piezoelectric theory. The chapter also discusses the implementation of three different control algorithms, i.e., shape based, sensor based and voltage based. The outcome of this chapter is a static shape control programme to that will be used to characterize the *MFC* actuator (objective 4).

Chapter 6 presents a series of test results to validate the accuracy of the developed piezoelectric finite element code and the piezoelectric actuation models implemented into *LS-DYNA*'s user defined material subroutine. The test cases selected for the validation were both numerical and experimental so that a high level of confidence could be established with the implemented models. The chapter highlights the inadequacy of the linear and electric field dependent actuation models in presenting the piezoelectric effects at high electric fields and when integrated with structural devices. The main outcome of this chapter is the identification of a most appropriate actuation model to be used in subsequent impact investigations.

Chapter 7 presents the investigation into the effects of piezoelectric actuations on structural deformation using the code developed in Chapter 5. The chapter highlights the effects of design parameters such as boundary conditions, materials properties, laminate thickness and actuator parameters such as actuator type, placements and actuation voltages on the nature of piezoelectric actuation. The outcomes of the parametric study constitute as guidelines towards the selection of a favourable laminate-actuator system to be used in subsequent impact investigations in order to validate the concept of impact induced delamination control using piezoelectric actuators.

Chapter 8 presents the mathematical formulation of a new damage model implemented into the *LS-DYNA* explicit finite element code. The derivation and implementation presented in this chapter are referenced to the work of Iannucci (2006). This chapter also presents a series of test results that highlight the inadequacies of a similar damage model in *LS-DYNA* in comparison to the new damage model.

Chapter 9 presents investigation into the effects of piezoelectric actuations on the elastic impact response of composite structures subjected to low velocity impact. The chapter outlines the different piezoelectric control actions that can be used to regulate the impact force and displacement histories of composite plates subjected to low velocity impact. The chapter also highlights the effects of the electrical loading rates on the impact histories.

Chapter 10 presents investigation into the potential use of piezoelectric actuators to reduce impact induced delamination based on the technique of force reduction demonstrated in Chapter 9 on simply supported cross-ply laminates. The highlights of the chapter include the effects of piezoelectric actuations on delamination, impact force and displacement.

Chapter 11 presents the summary, conclusions and recommendations for future work. The proposals for the future work are based on the limitations observed with the implementation of the present technique practically.

1.3 Contributions

The present work contains several significant contributions to advancing impact investigations using composite laminate-actuator system as an integrated tool for improving its impact tolerance. The original contributions of the present research work include the followings:

1. Chapter 4 - implementation of the three-dimensional linear, electric field dependent and induced strain dependent piezoelectric actuation models into *LS-DYNA* explicit finite element code. The piezoelectric actuation model available in other finite element codes such as *Ansys* and *Abaqus* is based on the linear actuation strain model. The linear model is only applicable at low operating fields and without the inclusion of the electrostrictive and elastostrictive effects under combined loading conditions. This is inadequate for actuators that operate at high electric fields such as the *MFC*. In addition, the actuation strains have also been shown to be affected by the constraints and loading conditions. This makes the linear and electric field dependent models to

be inaccurate for orthotropic host system. Furthermore, the piezoelectric analysis in *Abaqus* is restricted to implicit or implicit dynamics investigations only. The current piezoelectric implementation into *LS-DYNA* allows explicit analysis. This could be a powerful tool to analyse structural design problems integrated with piezoelectric actuator with an accurate and physically based actuation model.

2. Chapter 5 - development of an independent three-dimensional finite element code capable of performing static shape control analysis on structural system integrated with piezoelectric actuators based on the linear piezoelectric actuation model using three different control algorithms. Most finite element codes for smart structural analysis were developed based on two-dimensional plate or shell theories which inadequately represent the full electromechanical behaviour of the piezoelectric actuator. Since the code was developed based on three-dimensional formulation, it is more comprehensive and not limited to the plane stress assumption which is typical in the case of plate or shell theories. Furthermore, the three-dimensional effect becomes particularly important if the thickness effect needs to be included especially in the case of embedded actuators. The three different shape control algorithms would give wider options to analyse structural shape control problems integrated with piezoelectric actuators. For example, the *3DSHAPE-I* code is capable of performing inverse shape control analysis. Such capability is not available in commercial codes that offered piezoelectric analysis. The development of the *3DSHAPE-I* code would have been of profound use for the current research work if it could have been linked to *LS-DYNA* but this never materialized due to difficulties in implementation. This could, however, serve as a possible future work.
3. Chapter 7 - detailed characterization on the effects of *MFC* actuator on structural deformation using three-dimensional analysis. *MFC* actuator has been mostly used to control the behaviour of thin and flexible structural elements. The report on the effects of the *MFC* actuator on thick and stiff structural components is limited. Hence, a detail characterization on the effects of the *MFC* actuator on some standard or commonly used impact specimen was seen essential. For the present work this was considered to be important to gauge the performance of the actuator and identify a favourable laminate-actuator configuration with appreciable presence of the piezoelectric effects to be used in subsequent impact analysis.
4. Chapter 8 - detailed testing and validation on the damage predictive capabilities of the new damage model implemented into *LS-DYNA* with respect to low velocity impact

investigation. Though this model has been verified through a number fracture tests, validation for impact test was only done using a simplified *Boeing* and *CRAG* impact specimens. No detail testing of the model is available in the literature. A detailed impact testing has found that this model is both numerically stable and accurate. The testing also managed to highlight the deficiencies in a similar existing damage model in *LS-DYNA* finite element code.

5. Chapter 9 - characterization of the piezoelectric effects on the impact force and displacement histories. The impact response of the laminate-actuator system has been characterized using simple actuation techniques which include extension, compression and bending. From the tests conducted in this chapter, it has been found that the impact force and displacement of a laminate-actuator system could be reduced by regulating the voltages to the actuators. This might serve as useful design information not only for impact related problems but also in other analyses for which the effects of the external disturbances, of similar nature, must be reduced.
6. Chapter 10 - numerical validation of delamination reduction using the technique of impact force reduction demonstrated in Chapter 9. To the best of the authors' knowledge this is the first ever study that have demonstrated and verified the capabilities of piezoelectric actuators to be used as a tool to reduce delamination in composite laminates subjected to low velocity impact by incorporating damage model. However, the validation could be presented for limited cases only. This was due to limitations in the proposed control strategy and also with the existing piezoelectric materials. Although there are limitations to the practical implementation of the proposed technique, assuming powerful piezoelectric actuators are not impossible in near future, structural components integrated with piezoelectric actuators could be seen as additional and active damage control options and this study could be of valuable use for such attempts. In addition, in such circumstances the implemented piezoelectric actuation model would allow numerical test to be conducted with high level of accuracy to precede any experimental validation. If the proposed strategy of delamination reduction using piezoelectric actuator could be materialized, it has a wide range of application particularly in aerospace and automotive industries where extensive amount of laminated composite materials are being used and continuously exposed to threats that could lead to delamination.

1.4 Publications

1. Shaik Dawood, M. S. I., Iannucci, L., and Greenhalgh, E. S. (2008). Three-dimensional static shape control analysis of composite plates using distributed piezoelectric actuators. *Smart materials and structures*, 17(2).
2. Shaik Dawood, M. S. I., Iannucci, L., Greenhalgh, E. S., and Ariffin, A. K. (2010). Low velocity impact induced delamination control using MFC actuator. *Key engineering materials.* (Accepted for publication).

Chapter 2

Low velocity impact on composites - a review

2.1 Chapter introduction

The objective of this chapter is to provide an overview on the analysis of low velocity impact on composite laminates. The discussions include brief classifications of different types of composite materials, their applications and related advantages and disadvantages. As the main focus of this research is to numerically investigate the use of piezoelectric materials to reduce delamination in fibre reinforced composite laminates subjected to low velocity impact, subsequently, a review on impact dynamics and the commonly used failure models in *LS-DYNA* to predict delamination are presented.

The main outcomes of this chapter are highlights on the deficiencies of the existing damage models used in *LS-DYNA* and the identification of a suitable damage model to be used to predict delamination in composite laminates subjected to low velocity impact.

2.2 Composite materials

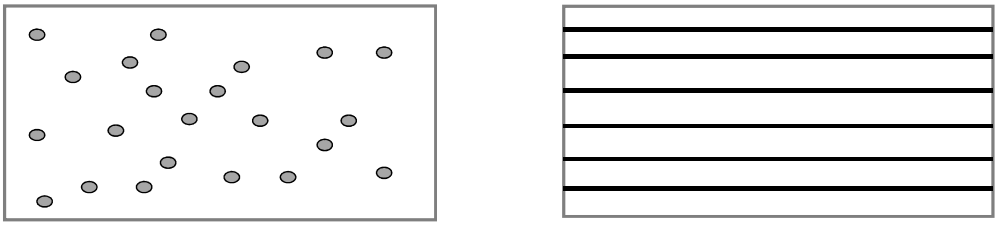
The need for high performance materials, particularly in the aerospace and military applications, has led to the development of many new materials that are capable of offering excellent strength and stiffness characteristics (Jones, 1999). The performance level of a

structural component mostly depends on its weight, strength and stiffness (Park et al., 2009). Conventional materials such as metallic alloys can be made to have improved strength and stiffness but they do not offer substantial weight reductions (Soutis, 2005). However, in most cases, particularly in the aerospace industry, these modest improvements are not viable options due to design and performance constraints (Yan et al., 2008).

Composite technology allows the development of high performance materials that are lighter and with superior strength and stiffness characteristics known as composite materials (Agarwal and Broutman, 1990). A composite material is basically formed by combining materials with different properties and the resulting material has forms, shapes and behaviours that are different from its constituent materials (Jones, 1999). A typical example of composite material would be concrete which is made through a mixture of sand, rock, cement and water (Jones, 1999). Concrete exhibits properties those are different from its constituent materials in terms of strength, stiffness and load bearing capacities. There are various types of composite materials and these are discussed in the following sections.

2.3 Classifications of composite materials

Over the years, many different types of composite materials have been developed. However, the advanced types are the particulate and the fibrous composites. These different categories of composite materials are illustrated in Figure 2.1 (Rosato and Grove, 1996).



(a) Particulate composite (b) Unidirectional fibre composite

Figure 2.1: Types of composite materials (Rosato and Grove, 1996)

2.3.1 Particulate composite

An advanced category of particulate composite is the *Metal Matrix Composite* (*MMC*). *MMC* consists of matrix materials which are normally metals with reinforcement materials made of

ceramics (Clyne and Withers, 1993). The ductility and toughness of the metallic materials and the high strength and stiffness of ceramic materials make *MMC* superior in performance in comparison to conventional metals (Ibrahim et al., 1991).

Aluminium Matrix Composite (*AMC*) is a representative example of *MMC*. The matrix material in an *AMC* is aluminium while the reinforcement is made of silicon carbide particles (Rawal, 2001). It has most of the characteristics of a typical composite material such as improved strength and stiffness while maintaining its isotropic behaviour, i.e., directional independent properties (Rawal, 2001). *MMC*s are widely used in many applications ranging from sport equipments to advanced aerospace components such as landing gears (Rawal, 2001).

2.3.2 Fibre reinforced composite

The next important category is the fibre reinforced composites. A fibre reinforced composite is essentially made of fibres embedded in a tough matrix material (Jones, 1999). The fibres serves as the main reinforcement materials from which the majority of the strength and stiffness are obtained while the matrix material acts as bonding and load transfer medium for the fibres in addition to serving as protective layer from environmental conditions (Reddy, 2004).

The most commonly used fibre materials are glass, carbon, graphite and Kevlar while the matrices are mainly made of polyesters and epoxies (Jones, 1999). Figure 2.2 shows the comparison of specific strength and stiffness characteristics of some of the commonly used fibres with other conventional materials such as steel and aluminium (Daniel and Ishai, 2006). From Figure 2.2 it can be seen that carbon fibre offers superior properties in terms of specific strength and stiffness compared to other materials and probably the reason for the widespread use of this material in many weight sensitive applications such as in fighter aircrafts, Figure 2.3 (Aeronautics Department, Imperial College London). Carbon fibre composite contributes to almost 40% of Eurofighter's weight (Deo et al., 2001).

Unlike a particulate composite a fibrous composite has properties such as strength and stiffness that are directional dependent with the highest level of performance displayed in the direction of the fibres.

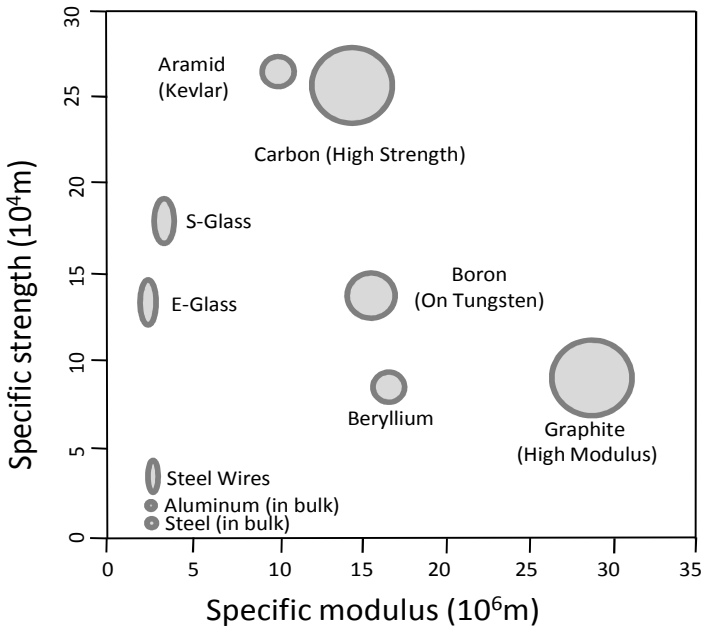


Figure 2.2: Specific strength and stiffness properties (Daniel and Ishai, 2006)

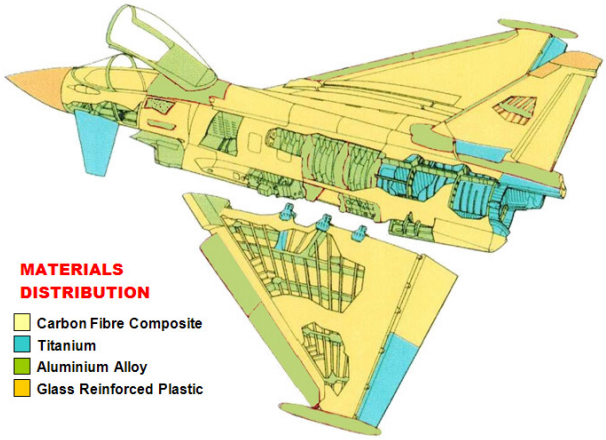


Figure 2.3: Eurofighter - material distributions (Aeronautics Department, Imperial College London)

2.3.3 Laminated composite material

Though fibre reinforced composites exhibit exceptional performance in the fibre direction, they become vulnerable to loads that are not aligned to the fibres especially if the loads are perpendicular to the fibre direction as the strength and stiffness in this direction are extremely low (Agarwal and Broutman, 1990), Figure 2.4.

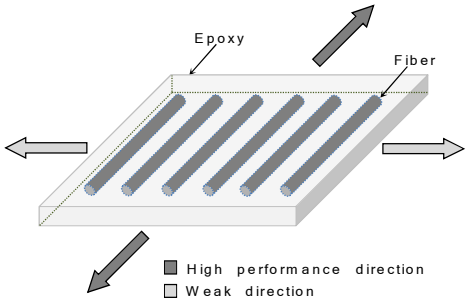


Figure 2.4: Characteristics of a unidirectional fibrous composite

To overcome this difficulty, several layers of fibrous composites oriented at different angles can be stacked together to form what is known as the laminated composite (Jones, 1999), Figure 2.5. A laminated composite can be used to improve the properties of the laminate in multi directions, Figure 2.5.

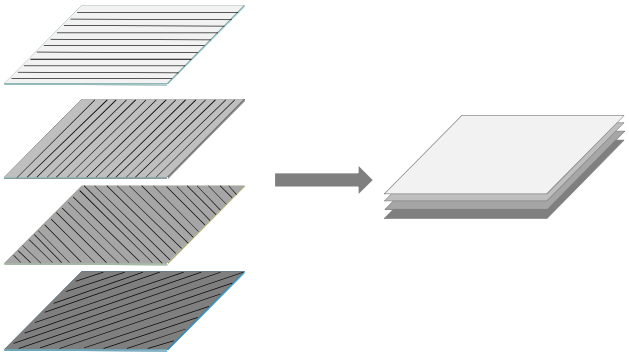


Figure 2.5: Laminated composite (Jones, 1999)

However, composite materials have marked anisotropy. The degree of anisotropy in a laminated composite can be reduced by adopting proper lamination scheme. Based on the classical plate theory the force resultant, N, and moment resultant, M, of a laminated composite can be written as (Reddy, 2004):

$$N = A\varepsilon_o + B\varepsilon_f$$
$$M = B\varepsilon_o + D\varepsilon_f \qquad (2\text{-}1)$$

where:

A : extensional stiffness

D : bending stiffness

B : extension-bending coupling stiffness

ε_o : mid-plane strain

ε_f : curvature

Equation (2-1) shows that composite materials can exhibit coupling between the extension and bending deformations, which is described by the coupling stiffness term B. The coupling term indicates that a laminate that is subjected to purely extensional load will not only extend but also bend. Likewise, a laminate that is subjected to bending loads will not only undergo bending deformation but also extension. The presence of this behaviour in a laminated composite is associated with its stacking sequence. In general the stacking sequence of a laminated composite can be of the followings (Jones, 1999):

1. Symmetric laminate
2. Anti-symmetric laminate

An anti-symmetric laminate would couple the extension and bending deformations as the coupling term B will not be zero. The coupling term can be made to be equal to zero by having a symmetric lay-up. A symmetric lay-up consists of fibre layers oriented at different angles with symmetry about the mid-plane of the laminate. Typical examples of symmetric laminates are (0/90/0) – cross-ply and (45/-45/90/0/0/90/-45/45) – quasi-isotropic. In these laminates the coupling action will be zero. A balanced quasi-isotropic laminate is the commonly used arrangement to approximate isotropic material behaviour (Farooq and Gregory, 2009). This is because the in-plane properties of a balanced quasi-isotropic laminate can be made to closely resemble isotropic conditions as the extensional stiffness coefficients A_{11} and A_{22} can be made to be equal (Farooq and Gregory, 2009). However, the bending stiffness of a balanced quasi-isotropic laminate does not correlate to that of isotropic material conditions as $D_{11} \neq D_{22}$ thus making it more vulnerable to bending loads such as impact (Cho and Zhao, 2002).

A study conducted by Cho and Zhao (2002) has shown that delamination is more prominent in laminated composites in which the mismatch in the bending stiffness is relatively high. Nevertheless, a laminated fibre reinforced composite can be made to exhibit specific properties that are superior to conventional metals or particulate composites (Jones, 1999). A laminated composite is not necessarily made of fibrous composites as other materials such as metals, alloys and even *MMC* can be used to construct laminated materials.

However, the scope of this review in line with the objectives of the current work is limited to fibre reinforced composite materials only.

2.4 Impact on composite materials

Composite materials do have several disadvantages. A major setback with the use of composite materials is their poor impact performance (Davies and Olsson, 2004). Though the in-plane stiffness and strength can be significantly improved by adopting proper lamination scheme and appropriate choice of fibre and matrix materials, composite materials are still vulnerable to incident loadings such as impact as the strength and stiffness in the incident direction mostly depend on the laminate reinforcement along the thickness (Abrate, 1998).

Impact is an inevitable occurrence in the aerospace environment. Typical examples would include runway debris impacting aircraft structures during takeoff and landing, bird strike during flight, tool drops and accidents during component manufacturing and handling (Abrate, 1998). The impact response of composite materials has been shown to be considerably different to that of isotropic materials. Beyond a damage sustaining limit most isotropic materials dissipate energy via plastic deformation, however, composite materials have complex failure mechanisms which are normally displayed in the form of damages such as matrix cracks, delaminations and fibre breakages at various locations of the laminate (Iannucci, 2006). These damages are typical for the case of non-penetrating impact such as low velocity impact. In the case of high velocity impact a complete perforation of the target may also ensue (Kasano, 1999).

The formation of matrix cracks is quite extensive during an impact but has been shown not to have significant contribution to the overall reduction of the structural strength (Abrate, 1998). However, severe matrix cracking will ultimately lead to delamination, which is considered as the major contributor to performance loss in composite laminates (Abrate, 1998). If the damage is internal, they will remain hidden in structural component during its service life and pose severe threat to its integrity and performance. Internal damages are commonly referred to as *Barely Visible Impact Damage* (*BVID*) (Cantwell and Morton, 1992).

The research publications on the subject of low velocity impact response of composite materials are extensive. Some relevant publications to the current work are reported here. Abrate (1991; 1994; 2001), Richardson and Wisheart (1996) and Davies and Olsson (2004)

have provided detail reviews on some of the important works that have been published in the area of low velocity impact of composite materials. Based on these reviews, the study on low velocity impact of composite materials can be broadly divided into the following areas: impact dynamics, contact laws, stress analysis, damage modelling and damage tolerance. Two of the relevant topics to the current research work would include damage modelling and damage tolerance. However, the other topics are also briefly discussed.

2.5 Impact dynamics

The impact response of a composite material is strongly associated with its material properties, stacking sequences, geometric and boundary conditions as well as impactor properties such as material, shape and impact energy (Robinson and Davies, 1992; Abrate, 1998). The material properties, stacking sequences and geometric as well as boundary conditions contribute to the overall strength and stiffness characteristics of the target material and changing any of these parameters or conditions would affect the contact force history (Abrate, 1998). A stiff laminate would have a shorter contact time as compared to a flexible laminate. However, increasing the stiffness would increase the contact force. A flexible laminate would result in longer contact duration and reduce the peak contact force. Both the contact duration and the peak contact force affect the stress formation at the location of impact and subsequent distribution in the entire structure (Liou, 1997; Chun and Lam, 1998).

Liou (1997) investigated the response of different cross ply laminates subjected to impact by a rigid cylinder with spherical head using a three-dimensional finite element program. He found that the formation of stresses during an impact was attributed not only to the impact load but also to the flexure waves which propagate the stresses. On the surface level, the in-plane and the normal stresses were found to be highest at the contact region while the transverse shear stresses to be highest away from the impact point. However, in comparison to the in-plane stresses, the magnitudes of the transverse shear stresses were found to be much lower. Chun and Lam (1998) conducted a similar impact investigation on fully clamped composite plates. They found that the transverse shear stresses underwent more oscillation during impact and could instigate delamination.

The anisotropy of composite laminates is associated with the material properties and stacking sequences. Stacking sequence such as balanced quasi-isotropic layup can be used to reduce the in-plane material anisotropy. Nevertheless, it still poses a problem when bending

loads are applied and impact is one of them. Adjacent plies with different stacking sequences would result in a bending stiffness mismatch (Liu, 1988). The bending mismatch has been shown to augment with increasing fibre angles between the adjacent plies and this would in turn affect the overall stiffness of the laminate (Liu, 1988). Cho and Zhao (2002) have found that laminates with wide disparity in their bending stiffness resulted in larger damage areas than the ones with lower disparities. They have shown that for an unbalanced quasi-isotropic laminate reducing the mismatch in the bending stiffness by rearranging the laminate lay-up reduced the damage area by almost 85% (Cho and Zhao, 2002).

The effect of laminate thickness is also very significant in determining the impact response of a composite laminate. A thick laminate is generally stiffer and have a shorter contact time and higher peak contact force as compared to a thin laminate (Abrate, 1998). Schoeppner and Abrate (2000) found that the increase in damage area was higher and abrupt in thick laminates as compared to thin laminates once the threshold force has been exceeded, suggesting that the size of the delaminated zone was proportional to the laminate thickness. A thick laminate would contribute to the bending stiffness mismatch between adjacent plies of fibre oriented at different angles (Liu, 1988). This could have been the contributing factor to a larger and a more abrupt damage formation within the thick laminates as observed by Schoeppner and Abrate (2000).

The nature of the impactor has also a major influence on the impact response of a composite laminate. A small mass impactor of the same kinetic energy of a heavy mass impactor induces entirely a different kind of response on the same target material (Olsson, 2003). In the former case the impact response is controlled by the target characteristics near the contact region while in the latter case the impact response depends on target characteristics as a whole including the boundary conditions (Olsson, 2003). A small mass impactor has been shown to result in higher impact loads and earlier damage initiation as compared to a heavy impactor with the same kinetic energy (Olsson, 2000). The effects of different impactor sizes, shapes and impact energies have been investigated by Mitrevski et al. (2005). They concluded that blunt impactors such as a hemispherical or sphere primarily caused non penetrating barely visible damages such as matrix cracks and delaminations, while sharp impactors such as cones resulted in permanent indentation or penetration of the target.

Theoretical and numerical investigations require contact models to describe the local interaction between the impactor and the target during an impact event. The pressure distribution at the contact region affects the stress formations and distributions in the target (Liou et al., 1996). A commonly used contact law in composite impact analysis is the Hertz

contact law which was originally developed for isotropic or homogeneous materials (Abrate, 1998). However, several modified forms have been proposed and extensively used in almost all cases of composite impact related studies. Most finite element codes such as *LS-DYNA* offer automatic contact definitions that could be used to analyse problems where complex states of contact may exist (*LS-DYNA* Theory Manual, 2006).

2.6 Damage evolution due to low velocity impact

As described earlier the threats caused by low velocity impact are of more concern due to the fact that these threats could remain in structural components during their service life. Various methods are in use to design more robust and damage tolerant structures, however, an effective design would require comprehensive understanding on the factors that contribute to the formation of damage (Greenhalgh and Hiley, 2003).

Low velocity impact can be classified as a non-penetrating impact and the damage mostly constitute matrix cracking, delamination and fibre breakage (Richardson and Wisheart, 1996). Figure 2.6 shows the damage patterns that comprise the different damage modes that are typical for composite materials under impact condition (Iannucci, 2006).

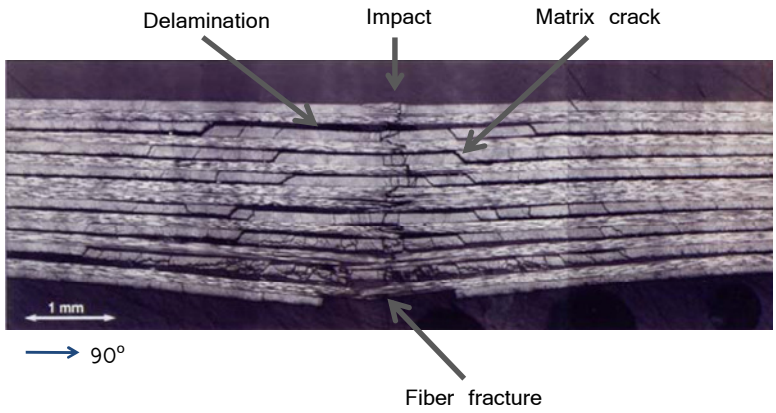


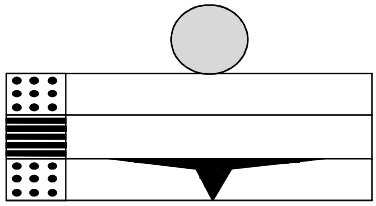
Figure 2.6: Impact induced damages in composites (Iannucci, 2006)

2.6.1 Matrix cracking

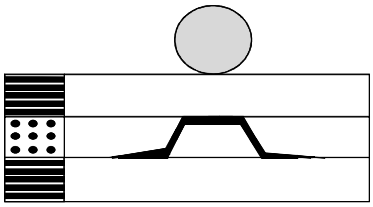
Impact causes compression in the through thickness direction in the target material at the contact region and this initiates an intralaminar shear damage known as matrix cracking and has been observed to be the first mode of damage to take place (Choi and Chang, 1992).

Matrix cracking can be typically described as the debonding process between the fibre and matrix materials due to mismatch in their material properties (Richardson and Wisheart, 1996). For a unidirectional laminate matrix cracking can be categorized into tensile and shear cracks and these are illustrated in Figure 2.7 (Abrate, 1998).

The formation of a tensile crack is attributed to the in-plane normal stresses. Tensile crack starts to form when the in-plane stresses exceed the ply's transverse tensile strength (de Freitas et al., 2000). This observation holds for thin laminate as the back surface to impact is normally under very high tensile stresses (Abrate, 1998). The formation of a shear crack is attributed to the development of large transverse shear stresses during an impact (Abrate, 1998). Both crack modes will appear inclined and perpendicular to the fibre direction of the respective layer in which the formation of the cracks takes place, Figure 2.7 (Abrate, 1998).



(a) Tensile crack (Laminate view – 90/0/90)



(b) Shear crack (Laminate view – 0/90/0)

Figure 2.7: Types of matrix cracks (Abrate, 1998)

The formation of matrix crack is very extensive and normally appears in a complicated pattern which makes the prediction very difficult (Abrate, 1998). Though matrix cracking does not cause significant degradation to the structural performance characteristics, once a critical level is reached, it will initiate the formation of interlaminar crack known as delamination (Choi and Chang, 1992).

2.6.2 Delamination

Delamination can be been described as an interlaminar crack that appears at the interface of two adjacent plies with dissimilar properties (Richardson and Wisheart, 1996). Choi and Chang (1992) have suggested that delamination is preceded by critical formation of matrix cracking though it is primarily instigated by interlaminar shear stresses (Davies and Olsson, 2004).

The formation and propagation of delamination could be enhanced by the mismatch in the bending stiffness of the adjacent plies (Liu, 1988). As the bending stiffness is a function of elastic modulus and layer thickness, adjacent plies with large disparities in their flexural rigidities as well as with considerable layer thickness have been shown to be more susceptible to delamination damage as compared to adjacent layers with lower disparities (Cho and Zhao, 2002).

Delamination causes significant degradation of structural properties especially to its post impact compressive strength. Laminates with severe delamination can lead to global and local instabilities such as buckling when exposed to post impact compressive loads (Richardson and Wisheart, 1996). As such, delamination could be distinguished as a more detrimental threat to structural performance and integrity than matrix cracking (Abrate, 1998).

2.6.3 Fibre failure

Under excessive bending or compression fibres may tend to split or buckle (Richardson and Wisheart, 1996). This depends on the nature of the stresses induced by the impact load on the laminate. Very high tensile stresses may cause fibre breakage and such failure is common in the case of thin laminates (Abrate, 1998).

Fibre failure may also be induced directly under the impact zone and is mostly due to shear forces (Richardson and Wisheart, 1996). It has been reported that fibre breakage may lead to more catastrophic damage such as penetration of the target, but under low velocity impact this may be a rare occurrence since this particular damage mode has received very little attention in low velocity impact investigations (Richardson and Wisheart, 1996).

2.7 Failure analysis

Experimental investigations have revealed quite a lot of information on the impact response of composite laminates specifically on the damage formation aspect. This information has been used to assist the development of appropriate numerical damage models for impact investigations.

From the numerical perspective, the damage formation in composites can be predicted and analysed using several approaches. The commonly used ones are the stress based methods, fracture mechanics and interface damage models (Davies et al., 1997). These different approaches are discussed in the following sections.

2.7.1 Stress based failure models

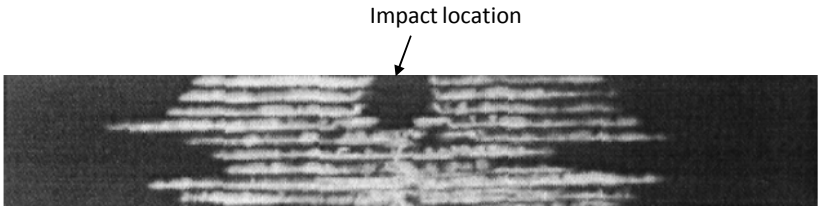
Stress based failure models have been widely used by many researchers to predict damages such as matrix cracking, delamination and fibre failure in composite materials. Stress based methods rely on the strength of the materials to predict damages under a given loading condition. There are quite a number of stress based failure models in use which include maximum stress theory, maximum strain theory, Tsai-Hill theory, Tsai-Wu theory and Chang-Chang theory (Orifici et al., 2008).

Aslan et al. (2003) conducted experimental and numerical investigations on the low velocity impact response of clamped cross ply laminates. The numerical investigation was carried out using finite element method employing the Choi and Chang (1992) failure criterion to predict delamination. Their numerical prediction of the impact force curve was close to the experimental prediction in the case of heavy mass impact which in this case was 2.6kg. However, in the case of 0.135kg impact, the numerical prediction of the impact force curve deviated from their experimental prediction with the maximum peak occurring at different contact period. Their investigation also highlighted the delamination sizes predicted by the failure model for different plate sizes but no experimental comparisons were given to validate the accuracy.

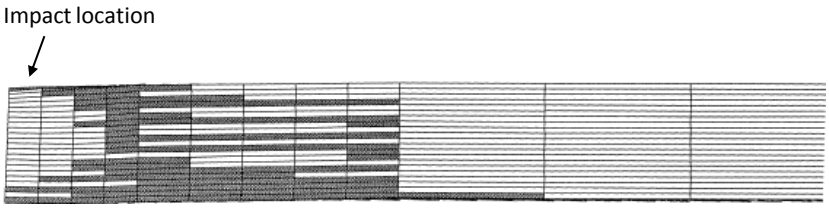
Her and Liang (2004) investigated delamination and matrix cracking induced by low velocity impact on cross ply and quasi isotropic laminates using *ANSYS/LS-DYNA* finite element code. The failure analyses were also based on the Choi and Chang (1992) failure

model for matrix crack and delamination. They have shown that the failure model was able to capture the delamination pattern accurately but there were no experimental validations.

Hou et al. (2000) examined impact induced delamination and other damage modes in composite laminates, both experimentally and numerically. The numerical investigation was performed using *LS-DYNA* explicit solver. They modified the existing failure criteria in *LS-DYNA* for more accurate description of the different damage modes. Figure 2.8, obtained from reference Hou et al. (2000), shows the predicted delamination pattern along the through thickness direction in the laminate. The figure indicates that the failure criteria approach offered a modest damage prediction. In Figure 2.8a the delamination is represented by the white shade while in Figure 2.8b by black shade.



(a): Experimental prediction



(b): Numerical prediction

Figure 2.8: Predicted delamination in composite plate at 6.5J impact (Hou et al., 2000)

Some of the stress based failure models have been made available in Finite Element Analysis (*FEA*) software such as *LS-DYNA* and *Abaqus*. The stress based failure models available in *LS-DYNA* are based on the Chang-Chang failure criteria for matrix and fibre failure (Chang and Chang, 1987) and for delamination the failure polynomial is given as (Hou et al., 2000):

$$e_d^2 = \left(\frac{\sigma_{33}}{Z_T}\right)^2 + \left(\frac{\sigma_{23}}{S_{23}}\right)^2 + \left(\frac{\sigma_{31}}{S_{31}}\right)^2 \tag{2-2}$$

where:

e_{d}	:	failure index for delamination
σ_{33}	:	out of plane through thickness normal stress
σ_{23} and σ_{31}	:	out of plane through thickness transverse shear stresses
Z_{T}	:	out of plane through thickness normal strength
S_{23} and S_{31}	:	out of plane through thickness transverse shear strengths

Delamination is anticipated when the failure index is greater or equal to one. In the above expression delamination is attributed to both the compressive and peeling through thickness stresses as σ_{33} is independent of the sign. However, through thickness compressive stresses do not contribute to delamination (Hou et al., 2000). This could be seen as one of the main disadvantages of the model when employed to predict delamination in composite laminates subjected to low velocity impact as the contact stress will be compressive. Hou et al. (2000) modified Equation (2-2) by imposing $\sigma_{33} \geq 0$, hence the results shown in Figure 2.8b agreed reasonably with their experimental prediction, Figure 2.8a.

The Choi and Chang failure model (Choi and Chang, 1992) for delamination differ with respect to the first term appearing in the failure polynomial in comparison to the Equation (2-2) in addition to the empirical constant term. The Choi and Chang failure model reads (Choi and Chang, 1992):

$$e_d^2 = D_a \left(\left(\frac{\sigma_{22}}{X_T} \right)^2 + \left(\frac{\sigma_{23}}{S_{23}} \right)^2 + \left(\frac{\sigma_{31}}{S_{31}} \right)^2 \right) \tag{2-3}$$

where:

σ_{22}	:	in-plane transverse stresses
X_T	:	transverse tensile strength for $\sigma_{22} \geq 0$, and transverse compressive strength for $\sigma_{22} < 0$
D_a	:	empirical constant determined from experiment

The above equation predicts delamination growth initiated by matrix cracking. Hence the use of the above model requires matrix crack to be modelled simultaneously.

Nevertheless, there are many inherent problems associated with stress based methods. Stress based failure models are mesh dependent for accurate damage predictions (Iannucci, 2006). In a dynamic loading condition such as impact, the stress based method could become numerically unstable and lead to premature failure indication and propagation (Iannucci, 2006). This could be the reason for the discrepancies observed in the impact investigation by Aslan et al. (2003). The small mass impact indicated a high degree of fluctuation in the load level which could make the stresses rate dependent and cause numerical instability in the system as a result of coarse mesh used in the analysis.

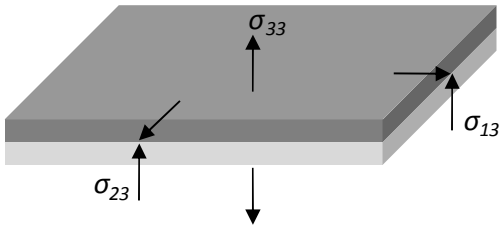
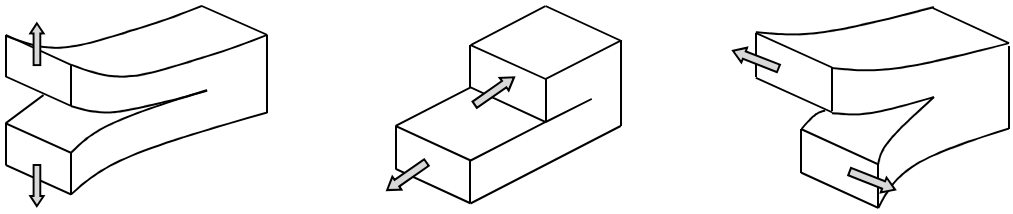


Figure 2.9: Stresses inducing delamination (Hou et al., 2000)

2.7.2 Fracture mechanics approach

The stress based methods cannot be used to model scale effects effectively in brittle materials (Davies et al., 1997). Hence, the fracture mechanics approach has been extended to investigate damage formation in composite materials (Davies et al., 1997). The fracture mechanics method was developed based on the assumption that the delamination is effectively an edge crack occurring at the interface and its propagation depends on the strain energy release rates (Iannucci, 2006). The use of fracture mechanics needs a pre-existing delamination front or initial flaw in the analysis before the prediction of its propagation can take place. However, in problems such as impact where the crack front is not known, the fracture mechanics approach may not be appropriate since the energy release rate for the damage propagation depends on the size of the initial crack (Davies et al., 1997).

Delamination can be caused by different fracture modes and these are the peeling (mode I), shear (mode II) and mixed (mode III), Figure 2.10 (Armas, 2008). Mode I delamination is attributed to the peeling forces as shown in Figure 2.10a. Mode II delamination is induced by shear force while mode III delamination is attributed to mixed mode loading condition.



(a) mode I (b) mode II (c) mode III

Figure 2.10: Fracture modes (Armas, 2008)

The use of fracture mechanics to predict the different fracture modes requires the information on the fracture energy and the energy release rate during the course of damage associated with each of the modes. The energy associated with each of the fracture modes can be determined through a number of fracture tests. For mode I, the standard test to determine the fracture toughness energy is the *Double Cantilever Beam* test (*DCB*), the mode II fracture toughness energy can be determined using *End Notched Flexure* test (*ENF*), while, for the mixed mode case, the fracture toughness energy can be determined using *Mixed Mode Bending* test (*MMB*) (Armas, 2008).

The energy release rate during the course of damage for an edge delamination can be derived using the *Virtual Crack Closure Technique* (*VCCT*) (Rybicki and Kanninen, 1977). This technique is an extension to the original crack closure method proposed by Irwin (1958). For the laminate system shown in Figure 2.11, the energy release rates associated with each mode can be determined as follows (Krueger, 2002):

$$G_I = -\frac{1}{2b\Delta a} F_{ef}^{z}(w_c - w_d)$$

$$G_{II} = -\frac{1}{2b\Delta a} F_{ef}^{x}(u_c - u_d) \qquad (2\text{-}4)$$

$$G_{III} = -\frac{1}{2b\Delta a} F_{ef}^{y}(v_c - v_d)$$

where:

b	:	element width
Δa	:	element/crack length
u_c,v_c,w_c,u_d,v_d,w_d	:	nodal displacements

F_{ef} : equivalent force required for crack closure at point *c* and *d*

In *VCCT* it is assumed that the nodal displacements behind the crack tip are equivalent to the nodal displacements at node *cd* (Krueger, 2002). Therefore the forces required to close the crack are then identical to the forces at the crack tip. Delamination will propagate if the energy release rates of any of the individual modes exceed their critical values as follows (Reeder, 1992):

$$G_I \geq G_{IC}$$
$$G_{II} \geq G_{IIC} \tag{2-5}$$
$$G_{III} \geq G_{IIC}$$

However, delamination may also occur if the sum of the energy release rate of the respective components exceeds the critical fracture toughness G_c (Krueger, 2002):

$$G_I + G_{II} + G_{III} \geq G_C \tag{2-6}$$

In the above equation the fracture toughness is assumed not to be a function of mixed mode ratio hence the above criterion is only applicable if G_{IC} is equal to G_{IIC} (Reeder, 1992). However since G_{IC} is not equal to G_{IIC} for most materials (Reeder, 1992) several modified forms have been proposed to account for the mixed mode ratios. One of them is the power law, Equation (2-7), which will be described in the following section. As mentioned earlier, the disadvantage of the fracture mechanics approach is that it could only be used to predict growth of delamination based on a pre-existing crack and could not be used to detect damage initiation (Davies et al., 1997).

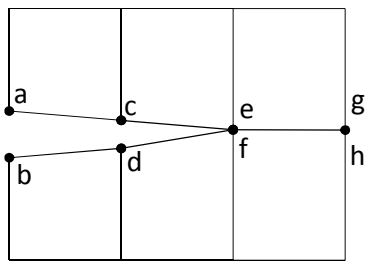


Figure 2.11: Sublaminate with delamination (Krueger, 2002)

2.7.3 Damage mechanics

The damage mechanics approach is based on continuum damage mechanics. In continuum damage mechanics, the micro mechanical process such as growth of microcracks can be treated at macro level as a distributed damage over a representative volume (Williams and Vaziri, 2001). An important characteristic of the damage mechanics approach is that it effectively combines the advantages of the stress based approach with fracture mechanics to predict the onset of damage and its propagation (Iannucci, 2006). The damage mechanics approach completely eliminates the need for initial flaw or crack front in the analysis (Iannucci, 2006). Hence, it can be used to predict damage of a completely intact material system with no damage to its complete disintegration (Iannucci, 2006).

The damage mechanics approach is introduced using a cohesive damage zone model where the cohesive damage zone describes the relationship between the traction and displacement at the interface where damages such as delamination may occur (Borg et al., 2004). For the three different crack modes illustrated in Figure 2.10 the traction-displacement relationships are illustrate in Figure 2.12 based on a bilinear law. The other forms of traction-displacement laws are illustrated in Figure 2.13.

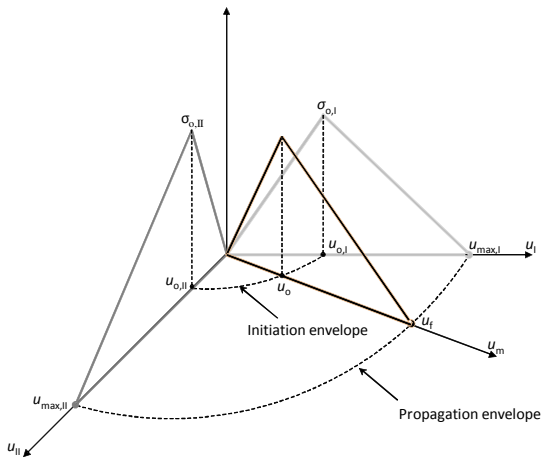
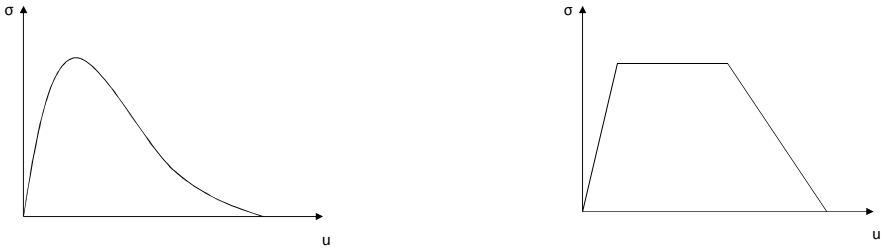


Figure 2.12: Mixed mode bilinear damage curve (*LS-DYNA* keyword user's manual, 2007)

Pinho et al. (2006) investigated the numerical stability of bilinear and third-order polynomial laws using a *DCB* test. At failure, the bilinear law was found to be numerically unstable at high load rates especially when higher values of initiation traction were used as these resulted in sudden and bigger crack jump. The instability in the bilinear law was

attributed to the discontinuity at the peak traction due to sudden change in the slope after damage has initiated (Pinho et al. 2006). The third-order polynomial law demonstrated a smoother crack prediction as there was no discontinuity in the traction-relative displacement before and after damage.



(a) Exponential law (b) Trapezoidal law

Figure 2.13: Traction-displacement laws (Zou et al., 2003)

Alfano (2006) conducted a similar investigation and found that the exponential law was numerically stable than the trapezoidal and bilinear law, however, concluded that bilinear law was numerically efficient and accurate.

The damage mechanics approach uses different criteria for damage initiation and propagation. Under mixed mode loading condition damage may initiate before individual loads reached their critical value. A quadratic damage initiation criterion under mixed mode loading condition reads (Ye, 1988):

$$\left(\frac{\langle\sigma_I\rangle}{\sigma_{o,I}}\right)^2 + \left(\frac{\sigma_{II}}{\sigma_{o,II}}\right)^2 + \left(\frac{\sigma_{III}}{\sigma_{o,III}}\right)^2 = \psi \qquad (2\text{-}7)$$

In the above equation damage initiation corresponds to ψ=1. The Macauley bracket restricts σ_I to the tensile direction as no delamination will be induced under pure compression state.

Since Equation (2-6) is only applicable for materials with G_{IC} equal to G_{IIC}, a power law can be used to predict the propagation of delamination with different mode I and mode II fracture toughness like composite materials. Under the mixed mode condition the damage propagation could be established using the following power law equation based on the fracture energy of the system as follows (Reeder, 1992):

$$\left(\frac{G_I}{G_{CI}}\right)^{\lambda} + \left(\frac{G_{II}}{G_{CII}}\right)^{\lambda} + \left(\frac{G_{III}}{G_{CIII}}\right)^{\lambda} = 1 \quad (2\text{-}8)$$

In the above equation, it can be seen that the propagation of damage is normalized according to the respective fracture toughness associated with each modes unlike in Equation (2-6) where no mixed mode is allowed. The value of λ is normally chosen between 1 and 2. For λ=1, the above equation is reduced to linear propagation criterion and a quadratic interaction is described by λ=2. The damage mechanics approach has been used by many researchers to predict delamination in composite laminates subjected to low velocity impact.

Amaro et al. (2009) investigated the effects of different boundary conditions on the impact response of carbon/epoxy cross ply laminates. They used a quadratic damage initiation criterion to predict damage initiation while damage propagation was modelled using a linear energy formulation. The constitutive model was bilinear. The accuracy of the numerical prediction was validated with their experimental findings with a maximum error margin of 15%. They attributed the discrepancies to other damage modes, such as matrix cracking which was not included in the analyses.

Aymerich et al. (2009) conducted a similar investigation to predict delamination and matrix cracking on simply supported clustered and dispersed cross ply laminates. They have also used the quadratic failure criterion for damage onset and linear energy relationship for damage propagation. Amaro et al. (2009) reported that the discrepancy between the experimental and numerical prediction was attributed to the formation of matrix crack which was not modelled in their numerical studies. In the study by Aymerich et al. (2009) bending crack was modelled by placing vertical cohesive elements parallel to the bottom 0^o ply. In the case of clustered laminates, their numerical model gave accurate prediction of the damage, both, in terms of size and shape of the delamination. However, in the case of dispersed laminates, their numerical model gave fair prediction with some noticeable differences at certain interfaces.

Iannucci (2006) has investigated the formation of damages in quasi-isotropic laminate using cohesive based damage model for delamination and the Chang-Chang failure model for other in-plane damage modes. The cohesive based damage model was coded into *LS-DYNA* through its user defined material subroutine. The laminate was modelled using continuum shell element with a single interface at the laminate centre. Two different impact energy levels were considered in the investigation, i.e., 0.67J and 3.11J. In the case of the lower impact energy, the numerical model predicted a small trace of delamination though in actual

experiment (Zhang et al., 1999) no delamination was found. This was assumed to be caused by the simplification assumed in the numerical model, where delamination was only modelled at the centre, i.e., at the 0/0 interface. Furthermore, when the initiation stress for mode II was increased from 100MPa to 125MPa, the numerical prediction confirmed the experimental findings of Zhang et al. (1999). At a 3.11J impact, fibre failure was noticed in addition to delamination.

A similar finding was reported by Zou et al. (2002). They conducted a numerical static indentation test to predict delamination in an edge clamped cross ply laminates using a cohesive based damage model. The experimental data for comparison was obtained from Finn and Springer (1992). Due to lack of material data for the interface parameters, they first assumed a higher G_{CII} value (0.315kJ/m^2) and in this case their numerical prediction contradicted the experimental finding reported by Finn and Springer (1992). They later used a smaller value (0.25kJ/m^2) for the critical energy release rate and had a much closer prediction to the experiment. The findings reported by Zou et al. (2002) and Iannucci (2006) confirmed that in a quasi-static like impact condition the interface parameters associated with mode II has greater influence on the delamination size than the parameters associated with the other modes.

Borg et al. (2004) conducted numerical investigations to study the effects of interface parameters on delamination induced by low velocity impact. Their investigations revealed that the delamination size and pattern were strongly associated with the interface parameters. Isotropic delamination pattern was observed when no mode and fibre dependencies were included in the damage models. Since the only well documented critical energy and damage initiation values were at the 0/0 interface and lacking the material data at the other interfaces, they did a qualitative comparison by assuming the critical values at the other interfaces. They found that although the delamination patterns were satisfactory predicted, the size of delamination could only be accurately predicted at several interface layers.

Iannucci and Willows (2006) conducted a similar investigation using the *CRAG* impact test specimen based on the same damage model reported in (Iannucci, 2006). Two cases were considered to numerically validate the model. In the first investigation no damage model was included in the analysis. This was to investigate the elastic response of the laminate. In the second test, the laminate was divided into two sublaminates with a single interface layer at the laminate centre. The laminate with the interface showed a drop in the peak impact force indicating loss of stiffness due to damage. This was confirmed by the difference in the kinetic energy plot which was an indication on the amount of energy consumed by the failed interface

element. The analytical threshold load for damage initiation was 1210N and this compared quite well with the value predicted numerically at 1500N. The introduction of a single interface layer at the laminate centre is based on the rationale that the transverse shear stresses are highest at this location. Such modelling strategy would give a representative estimate of the maximum damage map which would serve the design purpose if only the damage estimate is the primary concern. If a realistic prediction of damage is required interface layer has to be included in between every plies and this would be computationally demanding.

Though it has been noted that the bilinear law exhibit numerical instability (Pinho et al., 2006; Alfano 2006), all the impact investigations reported in this section were based on the bilinear law for the cohesive constitutive formulation. The stability issues associated with the bilinear formulation could be overcome using refined mesh in the finite element model and appropriate choice of interface parameters such as strength and stiffness (Pinho et al., 2006).

Delamination analysis using the cohesive models requires the introduction of additional solid elements between the composite plies where delaminations are anticipated. The introduction of a cohesive layer substantially increases the computational time. This is because in an explicit analysis, the time step is controlled by the shortest distance between two nodes within the *FEA* model. Since the thickness of the cohesive layers is usually assumed to be one fifth of the thickness of a ply (Iannucci, 2006) this could drastically reduce the time step and increase the computational time. Another factor that affects the time step is the stiffness of the cohesive layer. Ideally the cohesive layer should be assigned with large stiffness values to capture the elastic behaviour before the onset of delamination properly. However, this would lower the time step considerably (Pinho et al., 2006).

2.7.4 Delamination threshold force

An equation was proposed by Davies and Zhang (1995) to calculate the damage threshold force for the onset of mode II delamination for quasi isotropic laminate which reads:

$$P_c^2 = \frac{8\pi^2 E_D t^3 G_{CII}}{9(1-v^2)} \tag{2-9}$$

where:

E_D : Effective Young's modulus

t : Thickness

G_{CII} : Mode II fracture energy or interlaminar toughness

v : Poisson's ratio

Equation (2-9) shows that there exists a threshold or critical force for delamination to initiate. If the impact force is below the threshold limit no delamination is to occur. However, once the threshold load is reached damage initiates and beyond which the damage growth becomes indeterminate.

The equation shows that the critical force for delamination to initiate depends on the laminate bending stiffness and mode II critical energy release rate and independent on the size of delamination. Although the equation was developed based on isotropic material condition with the assumption of small displacement and does not include the effects of shear deformation, orthotropic material behaviour and large deformation, numerous laboratory tests have shown that the threshold force predictions were within good margin of accuracy (Davies and Zhang, 1995). In a study by Suemasu and Majima (1996) it has been shown that the critical shear force for the growth of delamination in a circular orthotropic plate to be:

$$F_{cr}^2 = \frac{32\pi^2 D^* G_{CII}}{(n_d + 2)} \tag{2-10}$$

where:

D^* : Effective bending stiffness of orthotropic plate

n_d : number of delaminations

The effective bending stiffness is approximated as (Olsson, 2001):

$$D^* \approx \sqrt{\frac{D_{11} D_{22} (A^* + 1)}{2}} \tag{2-11}$$

where:

$$A^* = \frac{D_{12} + 2D_{66}}{\sqrt{D_{11} D_{22}}} \tag{2-12}$$

Both the critical force equations show that the delamination onset and propagation depend on the bending stiffness of the plate in addition to the mode II energy release rate. Hence, it is postulated that for a low velocity impact increasing the bending stiffness would increase the critical load level and consequently help to reduce the formation of delamination in composite laminates. This would be one of the possible techniques that would be explored using piezoelectric actuators to reduce impact induced delamination.

2.8 Methods of improving the impact tolerance of composite laminates

Improving the impact tolerance of composite laminates has been a topic of extensive research over the years. This section provides a brief overview on some of the methods that are commonly used to improve the damage tolerance of composite laminates. In the literature the terms impact damage tolerant and impact resistant are both used to describe the material sustainability towards impact.

Impact resistance is defined as the ability of the material to respond to impact with minimum damage, while impact damage tolerant is defined as the ability of the material to respond to impact with minimum loss in structural performance (Greenhalgh and Hiley, 2003). Hence, impact tolerance is defined as the ability of the material to respond to an impact with least damage and minimum performance loss (Greenhalgh and Hiley, 2003). Some of the methods used to improve the impact tolerance in laminated composites include using woven fabrics, stitching and z-pinning.

2.8.1 Woven fabrics

Woven fabrics have been found to reduce the possibility of delamination compared to unidirectional fabrics (Kim and Sham, 2000). This is achieved by the surrounding fills and warp yarns which limit the propagation of damage (Greenhalgh and Hiley, 2003). In addition woven fabric has higher interlaminar fracture toughness compared to unidirectional laminates (Bascom et al., 1980).

2.8.2 Stitching

Stitching is another way of reinforcing laminated composites in the thickness direction. The laminates are stitched using Kevlar or glass fibres as these are flexible materials and can be easily curved (Greenhalgh and Hiley, 2003). Stitching has been found to improve the impact resistance and impact tolerance of composite laminates by reducing the delamination force, however, the load bearing fibres can be easily damaged by needle penetration and this may increase the risk of damage as it could lead to irreversible loss of stiffness and strength (Greenhalgh and Hiley, 2003). In addition, stitching also creates voids that could lead to stress concentration (Abrate, 1998).

2.8.3 Z-pinning

Z-pinning is a process by which the reinforcing pins are driven into composite laminate using ultrasonic gun. Unlike stitching, the process of z-pinning does not damage the fibres as the fibres are displaced to accommodate the pins (Greenhalgh and Hiley, 2003). Z-pins have been found to improve the damage resistance and damage tolerance of composite laminates by limiting the propagation of damage (Greenhalgh and Hiley, 2003).

2.8.4 Piezoelectric actuators

Over the past few years piezoelectric materials have gain entry into a wide range of structural applications (Benjeddou, 2000). One of the intensive areas of their applications is in vibration control of structural components (Chee et al., 1998). When exposed to an electric field piezoelectric actuators develop actuation strains which can be used to attenuate the vibration of structures. Today, a wide range of piezoelectric materials are available and their structural related applications have been extended to include but not limited to shape control, noise and acoustic control and health monitoring (Benjeddou, 2000; Mackerle, 2003).

There are several studies that have also suggested that piezoelectric materials hold the potential to prevent damage in composite structures due to low velocity impact and these are the works by Saravanos and Christoforou (2002a; 2002b). A theoretical frame work was established by Saravanos and Christoforou (2002a) to study the impact response of composite plates through distributed active and sensory piezoelectric layers using linear quadratic

regulator and output feedback control. The study has demonstrated that piezoelectric actuators and sensors could be effectively used to minimize or reduce the impact loads and deformation of composite plates using closed loop control mechanisms for quasi static loading condition. A similar investigation was carried out on composite shells with similar outcomes (Saravanos and Christoforou, 2002b). However, these studies lacked numerical or experimental evidence to indicate damages were indeed prevented as no damages were modelled.

2.9 Finite element analysis of low velocity impact

Finite element method remains as one of the most preferred tool for structural related investigations. Consequently, many of the impact related studies on composite materials have relied on this method since experimental investigations could be time consuming and costly while closed form or analytical solutions are mostly limited to models with simple geometries, boundaries and loading conditions.

Many of the finite element investigations have relied on the use of two-dimensional models since the thickness of a laminated composite is much smaller than its in-plane dimensions. The two-dimensional models are based on plane stress assumption, assuming the normal of the mid-plane in the undeformed configuration remains normal in the deformed configuration (Jones, 1999). This assumption neglects the contribution of the out-of-plane stress components. The plane stress condition may serve as a reasonable assumption for thin laminates since the out-of-plane stresses are generally smaller compared to the dominant in-plane stress components (Jones, 1999). However, since composite materials are weak in the through thickness direction, the out-of-plane stresses could contribute toward failure as damages such as delamination due to impact are associated with the out-of-plane stresses (Chun and Lam, 1998). Hence, a three-dimensional analysis becomes necessary.

However, three-dimensional analysis would increase the computational cost considerably as in the case of laminated composites each layer needs to be modelled individually using solid elements. *FEA* code such as *LS-DYNA* offers three-dimensional analysis to be carried out using computationally inexpensive elements such as the single integration solid elements. Though the use of single integration element reduces the computational cost considerably as compared to using other higher order elements, it suffers from several drawbacks such as poor bending performance, zero energy modes and mesh sensitive solutions that would require additional numerical treatments to improve the results (*LS-DYNA* theory manual, 2006).

2.10 Delamination modelling using *LS-DYNA*

LS-DYNA is a nonlinear material and geometrical explicit time integration finite element solver. It offers several options for predicting delamination in composite materials. The most common is the use of Material Model 22. However, the problems associated with this model had already been discussed in Section 2.7.1. In *LS-DYNA* cohesive based damage models have been made available and the most established being *MAT-COHESIVE-MIX-MODE* (*MAT 138* – refer to Appendix B or *LS-DYNA* Keyword User's Manual 2007) and *MAT-COHESIVE-GENERAL* (*MAT 186*). *MAT 138* is based on bilinear traction-relative displacement formulation while *MAT 186* is similar to *MAT138* but the traction-displacement curve could be arbitrary defined to assume either a bilinear or higher order relation (*LS-DYNA* Keyword manual, 2006).

Although the bilinear formulation has been reported to have the tendency to be numerically unstable (Pinho et al., 2006), almost all the impact investigations using damage mechanics reported so far have used the bilinear law. This was probably due to the associated computational cost with the use of exponential law. Hence, in this research *MAT 138* was initially selected to predict delamination induced by low velocity impact in composite laminates. Alternatively, the damage model proposed by Iannucci (2006) was also selected as it was also based on the bilinear formulation.

However, there were no reports in the literature describing the performance of *MAT 138* with respect to impact. Likewise, the damage model proposed by Iannucci (2006) though had been verified through a series of fracture tests, with respect to impact only a limited number of investigations were available. These were based on simplified version of the standard *Boeing* and *CRAG* impact test specimens (Iannucci, 2006; Iannucci and Willows, 2006). However, in those investigations the delamination was modelled only at the mid-plate where the transverse shear stresses are highest. Such an approach would only give an overall damage estimate and not the actual damage scenario.

In order to achieve confidence in these models, a series of impact test was conducted and it was found that the *MAT 138* to be sensitive to loading rate and resulted in numerical instabilities. However, the damage model proposed by Iannucci (2006) was found to accurately predict the damage with lesser computational effort as compared *MAT 138*. Detail of the study can be found in Chapter 8. Other existing techniques in *LS-DYNA* for simulating delamination such as the ones discussed in Section 2.7.1 are fairly simple but may not be

suitable for dynamic loading condition such as impact. Hence the damage model proposed by Iannucci (2006) was selected and used in further part of this research work.

2.11 Chapter summary

Delamination has been identified as one of the most important damage mode in any applications that involve the use of laminated composite materials with respect to impact as it could cause severe reduction in post impact compression strength and lead to further catastrophic failure. Numerical methods, in particular the *FEA*, have been widely used to predict delamination in laminated composites and this requires the use of appropriate failure models. Some of the common failure models used in numerical investigations include the failure criteria approach, fracture mechanics and damage mechanics. Damage model based on damage mechanics has been identified as the most appropriate tool for investigating damages such as delamination as it eliminates issues such as scaling and requirement for initial flaw that were commonly encountered with the other damage models.

LS-DYNA is one of the many existing numerical tools that being extensively used for nonlinear material and geometrical analyses. However, it was found that it lacks the appropriate damage models to simulate damages such as delamination as the commonly used failure model is based on the failure criteria approach. In the latest release of *LS-DYNA,* failure models based on damage mechanics have been made available and the one that used the bilinear formulation was *MAT 138*. However, a series of impact test conducted in Chapter 8 found that this model selectively fail to predict delamination accurately, particularly when the loading rate was increased. Alternatively, the damage model developed by Iannucci (2006) has shown improved and accurate results over the use of *MAT 138* and was also based on bilinear relationship. Since the use of exponential law for the cohesive modelling could be computationally demanding, the damage model proposed by Iannucci (2006) has been selected and used in all impact investigation contained in this research.

Piezoelectric materials have been used in many ways to increase the performance level of structural components and have also been demonstrated to have the capabilities to control impact induced damages in composite laminates. Method such as z-pinning and stitching though could help to reduce the risk of delamination, these are passive methods. Piezoelectric material could be used to control damage even when the structure is in service by *active* means. Hence one of the objectives of this research is to investigate the possible use of

piezoelectric material to control impact induced delamination. For this a proper damage model has already been selected and the remaining would be to identify an appropriate piezoelectric material model to be implemented into *LS-DYNA* finite element code.

Chapter 3

Piezoelectric materials – a review

3.1 Chapter introduction

The objective of this chapter is to provide an overview on the applications and modelling techniques of smart materials in the field of structural engineering. The discussions include brief classifications on the different types of smart materials, their applications and related advantages and disadvantages. Since the main focus of this research is with the use of piezoelectric materials, subsequently, discussions on the fundamentals, applications and modelling of piezoelectric materials that are relevant to the current research work are presented. The main outcomes of this chapter are highlights on the limitation and inadequacy of the existing piezoelectric constitutive models available in existing *FEA* codes such as *Abaqus* and *Ansys* and the identification of a suitable piezoelectric model to be implemented into *LS-DYNA*'s user defined material subroutine.

3.2 Smart materials

Materials that can react to changes associated with their environments can be termed as smart materials. The earliest record on the discovery of smart materials dates back to 1880 when the Currie brothers discovered the *direct* piezoelectric effect of Rochelle salt and quartz crystals (Jordan and Ounaies, 2001). Through their experiment the Currie brothers discovered the potential of the crystals to develop electric charges when exposed to external stress fields.

However, the ability of the material to produce stresses when exposed to electric fields was first deduced mathematically by Lippmann in 1881 and the existence of this behaviour in the crystals was subsequently verified by the Currie brothers (Jordan and Ounaies, 2001). This phenomenon is known as the *converse* piezoelectric effect.

Today, a wide range of smart materials are available both at commercial and research levels. Some of these materials include piezoelectric sensors and actuators, shape memory alloys, electro- and magnetorheological fluids and electro- and magnetostrictive materials (Mackerle, 2003). Smart materials are often integrated with structural devices to provide sensing and actuation capabilities to detect and control changes in structural behaviour such as vibration and shape as alternatives to the use of conventional actuators and sensors such as electric motors and hydraulic pumps (Chee et al., 1998). Conventional actuators and sensors often increase the weight of the host system. Smart materials such as piezoelectric devices come in many forms and sizes and could be easily integrated into structural components without significant interference to the structural performances in their inactive mode.

Structural components integrated with smart materials are often termed as smart or intelligent structures (Lazarus and Napolitano, 1993). In essence a smart structure can be defined as an advanced structure with the capabilities to autonomously sense and react to changes in its operating conditions based on a predefined computing and control logic (Lazarus and Napolitano, 1993) while an intelligent structure can be termed as a knowledge based system (Gandhi and Thompson, 1992). The changes affecting the operating conditions could be related to factors such as stresses, strains, temperatures, magnetic and electric fields (Mackerle, 2003). The classifications of smart materials are often based on the types of energy conversions they undergo which are typically, but not limited to, thermo-mechanical, electrical-mechanical and magnetic-mechanical (Chee et al., 1998). The energy conversions describe the potential of a smart material as either a sensor or an actuator. Some smart materials such as piezoelectric devices can act both as sensors and actuators. The different types of smart materials based on their energy conversions are briefly described in the following sections (Chee et al., 1998).

3.2.1 Shape memory alloys

Shape memory alloys belong to the class of materials exhibiting shape memory effects that are related to strain recovery under the influence of heat (Lazarus and Napolitano, 1993). The

energy conversion involved is thermo-mechanical. These materials produce significant amount of deformation and actuation force during the phase transformation process to achieve shape recovery (Hurlebaus and Gaul, 2006).

The most commonly used material composition in shape memory alloys is Nickel-Titanium due to its exceptional force actuation capabilities (Suleman and Venkayya, 1994). However, there are many factors that need to be considered for the effective usage of shape memory alloys in structural applications. Shape memory alloys are generally slow in response owing to their high thermal time constants, have limited operating range due to temperature constraints as they may lose the memory effect at high temperature and require substantial amount of input energy due to high thermal losses (Chee et al., 1998).

3.2.2 Magneto- and electrostrictive materials

Magnetostrictive materials are materials that can respond both to mechanical and magnetic excitations and hence can be used as actuators and sensors (Olabi and Grunwald, 2008). Commercial magnetostrictive materials such as Terfenol-D are reported to have the capabilities to produce strains up to 0.2% (Lazarus and Napolitano, 1993). Magnetostrictive materials are used as linear motors and sonar transducers (Olabi and Grunwald, 2008). However, the use of these materials in structural devices is hindered by issues such as weight, mechanical resonance, large input energy requirement and their highly nonlinear behaviour (Suleman and Venkayya, 1994; Chee et al., 1998).

Electrostrictive materials are another form of smart materials that respond to electrical excitations. They exhibit low hysteresis but their mechanical-electrical response is nonlinear (Suleman and Venkayya, 1994; Chee et al., 1999). The strains induced by electrostrictive materials are only extensional and not affected by the polarity change in the driving electric fields (Chee et al., 1998). This factor limits their application as affective actuators even though they have very high actuation strain capability.

3.2.3 Electro- and magnetorheological fluids

Electro- and magnetorheological fluids are liquid based smart materials. They belong to the class of materials whose properties such as viscosity that can be altered by the application of electric or magnetic field accordingly (Lazarus and Napolitano, 1993). They are mostly used

in vibration control and shock related applications. However, their usages in structural applications are mostly limited as they are not easily integrated into the host structure (Chee et al., 1998).

3.2.4 Piezoelectric materials

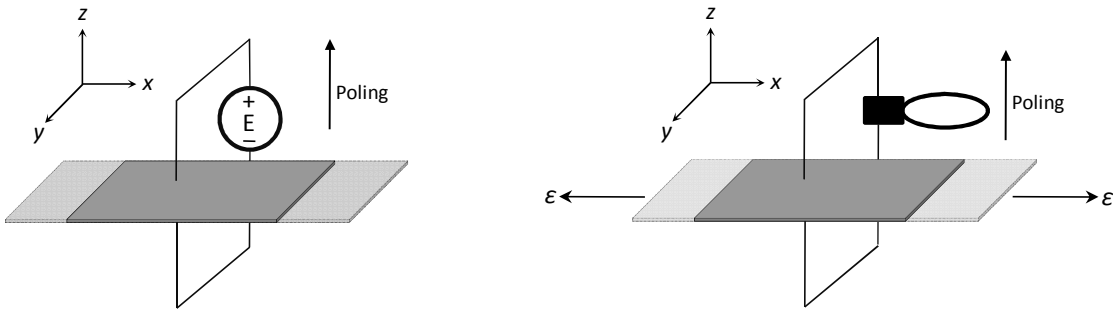
Piezoelectric materials such as piezoceramics basically belong to the family of ferroelectric materials with the ability to couple their mechanical and electrical responses (Hall, 2001). They are widely used as sensors and actuators due to their ease of usage, voltage dependent actuation, low input energy requirement, fast response, miniature size and fairly linear response at low electric fields (Mackerle, 2003). They come in many forms and sizes and have a wide range of applications to their credit.

The commonly used piezoelectric materials are either polymer or ceramic based. Piezopolymers are very flexible and tough but due to their low stiffness and strain coefficients their actuation capabilities are limited (Williams, 2004). On the other hand, piezoceramics have higher actuation capabilities (Williams, 2004) but are brittle and have limited conformation to curved surfaces (Zhang et al., 2008) thus limiting their applications as their use in dynamic events such as impact may lead to premature failure. However, new generations of piezoelectric materials such as the *Active Fibre Composite* (*AFC*) and *Macro Fibre Composite* (*MFC*) have overcome many of the problems associated with the use of conventional piezoceramics and piezopolymers (Bent, 1997; Williams, 2004).

Piezoelectric materials also suffer from hysteresis and exhibit significant nonlinearity at high electric fields and may lose their effects under extreme operating conditions (Ducharne et al., 2007). Nevertheless, the use of piezoelectric materials in structural applications supersedes the other materials (Benjeddou, 2000; Mackerle, 2003). This is attributed to the facts that these materials are easily integrated into the structural components unlike the other group of smart materials which are normally hindered by performance limitations or requirements of special techniques of integration.

3.3 Piezoelectric materials

The key characteristics of piezoelectric materials are the *converse* and *direct* effects which make them applicable as sensors and actuators.



(a) *Converse* effect (b) *Direct* effect

Figure 3.1: Piezoelectric effects

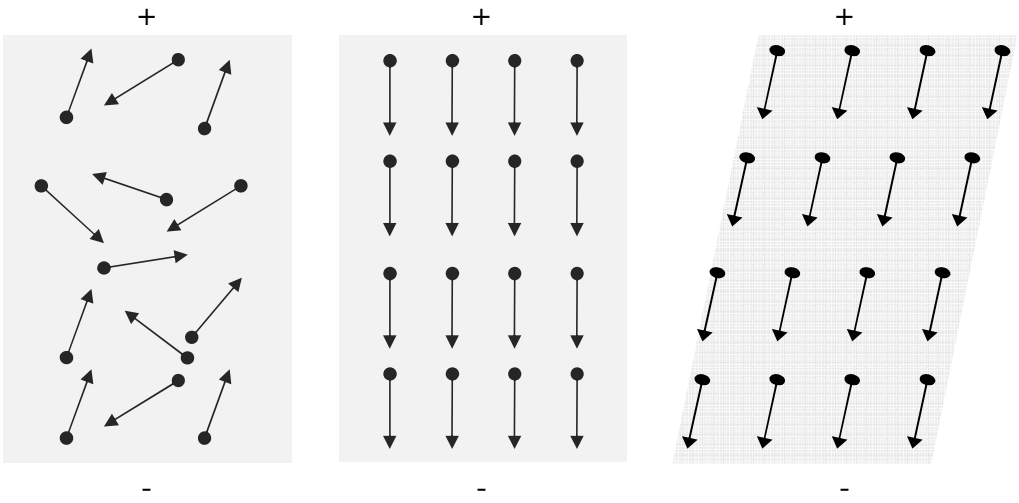
The *converse* effect describes the ability of the material to undergo mechanical deformation when exposed to an electric field, whereas the *direct* effect describes the ability of the material to produce electric charges when being deformed mechanically (Jordan and Ounaies, 2001). These effects are illustrated in Figure 3.1. The *converse* effect is the basis for structural actuation while structural sensing is realized through the *direct* effect.

3.3.1 Poling and depoling of piezoelectric materials

A piezoelectric material consists of randomly oriented electric dipoles, Figure 3.2a (Introduction, piezoelectric ceramics, 2001). A piezoelectric material does not possess any piezoelectric effects until its randomly oriented dipoles are aligned which is achieved through a process called poling. This process involves the application of a high electric field across the piezoelectric electrodes, which aligns the random dipoles to create a net piezoelectric effect in the direction of poling, Figure 3.2b (Introduction, piezoelectric ceramics, 2001). Figure 3.2b represents the poling process used to achieve extensional and contraction effects. The shear effects can be achieved if the electrodes are arranged in a skewed manner as shown in Figure 3.2c and poled accordingly. In this case the electric dipoles will appear inclined to the electrodes and produces shear deformation upon actuation, described by d_{24}, and d_{15}.

The direction of poling is normally determined during the fabrication process (Chopra, 2002). A piezoelectric material is actuated by applying electric fields parallel to the direction of poling (Chopra, 2002). Every piezoelectric material has coercive strength which is the maximum electric field that can be applied in the opposite direction of poling and a piezoelectric material can be depoled if this field strength is exceeded (Chopra, 2002). Likewise, a piezoelectric material can also be depoled by inducing large mechanical stresses

(Crawley and Anderson, 1990) or exposing it to a temperature beyond its Currie point (Srinivasan and McFarland, 2001). Once depoled, the effectiveness of a piezoelectric material will be reduced or permanently removed. On the other hand, the application of a high electric field in the direction of the poling will lead to electrical breakdown (Chopra, 2002).



(a) Before poling (b) During poling (c) Shear mode

Figure 3.2: Piezoelectric domains (Introduction, piezoelectric ceramics, 2001)

3.3.2 Hysteresis in piezoelectric materials

Hysteresis in a piezoelectric material is described by the difference in the strain levels at the application of same fields during the ascending and descending processes (Smith and Ounaies, 1999). Figure 3.3 shows the electric field-strain hysteresis curves for an unconstrained piezoceramic actuator from moderate to high operating field levels (Anderson, 1989). The figure shows that hysteresis is present at all field levels but gets more pronounced at higher electric fields. Several studies have suggested that one way of keeping this effect low is by minimizing the input fields or the stress levels but this would instead reduce the performance of the piezoelectric materials (Smith and Ounaies, 1999).

Another form of hysteresis is associated with polarization reversal. When the electric field is applied in the direction of poling, there will be an increase in the induced strain accordingly. This will continue until maximum field is applied which will stretch the dipoles. When the electric field is reduced, the induced strain will decrease and the dipoles will contract and if the field now is opposite to the direction of poling, the induced strain will be

negative. If the field strength in the opposite direction is increased beyond the coercive field, there will be an immediate polarization reversal (dipoles will be switch by 180^{o}) and the induced strain will be switched to positive. If the field is reduced and below its coercive field, there will be an immediate polarization reversal again (dipoles will be reoriented by 180^{o}) and the induced strain will be negative. A repeated process of such nature will create a hysteresis loop know as the butterfly loop (Damjanovic, 2005).

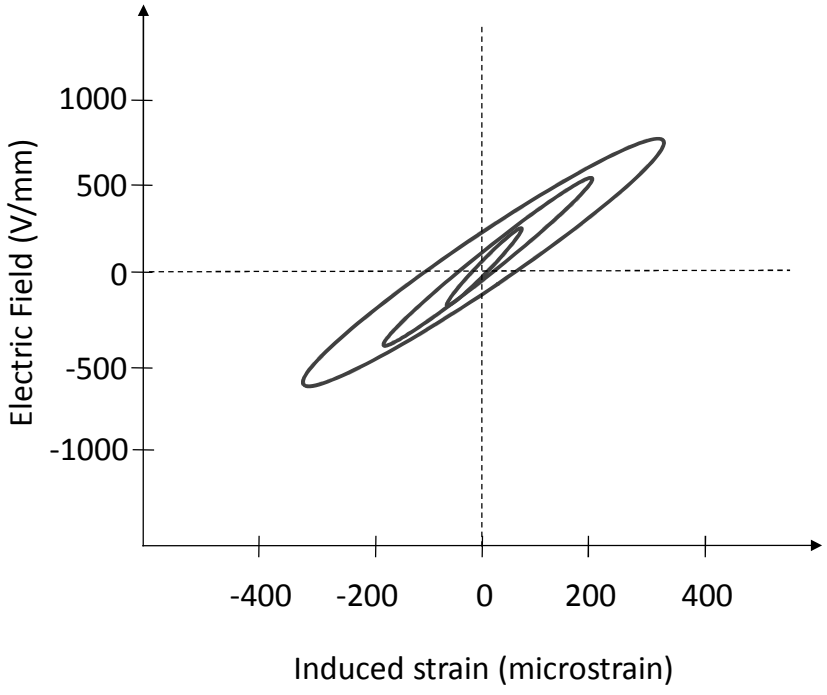


Figure 3.3: Hysteresis effect in piezoceramic (Anderson, 1989)

3.3.3 Piezoelectric electromechanical response

The electromechanical relationship of a piezoelectric material is described by the piezoelectric coefficients. As piezoelectric materials are applicable as both sensors and actuators, the piezoelectric coefficients which normally denoted with the symbol *d* can be expressed in two ways. In the *direct* form the piezoelectric coefficient can be defined as the quantity that describes the amount of charge density generated per unit applied stress (Prasad et al., 2005):

$$d = \text{charge density/applied stress}$$

The unit of *d* is C/N and known as the piezoelectric charge coefficient. In the *converse* form, the same coefficient is alternatively defined as the quantity that describes the amount of strain generated per unit applied electric field (Prasad et al., 2005):

$$d = \text{strain/applied electric field}$$

To distinguish from the *direct* effect the unit of *d* in the *converse* form is m/V and is known as the piezoelectric strain coefficient. A piezoelectric material normally has the piezoelectric coefficients to be highest in the direction of poling and since conventional piezoelectric materials such as piezopolymers and piezoceramics are normally poled in the third material direction (thickness direction) they tend to have lower in-plane strain coefficients (Chee et al., 1998).

To maximize the piezoelectric effect, it is desired to have the piezoelectric strain coefficients to be highest in the direction of actuation which is normally in-plane. The in-plane actuation has been made possible by a new form of electrode technology called the *Inter Digitated Electrodes* (*IDE*) which was developed by Hagood et al. (1993). Figure 3.4 shows a schematic drawing of an *IDE* (Bowen et al., 2006). Though *IDE* allows in-plane actuation there are several issues associated with the use of *IDE*.

From Figure 3.4 it can be seen that the *IDE* results in non uniform electric field distributions between the electrodes. This makes quantifying the electric field a difficult task (Williams, 2004). In addition there exists a dead zone under the electrode with same terminals. The dead zone decreases the effective actuation strain as the strain at the dead zone is virtually small (Nelson, 2002; Bowen et al., 2006). The number of dead zones can be reduced by increasing the electrode spacing between the different terminals or reducing the electrode length (Nelson, 2002; Bowen et al., 2006).

Reducing the number of dead zones allows a more uniform distribution of the electric field. However, increasing the spacing between the electrodes of different terminals poses the risk of electrical breakdown while reducing the electrode length decreases the strength of the electric field and hence lowering the actuation strain (Nelson, 2002). It has been suggested that a ratio of 6 between the spacing of electrodes with different terminals and electrode length gives the best possible actuation (Nelson, 2002) while the optimum ratio between electrode length and electrode spacing between the same terminal has been found to be 0.5 (Bowen et al., 2006).

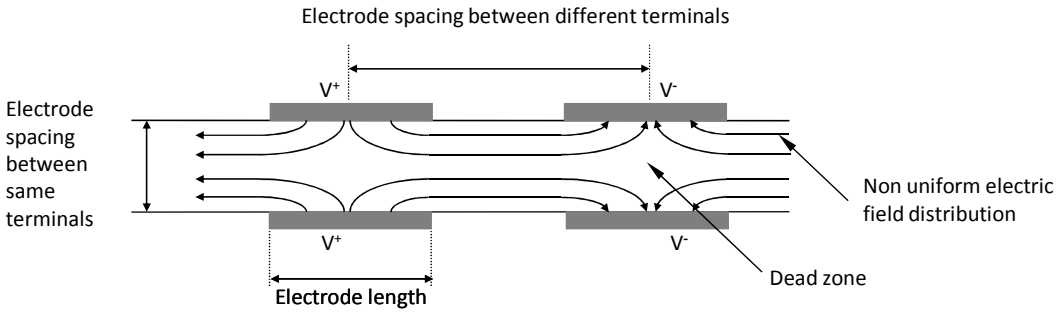


Figure 3.4: Schematic illustration of an *IDE* circuit (Bowen et al., 2006)

3.4 Types of piezoelectric materials

Piezoelectric materials come in many forms such as rectangular patches, thin disks and tubes among many other complex shapes. The simplest type of piezoelectric materials that are used as sensors and actuators in structural applications are usually in the form of layers or patches and the commonly used ones are the ceramic type – *Lead Zirconate Titanate* (*PZT*) and the polymer type – *Polyvinylidene Fluoride* (*PVDF*) (Chee et al., 1998). Piezoceramic such as *PZT* are non-central symmetric crystals and the process of poling creates a net permanent polarization to the crystals which also creates a permanent mechanical distortions and the material becomes transversely isotropic in plane normal to the poling direction (Sirohi and Chopra, 2000).

As the use of piezoelectric materials has been extended to more demanding applications, new form of actuators with improved properties both mechanically and electrically have been developed. One of such is the *Piezoelectric Fibre Composite* (*PFC*) which allows anisotropic actuation as opposed to the conventional monolithic *PZT* actuators which normally provide transversely isotropic actuation (Bent and Hagood, 1997). *AFC* and *MFC* are some of the more advanced actuators that capitalize on the benefits of fibre based actuation and *IDE* technology (Bent, 1997 and Williams, 2004).

3.4.1 Piezopolymer and piezoceramic actuators

As an actuator the effectiveness of a piezoelectric material to induce actuation depends on its mechanical and electrical properties. Table 3.1 lists some of the mechanical and electrical properties of piezopolymers and piezoceramics (Lazarus and Napolitano, 1993).

Table 3.1: Properties of *PVDF* and *PZT* actuators[1]

Properties	*PVDF*	*PZT*
Elastic Modulus, GPa	2	62
Yield strength, MPa	140-210	70
Strain constant, m/V×10^{-12}, d_{31}, d_{32}, d_{33}	23, 4, -33	254, 254, -360
Stress constant, m/C×10^{-3}	-339	25
Dielectric constant	12	1700
Coercive field V/μm	30	1.2
Density, kg/m^3	1780	7600
Thickness, μm	9, 28, 52, 110, 250	125, 250

1 Data obtained from (Lazarus and Napolitano, 1993)

The strain coefficient of the ceramic actuator is almost 11 times that of the polymer actuator. In addition, the elastic constants of piezopolymer are very small in comparison to the piezoceramic. With a high elastic modulus and strain constants piezoceramics are more effective as actuators as compared to piezopolymers. Piezopolymers are extremely flexible and have higher yield strength, almost twice that of the ceramic type. In addition, due to the higher stress coefficients, piezopolymers make better sensors as compared to piezoceramics.

Piezopolymers have very low material densities and are available as thin films, as low as 9μm, hence, as actuators or sensors they have negligible mechanical interference when integrated with structural devices, unlike ceramic actuators whose thickness and material densities are much higher. With a material density close to steel and elastic modulus comparable to aluminium, ceramic actuators would affect the inertia and stiffness of the host system (Hurlebaus and Gaul, 2006). Ceramic actuators are also brittle and have very low conformation to curved surfaces and these are the main drawbacks that limit their applications. For piezopolymers and piezoceramics the electrodes are aligned in the thickness direction. Hence, these types of actuators are poled in the thickness direction as shown in Figure 3.5 (adopted similar to Figure 3.7). Consequently, the direction of the primary actuation is also in the thickness direction (Chee et al., 1998).

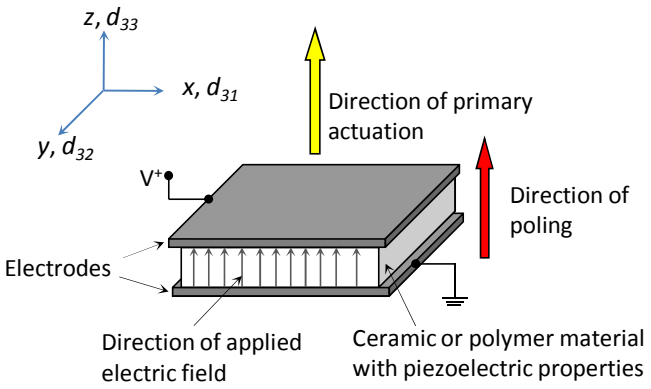


Figure 3.5: Actuation mode of *PVDF* and *PZT* actuators

Such actuation technology has the advantage of uniform electric field distributions between the electrodes but lower in-plane actuation capabilities. Piezopolymers and piezoceramics have been used as sensors and actuators in many applications mainly in structural vibration and shape control as well as structural health monitoring and damage suppression devices (Benjeddou, 2000; Mackerle, 2003).

3.4.2 *AFC* and *MFC* actuators

The low actuation capabilities of piezopolymers and limited applicability of piezoceramics have led to the development of new form of actuators such as the *AFC* and *MFC*. These actuators have improved actuation capabilities in addition to being very flexible and tough. The material densities are lower than ceramic actuators but higher than polymer based actuators. Both the *MFC* and *AFC* actuators' actuation technology is based on the *IDE*. However, the difference between the two actuators is in the shape of the piezoelectric fibres.

The piezoelectric fibres of the *AFC* actuator are circular in cross section (Bent, 1997). This reduces the contact area between the fibres and the electrodes (Williams, 2004). The *MFC* actuator is made of piezoelectric fibres with rectangular cross section which improves the contact area between the fibres and the electrodes and results in higher actuation as compared to the *AFC* actuator (Williams, 2004). Since the actuation of *AFC* and *MFC* actuators is based on the *IDE* technology they are able to offer higher in-plane actuation as compared to the piezopolymers or piezoceramics. Figures 3.6 (adopted similar to Figure 3.7) and 3.7 show the geometric configurations of *AFC* and *MFC* actuators respectively.

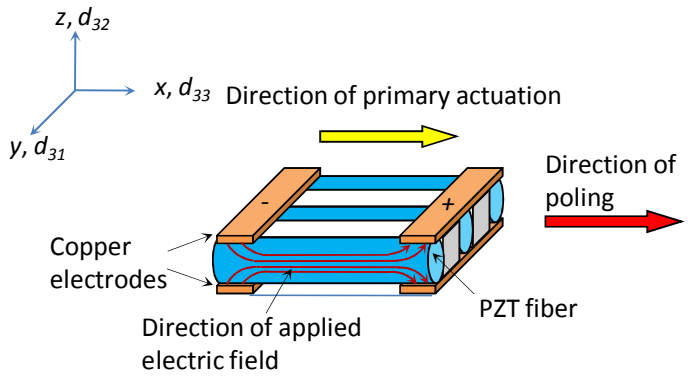


Figure 3.6: Geometric configurations of *AFC* actuator

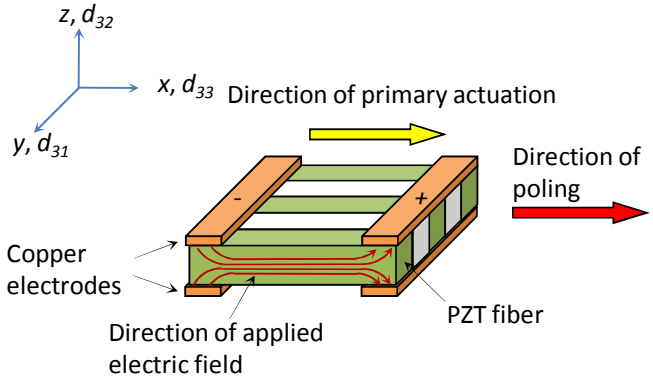


Figure 3.7: Geometric configurations of *MFC* actuator (www.smart-material.com)

The operating requirement of *MFC* actuators is much higher than normal piezoceramics. A *P1* type *MFC* actuator has an operating range of -1kV/mm to 3kV/mm (www.smart-material.com). Together with its higher strain coefficients and operating fields *MFC* actuators could produce actuation strain up to 1380με (www.smart-material.com). *MFC* actuators have been used in many applications such as shape control of tail fins in fighter aircrafts (Williams et al., 2002), vibration control of inflatable spacecraft (Sodano et al., 2004) and in the application of bi-stable composites (Bowen et al., 2007).

3.5 Piezoelectric applications

Piezoelectric materials are used in many applications that require real time sensing and actuation. Some of the applications related to structural engineering include active vibration and shape control, dynamic stability control, health monitoring, bi-stable structures and

damage detection and suppression. The following sections highlight some of the selected applications of piezoelectric materials.

3.5.1 Vibration control

Active vibration control of structural devices using piezoelectric sensors and actuators has been treated far more extensively than any other applications (Chee et al., 1998). Since polymer based actuators are highly flexible and could be easily attached to structures with complex shapes, actuators such as *PVDF* and *KYNAR* have been used as active dampers in flexible structures (Bailey and Hubbard, 1985; Tzou and Tseng, 1990; Samanta et al., 1996).

However, with the use of advanced composites as main materials in aerospace and other weight sensitive structural applications, polymer based actuators become less effective due to their lower actuation capabilities. Hence, investigations on active vibration control have relied on ceramic based actuators such as *PZT* as the higher strain and stiffness coefficients of ceramic actuators have proven to be more effective in damping out vibration in structural devices (Chandrashekhara and Agarwal, 1993). However, ceramic actuators have limited conformation to curved surfaces and hence limiting their application to flat or plate like structures. With the introduction of fibre based actuators such as *MFC*, vibration control of highly flexible structures such inflatable space devices have been made possible (Sodano et al., 2004). The use of *MFC* over the use of *PVDF* in such applications has added advantages in terms of higher actuation strain output in addition to improved mechanical properties.

3.5.2 Shape control

Structural shape control using piezoelectric devices is another area that has received great importance as the potentials of such application are enormous. Structural shape distortions could be caused by external disturbances such as mechanical and thermal loads. Shape distortions may alter the intended performance of a structural component. There are numerous publications that have addressed issue of shape control using piezoelectric devices and some notable ones are the work by Crawley and Lazarus (1991), Koconis et al. (1994a; 1994b) and Ajit et al. (2001).

Prior to the study of Koconis et al. (1994b), most shape control studies assumed the input voltages to the actuators are known or determined from sensor outputs. Koconis et al. (1994b)

were the first to study the shape control of structures using distributed actuators for which the required input voltages for shape control determined inversely by specifying the desired output shape. Crawley and Lazarus (1991) introduced an induced strain based actuation model to investigate the response of piezoelectric material at high fields. This model was found to accurately predict the response of the actuator at high fields. Ajit used the nonlinear actuation model of Crawley and Lazarus (1991) to investigate the voltage required for shape change using the inverse technique proposed by Koconis et al. (1994b) on composite beams. They found that with more actuators placed along the beam, the shape change could be easily achieved and the required voltages on each actuator were significantly reduced.

3.5.3 Buckling control

Structural components made of composite materials could be easily exposed to dynamic instability problems. This is because composite structures are fabricated as thin parts to achieve weight saving. However, thin parts have the tendency to buckle under compressive loads. There have been several research studies that have investigated the potential of piezoelectric materials to actively control the dynamic buckling of structures. One of the notable works is by Chandrashenkhara and Bhatia (1993). They have used a finite element approach with closed loop control strategy to actively increase the critical buckling load of composite plates using piezoelectric materials.

3.5.4 Bi-stable structures

A multi-stable structure can be defined as structures with multiple stable states. Asymmetric structures such as (0/90) composites could have more than one stable state as a result of thermal residual stresses induced during the curing process. The concept of bi-stable composite structures through snap-through behaviour was examined by Schultz (2003) using *MFC* actuators. Some of the recent works in this field include the works by Bowen et al. (2007), Giddings et al. (2008) and Portela et al. (2008).

Schultz (2003) investigated the snap through behaviour in asymmetric composite using *MFC* actuator both experimentally and numerically. He highlighted some of the challenges to induce successful snap through using numerical models. One of them is the bonding of the *MFC* to the plate in the numerical model. He suggested loose contact definition between the

actuator and the plate during the curing process to minimize the effect of the actuator stiffness on the laminate's final curvature. A qualitative agreement was reported between the experimental and the numerical models with respect to the snapping voltages.

Bowen et al. (2007) experimentally examined the morphing of thick and thin composite plates using *MFC* actuator. They found that the *MFC* actuator can be effectively used to induce large changes in shape and deflection in an unsymmetrical composite laminate. Giddings et al. (2008) conducted experimental investigation to characterize a bi-stable composite laminate bonded with piezoelectric actuator in terms of free deflection, blocking force and force-deflection behaviour. They have found that the snap through force could be increased by regulating the voltages to the actuators.

Portela et al. (2008) examined the snap through behaviour in asymmetric composite plates with various material properties using *MFC* actuators. They found that in a dry state, the actuation voltages required to induce the snap through were high and exceeded the maximum operating voltage of the *MFC*. However, when the effect of the moisture content on the composite laminate was included in the analysis, the required voltages to induce the snap through were found to reduce substantially. They also highlighted that the voltage/strain relationship of *MFC* actuator is highly nonlinear and used a proportionality factor of 1.5με/V to estimate the actuation strain using the linear model.

3.5.5 Structural health monitoring

The demand for a non-destructive structural damage assessment technique has been realized through the use of piezoelectric materials. Piezoelectric materials are surface bonded to structural components to detect damages by monitoring the changes in structural mechanical impedance by using high frequency excitation (Park and Inman, 2007). The use of piezoelectric materials to monitor structural health has more merits than other methods as it is automated and could be used to capture structural damages with minimum service downtime (Tseng and Wang, 2004).

3.5.6 Structural damage control

Crack propagations such as delamination and matrix cracking remain as major problems in applications that involve the use of composite materials. While there are a fair number of

publications on the use of piezoelectric materials in the earlier discussed areas, there are very limited works reported on the use of piezoelectric materials as damage controlling devices. Shah et al. (1994a) have investigated the possible use of embedded piezoelectric actuators to control delamination in composite structures with edge cracks subjected to mode I delamination. *PZT* actuators were placed close to the crack edge and excited with voltages to prevent the growth of the crack. In a later investigation they have also shown that it was possible to use piezoelectric materials to reduce the stress concentrations in the vicinity of holes of an aluminium plate subjected to tensile loading (Shah et al., 1994b).

The potential of piezoelectric materials to control damages in composite structures due to low velocity impact has been investigated numerically by Saravanos and Christoforou (2002a; 2002b). In those studies piezoelectric materials have been used to actively control the impact forces and plate deflections using a simple feedback control method. They have successfully shown that piezoelectric actuators could be used to reduce the peak impact force and displacement by actively regulating the voltages to the actuator. The authors concluded that damage due to impact could be prevented by actively reducing the net resultant impact force acting on the plate. However, they did not incorporate any damage models in their studies to validate their claims.

3.6 Analysis of smart structures

The analyses of smart structures often involve the use of numerical, analytical and experimental techniques (Chee et al., 1999). There are several analytical models proposed and applied for example in the shape control analyses of composite structures using piezoelectric materials (Koconis et al., 1994a; Koconis et al., 1994b). In the first part of the study, Koconis et al. (1994a) developed a mathematical model to investigate the effect of piezoelectric actuation on composite laminates using predefined control voltages. In the later study, they examined the required control voltages to achieve a predefined actuation shape (Koconis et al., 1994b).

There are also several experimental investigations reported in the literature to gauge the performance of piezoelectric materials. Crawley and Lazarus (1991) investigated the induced strain actuation characteristics of ceramic based actuators on aluminium and composite plates. They found that the piezoelectric strain coefficients are not constant as normally assumed but instead depend on the driving electric fields and the induced strains. In a similar investigation,

Williams (2004) has performed nonlinear characterizations of *MFC* actuator on its mechanical and electrical properties. He has found that *MFC* actuator exhibits highly nonlinear actuation behaviour at high electric fields.

From the majority of research publications that have appeared in the literature it has been found that the numerical approach, in particular the finite element method to be the most preferred tool of analysis for piezoelectric related studies (Chee et al., 1999; Benjeddou, 2000; Mackerle, 2003). One of the earliest works using the finite element method for piezoelectric related applications was explored by Allik and Hughes (1970) in which the vibration of piezoelectric materials was investigated. Presently, the finite element method has been applied to almost all branches of studies related to piezoelectric applications (Benjeddou, 2000; Mackerle, 2003).

Most of the finite element investigations have relied on plate and shell theories in which the piezoelectric devices together with the host structures modelled using simple classical or higher order displacement models (Crawley and Lazarus, 1991; Sun and Tong, 2005). However, it has been noted that piezoelectric effects are truly three-dimensional phenomena and most appropriately modelled using three-dimensional elements, such as solids, that allow thickness changes to fully account the anisotropy and coupled field effects of the piezoelectric materials (Kim, Varadan, and Varadan, 1997; Lee et al., 2004). In addition, the use of discrete type of actuators results in a complex stress fields and the resulting displacements are often inadequately represented using simplified models (Ajit et al., 2003).

However, solid elements are stiff elements and suffer from inherent locking phenomena (Lee et al., 2004). Nevertheless, this can be overcome by using techniques such as selective integration or incorporating incompatible modes in calculating the stiffness parameters (Ha et al., 1992). The other challenge using solid elements is the computational cost. Kim, Varadan and Varadan (1997) studied the response of composite plates using piezoelectric actuators in which the finite element model was represented using mixed three-dimensional and two-dimensional elements with the piezoelectric layers modelled using three-dimensional elements and the host layer modelled using two-dimensional elements to reduce the computational effort.

3.7 Piezoelectric constitutive relation

As mentioned in the earlier sections, a piezoelectric material is described by its *direct* and *converse* effects. These effects are expressed in their constitutive forms as follows (Joshi, 1992):

$$\begin{aligned} \varepsilon_\alpha &= S^E_{\alpha\beta}\sigma_\beta + d_{\alpha n}E_n \\ D_k &= d_{k\beta}\sigma_\beta + \varepsilon^\sigma_{kn}E_n \end{aligned} \tag{3-1}$$

The second term on the right hand site of the first equation in Equation (3-1) describes the piezoelectric actuation strain. The equation assumes the piezoelectric actuation strain varies linearly with respect to the applied electric field and this model has been used in most piezoelectric related investigations. The terms appearing in Equation (3-1) are detailed in Chapter 4. However, the applicability of such model is rather restricted. This is because the linear model is limited to applications that require or operate at low operating fields (Crawley and Lazarus, 1991). Actuators such as *MFC* can operate at high electric field reaching 3kV/mm. At such high field the strain-electric field relationship is not linear (Williams, 2004) and the standard piezoelectric constitutive relation described by Equation (3-1) will fall short of describing the full electromechanical behaviour of a piezoelectric material.

Figure 3.8 shows the induced strain-electric field relationship of an unconstrained *MFC* actuator in the longitudinal direction. The material data to reproduce the nonlinear curve was obtained from Williams (2004). It can be clearly seen that the linear model is only valid at low electric fields and in this case for fields less than 0.6kV/mm. At a field of 3kV/mm the linear model underestimates the actuation strain by almost 19%. This difference could be more prominent when the actuator is integrated with structural components. This is because the actuation strain would then be a function of the actual strain in the actuator in addition to the applied electric field (Crawley and Lazarus, 1991).

In order to predict the actuator performances beyond the linear range, it becomes necessary to formulate material models that are capable of addressing piezoelectric nonlinearities. The nonlinear phenomena exhibited by a piezoelectric material can be due to many factors and are often too complex to model (Hall, 2001). Some of the commonly observed piezoelectric nonlinearities include polarization reversal, large induced stresses due

to large electric fields, non uniform and complex electric field distributions and hysteresis (Hall, 2001; Samal et al., 2006).

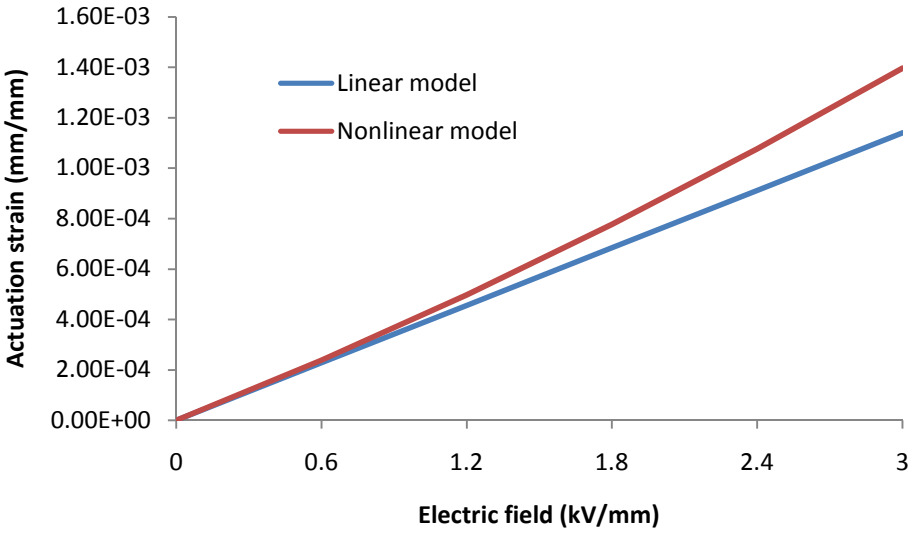


Figure 3.8: Strain-electric field plot of unconstrained *MFC*

Another form of nonlinearity that has been commonly investigated is the dependency of the piezoelectric actuation strain on the actual strain developed within the piezoelectric actuator which is of more relevance to the current work. Crawley and Lazarus (1991) described the strain coefficients of a piezoceramic actuator as a functional dependent term obtained by fitting a quadratic polynomial through the strain-electric field experimental data of an unconstrained actuator. They found that for an unconstrained actuator the actuation strain is a second order function of the electric field. However, when the actuator was integrated with an aluminium plate significant deviations were observed in the strain predictions in comparison to the experimental results. They concluded that the actuation strain of a piezoelectric material integrated with structural component was affected both by the electric field and the actual strain in the actuator. From their experiment they proposed two actuation models, i.e., the electric field dependent model and the induced strain dependent model. They found that the induced strain model gave closer strain predictions with their experimental results in comparison to the electric field dependent model (Crawley and Lazarus, 1991). The strain coefficients of electric field dependent and induced strain dependent models are given in Equations (3-2) and (3-3) respectively (Crawley and Lazarus, 1991):

$$d(E) = d_0 + d_E E \tag{3-2}$$

$$d(\varepsilon) = d_0 + d_\varepsilon \varepsilon \tag{3-3}$$

where:

d_o : Strain constant

d_ε : Induced strain dependent strain coefficient

d_E : Electric field dependent strain coefficient

From Equation (3-2) it can be seen that the strain coefficient in an electric field dependent model increases linearly with the applied field and is not affected by the constraints set upon the actuator. However, Equation (3-3) shows that the strain coefficient is now a function of the actual strain in the actuator. The effective value of the strain coefficient will vary according to the direction and magnitude of the actual strain in the actuator. The actual strain could be affected by various factors, such as material orthotropy and boundary condition of the host system. This could be seen as a more physically based actuation model than the linear and electric field dependent models as indeed the actuation strains are affected by these parameters (Crawley and Lazarus, 1991).

However, the dependence of the actuation strain on the induced strain significantly complicates the analysis as the solution procedure becomes iterative even for a static analysis. Chattopadhyay and Seeley (1997) investigated the modelling of composite laminates with induced strain actuators. The laminate and the actuator were modelled using a higher order laminate theory while the actuation was modelled using the nonlinear actuation model proposed by Crawley and Lazarus (1991). Part of the findings was that the piezoelectric coupling coefficient was not constant as normally assumed but instead depend on the actual strain in the actuator. They found that the coupling coefficient varied in cubic order through the thickness of one actuator layer.

In another investigation Chattopadhyay et al. (1999) investigated the modelling of smart composite box beam with nonlinear induced strain actuation. The primary objective of the work was to investigate vibratory load reduction of rotor blades using piezoelectric actuators. To emphasize the effects of piezoelectric nonlinear actuation, the static response of the beam flap deflection was compared between the linear and nonlinear actuation models. Two beam

models were constructed with different materials, i.e., one with graphite/epoxy the other with glass/epoxy. In the case of the graphite/epoxy beam the linear actuation model was found to produce about 4% deviation in the flap deflection as compared to the nonlinear model. However, in the case of glass/epoxy beam the deviation in the flap deflection was observed to be 10%. They concluded that the nonlinear effects were closely related to the stiffness of the primary structure.

Thornburgh and Chattopadhyay (2001) examined the deflection of composite and isotropic beams using both the strain induced and electric field dependent models in their analyses. They concluded that while both models predicted the actuation strain of a free piezoelectric actuator accurately, the strain induced model was the most appropriate when the actuator was bonded to structural elements. The induced strain model was found to closely match the experimental results especially in the case of composite materials which has a high degree of material orthotropy. All the works reported were based on in-house code development.

Joshi (1992) proposed a nonlinear piezoelectric constitutive equation based on the *Gibbs* energy function that reads:

$$\varepsilon_\alpha = S^E_{\alpha\beta}\sigma_\beta + d_{\alpha n}E_n + \frac{1}{2}d_{\alpha nr}E_nE_r + \kappa_{\alpha\beta n}\sigma_\beta E_n \tag{3-4}$$

The terms appearing in Equation (3-4) are detailed in Chapter 4. The third term on the right hand site of Equation (3-4) is the electrostrictive effect accounting for the nonlinear actuation strains at high electric fields. The last term in Equation (3-4) is the elastostrictive effect which is present within piezoelectric materials under combined electrical and mechanical loadings. The elastostrictive effect describes the reduction in the actuation capabilities of piezoelectric materials under combined electrical and mechanical loading conditions (Williams, 2004). The elastostrictive effect is not easily determined as the elastostrictive coefficients, $\kappa_{\alpha\beta n}$, evolve with the stresses, strains and electric fields within the piezoelectric material (Williams, 2004). In addition, a complete determination of these coefficients is not feasible as complex experimentations are required (Williams, 2004).

However, since the magnitude of the elastostrictive coefficients are much smaller than the piezoelectric strain and electrostrictive coefficients, a simplified model can be used to represent this effect. Williams (2004) has investigated the elastostrictive effects in *MFC* actuators using a simplified unidirectional loading condition. He has found that, though the

MFC has very high strain output, the effective actuation was reduced under the state of combined loading conditions.

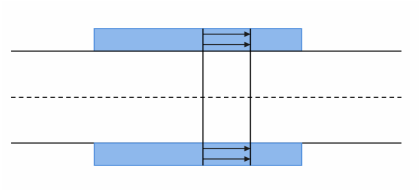
Wang et al. (1999) and Yao et al. (2004) have used a simplified equation based on Joshi's nonlinear model to investigate the nonlinear actuation characteristics of ceramic actuator by including the elastostrictive effect. The higher order effects were found to be not only more pronounced at higher electric fields and mechanical loading conditions but also at different levels of material orthotropy. Variation in the elastic modulus of the substrate layers was found to affect the induced strain.

The nonlinear model proposed by Crawley and Lazarus (1991) requires lesser number of coefficients and could be easily determined using free strain-electric field plot unlike the model proposed by Joshi (1992) which requires complex experimentation. The nonlinear model proposed by Crawley and Lazarus is in fact a simplified version of the full nonlinear model proposed by Joshi. In this work the formulations of the two models will be presented and a simplified version will be chosen to be implemented into *LS-DYNA* finite element code. The details of the formulation are presented in Chapter 4.

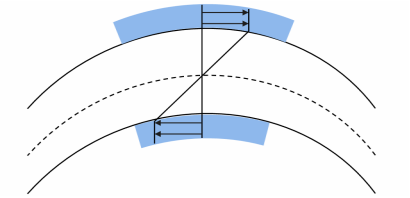
3.8 Piezoelectric strain models

The piezoelectric-substrate interaction is generally represented using either a uniform or a linear strain model (Anderson, 1989). The uniform strain model was introduced by Bailey and Hubbard (1985) to describe beam extension and bending using symmetrically surface mounted actuators. In a uniform strain model, the strains in the piezoelectric layers are assumed to be constant both in the extension and bending modes (Anderson, 1989). In the substrate layer, the strains are assumed to be constant in the extension mode and linear in the bending mode (Anderson, 1989).

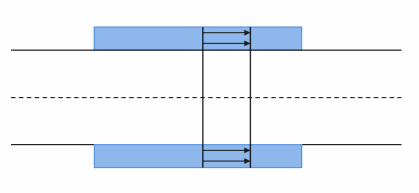
The uniform strain model was found to be applicable only when the structure is much thicker than the actuator and has been shown to fall short for structures with thickness smaller or comparable to the actuator (Anderson, 1989). The linear strain model assumes the strain to vary linearly across the entire structure and has been found to be more accurate for both bending and extension analyses as compared to the uniform strain model (Anderson, 1989). The actuation characteristics of the uniform and linear models are illustrated in Figure 3.9 (Anderson, 1989). In Figure 3.9 the actuators are shaded in blue.



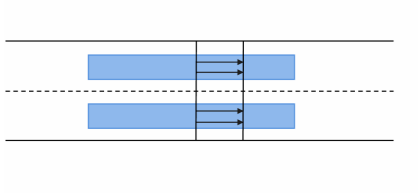
(a)
Surface bonded uniform extension model



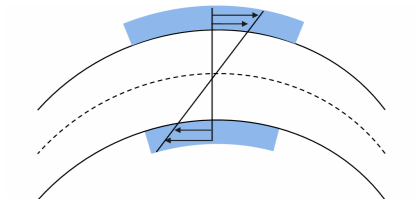
(b)
Surface bonded uniform bending model



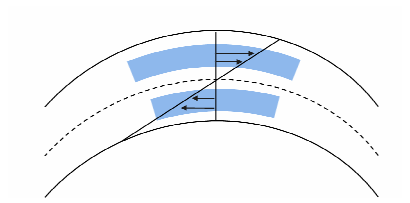
(c)
Surface bonded Bernoulli extension model



(d)
Embedded Bernoulli extension model



(e)
Surface bounded Bernoulli bending model



(f)
Embedded Bernoulli bending model

Figure 3.9: Induced strain models (Anderson, 1989)

3.9 Effect of piezoelectric actuation on bending deformation

Substituting Equation (3-2) into Equation (3-1) and expressing the moment resultant based on Equation (2-1), the resultant bending moment of an isotropic beam with a pair of symmetrically surface bonded actuator can be written as:

$$M_\varepsilon = \left(\frac{2}{3}E_a(3t_s^2t_a + 3t_st_a^2 + t_a^3) + \frac{2}{3}E_st_s^3 - \frac{1}{3}E_ad_\varepsilon(3t_s^2t_a + 3t_st_a^2 + t_a^3)(E_v^B + E_v^T)\right)\varepsilon_f + \frac{1}{2}E_ad_o(t_a^2 + 2t_st_a)(E_v^B - E_v^T) \quad (3\text{-}5)$$

where:

E_a : Actuator modulus

E_s : Substrate modulus

t_a : Thickness of actuator

t_s : Thickness of substrate

E_v^B : Electric field at bottom actuator

E_v^T : Electric field at top actuator

In Equation (3-5), the coefficient in bracket of ε_f is the equivalent beam bending stiffness. The equation shows that the bending stiffness of the beam could be adjusted by applying same electric field to the actuator pair which reduces the equation to:

$$M_\varepsilon = \left(\frac{2}{3}E_a(3t_s^2t_a + 3t_st_a^2 + t_a^3) + \frac{2}{3}E_st_s^3 - \frac{1}{3}E_ad_\varepsilon(3t_s^2t_a + 3t_st_a^2 + t_a^3)(2E_v^B)\right)\varepsilon_f \quad (3\text{-}6)$$

From the above equation it can be seen that the bending stiffness could be regulated by changing the electric fields to the actuator pair. The change in the bending stiffness will affect the bending deformation and consequently the impact force. Alternatively, applying different electric fields to the actuators induces electrically driven moment which reduces Equation (3-5) to:

$$M_\varepsilon = \left(\frac{2}{3}E_a(3t_s^2t_a + 3t_st_a^2 + t_a^3) + \frac{2}{3}E_st_s^3\right)\varepsilon_f + \frac{1}{2}E_ad_o(t_a^2 + 2t_st_a)(2E_v^B) \quad (3\text{-}7)$$

The piezoelectric induced moment could also be used to have an effect on the bending deformation of the beam as the moment will result in a net piezoelectric force that could be directed in the counter direction of the impact force. Damage threshold and propagation loads for composite materials have been previously shown to be influenced by the bending stiffness and mode II energy release rate. In a low velocity impact it is postulated that piezoelectric materials could be used to prevent delaminations in composite laminates either by inducing a counter moment to the incoming impact load or by regulating the bending stiffness.

3.10 Selection of a suitable actuation model

In this research a parametric study had been conducted in Chapter 7 to characterize the actuation capabilities of *MFC* actuator in terms of actuator placement, voltages, material and geometric properties as well as boundary conditions. It has been found that the actuation of the *MFC*, apart from being influenced by other parameters, required very high electric fields for effective structural actuation. In Chapter 9, in relation to impact investigation, it was noticed that the required voltages to reduce the effect of the impact force could only be achieved at voltages which exceeded the operating range of the *MFC* actuator. In such conditions, the use of a linear model would significantly underestimate the actual actuation strain that can be produced by the actuator.

The effects of material orthotropy on the piezoelectric actuation characteristic were found to be significantly affected by the boundary conditions (Chapter 7). Complex deformation patterns were observed with respect to actuator placement and this could affect the stresses, both, in the laminate as well as in the piezoelectric layer. The linear model will not be able to account such complexities. In addition, the level of material orthotropy of the substrate layers has been found to affect the piezoelectric actuation as the induced strain effectively depends on the actual strain in the actuator (Chapter 6).

Hence, for this purpose a full electromechanical model that includes the nonlinear piezoelectric effects is required to model the piezoelectric materials since a linear model will not be adequate for the said purpose. Though *FEA* codes such as *ANSYS* and *Abaqus* offer the piezoelectric material module, the piezoelectric analysis is restricted to the linear range and is based on the implicit or implicit dynamics solver hence will not be suitable tools for the present work.

LS-DYNA is one of the many existing tools widely used for dynamic analyses such as impact. However, it lacks the piezoelectric material module. The closest substitute for piezoelectric material is the material module *MAT-ORTHOTROPIC-THERMAL* (*MAT 021*) due to one-to-one relation between temperature and voltage. This material option again limits the analysis to the linear range as the thermal strain is described as a linear function of the applied temperature. Hence, this will not be suitable for the present investigation.

The damage model that will be used in the present work had already been implemented into *LS-DYNA* by Iannucci (2006). Hence, the development and implementation of a three-dimensional nonlinear piezoelectric actuation model that can be integrated with an existing explicit code, in particular *LS-DYNA* becomes necessary and serves as one of the main objectives of the present research work.

3.11 Chapter summary

Piezoelectric material has been identified as the widely used smart material in structural related applications. The flexibility and high strain actuation of the *MFC* actuator distinguish this material as a possible candidate to be used in impact related analysis. However, the *MFC* actuator has been shown to have nonlinear electromechanical response at high electric fields. Furthermore, the analyses conducted in Chapter 7 have shown that the voltages required to effectively deform the structure are higher than the operating limits of the *MFC* actuator. Although the linear piezoelectric model has been widely used in modelling the piezoelectric behaviour, this material model has been found to be inadequate at high electric fields and under combined electrical and mechanical loading conditions.

Most finite element software such as *Ansys* and *Abaqus* offer only the linear piezoelectric material module and restricted to implicit analysis. On the contrary, *LS-DYNA* does not have the piezoelectric material module and the closest substitute is *MAT 021* which is again based on linear strain formulation. The nonlinear model proposed by Joshi (1992) requires complex experimentation to determine the higher order piezoelectric material properties and not easily implemented. The nonlinear model proposed by Crawley and Lazarus (1991) has been found to be fairly simple yet accounts for the nonlinear effects at high fields and combined loading conditions. Hence one of the objectives of this research is to implement the nonlinear piezoelectric material model proposed by Crawley and Lazarus (1991) into *LS-DYNA* through its user defined material subroutine.

Chapter 4

Piezoelectric constitutive model

4.1 Chapter introduction

This chapter presents the derivations of the linear and nonlinear piezoelectric constitutive models that will be used in subsequent chapters. All the derivations presented in Sections 4.2 and 4.3 are referenced to the work of Joshi (1992) unless specified otherwise. The nonlinear model proposed by Crawley and Lazarus (1991) are discussed in Section 4.4. The outcomes of this chapter are the formulation and implementation of the linear and nonlinear three-dimensional piezoelectric material models into the *LS-DYNA* finite element code through its user defined material subroutine.

4.2 Piezoelectric linear constitutive equation

Based on the principles of thermodynamics the *Gibbs* free energy function can be written as:

$$G = U + PV - TS \tag{4-1}$$

where:

U : internal energy
P : pressure
V : volume

T : absolute temperature

S : entropy

Equation (4-1) can be expressed in terms of independent and dependent variables as follows:

$$G = U - \sigma_{ij}\varepsilon_{ij} - E_k D_k - TS \tag{4-2}$$

where:

σ_{ij} : stress components

ε_{ij} : strain components

E_k : electric field components

D_k : electric displacement components

In Equation (4-2), the stress, electric field and temperature represent the independent variables while the strain, electric displacement and the entropy are the dependent variables. For a reversible adiabatic system the differential of the internal energy is given as:

$$\mathrm{d}U = \sigma_{ij}\mathrm{d}\varepsilon_{ij} + E_k\mathrm{d}D_k + T\mathrm{d}S \tag{4-3}$$

By substituting Equation (4-3) into (4-2), the *Gibbs* energy function in its differential form can be expressed as:

$$\mathrm{d}G = -\varepsilon_{ij}\mathrm{d}\sigma_{ij} - D_k\mathrm{d}E_k - S\mathrm{d}T \tag{4-4}$$

The first, second and last terms on the right hand site of Equation (4-4) represent the mechanical, electrical and temperature effects respectively. In subsequent derivations the temperature effect will be omitted as it is not within the scope of the current research work. Hence, by neglecting the temperature effect and expanding Equation (4-4) using the Taylor series to include the first order terms gives:

$$\mathrm{d}G = \left(\frac{\partial G}{\partial \sigma_{ij}}\right)_E \mathrm{d}\sigma_{ij} + \left(\frac{\partial G}{\partial E_k}\right)_\sigma \mathrm{d}E_k \tag{4-5}$$

By comparing Equations (4-5) and (4-4), the dependent variables can be expressed as follows:

$$\varepsilon_{ij} = -\left(\frac{\partial G}{\partial \sigma_{ij}}\right)_E \tag{4-6}$$

$$D_k = -\left(\frac{\partial G}{\partial E_k}\right)_\sigma \tag{4-7}$$

Expanding the differential of the dependent variables using the Taylor series to include the first order terms gives:

$$d\varepsilon_{ij} = \left(\frac{\partial \varepsilon_{ij}}{\partial \sigma_{lm}}\right)_E \mathrm{d}\sigma_{lm} + \left(\frac{\partial \varepsilon_{ij}}{\partial E_n}\right)_\sigma \mathrm{d}E_n \tag{4-8}$$

$$dD_k = \left(\frac{\partial D_k}{\partial \sigma_{lm}}\right)_E \mathrm{d}\sigma_{lm} + \left(\frac{\partial D_k}{\partial E_n}\right)_\sigma \mathrm{d}E_n \tag{4-9}$$

The differential of the dependent variables with respect to the independent variables describes the physical properties of a piezoelectric material which are designated as follows:

$$\left(\frac{\partial \varepsilon_{ij}}{\partial \sigma_{lm}}\right)_E = S^E_{ijlm} \qquad \textit{Elastic compliance coefficients} \tag{4-10}$$

$$\left(\frac{\partial \varepsilon_{ij}}{\partial E_n}\right)_\sigma = \left(\frac{\partial D_n}{\partial \sigma_{ij}}\right)_E = d_{ijn} \qquad \textit{Piezoelectric strain coefficients} \tag{4-11}$$

$$\left(\frac{\partial D_k}{\partial E_n}\right)_\sigma = \varepsilon^\sigma_{kn} \qquad \textit{Dielectric permittivity coefficients} \tag{4-12}$$

Replacing the differentials in Equations (4-8) and (4-9) with the respective material parameters and subsequently integrating them, yield the following set of linear constitutive equations of a piezoelectric material which are written in matrix notation:

$$\{\varepsilon\} = [S^E]\{\sigma\} + [d]\{E\} \tag{4-13}$$

$$\{D\} = [d]^{\mathrm{T}}\{\sigma\} + [\varepsilon^{\sigma}]\{E\} \tag{4-14}$$

Alternatively, by switching the orders Equations (4-13) and (4-14) can also be written as:

$$\{\sigma\} = [C^{E}]\{\varepsilon\} - [\epsilon]\{E\} \tag{4-15}$$

$$\{D\} = [\epsilon]^{\mathrm{T}}\{\varepsilon\} + [\varepsilon^{\varepsilon}]\{E\} \tag{4-16}$$

where:

$[C^{E}] = [S^{E}]^{-1}$

$[\epsilon] = [C^{E}][d]$

$[\varepsilon^{\varepsilon}] = [\varepsilon^{\sigma}] - [\epsilon]^{\mathrm{T}}[d]$

Equation (4-13) represents the strain formulation of the *converse* effect while Equation (4-15) represents the stress formulation of the same effect. The *direct* effect is described by Equations (4-14) and (4-16) in the respective strain and stress forms. Both the formulations describe the same physical behaviour of a coupled piezoelectric material. In all the equations presented in this chapter, E, σ and ε appearing as either subscripts or superscripts indicate that the variables of concern are measured at constant electric field, stress and strain accordingly. The *Greek* subscripts assume values from one to six while the non-*Greek* subscripts are assigned values from one to three. The non-italic superscript T indicates the matrix transpose operator. Based on Equation (4-13) the full linear actuator equation of a piezoelectric actuator can be written as:

$$[S^E]\{\sigma\} = \begin{bmatrix} \frac{1}{E_{11}} & -\frac{\nu_{21}}{E_{22}} & -\frac{\nu_{31}}{E_{33}} & 0 & 0 & 0 \\ -\frac{\nu_{12}}{E_{11}} & \frac{1}{E_{22}} & -\frac{\nu_{32}}{E_{33}} & 0 & 0 & 0 \\ -\frac{\nu_{13}}{E_{11}} & -\frac{\nu_{23}}{E_{22}} & \frac{1}{E_{33}} & 0 & 0 & 0 \\ 0 & 0 & 0 & \frac{1}{G_{12}} & 0 & 0 \\ 0 & 0 & 0 & 0 & \frac{1}{G_{23}} & 0 \\ 0 & 0 & 0 & 0 & 0 & \frac{1}{G_{13}} \end{bmatrix} \begin{Bmatrix} \sigma_1 \\ \sigma_2 \\ \sigma_3 \\ \tau_4 \\ \tau_5 \\ \tau_6 \end{Bmatrix} \tag{4-17}$$

$$[d]\{E\} = \begin{bmatrix} 0 & 0 & d_{31} \\ 0 & 0 & d_{32} \\ 0 & 0 & d_{33} \\ 0 & 0 & 0 \\ 0 & d_{25} & 0 \\ d_{16} & 0 & 0 \end{bmatrix} \begin{Bmatrix} 0 \\ 0 \\ E_3 \end{Bmatrix} \tag{4-18}$$

where:

E_{11}, E_{22}, E_{33}	:	Young's modulus
G_{12}, G_{23}, G_{13}	:	shear modulus
$\nu_{12}, \nu_{21}, \nu_{13}, \nu_{31}, \nu_{23}, \nu_{32}$	:	Poisson's ratio
d_{31}, d_{32}	:	in-plane piezoelectric strain constants
d_{33}, d_{25}, d_{16}	:	out-of-plane piezoelectric strain constants
E_3	:	electric field in direction-3

The relationship between the Poisson's ratio and the elastic modulus can be established as follows (*LS-DYNA* theory manual, 2006):

$$\frac{\nu_{12}}{E_{11}} = \frac{\nu_{21}}{E_{22}} \tag{4-19}$$

$$\frac{\nu_{13}}{E_1} = \frac{\nu_{31}}{E_3} \tag{4-20}$$

$$\frac{\nu_{23}}{E_2} = \frac{\nu_{32}}{E_3} \tag{4-21}$$

Equation (4-18) is applicable for conventional actuators such as *PZT* and *PVDF* whose poling direction is in material direction-3 as shown in Figure 3.5. However, for actuator such as the *MFC* which is based on in-plane actuation technology the piezoelectric strain constant matrix is written as:

$$\begin{bmatrix} d_{11} & 0 & 0 \\ d_{12} & 0 & 0 \\ d_{13} & 0 & 0 \\ 0 & 0 & 0 \\ 0 & d_{25} & 0 \\ 0 & 0 & d_{36} \end{bmatrix} \begin{Bmatrix} E_1 \\ 0 \\ 0 \end{Bmatrix} \tag{4-22}$$

where:

d_{11}, d_{12} : in-plane piezoelectric strain constants

d_{13}, $d_{25,}$ d_{36} : out-of-plane piezoelectric strain constants

E_1 : electric field in direction-1

The first subscript attached to the piezoelectric strain constant indicates the direction of the applied field while the second subscript indicates the direction of the piezoelectric effect. A piezoelectric actuator is described by its response to an electric field which is controlled by a voltage source applied across its electrodes. The actuator will either expand or contract depending on the magnitude and direction of the driving voltage as well as the piezoelectric strain constant. The electric field is described by the gradient of the electric potential as follows:

$$E = -\nabla v(x, y, z) \tag{4-23}$$

where:

v(x,y,z) : scalar field representing the electric potential

Since the electric field is applied in the direction of poling, for conventional actuators such as piezoceramics and piezopolymers the gradient of the electric potential can be written as:

$$E_3 = \frac{v}{t_3} \tag{4-24}$$

where:

t_3 : electrode spacing (in material direction-3)

However, for *AFC* and *MFC* type of actuators which capitalize on the in-plane actuation technology, the electric field distribution has been described to be more complex (Bowen, 2006). Nevertheless, the uniform field approximation has been shown to be equally valid for *MFC* and *AFC* actuators (Williams, 2004). Hence, the electric field for these types of actuator can be written as:

$$E_1 = \frac{v}{t_{IDE}} \tag{4-25}$$

where:

t_{IDE} : *IDE* spacing

4.3 Piezoelectric nonlinear constitutive relation

Expanding Equation (4-8) and (4-9) using the Taylor series to include the second order terms gives the following expressions:

$$\begin{aligned} d\varepsilon_{ij} = & \left(\frac{\partial \varepsilon_{ij}}{\partial \sigma_{lm}}\right)_E \mathrm{d}\sigma_{lm} + \left(\frac{\partial \varepsilon_{ij}}{\partial E_n}\right)_\sigma \mathrm{d}E_n \\ & + \frac{1}{2}\left[\left(\frac{\partial^2 \varepsilon_{ij}}{\partial \sigma_{lm}\partial \sigma_{pq}}\right)_E \mathrm{d}\sigma_{lm}\mathrm{d}\sigma_{pq} + \left(\frac{\partial^2 \varepsilon_{ij}}{\partial E_n \partial E_r}\right)_\sigma \mathrm{d}E_n \mathrm{d}E_r \right. \\ & \left. + 2\left(\frac{\partial^2 \varepsilon_{ij}}{\partial \sigma_{lm}\partial E_n}\right) \mathrm{d}\sigma_{lm}\mathrm{d}E_n\right] \end{aligned} \tag{4-26}$$

$$dD_k = \left(\frac{\partial D_k}{\partial \sigma_{lm}}\right)_E \mathrm{d}\sigma_{lm} + \left(\frac{\partial D_k}{\partial E_n}\right)_\sigma \mathrm{d}E_n + \frac{1}{2}\left[\left(\frac{\partial^2 D_k}{\partial \sigma_{lm}\partial \sigma_{pq}}\right)_E \mathrm{d}\sigma_{lm}\mathrm{d}\sigma_{pq} + \left(\frac{\partial^2 D_k}{\partial E_n \partial E_r}\right)_\sigma \mathrm{d}E_n \mathrm{d}E_r + 2\left(\frac{\partial^2 D_k}{\partial \sigma_{lm}\partial E_n}\right) \mathrm{d}\sigma_{lm}\mathrm{d}E_n\right] \quad (4\text{-}27)$$

where:

$$\left(\frac{\partial^2 \varepsilon_{ij}}{\partial \sigma_{lm}\partial \sigma_{pq}}\right)_E = s^E_{ijlmpq} \qquad \textit{nonlinear compliance coefficients} \quad (4\text{-}28)$$

$$\left(\frac{\partial^2 \varepsilon_{ij}}{\partial E_n \partial E_r}\right)_\sigma = \left(\frac{\partial^2 D_k}{\partial \sigma_{ij}\partial E_n}\right) = d_{ijnr} \qquad \textit{electrostrictive coefficients} \quad (4\text{-}29)$$

$$\left(\frac{\partial^2 \varepsilon_{ij}}{\partial \sigma_{lm}\partial E_n}\right) = \left(\frac{\partial^2 D_k}{\partial \sigma_{lm}\partial \sigma_{pq}}\right)_E = \kappa_{ijlmn} \qquad \textit{elastostrictive coefficients} \quad (4\text{-}30)$$

$$\left(\frac{\partial^2 D_k}{\partial E_r \partial E_n}\right)_\sigma = \varepsilon_{knr} \qquad \textit{nonlinear dielectric permittivity coefficients} \quad (4\text{-}31)$$

By neglecting the nonlinear compliance coefficients, the nonlinear constitutive equation of a piezoelectric material can be written as:

$$\varepsilon_\alpha = S^E_{\alpha\beta}\sigma_\beta + d_{\alpha n}E_n + \frac{1}{2}d_{\alpha nr}E_nE_r + \kappa_{\alpha\beta n}\sigma_\beta E_n \quad (4\text{-}32)$$

$$D_k = d_{k\beta}\sigma_\beta + \varepsilon^\sigma_{kn}E_n + \frac{1}{2}\kappa_{k\beta\gamma}\sigma_\beta\sigma_\gamma + d_{k\beta n}\sigma_\beta E_n \quad (4\text{-}33)$$

The higher order terms appearing in the actuator Equation (4-32) are:

$$\left[\kappa_{\alpha\beta n}\right]^{\mathrm{T}} = \begin{bmatrix} \kappa_{111} & \kappa_{112} & \kappa_{113} & 0 & 0 & 0 \\ \kappa_{112} & \kappa_{212} & \kappa_{213} & 0 & 0 & 0 \\ \kappa_{113} & \kappa_{213} & \kappa_{313} & 0 & 0 & 0 \\ 0 & 0 & 0 & \kappa_{414} & 0 & 0 \\ 0 & 0 & 0 & 0 & 0 & 0 \\ 0 & 0 & 0 & 0 & 0 & 0 \\ \kappa_{121} & \kappa_{122} & \kappa_{123} & 0 & 0 & 0 \\ \kappa_{122} & \kappa_{222} & \kappa_{223} & 0 & 0 & 0 \\ \kappa_{123} & \kappa_{223} & \kappa_{323} & 0 & 0 & 0 \\ 0 & 0 & 0 & 0 & 0 & 0 \\ 0 & 0 & 0 & 0 & \kappa_{525} & 0 \\ 0 & 0 & 0 & 0 & 0 & 0 \\ \kappa_{131} & \kappa_{132} & \kappa_{133} & 0 & 0 & 0 \\ \kappa_{132} & \kappa_{232} & \kappa_{233} & 0 & 0 & 0 \\ \kappa_{133} & \kappa_{233} & \kappa_{333} & 0 & 0 & 0 \\ 0 & 0 & 0 & \kappa_{434} & 0 & 0 \\ 0 & 0 & 0 & 0 & \kappa_{535} & 0 \\ 0 & 0 & 0 & 0 & 0 & \kappa_{636} \end{bmatrix} \tag{4-34}$$

$$[d_{\alpha nr}] = \begin{bmatrix} d_{111} & d_{122} & d_{133} & 0 & 0 & 0 \\ d_{122} & d_{222} & d_{233} & 0 & 0 & 0 \\ d_{133} & d_{233} & d_{333} & 0 & 0 & 0 \\ 0 & 0 & 0 & d_{412} & 0 & 0 \\ 0 & 0 & 0 & 0 & d_{523} & 0 \\ 0 & 0 & 0 & 0 & 0 & d_{613} \end{bmatrix} \tag{4-35}$$

$$\{E_n E_r\} = \{E_1^2, \quad E_2^2, \quad E_3^2, \quad E_1E_2, \quad E_2E_3, \quad E_1E_3\}^{\mathrm{T}} \tag{4-36}$$

$$\begin{aligned} \{\sigma_\beta E_n\} = \{&\sigma_1E_1, \quad \sigma_2E_1, \quad \sigma_3E_1, \quad \sigma_4E_1, \quad \sigma_5E_1, \quad \sigma_6E_1, \\ &\sigma_1E_2, \quad \sigma_2E_2, \quad \sigma_3E_2, \quad \sigma_4E_2, \quad \sigma_5E_2, \quad \sigma_6E_2, \\ &\sigma_1E_3, \quad \sigma_2E_3, \quad \sigma_3E_3, \quad \sigma_4E_3, \quad \sigma_5E_3, \quad \sigma_6E_3\}^{\mathrm{T}} \end{aligned} \tag{4-37}$$

The electrostrictive coefficients quantify the nonlinear strain components at high electric fields and can be determined from the strain-electric field experimental curve of an unconstrained actuator (Crawley and Lazarus, 1991). However, the elastostrictive coefficients are not easily determined as they evolve with the stresses, strains and electric fields within the piezoelectric material (Williams, 2004). Basically, the elastostrictive effect describes the

performance of piezoelectric materials under combined electrical and mechanical loading conditions (Joshi, 1992).

Commercial *FEA* codes, such as *ANSYS* and *Abaqus*, have the capabilities to perform coupled piezoelectric-structural related analyses. However, the analyses are limited to the use of the linear piezoelectric theory as described by Equations (4-13) – (4-16). As can be seen from Figure 3.8 the inclusion of the electrostrictive effects becomes particularly important at high electric fields and likewise under combined electrical and mechanical loading conditions the inclusion of the elastostrictive effects becomes equally significant. Moreover, in *Abaqus* the piezoelectric analysis is limited to implicit methods only. Hence, as one of the objectives of this research work, the implementations of a three-dimensional nonlinear piezoelectric constitutive model into *LS-DYNA* explicit finite element code will be discussed in the following sections.

4.4 A simplified three-dimensional nonlinear piezoelectric constitutive model

Equation (4-32) is not implementable in the form it is shown as there are many material parameters that need to be determined. A sequence of simplifications can be used to simplify Equation (4-32) (Williams, 2004). Firstly, for actuators with poling direction-*3*, setting $E_1 = E_2 = 0$ the actuator Equation (4-32) can be simplified and written as:

$$\varepsilon_1 = s_{11}\sigma_1 + s_{12}\sigma_2 + s_{13}\sigma_3 + d_{31}E_3 + \frac{1}{2}d_{133}E_3^2 + \kappa_{131}\sigma_1 E_3 + \kappa_{132}\sigma_2 E_3 + \kappa_{133}\sigma_3 E_3$$

$$\varepsilon_2 = s_{12}\sigma_1 + s_{22}\sigma_2 + s_{23}\sigma_3 + d_{32}E_3 + \frac{1}{2}d_{233}E_3^2 + \kappa_{132}\sigma_1 E_3 + \kappa_{232}\sigma_2 E_3 + \kappa_{233}\sigma_3 E_3$$

$$\varepsilon_3 = s_{13}\sigma_1 + s_{23}\sigma_2 + s_{33}\sigma_3 + d_{33}E_3 + \frac{1}{2}d_{333}E_3^2 + \kappa_{133}\sigma_1 E_3 + \kappa_{233}\sigma_2 E_3 + \kappa_{333}\sigma_3 E_3 \quad (4\text{-}38)$$

$$\gamma_4 = S_{44}\tau_4 + \kappa_{434}\tau_4 E_3$$

$$\gamma_5 = S_{55}\tau_5 + \kappa_{435}\tau_5 E_3$$

$$\gamma_6 = S_{66}\tau_6 + \kappa_{436}\tau_6 E_3$$

Based on Equation (4-38) the important material parameters for structural actuation are d_{31}, d_{32}, d_{33}, d_{133}, d_{233}, d_{333}, κ_{131}, κ_{132}, κ_{133}, κ_{232}, κ_{233}, κ_{333}, κ_{434}, κ_{435} and κ_{436}. A complete determination of the higher order piezoelectric properties requires complex experimentation (Williams, 2004). However, Equation (4-38) can be simplified further through some assumptions. Polarization creates anisotropy and hysteresis in piezoelectric materials. Materials with axisymmetric properties around the direction of polarization can be termed as transversely isotropic (Sirohi and Chopra, 2000). In monolithic actuators such as *PZT* the poling direction is normally in direction-*3*. Since directions *1* and *2* are transverse to the poling direction they will have the same material coefficient. *G1195* are basically *PZT* actuator with transversely isotropic actuation capabilities and the primary actuation mode is planar. Consequently, the nonlinear piezoelectric effects can be considered only in the in-plane direction. Hence Equation (4-38) can be simplified and written as:

$$\varepsilon_1 = s_{11}\sigma_1 + s_{12}\sigma_2 + s_{13}\sigma_3 + d_{31}E_3 + \frac{1}{2}d_{133}E_3^2 + \kappa_{131}\sigma_1 E_3 + \kappa_{132}\sigma_2 E_3$$

$$\varepsilon_2 = s_{12}\sigma_1 + s_{22}\sigma_2 + s_{23}\sigma_3 + d_{32}E_3 + \frac{1}{2}d_{233}E_3^2 + \kappa_{132}\sigma_1 E_3 + \kappa_{131}\sigma_2 E_3$$

$$\varepsilon_3 = s_{13}\sigma_1 + s_{23}\sigma_2 + s_{33}\sigma_3 + d_{33}E_3 \tag{4-39}$$

$$\gamma_4 = S_{44}\tau_4$$

$$\gamma_5 = S_{55}\tau_5$$

$$\gamma_6 = S_{66}\tau_6$$

As mentioned earlier the piezoelectric strain constants and the electrostrictive coefficients can be determined from strain-electric field experimental data of an unconstrained piezoelectric actuator. The elastostrictive coefficients can be calculated with known parameters such as stresses, strains, electric field and piezoelectric material properties as follows:

$$\kappa_{131} = \frac{\varepsilon_1 - \lambda_1 - \varepsilon_2\frac{\sigma_2}{\sigma_1} + \lambda_2\frac{\sigma_2}{\sigma_1}}{\left(\sigma_1 E_3 - \frac{\sigma_2^2}{\sigma_1}E_3\right)}$$

$$\kappa_{132} = \frac{\varepsilon_2 - \lambda_2 - \kappa_{131}\sigma_2 E_3}{\sigma_1 E_3} \tag{4-40}$$

where:

$$\lambda_1 = s_{11}\sigma_1 + s_{12}\sigma_2 + s_{13}\sigma_3 + d_{31}E_3 + \frac{1}{2}d_{133}E_3^2$$

$$\lambda_2 = s_{12}\sigma_1 + s_{22}\sigma_2 + s_{23}\sigma_3 + d_{32}E_3 + \frac{1}{2}d_{233}E_3^2 \tag{4-41}$$

From Equations (4-40) and (4-41) it can be seen that to calculate the elastostrictive coefficients the stress values need to be known which otherwise would create a singularity in the equation. Hence the elastostrictive coefficients can only be calculated and included in the equation once the stresses have evolved over a time period.

For the *MFC*, the actuator Equation (4-32) can be simplified by setting $E_2 = E_3 = 0$ (Williams, 2004). In addition, the actuations in direction-2 and -3 are assumed to be the same

and the in-plane to be the primary actuation mode. Through these assumptions the actuator Equation (4-32) can be simplified and written as:

$$\varepsilon_1 = s_{11}\sigma_1 + s_{12}\sigma_2 + s_{13}\sigma_3 + d_{11}E_1 + \frac{1}{2}d_{111}E_1^2 + \kappa_{111}\sigma_1 E_1 + \kappa_{112}\sigma_2 E_1$$

$$\varepsilon_2 = s_{12}\sigma_1 + s_{22}\sigma_2 + s_{23}\sigma_3 + d_{12}E_1 + \frac{1}{2}d_{211}E_1^2 + \kappa_{112}\sigma_1 E_1 + \kappa_{212}\sigma_2 E_1$$

$$\varepsilon_3 = s_{13}\sigma_1 + s_{23}\sigma_2 + s_{33}\sigma_3 + d_{13}E_1 \qquad (4\text{-}42)$$

$$\gamma_4 = S_{44}\tau_4$$

$$\gamma_5 = S_{55}\tau_5$$

$$\gamma_6 = S_{66}\tau_6$$

Unlike in the case of transversely isotropic actuators, there are three elastostrictive coefficients that need to be determined using only two equations to describe the electromechanical behaviour of *MFC* actuator which are not easily achieved. If the elastostrictive effects are neglected the piezoelectric effects can be reduced and written in general form as follows (Crawley and Lazarus, 1991):

$$\varepsilon_{p_1} = A_1 E + B_1 E^2$$

$$\varepsilon_{p_2} = A_2 E + B_2 E^2 \qquad (4\text{-}43)$$

$$\varepsilon_{p_3} = A_3 E$$

where:

ε_{p1} : actuation strain in direction-1

ε_{p2} : actuation strain in direction-2

ε_{p3} : actuation strain in direction-3

A_1 : d_{31} and d_{11} for transversely isotropic and *MFC* actuators respectively

A_2 : d_{32} and d_{12} for transversely isotropic and *MFC* actuators respectively

A_3 : d_{33} and d_{13} for transversely isotropic and *MFC* actuators respectively

B_1 : $1/2d_{133}$ and $1/2d_{111}$ for transversely isotropic and *MFC* actuators respectively

B_2 : $1/2d_{233}$ and $1/2d_{211}$ for transversely isotropic and *MFC* actuators respectively

The above equation represents the electric field dependent piezoelectric actuator equation. For implementation into *LS-DYNA* explicit finite element code the above equation can be converted into incremental form as follows:

$$\begin{aligned} \Delta\varepsilon_{p_1} &= A_1\Delta E + 2B_1 E\Delta E \\ \Delta\varepsilon_{p_2} &= A_2\Delta E + 2B_2 E\Delta E \\ \Delta\varepsilon_{p_3} &= A_3\Delta E \end{aligned} \tag{4-44}$$

The cumulative actuation strain can then be simply defined as:

$$\varepsilon_{p_k}^{n+1} = \varepsilon_{p_k}^{n} + \Delta\varepsilon_{p_k}^{n+1} \tag{4-45}$$

However, Equation (4-43) is only applicable if the actuator is unconstrained. If the actuators are constrained, the use of Equation (4-43) will tend to overestimate the actuation strain. Crawley and Lazarus (1991) have alternatively proposed a nonlinear model based on induced strain actuation in which the strain coefficient, *d*, is expressed as a term that is dependent on actual strain in the actuator. The equation reads:

$$d_{3c}(\varepsilon_c) = \frac{A_c}{2} + \frac{A_c}{2}\sqrt{1 + \frac{4B_c\varepsilon_c}{A_c^2}} \tag{4-46}$$

where:

c : 1, 2

The second term on the right hand side of Equation (4-46) is the strain dependent portion of the piezoelectric strain coefficient which accounts for the constraints set upon the actuator such as when it is bonded to structural components. If the strain effect is neglected, Equation (4-46) reduces to the constant portion. The above equation was expanded using a binomial expansion and the induced strain was then expressed as (Crawley and Lazarus, 1991):

$$\varepsilon_{p_1} = A_1 E + \frac{B_1}{A_1}\varepsilon_1 E$$

$$\varepsilon_{p_2} = A_2 E + \frac{B_2}{A_1}\varepsilon_2 E \qquad (4\text{-}47)$$

$$\varepsilon_{p_3} = A_3 E$$

where:

ε_1 : actual strain in direction-1

ε_2 : actual strain in direction-2

In Equation (4-47) the induced strains are shown to be dependent on the actual strains in the actuator. Hence, the performance of the actuator will be somewhat restricted by the constraints and loading conditions. Unlike the equation proposed by Joshi (1992), the induced strain model proposed by Crawley and Lazarus (1991) requires only five material parameters to describe the electrical behaviour. This material data could be easily obtained by curve fitting the electromechanical response of an unconstraint actuator. Williams (2004) has characterized the behaviour of *MFC* actuator both mechanically and electrically and provided extensive amount of information regarding its nonlinear behaviour under various design conditions.

Equation (4-47) is a simplified form of Equation (4-39) or (4-42). Since the induced strain is a function of the actual strain, an iterative procedure is required to solve the problem. However, this is not an issue using *LS-DYNA* as strains are calculated incrementally. For explicit implementation Equation (4-47) is converted to incremental form as follows:

$$\Delta\varepsilon_{p_1} = A_1 \Delta E + \frac{B_1}{A_1}\varepsilon_1 \Delta E + \frac{B_1}{A_1} E \Delta\varepsilon_1$$

$$\Delta\varepsilon_{p_2} = A_2 \Delta E + \frac{B_2}{A_2}\varepsilon_2 \Delta E + \frac{B_2}{A_2} E \Delta\varepsilon_2 \qquad (4\text{-}48)$$

$$\Delta\varepsilon_{p_3} = A_3 \Delta E$$

The cumulative strain is defined using Equation (4-45). The nonlinear piezoelectric model described by Equations (4-43) and (4-48) have been implemented into *LS-DYNA* through its

user defined material subroutine and designated as *umat48* and *umat49* respectively. For explicit implementation the linear piezoelectric strain equation can be written as:

$$\Delta\varepsilon_{p_1} = A_1\Delta E$$
$$\Delta\varepsilon_{p_2} = A_2\Delta E \quad (4\text{-}49)$$
$$\Delta\varepsilon_{p_3} = A_3\Delta E$$

The above equation was also implemented into *LS-DYNA* through its user defined material subroutine and assigned the material number *umat50*.

All the piezoelectric material models have been implemented into *LS-DYNA* using solid element formulation. The required material parameters are described by Equations (4-17). Since the piezoelectric effects are normally in-plane, d_{25} and d_{36} for the *MFC* and d_{16} and d_{25} for the ceramic actuators are assumed to be zero. The electrostrictive properties required as input for the *MFC* actuator are d_{111} and d_{211}, while for the ceramic actuator these are d_{133} and d_{233}. The nonlinear piezoelectric properties used in this research were obtained from Williams (2004) for the *MFC* and Crawley and Lazarus (1991) for the *G1195* piezoceramic.

4.5 Chapter summary

This chapter presented the derivations of the linear and nonlinear piezoelectric actuation models using the *Gibbs* energy (Joshi, 1992) along with the nonlinear model proposed by Crawley and Lazarus (1991).The outcome of this chapter was the implementation of three-dimensional linear and nonlinear piezoelectric material models into *LS-DYNA* through its user defined material subroutine. The linear model was based on the standard piezoelectric equation described by Equation (4-49). The nonlinear models were based on Equations (4-44) and (4-48) that described the electric field dependent and induced strain dependent models respectively. Although the electric field dependent model accounts for the strains at high electric fields, the linear and the electric field dependent models do not account for the constraint set upon the actuator.

The full nonlinear model proposed by Joshi (1992) requires complex experimentation to determine the higher order material properties to describe the elastostrictive and electrostrictive effects of a piezoelectric. The nonlinear model proposed by Crawley and

Lazarus (1991) requires only two parameters to describe the higher order effects that would account for the nonlinearity at high electric fields (electrostrictive effects) and under combined loading conditions (elastostrictive effects). These parameters could be easily achieved using a strain-electric field plot and has been well documented by Williams (2004) for the *MFC* actuator. The performance of the different piezoelectric actuation models have been tested and validated in Chapter 6.

Chapter 5

Finite element formulation of static shape control codes

5.1 Chapter introduction

This chapter presents three-dimensional finite element formulation and code development for composite plates integrated with piezoelectric actuators and sensors based on the linear piezoelectric theory. The piezoelectric formulation was implemented into an eight-node solid hexahedron element with three translational degrees of freedom per node. To accommodate the electrical actions, the element was extended to include one electrical degree of freedom per node. Three different shape control procedures were implemented, i.e., shape based, sensor based and voltage based. The outcome of this chapter is an independent three-dimensional finite element code designed to perform static shape control analysis on composite plates integrated with piezoelectric actuators and sensors.

5.2 Finite element formulation

This section presents the standard three-dimensional finite element formulations for plate like structures integrated with piezoelectric sensors and actuators similar to those proposed by Ha et al. (1992) and Tzou and Tzeng (1990).

5.2.1 Strain-displacement relationship

The linear piezoelectric constitutive model outlined in Chapter 4 was implemented using solid element formulation. An eight-node solid hexahedron element with three translational degrees of freedom per node is shown in Figure 5.1 (*LS-DYNA* theory manual, 2006).

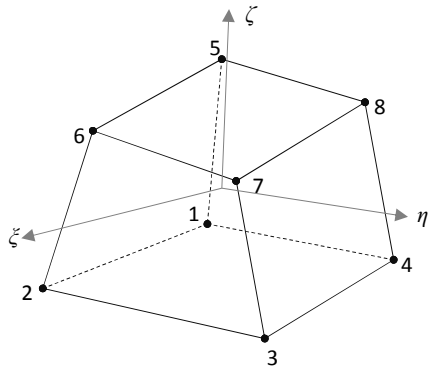


Figure 5.1: Eight-node solid hexahedron element

For the purpose of the present work this element was extended to include one electrical degree of freedom per node. The nodal interpolation function of the element shown in Figure 5.1 in the natural coordinate, (ζ,η,ξ), is given as (*LS-DYNA* Theory Manual, 2006):

$$N_i = \frac{1}{8}(1 + \xi_i\xi)(1 + \eta_i\eta)(1 + \zeta_i\zeta) \tag{5-1}$$

where$i$ = 1…8 and for:

$i = 1$ $(\xi_1, \eta_1, \zeta_1) = (-1,-1,-1)$
$i = 2$ $(\xi_2, \eta_2, \zeta_2) = (1,-1,-1)$
$i = 3$ $(\xi_3, \eta_3, \zeta_3) = (1,1,-1)$
$i = 4$ $(\xi_4, \eta_4, \zeta_4) = (-1,1,-1)$
$i = 5$ $(\xi_5, \eta_5, \zeta_5) = (-1,-1,1)$
$i = 6$ $(\xi_6, \eta_6, \zeta_6) = (1,-1,1)$
$i = 7$ $(\xi_7, \eta_7, \zeta_7) = (1,1,1)$
$i = 8$ $(\xi_8, \eta_8, \zeta_8) = (-1,1,1)$

Based on the shape functions described by Equation (5-1), the displacements of a point within the element can be extrapolated using the nodal displacements as follows:

$$u_x = N_i u_{xi}$$
$$u_y = N_i u_{yi} \quad (5\text{-}2)$$
$$u_z = N_i u_{zi}$$

where:

u_{xi} : nodal displacement along x
u_{yi} : nodal displacement along y
u_{zi} : nodal displacement along z

Alternatively, Equation (5-2) can be written in matrix notation as:

$$\{u\} = [N_i]\{u_i\} \quad (5\text{-}3)$$

The strain-displacement relationship can be established using the following definition for strain:

$$\{\varepsilon_{kl}\} = \frac{1}{2}\{u_{k,l} + u_{l,k}\} \quad (5\text{-}4)$$

where:

k,l : 1,2,3

By applying Equation (5-4) to Equation (5-2), the strain vector can be written as:

$$\begin{Bmatrix} \varepsilon_x \\ \varepsilon_y \\ \varepsilon_z \\ \gamma_{xy} \\ \gamma_{yz} \\ \gamma_{xz} \end{Bmatrix} = \begin{Bmatrix} \dfrac{\partial u_x}{\partial x} \\ \dfrac{\partial u_y}{\partial y} \\ \dfrac{\partial u_z}{\partial z} \\ \dfrac{\partial u_x}{\partial y} + \dfrac{\partial u_y}{\partial x} \\ \dfrac{\partial u_y}{\partial z} + \dfrac{\partial u_z}{\partial y} \\ \dfrac{\partial u_x}{\partial z} + \dfrac{\partial u_z}{\partial x} \end{Bmatrix} \tag{5-5}$$

where:

$$\begin{Bmatrix} \varepsilon_x \\ \varepsilon_y \\ \varepsilon_z \\ \gamma_{xy} \\ \gamma_{yz} \\ \gamma_{xz} \end{Bmatrix} = \begin{bmatrix} \dfrac{\partial N_i}{\partial x} & 0 & 0 \\ 0 & \dfrac{\partial N_i}{\partial y} & 0 \\ 0 & 0 & \dfrac{\partial N_i}{\partial z} \\ \dfrac{\partial N_i}{\partial y} & \dfrac{\partial N_i}{\partial x} & 0 \\ 0 & \dfrac{\partial N_i}{\partial z} & \dfrac{\partial N_i}{\partial y} \\ \dfrac{\partial N_i}{\partial z} & 0 & \dfrac{\partial N_i}{\partial x} \end{bmatrix} \begin{Bmatrix} u_{xi} \\ u_{yi} \\ u_{zi} \end{Bmatrix} \tag{5-6}$$

The first term on the right-hand-side of Equation (5-6) is known as the strain-displacement matrix and denoted as B_u. Alternatively, Equation (5-6) can be written as:

$$\{\varepsilon\} = [B_u]\{u\} \tag{5-7}$$

Since the shape functions are expressed in terms of the natural coordinate system, (ζ,η,ξ), the derivative of the shape functions with respect to global coordinate system, (x,y,z), can be established using a chain rule of differentiation as follows:

$$\frac{\partial N_i}{\partial \xi} = \frac{\partial N_i}{\partial x}\frac{\partial x}{\partial \xi} + \frac{\partial N_i}{\partial y}\frac{\partial y}{\partial \xi} + \frac{\partial N_i}{\partial z}\frac{\partial z}{\partial \xi}$$

$$\frac{\partial N_i}{\partial \eta} = \frac{\partial N_i}{\partial x}\frac{\partial x}{\partial \eta} + \frac{\partial N_i}{\partial y}\frac{\partial y}{\partial \eta} + \frac{\partial N_i}{\partial z}\frac{\partial z}{\partial \eta} \tag{5-8}$$

$$\frac{\partial N_i}{\partial \zeta} = \frac{\partial N_i}{\partial x}\frac{\partial x}{\partial \zeta} + \frac{\partial N_i}{\partial y}\frac{\partial y}{\partial \zeta} + \frac{\partial N_i}{\partial z}\frac{\partial z}{\partial \zeta}$$

Equation (5-8) can be rearranged and written as:

$$\begin{Bmatrix} \frac{\partial N_i}{\partial \xi} \\ \frac{\partial N_i}{\partial \eta} \\ \frac{\partial N_i}{\partial \zeta} \end{Bmatrix} = \begin{bmatrix} \frac{\partial x}{\partial \xi} & \frac{\partial y}{\partial \xi} & \frac{\partial z}{\partial \xi} \\ \frac{\partial x}{\partial \eta} & \frac{\partial y}{\partial \eta} & \frac{\partial z}{\partial \eta} \\ \frac{\partial x}{\partial \zeta} & \frac{\partial y}{\partial \zeta} & \frac{\partial z}{\partial \zeta} \end{bmatrix} \begin{Bmatrix} \frac{\partial N_i}{\partial x} \\ \frac{\partial N_i}{\partial y} \\ \frac{\partial N_i}{\partial z} \end{Bmatrix} \tag{5-9}$$

The first term on the right hand side of Equation (5-9) is known as the *Jacobian* operator and denoted as *J*. The derivative of the shape functions with respect to the global coordinate system can then be established as follows:

$$\begin{Bmatrix} \frac{\partial N_i}{\partial x} \\ \frac{\partial N_i}{\partial y} \\ \frac{\partial N_i}{\partial z} \end{Bmatrix} = [J]^{-1} \begin{Bmatrix} \frac{\partial N_i}{\partial \xi} \\ \frac{\partial N_i}{\partial \eta} \\ \frac{\partial N_i}{\partial \zeta} \end{Bmatrix} \tag{5-10}$$

The transformation from the natural coordinate system to the global coordinate system requires the *Jacobian* operator to be positive definitive. Based on Equation (5-7), the stresses can be defined as:

$$\{\sigma\} = [C][B_u]\{u\} \tag{5-11}$$

5.2.2 Electric field-voltage relationship

The electric field-voltage relationship is given as (Joshi, 1992):

$$E_j = \frac{\partial v}{\partial x_j} \tag{5-12}$$

where:

j : 1,2,3

v : nodal voltage

x_j : direction of electric field

Alternatively, Equation (5-12) can be expressed in matrix notation as:

$$\begin{Bmatrix} E_1 \\ E_2 \\ E_3 \end{Bmatrix} = \begin{Bmatrix} \frac{\partial v}{\partial x_1} \\ \frac{\partial v}{\partial x_2} \\ \frac{\partial v}{\partial x_3} \end{Bmatrix} \tag{5-13}$$

The shape functions described in Equation (5-1) can also be used to represent the nodal electrical degrees of freedom as follows:

$$\{v\} = [N_i]\{v_i\} \tag{5-14}$$

Based on relation (5-14), Equation (5-13) can be written as:

$$\begin{Bmatrix} E_1 \\ E_2 \\ E_3 \end{Bmatrix} = \begin{bmatrix} \frac{\partial N_i}{\partial x_1} \\ \frac{\partial N_i}{\partial x_2} \\ \frac{\partial N_i}{\partial x_3} \end{bmatrix} \{v_i\} \tag{5-15}$$

Equation (5-15) needs to be simplified as it states that the nodal voltage for a given piezoelectric element varies along directions-1, -2 and -3. In reality the voltage applied to individual piezoelectric elements must be constant and across its electrodes. For conventional actuators the electric field is applied in material direction-3. Hence, by setting the voltage

gradients with respect to x_1 and x_2 to zero and $\xi=\zeta=\eta=0$, the electric field for conventional actuators can be written as:

$$\begin{Bmatrix} 0 \\ 0 \\ E_3 \end{Bmatrix} = \begin{bmatrix} 0 \\ 0 \\ \dfrac{\partial N_i}{\partial x_3} \end{bmatrix} \{v_i\} \tag{5-16}$$

The above equation of electric field-voltage relationship was established using the nodal shape functions. Alternatively, the electric field-voltage relationship can also be written as:

$$\begin{Bmatrix} 0 \\ 0 \\ E_3 \end{Bmatrix} = \begin{bmatrix} 0 \\ 0 \\ \dfrac{1}{t_3} \end{bmatrix} \{v_i\} \tag{5-17}$$

where:

t_3 = electrode spacing for conventional actuators

For actuators such as *MFC* which is based on in-plane actuation technology the poling direction is in material direction-1. Accordingly, by setting the voltage gradients with respect to x_2 and x_3 to zero, for *IDE* based actuators the voltage gradient can be defined as:

$$\begin{Bmatrix} E_1 \\ 0 \\ 0 \end{Bmatrix} = \begin{bmatrix} \dfrac{\partial N_i}{\partial x_1} \\ 0 \\ 0 \end{bmatrix} \{v_i\} \tag{5-18}$$

or:

$$\begin{Bmatrix} E_1 \\ 0 \\ 0 \end{Bmatrix} = \begin{bmatrix} \dfrac{1}{t_{IDE}} \\ 0 \\ 0 \end{bmatrix} \{v_i\} \tag{5-19}$$

where:

t_{IDE}= electrode spacing for *IDE* based circuits

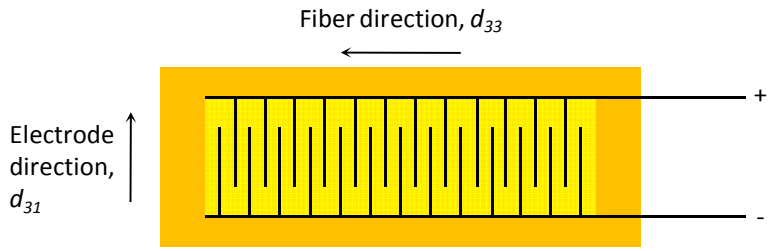


Figure 5.2: *MFC* actuator - planar actuation directions

Figure 5.2, adopted from Williams (2004), shows the planar actuation direction of an *MFC* actuator. The first terms on the right-hand-side of Equations (5-16) to (5-19) are known as the voltage gradient operators and denoted as B_p. Consequently, these equations can be written as:

$$\{E\} = [B_p]\{v\} \tag{5-20}$$

5.2.3 System potential energy

This section presents the derivations of the governing equations of a structure integrated with piezoelectric actuators and sensors based on Hamilton's variational principle. For a laminated composite plate integrated with piezoelectric actuators and sensors, the Hamilton's principle can be written as (Yin and Shen, 1997):

$$\delta \int_{t_2}^{t_1} (K - H + W)\mathrm{d}t = 0 \tag{5-21}$$

where:

K : kinetic energy

H : potential energy

W : work of external load

and:

$$K = \frac{1}{2}\int_V \rho\{\dot{u}\}^{\mathrm{T}}\{\dot{u}\}\mathrm{d}V \tag{5-22}$$

$$H = H_M + H_E = \frac{1}{2}\int_V \{\varepsilon\}^{\mathrm{T}}\{\sigma\}\mathrm{d}V - \frac{1}{2}\int_V \{E\}^{\mathrm{T}}\{D\}\mathrm{d}V \tag{5-23}$$

$$W = \int_A \{u\}^{\mathrm{T}}\{q\}\mathrm{d}A_{\mathrm{t}} + \int_{A_a} vQ\mathrm{d}A_a \tag{5-24}$$

where:

ρ : mass density
q : surface traction
Q : surface charge density
V : Volume
A_{t} : surface area of surface traction
A_a : surface area of charge density

Unless specified otherwise the upper and lower scripts *u*, *a* and *s* represent the structure, actuator and sensor respectively. Substituting Equations (5-22), (5-23) and (5-24) into (5-21) yields:

$$\begin{aligned}\int_{t_2}^{t_1}\Bigg(&\int_V \rho\{\delta u\}^{\mathrm{T}}\{\ddot{u}\}\mathrm{d}V + \int_V \{\delta\varepsilon\}^{\mathrm{T}}[C]\{\varepsilon\}\mathrm{d}V - \int_{V_a} \{\delta\varepsilon\}^{\mathrm{T}}[e]^{\mathrm{T}}\{E\}\mathrm{d}V_a \\ &- \int_{V_a} \{\delta E\}^{\mathrm{T}}[e]\{\varepsilon\}\mathrm{d}V_a - \int_{V_a} \{\delta E\}^{\mathrm{T}}[\varepsilon^{\varepsilon}]\{E\}\mathrm{d}V_a \\ &- \int_{V_s} \{\delta\varepsilon\}^{\mathrm{T}}[e]^{\mathrm{T}}\{E\}\mathrm{d}V_s - \int_{V_s} \{\delta E\}^{\mathrm{T}}[e]\{\varepsilon\}\mathrm{d}V_s \\ &- \int_{V_s} \{\delta E\}^{\mathrm{T}}[\varepsilon^{\varepsilon}]\{E\}\mathrm{d}V_s - \int_{A_t} \{\delta u\}^{\mathrm{T}}\{q\}\mathrm{d}A_t - \int_{A_a} \{\delta v_a\}^{\mathrm{T}} Q\mathrm{d}A_a\Bigg)\mathrm{d}t \\ &= 0\end{aligned} \tag{5-25}$$

Substituting Equations (5-3), (5-7), (5-11) and (5-20) into (5-25) gives:

$$\int_{t_2}^{t_1}\left(\int_V \{\delta u\}^{\mathrm{T}}[N]^{\mathrm{T}}\rho[N]\{\ddot{u}\}\mathrm{d}V + \int_V \{\delta u\}^{\mathrm{T}}[B_u]^{\mathrm{T}}[C][B_u]\{u\}\mathrm{d}V\right.$$

$$-\int_{V_a}\{\delta u\}^{\mathrm{T}}[B_{ua}]^{\mathrm{T}}[e_a]^{\mathrm{T}}\left[B_{pa}\right]\{v_a\}\mathrm{d}V_a$$

$$-\int_{V_a}\{\delta v_a\}^{\mathrm{T}}\left[B_{pa}\right]^{\mathrm{T}}[e_a][B_{ua}]\{u\}\mathrm{d}V_a$$

$$-\int_{V_a}\{\delta v_a\}^{\mathrm{T}}\left[B_{pa}\right]^{\mathrm{T}}[\varepsilon_a^{\varepsilon}]\left[B_{pa}\right]\{v_a\}\mathrm{d}V_a \qquad (5\text{-}26)$$

$$-\int_{V_s}\{\delta u\}^{\mathrm{T}}[B_{us}]^{\mathrm{T}}[e_s]^{\mathrm{T}}\left[B_{ps}\right]\{v_s\}\mathrm{d}V_s$$

$$-\int_{s}\{\delta v_s\}^{\mathrm{T}}\left[B_{ps}\right]^{\mathrm{T}}[e_s][B_{us}]\{u\}\mathrm{d}V_s - \int_{V_s}\{\delta v_s\}^{\mathrm{T}}\left[B_{ps}\right]^{\mathrm{T}}[\varepsilon_s^{\varepsilon}]\left[B_{ps}\right]\{v_s\}\mathrm{d}V_s$$

$$\left.-\int_{A_t}\{\delta u\}^{\mathrm{T}}[N]^{\mathrm{T}}\{q\}\mathrm{d}A_t - \int_{A_a}\{\delta v_a\}^{\mathrm{T}}[N]^{\mathrm{T}}\,Q\mathrm{d}A_a\right)\mathrm{d}t = 0$$

Equating the common terms in Equation (5-26) gives:

$$\int_V [N]^{\mathrm{T}}\rho[N]\{\ddot{u}\}\mathrm{d}V + \int_V [B_u]^{\mathrm{T}}[C][B_u]\{u\}\mathrm{d}V - \int_{V_a}[B_{ua}]^{\mathrm{T}}[e_a]^{\mathrm{T}}\left[B_{pa}\right]\{v_a\}\mathrm{d}V_a$$
$$-\int_{V_s}[B_{us}]^{\mathrm{T}}[e_s]^{\mathrm{T}}\left[B_{ps}\right]\{v_s\}\mathrm{d}V_s = \int_{A_t}[N]^{\mathrm{T}}\{q\}\mathrm{d}A_t \qquad (5\text{-}27)$$

$$\int_{V_a}\left[B_{pa}\right]^{\mathrm{T}}[e_a][B_{ua}]\{u\}\mathrm{d}V_a + \int_{V_a}\left[B_{pa}\right]^{\mathrm{T}}[\varepsilon_a^{\varepsilon}]\left[B_{pa}\right]\{v_a\}\mathrm{d}V_a = -\int_{A_a}[N]^{\mathrm{T}}\,Q\mathrm{d}A_a \qquad (5\text{-}28)$$

$$\int_{s} \left[B_{ps}\right]^{\mathrm{T}} [e_s][B_{us}]\{u\}\mathrm{d}V_s + \int_{V_s} \left[B_{ps}\right]^{\mathrm{T}} [\varepsilon_s^{\varepsilon}]\left[B_{ps}\right]\{v_s\}\mathrm{d}V_s = 0 \tag{5-29}$$

Equations (5-27), (5-28) and (5-29) can be simplified and written as:

$$[m]\{\ddot{u}\} + [k_{uu}]\{u\} - [k_{ua}]\{v_a\} - [k_{us}]\{v_s\} = \{f_m\} \tag{5-30}$$

$$[k_{au}]\{u\} + [k_{aa}]\{v_a\} = \{f_e\} \tag{5-31}$$

$$[k_{su}]\{u\} + [k_{ss}]\{v_s\} = \{0\} \tag{5-32}$$

where:

- m : element mass
- k_{uu} : element stiffness
- k_{ua} : element structure-actuator coupling stiffness
- k_{us} : element structure-sensor coupling stiffness
- k_{aa} : element actuator electrical stiffness
- k_{ss} : element sensor electrical stiffness
- f_m : element external mechanical load
- f_e : element electrical load
- v_a : element actuator voltage
- v_s : element sensor voltage
- $\ddot{u}$: element nodal acceleration
- u : element nodal displacement

and:

$$[m] = \int_{V} [N]^{\mathrm{T}} \rho [N]\mathrm{d}V \tag{5-33}$$

$$[k_{uu}] = \int_V [B_u]^{\mathrm{T}}[C][B_u]\mathrm{d}V \tag{5-34}$$

$$[k_{ua}] = \int_{V_a} [B_{ua}]^{\mathrm{T}}[e_a]^{\mathrm{T}}\left[B_{pa}\right]\mathrm{d}V_a \tag{5-35}$$

$$[k_{us}] = \int_{V_s} [B_{us}]^{\mathrm{T}}[e_s]^{\mathrm{T}}\left[B_{ps}\right]\mathrm{d}V_s \tag{5-36}$$

$$[k_{aa}] = \int_{V_a} \left[B_{pa}\right]^{\mathrm{T}}[\varepsilon_a^{\varepsilon}]^{\mathrm{T}}\left[B_{pa}\right]\mathrm{d}V_a \tag{5-37}$$

$$[k_{ss}] = \int_{V_s} \left[B_{ps}\right]^{\mathrm{T}}[\varepsilon_s^{\varepsilon}]^{\mathrm{T}}\left[B_{ps}\right]\mathrm{d}V_s \tag{5-38}$$

$$[k_{au}] = [k_{ua}]^{\mathrm{T}} \tag{5-39}$$

$$[k_{su}] = [k_{us}]^{\mathrm{T}} \tag{5-40}$$

$$\{f_m\} = \int_A [N]^{\mathrm{T}}\{q\}\, dA_t \tag{5-41}$$

$$\{f_e\} = -\int_{A_a} [N]^{\mathrm{T}} Q\, dA_a \tag{5-42}$$

By assembling the element stiffness matrices, the global system of equations can be written as:

$$[M_u]\{\ddot{X}\} + [K_{uu}]\{X\} - [K_{ua}]\{\mathcal{V}_a\} - [K_{us}]\{\mathcal{V}_s\} = \{F_m\} \tag{5-43}$$

$$[K_{au}]\{X\} + [K_{aa}]\{\mathcal{V}_a\} = \{F_e\} \tag{5-44}$$

$$[K_{su}]\{X\} + [K_{ss}]\{\mathcal{V}_s\} = \{0\} \tag{5-45}$$

where:

M_u : global mass
K_{uu} : global stiffness
K_{ua} : global structure-actuator coupling stiffness
K_{us} : global structure-sensor coupling stiffness
K_{aa} : global actuator electrical stiffness
K_{ss} : global sensor electrical stiffness
F_m : global external mechanical load
F_e : global electrical load
$\mathcal{V}_a$: global actuator voltage
$\mathcal{V}_s$: global sensor voltage
$\ddot{X}$: global nodal acceleration
X : global nodal displacement

and:

$$[M_u] = \sum_{j=1}^{n_u} \int_V [N]^{\mathrm{T}} \rho [N] \mathrm{d}V \tag{5-46}$$

$$[K_{uu}] = \sum_{j=1}^{n_u} \int_V [B_u]^{\mathrm{T}} [C] [B_u] \mathrm{d}V \tag{5-47}$$

$$[K_{ua}] = \sum_{j=1}^{n_a} \int_{V_a} [B_{ua}]^{\mathrm{T}} [e_a]^{\mathrm{T}} [B_{pa}] \mathrm{d}V_a \tag{5-48}$$

$$[K_{us}] = \sum_{j=1}^{n_s} \int_{V_s} [B_{us}]^{\mathrm{T}} [e_s]^{\mathrm{T}} [B_{ps}] \mathrm{d}V_s \tag{5-49}$$

$$[K_{aa}] = \sum_{j=1}^{n_a} \int_{V_a} [B_{pa}]^{\mathrm{T}} [\varepsilon_a^{\varepsilon}]^{\mathrm{T}} [B_{pa}] \mathrm{d}V_a \tag{5-50}$$

$$[K_{ss}] = \sum_{j=1}^{n_s} \int_{V_s} [B_{ps}]^{\mathrm{T}} [\varepsilon_s^{\varepsilon}]^{\mathrm{T}} [B_{ps}] \mathrm{d}V_s \tag{5-51}$$

$$[K_{au}] = [K_{ua}]^{\mathrm{T}} \tag{5-52}$$

$$[K_{su}] = [K_{us}]^{\mathrm{T}} \tag{5-53}$$

$$\{F_m\} = \sum_{j=1}^{n_m} \int_{A} [N]^{\mathrm{T}} \{q\} \, dA_t \tag{5-54}$$

$$\{F_e\} = -\sum_{j=1}^{n_e} \int_{A_a} [N]^{\mathrm{T}} Q \, dA_a \tag{5-55}$$

where

n_u : total number of structural elements (includes the piezoelectric elements)

n_a : total number of actuator elements

n_s : total number of sensor elements

n_m : total number of elements applied with mechanical load

n_e : total number of elements applied with electrical load

5.3 Static shape control

This section presents control algorithms for inverse (shape as input), active (sensor voltage as input) and voltage based (actuator voltage as input) shape control analyses. The inverse shape control problem is based on the assumption that a desired shape is known prior to the control action. The control voltages are achieved by minimizing the cost function between the actuated and the desired shape (Koconis et al., 1994b). In an active control the control voltages are determined from sensor voltages. The voltage based approach simply involves determining the shape change resulting from the application of predefined control voltages. The derivation presented in this section is referenced to the work of Sun and Tong (2004) but the implementation is three-dimensional.

5.3.1 Inverse shape control

In an inverse shape control problem, the host plate is normally bonded with discrete actuator patches rather than a single continuous patch. Discretely distributed actuators normally provide better control authority as compared to a single actuator patch (Chee, 2000). The sequence of derivations is referenced to the work of (Sun and Tong, 2004). In an inverse control problem all the piezoelectric patches are assumed to act as actuators. Consequently, for this type of system, Equation (5-43) can be simplified to:

$$[K_{uu}]\{X\} - [K_{ua}]\{\mathcal{V}_a\} = \{F_m\} \tag{5-56}$$

The actuation force is the product between the structure-actuator coupling stiffness, K_{ua} and control voltage,$\mathcal{V}_a$, the only unknown term in Equation (5-56). A direct solution approach to determine the control voltage would be:

$$\{\mathcal{V}_a\} = [K_{ua}]^{-1}([K_{uu}]\{X\} - \{F_m\}) \tag{5-57}$$

However, the coupling term is not a square matrix and the inverse of it does not exist. Hence, a cost function needs to be defined to find the control voltages (Koconis et al., 1994b). In doing so, the desired shape, y_d, is assumed to be known and the actuated shape, y_c, is defined as:

$$\{y_c\} = [R]\{X\} \tag{5-58}$$

where, R is a weighting matrix related to the nodal degrees of freedom defined as follows:

$$[R] = \begin{bmatrix} R_{uxi_d} & 0 & 0 & 0 & 0 & 0 & 0 & 0 & 0 \\ 0 & R_{uyi_d} & 0 & 0 & 0 & 0 & 0 & 0 & 0 \\ 0 & 0 & R_{uzi_d} & 0 & 0 & 0 & 0 & 0 & 0 \\ 0 & 0 & 0 & . & 0 & 0 & 0 & 0 & 0 \\ 0 & 0 & 0 & 0 & . & 0 & 0 & 0 & 0 \\ 0 & 0 & 0 & 0 & 0 & . & 0 & 0 & 0 \\ 0 & 0 & 0 & 0 & 0 & 0 & R_{uxn_d} & 0 & 0 \\ 0 & 0 & 0 & 0 & 0 & 0 & 0 & R_{uyn_d} & 0 \\ 0 & 0 & 0 & 0 & 0 & 0 & 0 & 0 & R_{uzn_d} \end{bmatrix} \tag{5-59}$$

where:

i_d : $1 \ldots n_d$: total number of nodes of the *FEA* model

R_{ux} : weighting function corresponding to displacement along x

R_{uy} : weighting function corresponding to displacement along y

R_{uz} : weighting function corresponding to displacement along z

The squared error between the actuated and the desired shapes can be defined as:

$$e_y = |y_c - y_d|^2 = (y_c - y_d)^{\mathrm{T}}(y_c - y_d) \tag{5-60}$$

Expressing Equation (5-56) in terms of X and subsequently substituting it into Equation (5-58) and (5-60) gives:

$$\begin{aligned} e_y = {} & \{F_m\}^{\mathrm{T}}[K_{uu}]^{-\mathrm{T}}[R]^{\mathrm{T}}[R][K_{uu}]^{-1}\{F_m\} \\ & + \{\mathcal{V}_a\}^{\mathrm{T}}[K_{ua}]^{\mathrm{T}}[K_{uu}]^{-\mathrm{T}}[R]^{\mathrm{T}}[R][K_{uu}]^{-1}[K_{ua}]\{\mathcal{V}_a\} \\ & + 2\{\mathcal{V}_a\}[K_{ua}]^{\mathrm{T}}[K_{uu}]^{-\mathrm{T}}[R]^{\mathrm{T}}[R][K_{uu}]^{-1}\{F_m\} \\ & - 2\{F_m\}^{\mathrm{T}}[K_{uu}]^{-\mathrm{T}}[R]^{\mathrm{T}}\{y_d\} - 2\{\mathcal{V}_a\}^{\mathrm{T}}[K_{ua}]^{\mathrm{T}}[K_{uu}]^{-\mathrm{T}}[R]^{\mathrm{T}}\{y_d\} \\ & + \{y_d\}^{\mathrm{T}}\{y_d\} \end{aligned} \tag{5-61}$$

Equation (5-61) can be simplified and written as:

$$e_y = \{F_m\}^{\mathrm{T}}[K_{uu}]^{-\mathrm{T}}[R]^{\mathrm{T}}[R][K_{uu}]^{-1}\{F_m\} + \{\mathcal{V}_a\}^{\mathrm{T}}[A1]\{\mathcal{V}_a\} + 2\{\mathcal{V}_a\}[A2]\{F_m\} - 2\{F_m\}^{\mathrm{T}}[K_{uu}]^{-\mathrm{T}}[R]^{\mathrm{T}}\{y_d\} - 2\{\mathcal{V}_a\}^{\mathrm{T}}[A3]\{y_d\} + \{y_d\}^{\mathrm{T}}\{y_d\} \tag{5-62}$$

where:

$$[A1] = [K_{ua}]^{\mathrm{T}}[K_{uu}]^{-\mathrm{T}}[R]^{\mathrm{T}}[R][K_{uu}]^{-1}[K_{ua}] \tag{5-63}$$

$$[A2] = [K_{ua}]^{\mathrm{T}}[K_{uu}]^{-\mathrm{T}}[R]^{\mathrm{T}}[R][K_{uu}]^{-1} \tag{5-64}$$

$$[A3] = [K_{ua}]^{\mathrm{T}}[K_{uu}]^{-\mathrm{T}}[R]^{\mathrm{T}} \tag{5-65}$$

For a specified desired shape the control voltages required for the shape control can be achieved by minimizing the error function with respect to the control voltages as follows:

$$\frac{\partial e_y}{\partial \mathcal{V}_a} = 0 \tag{5-66}$$

From the above step, the control voltages can be defined as:

$$\{\mathcal{V}_a\}^{\mathrm{T}} = (\{y_d\}^{\mathrm{T}}[A3] - \{F_m\}^{\mathrm{T}}[A2]^{\mathrm{T}})[A1]^{-1} \tag{5-67}$$

5.3.2 Active shape control

The sequence of derivations presented in this section is referenced to (Ha et al., 1992). In an active control approach, the host structure is bonded with both sensors and actuators. Consequently, Equations (5-43) and (5-45) can be written as:

$$[K_{uu}]\{X\} - [K_{ua}]\{\mathcal{V}_a\} - [K_{us}]\{\mathcal{V}_s\} = \{F_m\} \tag{5-68}$$

$$[K_{su}]\{X\} + [K_{ss}]\{\mathcal{V}_s\} = \{0\} \tag{5-69}$$

From Equations (5-68) and (5-69) it can be seen that there are two unknowns required to be solved, i.e., $\mathcal{V}_s$ and $\mathcal{V}_a$. For a known displacement the sensor voltage can be computed using Equation (5-69) as follows:

$$\{\mathcal{V}_s\} = -[K_{ss}]^{-1}[K_{su}]\{X\} \tag{5-70}$$

The actuator voltage can then be obtained from sensor voltage using the following equation:

$$\{\mathcal{V}_a\} = G_v\{\mathcal{V}_s\} \tag{5-71}$$

where G_v is a negative voltage gain that is used to amplify the sensor voltage before being applied to the actuator.

5.3.3 Voltage based shape control

In a voltage based shape control, the control voltages are defined and the resulting shape changes due to the application of the control voltages are determined. Hence Equation (5-43) can be simplified and written as (Koconis et al., 1994a):

$$\{X\} = [K_{uu}]^{-1}\{\{F_m\} + [K_{ua}]\{\mathcal{V}_a\}\} \tag{5-72}$$

5.4 Chapter summary

This chapter presented the finite element formulation for the development of static shape control codes based on the linear piezoelectric theory. The formulations have been coded using Matlab m-code programming tool. Three different codes have been developed and these were the inverse, active and voltage based shape control codes and code named as *3DSHAPE-I*, *3DSHAPE-A* and *3DSHAPE-V* respectively. Figures 5.3, 5.4 and 5.5 show the flow charts of the code implementations for *3DSHAPE-I*, *3DSHAPE-A* and *3DSHAPE-V* respectively.

The *3DSHAPE-I* code is based on inverse shape control technique which requires the desired shape of the laminate as input. The output from the code will be the required voltages needed to be applied on the actuators to achieve a desired shape. The *3DSHAPE-A* code is based on active shape control approach. The voltage required to perform the shape control

will be determined based on sensor input. The voltage from the sensor will be amplified and fed to the actuator. The *3DSHAPE-V* is based on voltage actuation technique. The actuator is applied with a prescribed voltage and the resulting deformation is then investigated.

The codes were developed to be integrated with *LS-DYNA* to actively control the impact load particularly through the inverse shape control procedure. However, this was found to be a formidable task. In order to perform the shape control analysis, the codes required the structural stiffness matrix as part of the input. Although there were options to extract the stiffness matrix, this could be only done at element level. The global stiffness matrix must then be assembled and inverted outside the *LS-DYNA* platform. This would require large storage capacity and enormous computing effort depending on the number of elements in the *FEA* model and *Matlab* could not handle such requirement. Another obstacle encountered was to dynamically link the code with *LS-DYNA*. In order to link the code to *LS-DYNA* a standalone file needs to be created. A special licence need to be purchased to perform this task. However, the major obstacle was with extracting the stiffness matrix and issues related to it. Hence the attempt to link the codes was not pursued further.

Instead the *3DSHAPE-V* code was used independently to investigate the effects of piezoelectric actuation on structural deformation. Since the code was developed based on solid element formulation, it does not include assumption such as plane stress condition in the formulation. The use of solid element would allow thickness change of the piezoelectric element although this may only be crucial for embedded actuator system.

The *3DSHAPE-A* code was never used but it may have future use beyond this research work. The inverse shape control code would have been of profound use if it could have been linked to *LS-DYNA*. However, out of interest a shape control investigation was performed using this code and the findings have been published in the journal of Smart Materials and Structures (Dawood et al, 2009). The code relevant to the current research work is the *3DSHAPE-V*. This code has been used to characterize the effects of *MFC* actuation on composite laminate considering various design and actuation parameters. The detail of the study can be found in Chapter 7.

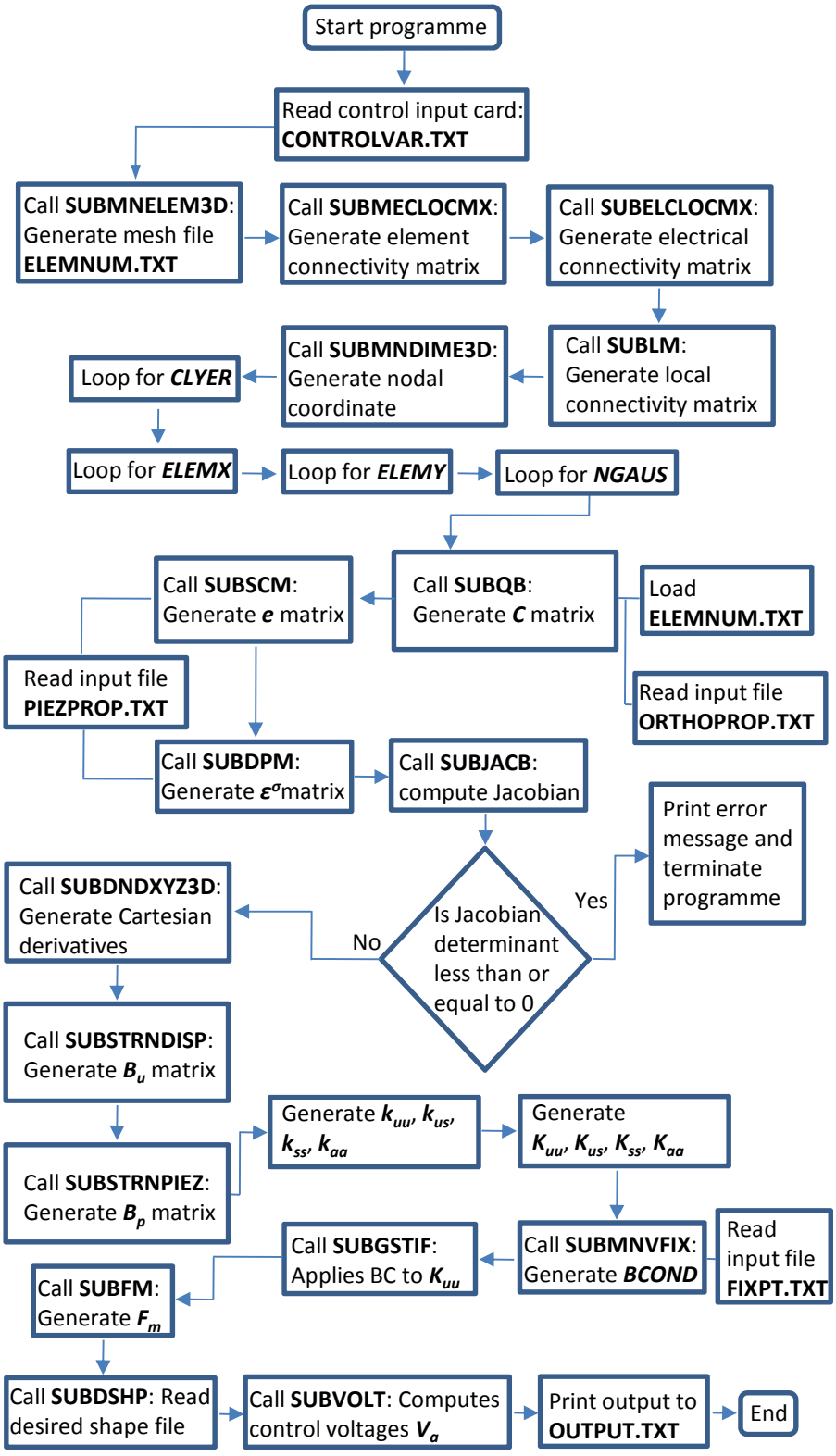


Figure 5.3: Flowchart - *3DSHAPE-I* code

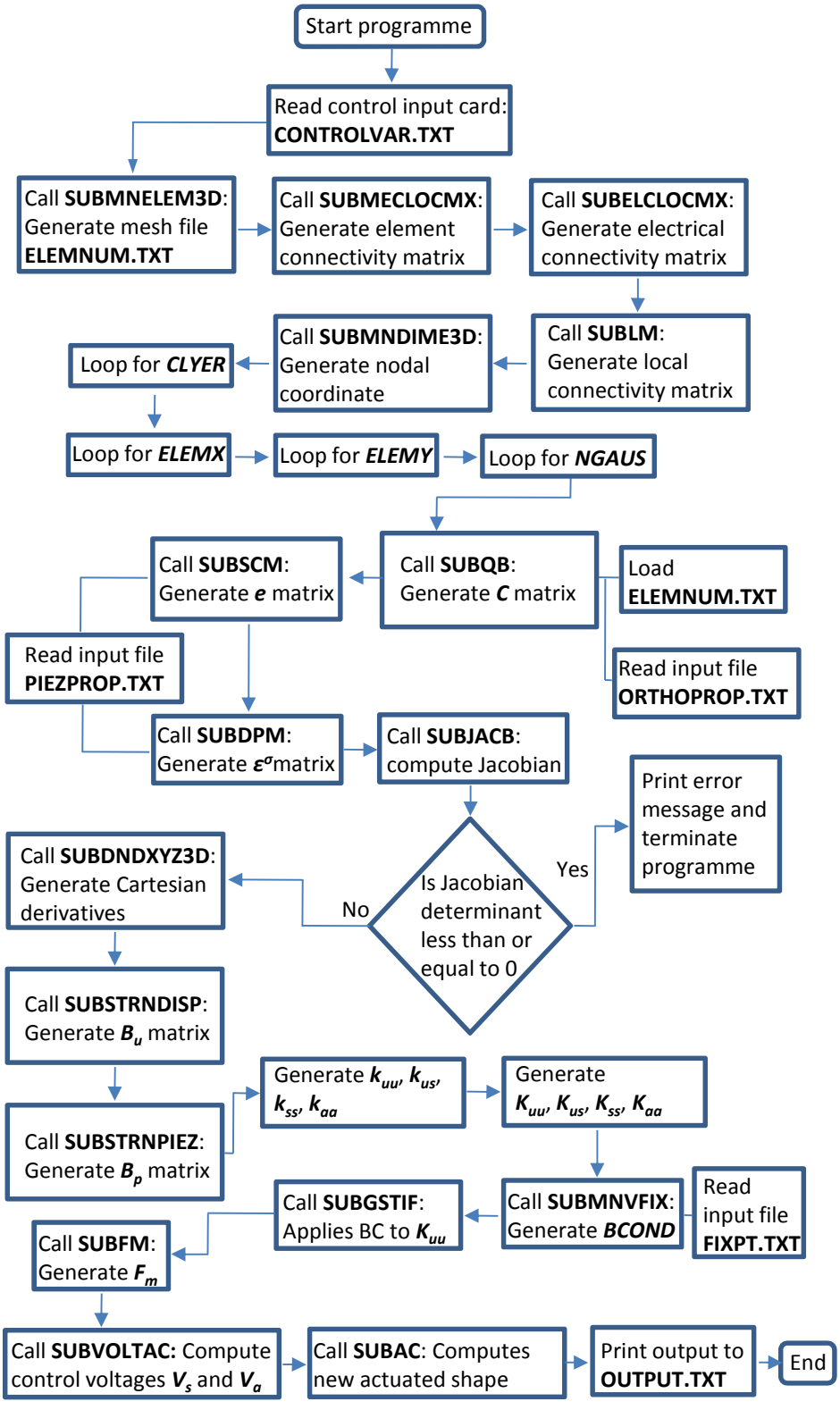


Figure 5.4: Flowchart - *3DSHAPE-A* code

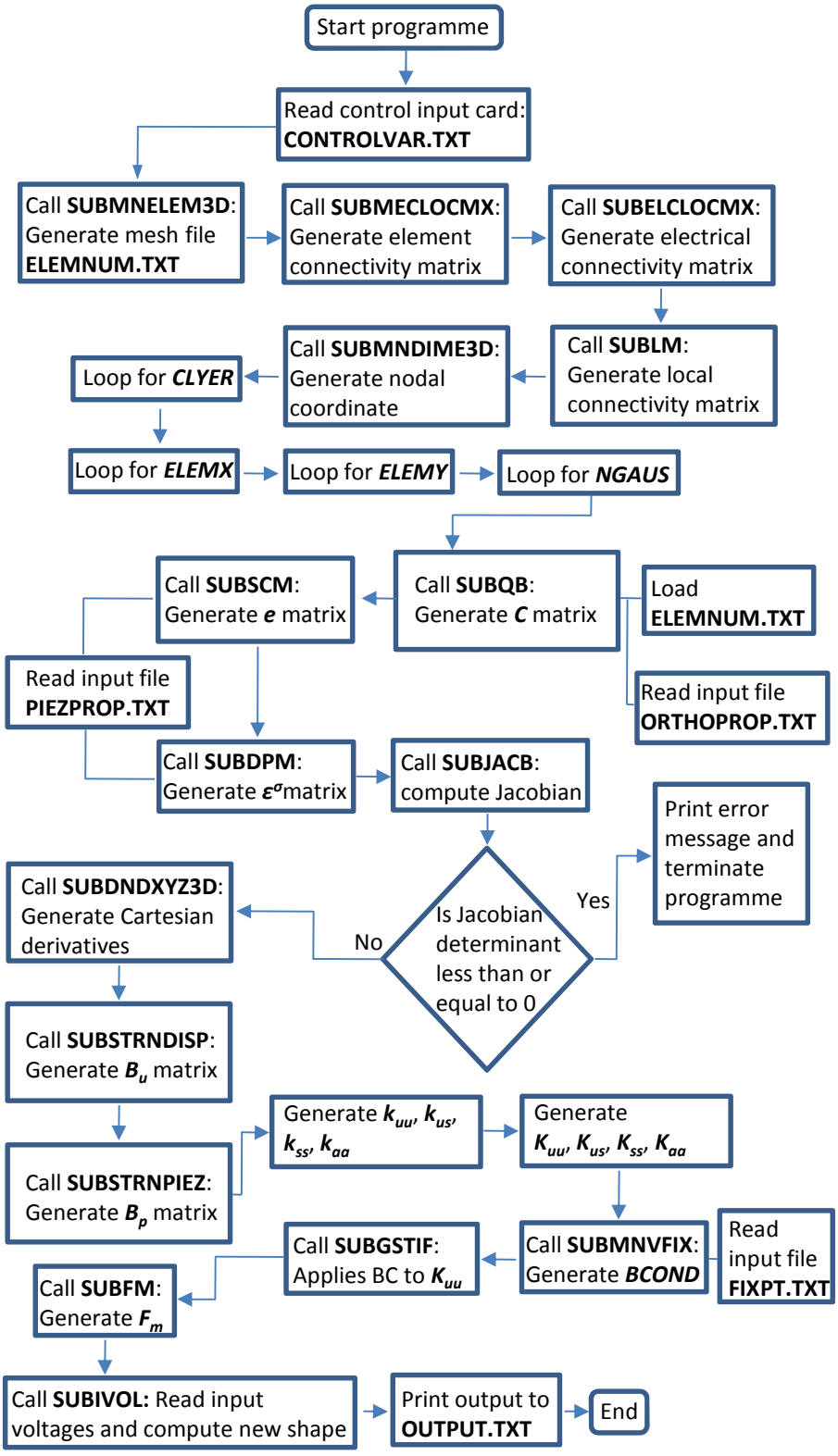


Figure 5.5: Flowchart - *3DSHAPE-V* code

Chapter 6

Validation of the finite element codes

6.1 Chapter introduction

In this chapter a series of test results are presented to validate the accuracy of the developed piezoelectric finite element code, *3DSHAPE-V*, and the different piezoelectric actuation models implemented into *LS-DYNA*. In Section 6.2 simulation results are presented to demonstrate the actuation characteristics of piezoelectric actuators based on the linear actuation model using static and dynamic solvers. In Section 6.3 validation results are presented for the linear and nonlinear piezoelectric actuation models based on the test results extracted from the work of Crawley and Lazarus (1991). Section 6.5 presents simulation results to demonstrate the actuation capabilities of *MFC* actuator based on the experimental work of Giddings et al. (2008). The outcome of this chapter is the identification of the most suitable piezoelectric actuation model to be used in subsequent impact investigations.

6.2 Linear piezoelectric material model

This section presents validation results for the *3DSHAPE-V* code and material model *umat50*. The test cases consist of a single element free strain measurement and a piezoelectric bimorph beam bending simulation.

6.2.1 Free strain test

A single element test was first considered to illustrate the free strain response of a piezoelectric actuator under electrical loading condition. In this simulation the linear piezoelectric material model was used to determine the free strain of an unconstrained actuator subjected to a constant voltage. The strains obtained using the *3DSHAPE-V* and *umat50* were compared with the ones computed using Equation (4-13).

Table 6.1: Material properties of *PZT-G1195* piezoceramic[2]

Properties	***PZT-G1195***
Elastic modulus (GPa):	
E_{11}, E_{22}, E_{33}	63, 63, 63
Shear modulus (GPa):	
G_{12}, G_{23}, G_{13}	24.2, 24.2, 24.2
Poisson's ratio:	
v_{12}, v_{23}, v_{13}	0.3, 0.3, 0.3
Piezoelectric strain constant (pm/V):	
d_{31}, d_{32}, d_{33}	254, 254, -374

2 Data obtained from Ha et al. (1992)

The actuator used in the investigation was bulk *PZT-G1195* piezoceramic and its material and piezoelectric properties are given in Table 6.1 (Ha et al., 1992). The *PZT* actuators are normally transversely isotropic hence the elastic modulus in the direction of poling will not be the same as the in-plane modulus. However, when such material data is not available, the elastic modulus in the direction of poling is assumed to be the same as the in-plane modulus (Ha et al., 1992). Hence, an isotropic condition was used to describe the *G1195* piezoceramic. The geometric configuration of the test model is shown in Figure 6.1. The local coordinate (*1*, *2, 3*) of the actuator was set to be along its global coordinate system (*x*, *y*, *z*). Table 6.2 shows the test results obtained from *3DSHAPE-V* code against the free strains calculated using the second term on the right hand side of Equation (4-13) for an actuation voltage of 10V.

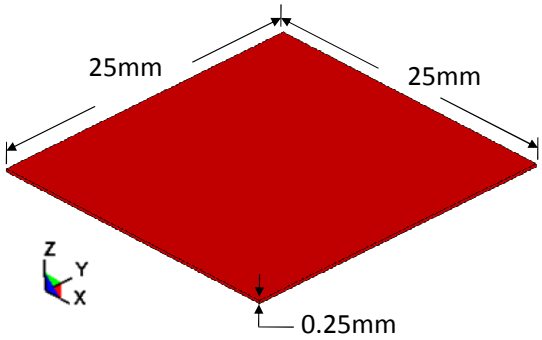


Figure 6.1: Unconstrained *G1195* piezoceramic

Table 6.2: Free strain

Strain component	***Equation (4.13)***	***3DSHAPE-V***
	microstrain	
x direction	10.16	10.16
y direction	10.16	10.16
z direction	-14.96	-14.96

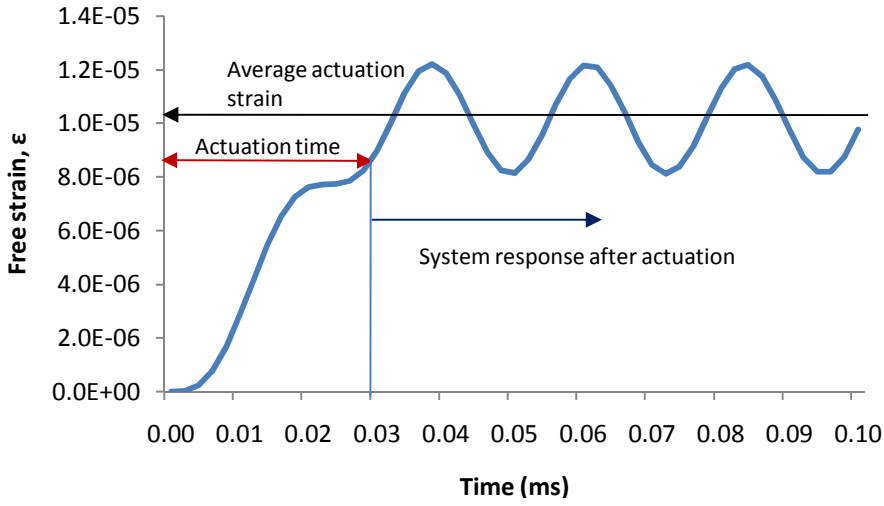


Figure 6.2: Strain in *x* direction obtained from *umat50* (T_{min}=30 μs)

From Table 6.2 it can be seen that the free strains obtained from the code matched exactly with those computed using Equation (4-13). However, some discrepancies were noticed with the free strain values obtained using *umat50*. To explain the discrepancies the free strain plots along *x* and *z* directions are shown in Figures 6.2 and 6.3 respectively. The free strain plot in *y* direction is the same as the plot in Figure 6.2, hence, not shown as a separate figure.

From Figures 6.2 and 6.3 it can be seen that the respective actuation strain components increased nonlinearly with the actuation voltage and went into oscillation beyond the specified actuation time. This was associated with the actuation time used in the numerical simulation. In the above simulation the actuation time was computed using the following equation (www.piceramic.com):

$$T_{min} \approx \frac{1}{3f_o} \tag{6-1}$$

where:

T_{min} : response time to achieve nominal actuation

f_o : resonant frequency

The resonant frequency of a piezoelectric material depends on the stiffness and effective mass of the material. For simulation purpose, the resonant frequency was assumed to be 10kHz and based on the above equation the estimated response time was 30μs. Since *LS-DYNA* is a time dependent solver the dynamic effect of the short loading rate was reflected on the system's response. Nevertheless, from the plots shown in Figures 6.2 and 6.3, it can be seen that the average actuation strains were very close to the ones computed using Equation (4-13).

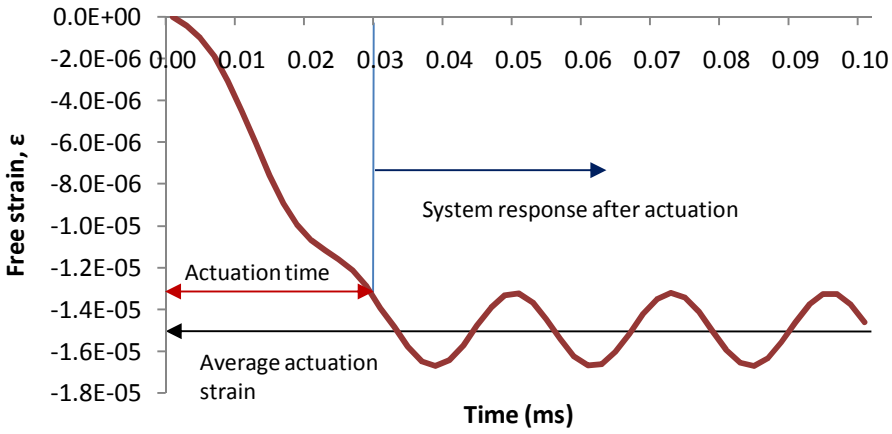


Figure 6.3: Strain in z direction obtained from *umat50* (T_{min}=30 μs)

Figures 6.4 and 6.5 show the respective free strain plots in x and z directions for an actuation time of 0.5ms. In this case the actuation strains increased linearly over the actuation period and exhibited a stable response. The figures also show that the oscillatory behaviours

were significantly reduced and the strain predictions were also much closer to the ones predicted in Table 6.2.

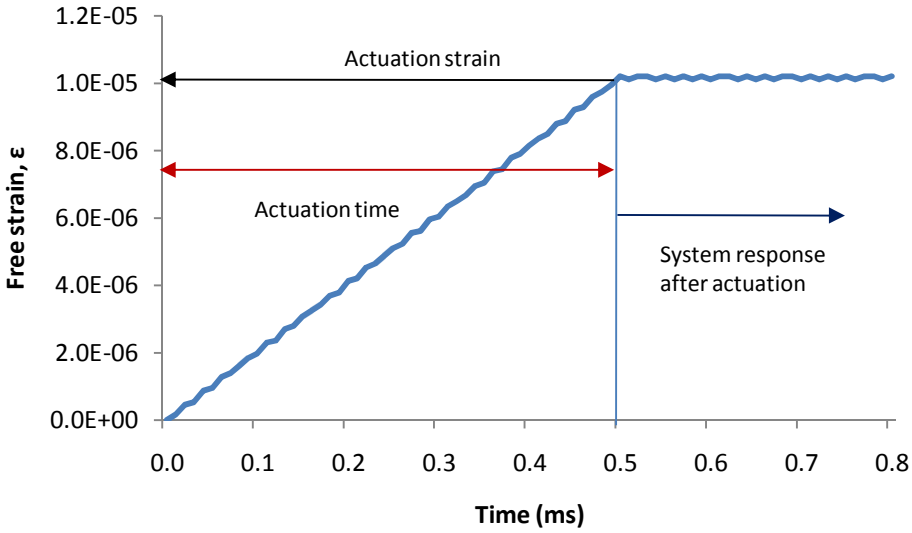


Figure 6.4: Strain in *x* direction obtained from *umat50* (T_{min}=0.5ms)

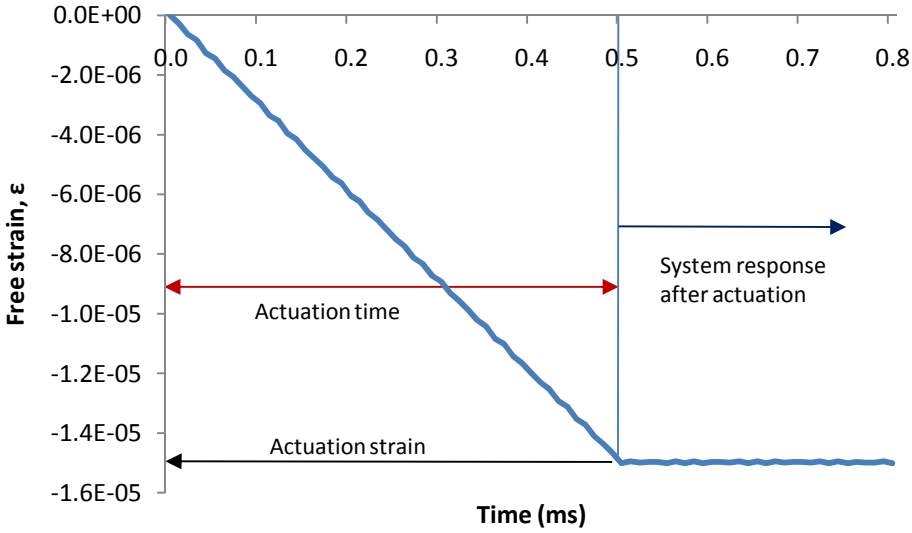


Figure 6.5: Strain in *z* direction obtained from *umat50* (T_{min}=0.5ms)

The analyses conducted using *LS-DYNA* show that the piezoelectric actuation response depends on the loading rate. A smooth response could be achieved if a longer loading rate is used. However, longer loading would increase the computational time. Another possible alternative is to introduce damping into the system but this would stiffen the response and may affect the results. Hence the best compromise between computational cost and accuracy would be to keep the loading rate sufficiently longer with the introduction of minimal

damping parameters. However, in all the investigations presented in this report no damping was considered.

6.2.2 Piezoelectric bimorph beam

This test was extracted from the experimental work conducted by Tzou (1993) on a cantilevered piezoelectric bimorph beam. The beam was made by bonding two *PVDF* polymers together. The experimental configuration of the bimorph beam is shown in Figure 6.6. In this investigation, the top and bottom layers were subjected to the same voltages with opposing polarities to create a bending deformation. The material and piezoelectric properties of the piezopolymer are given in Table 6.3 (Lee et al., 2004). The *PVDF* was assumed isotropic, since the material data in direction E_{33} was not available (Lee et al., 2004).

For the finite element investigation the beam was discretized into 100×1×2 elements along x, y and z respectively for the *umat50* and into 10×1×2 elements along x, y and z for the *3DSHAPE-V*, Figure 6.7. For the numerical simulation using *umat50* two different actuation times were considered to highlight the effects of loading rates on the response of the beam, i.e., T_{min}=5ms and T_{min}=15ms. Table 6.4 compares the deflections of the cantilevered bimorph beam obtained from the *3DSHAPE-V* code and *umat50* with the experimental and numerical results obtained from reference Suleman and Venkayya (1994).

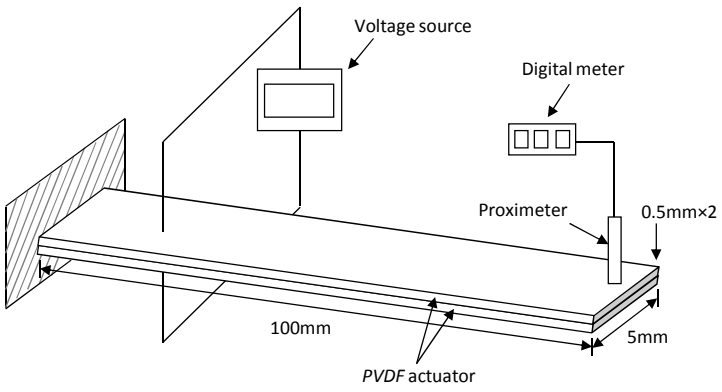


Figure 6.6: Experimental configuration of piezoelectric bimorph beam (Tzou, 1993)

Table 6.3: Material properties of *PVDF* polymers[3]

Properties	*PVDF*
Elastic modulus (GPa):	
E_{11}, E_{22}, E_{33}	2, 2, 2
Shear modulus (GPa):	
G_{12}, G_{23}, G_{13}	0.78, 0.78, 0.78
Poisson's ratio:	
v_{12}, v_{23}, v_{13}	0.29, 0.29, 0.29
Piezoelectric strain constant (pm/V):	
d_{31}, d_{32}	23, 3, -33

3 Data obtained from Lee et al. (2004)

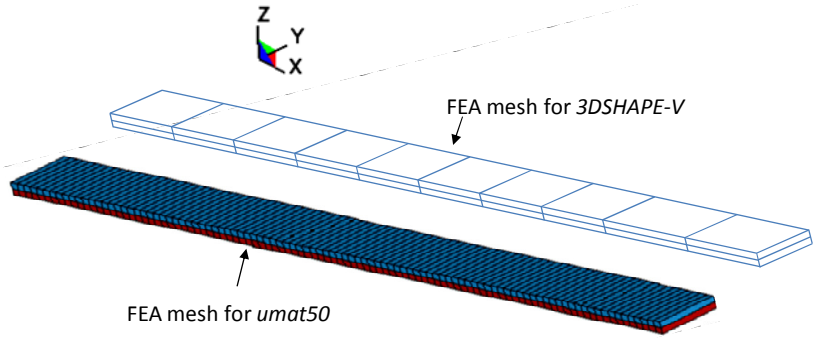


Figure 6.7: Finite element model used in the bimorph analysis

Table 6.4: Deflection along the length of the bimorph *PVDF* beam

Model	Deflection ($\times 10^{-4}$mm) at				
	20mm	40mm	60mm	80mm	100mm
Experiment[4]	-	-	-	-	3.15
Theory[4]	0.138	0.552	1.24	2.21	3.45
3DSHAPE-V	0.137	0.550	1.24	2.21	3.45
umat50 (T_{min}=5ms)	0.145	0.575	1.29	2.29	3.56
umat50 (T_{min}=15ms)	0.138	0.555	1.24	2.21	3.46

4 Data obtained from Suleman and Venkayya (1994)

The results of the *3DSHAPE-V* matched the theoretical results reported by Suleman and Venkayya (1994) and a good agreement was also observed when it is being compared with the experimentally determined value for the tip deflection. The difference between the experiment and the numerical results can be attributed to assumptions such as perfect bonding in the numerical model. The results obtained using *umat50* closely matched the reported results using 15ms actuation time. Like in the previous cases, the results shown for *umat50* are the averaged displacement values. From this analysis it can be concluded that the effect of the electrical loading rate is very important for the solution accuracy using the piezoelectric actuation model implemented into *LS-DYNA*.

6.3 Nonlinear piezoelectric material model

In this section validation results for *umat48* and *umat49* are presented to verify the accuracy of the respective nonlinear piezoelectric material models. The test case was extracted from the experimental work of Crawley and Lazarus (1991). In this test a *G1195* piezoceramic actuator was sandwiched between two substrate layers and four different sandwich structures were

constructed. The first three sandwich structures were constructed using an aluminium substrate with thickness of 0.32mm, 0.51mm and 0.84mm while the fourth sandwich was constructed using a graphite/epoxy substrate with thickness of 0.41mm. The thickness of the actuator was 0.25mm.

Table 6.5: Material properties of the sandwich specimen[5]

Properties	*G1195*	Aluminium	Graphite/epoxy
Elastic modulus (GPa):			
E_{11}, E_{22}	63, 63	70, 70	95.8, 6.7
Poisson's ratio:			
v_{12}	0.28	0.32	0.27
Piezoelectric strain constant (pm/V):			
d_{31}, d_{32}	254,254	-	-
Electrostrictive constant (fm^2/V^2):			
d_{311}, d_{322}	0.388,0.388	-	-

5 Data obtained from Crawley and Lazarus (1991)

The material properties of the respective substrate layers and the actuator are given in Table 6.5 and the geometric configuration of the test model is shown in Figure 6.8. Figure 6.8 also represents the *FEA* model used in the numerical simulation which consisted of 1×1×3 elements along *x*, *y* and *z* respectively. The material axes of the test articles were set along their global axes. In all the test cases, the actuator was applied with an electric field of 551V/mm. The strains predicted from the present simulations are compared in Table 6.6 with the experimental and analytical results of Crawley and Lazarus (1991).

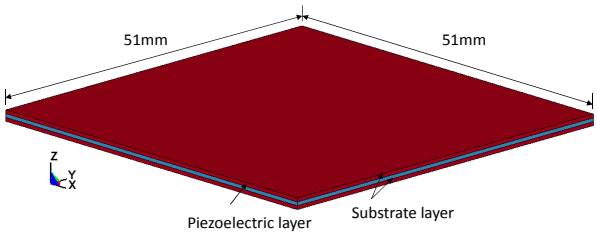


Figure 6.8: Piezoelectric sandwich structure (Crawley and Lazarus, 1991)

Table 6.6: Strain prediction in piezoelectric sandwich structure

	Graphite/epoxy	Aluminium	Aluminium	Aluminium
Thickness (mm)	0.41	0.32	0.51	0.84
Longitudinal strain (microstrain)				
Experiment[5]	23.2	38.1	28.1	14.6
Analytical[5]	20.4	39.7	26.6	16.9
umat50	23.4 (-0.9)	36.4 (4.5)	24.2 (13.9)	15.8 (-8.2)
umat49	25.3 (-9.1)	40.9 (-7.3)	26.1 (7.1)`	16.6 (-13.7)
umat48	33.5 (-44.4)	51.9 (-36.2)	34.5 (-22.7)	22.6 (-54.8)
Transverse strain (microstrain)				
Experiment[5]	183.2	40.9	28.2	15.1
Analytical[5]	187.0	39.7	26.6	16.9
umat50	128.9 (29.6)	36.4 (11.0)	24.2 (14.2)	15.8 (-4.7)
umat49	191.4 (-4.5)	40.9 (0.0)	26.1 (7.4)	16.6 (-9.9)
umat48	183.6 (-0.2)	51.9 (-26.9)	34.3 (-21.6)	22.6 (-49.7)

5 Data obtained from Crawley and Lazarus (1991). Bracketed terms indicate percentage of error with respect to experiment.

Since the elastic modulus of the graphite epoxy sandwich is higher in the longitudinal direction, it was expected to have a lower strain prediction in the longitudinal direction as compared to the transverse direction. From Table 6.6 it can be seen that the longitudinal strain predicted by the linear and strain induced models were comparatively close to the experimental and analytical results reported by Crawley and Lazarus (1991). However, the strain induced model could be seen to over predict the longitudinal strain in the graphite/epoxy sandwich by 9.1%. The electric field dependent model was shown to give the highest strain prediction in the longitudinal direction with an overestimation of 44.4% for the graphite/epoxy sandwich. In the case of the transverse strain, the electric field dependent model gave the most accurate prediction of the actuation strain with an error of 0.2%, whereas the strain induced model overestimated the strain by 4.5%. The linear model underestimated the transverse strain by almost 29.6%.

The difference in the elastic modulus of the graphite epoxy sandwich would lower the deformation in the longitudinal direction and this behaviour was accurately captured by the strain induced model due to its dependence on the actual strain within the actuator. In the case of the linear model, the strain could be seen to be much closer to the experimental prediction probably due to the lower strain coefficient. The electric field dependent model was not

affected by the strain in the actuator and depends exclusively on the applied electric field. Hence, this model tends to overestimate the strain prediction in the longitudinal direction. In the case of the linear model the lower strain coefficient was not sufficient to predict the strains accurately for substrates with large difference in its elastic modulus especially in the transverse direction. The best compromise was observed with the strain induced model with respect to the strain predictions in both directions.

In the case of aluminium substrate the strain induced model was found to provide the best match with the experimental predictions. The linear model mostly predicted lower strain values, while the electric field dependent model gave higher strain prediction in comparison to the experimental values. Thus in all cases the strain dependent model has been found to be more appropriate and accurate for structural actuation.

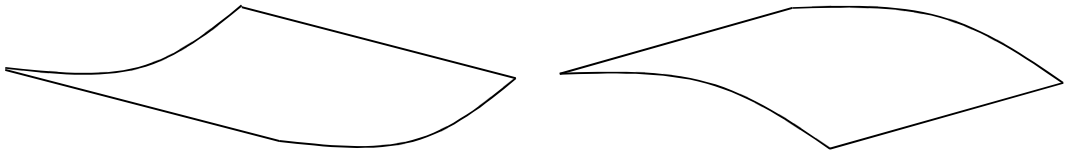
It is also important to be mentioned that different investigators have used different values for the strain coefficients and reported almost similar predictions in comparison with the experimental values for the test case considered in this section. Thornburgh and Chattopadhyay (2001) used $d_{31} = d_{32} = 247\text{pm/V}$ and $d_{311} = d_{322} = 0.276\text{fm}^2/\text{V}^2$ to predict the actuation strain for the graphite/epoxy sandwich using a similar induced strain approach. However, an attempt to simulate the experiment with those values found that the strain prediction to be underestimated. The transverse strain value was found to be 165.1$\mu\varepsilon$, which was 10% less than the value predicted in the experiment. For the electric field model they have used $d_{311} = d_{322} = 0.414\text{fm}^2/\text{V}^2$. Hence, it is highly probable that the differences in the strain predictions by the induced strain model reported in Table 6.6 were also caused by d_{311} and d_{322} values used in the investigation.

6.4 Bistable composite

The test case considered in this section was extracted from the work of Giddings et al. (2008). Part of the investigation involved examining the use of *MFC* actuator to increase the curvature of a bistable (0/90) composite. The actuator was surface bonded to the laminate according to the following layup (0_{MFC}/0/90). The dimensions of the composite laminate and the *MFC* patch used in the investigation were $150\times150\times0.32\text{mm}^3$ and $85\times57\times0.3\text{mm}^3$ (active area) respectively.

The *MFC* was centrally bonded to the laminate with its major axis (fibre direction) aligned along the 0^o of the top composite ply. In the experiment conducted by Giddings et al.

(2008), the laminate was cured to one of its bistable state using a curing temperature of 125°C (State A), Figure 6.9a. However, in order to investigate the effect of *MFC* actuation on the laminate curvature, the laminate was manually switched to its other bistable state and this is shown in Figure 6.9b (Giddings et al., 2008).



(a) State A (b) State B

Figure 6.9: Bistable state of (0/90) composite (Giddings et al., 2008)

In the present investigation, the experiment conducted by Giddings et al. (2008) was simulated using *LS-DYNA* explicit solver. The piezoelectric behaviour was described using *umat49*. Table 6.7 lists the material properties of the composite material and *MFC* actuator used in the investigation. The nonlinear properties of the *MFC* actuator were obtained from Williams (2004). It must be mentioned that Williams (2004) provided a range of actuation data and these differed for low field and high field actuations. In this simulation the piezoelectric data were chosen within the high field regime which gave approximately 1400με at 1500V.

The *FEA* model used in the simulation is shown in Figure 6.10. For the *MFC* only the active area was modelled. Since the laminate curvature was not known, the laminate shape in State B was obtained by appropriately applying the temperature field to achieve a qualitative match with the shape reported by Giddings et al. (2008). In the cured shape the laminate curvature can be estimated using the following equation (Tawfik, 2008):

$$\kappa = \frac{8z_d}{L_d^2 + 4z_d^2} \tag{6-2}$$

where:

z_d : relative displacement in the z-direction

L_d : relative displacement along the curved length of the laminate

Using Equation (6-2), the laminate curvature from the *FEA* simulation was estimated to be 2.45/m which corresponded to a radius of 0.41m based on predicted values of 149mm and 6.9mm for L_d and z_d respectively. A good qualitative match was achieved between the numerical simulation and with that reported by Giddings et al. (2008), Figure 6.11.

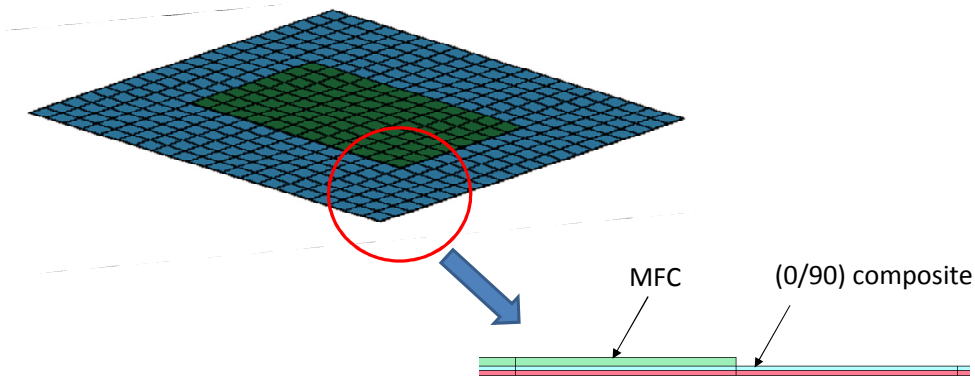
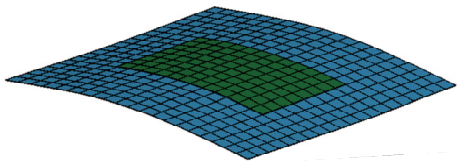


Figure 6.10: *FEA* model of the bistable (0_{MFC}/0/90) composite



(a) Experimental shape (Giddings et al., 2008)



(b) Shape simulated with *FEA*

Figure 6.11: Bistable State B of (0_{MFC}/0/90) laminate

Table 6.7: Material properties used in the bistable simulation

Properties	Composite[6]	*MFC*[7]
Elastic modulus (GPa):		
E_{11}, E_{22}, E_{33}	135,18.5,18.5	30.3,15.9,11.5
Shear modulus (GPa):		
G_{12}	5.98	5.5
Poisson's ratio:		
v_{12}	0.29	0.31
Strain constant (pm/V):		
d_{11}, d_{12}, d_{13}	-	380,-170,-170
Electrostrictive coefficient (fm^2/V^2):		
d_{111},d_{211}	-	0.0568,-0.0392

6 Data from Giddings et al. (2008); 7 Data from Williams (2004)

To determine the effects of piezoelectric actuation on the laminate curvature, the *MFC* was subjected to a range of voltages. The predicted values of z_d from the *FEA* simulation are compared with those reported by Giddings et al. (2008) in Figure 6.12. The z_d values were measured relative to the laminate state at 0V.The numerical results obtained using the piezoelectric material data given in Table 6.7 are represented by the *FEA-1* plot.

From the figure it could be seen that the results of the *FEA-1* plot showed similar displacement trend as reported by Giddings et al. (2008). However, the results of the *FEA-1* simulation were much lower than the ones reported especially at high actuation voltages. At 1400V the difference between the *FEA-1* result and the one reported by Giddings et al. (2008) was almost 30.4%. The observed discrepancy was mainly due to the piezoelectric strain coefficients used in the analysis. The standard published value of the piezoelectric strain coefficient for *MFC* actuator is 460pm/V at high field which corresponds to 1400με at 1500V (www.smart-materials.com). The strain coefficients given in Table 6.7 were selected to match this strain value. However, it is also documented that the M-8557-P1 type *MFC* could produce up to 1800με (www.smart-materials.com).

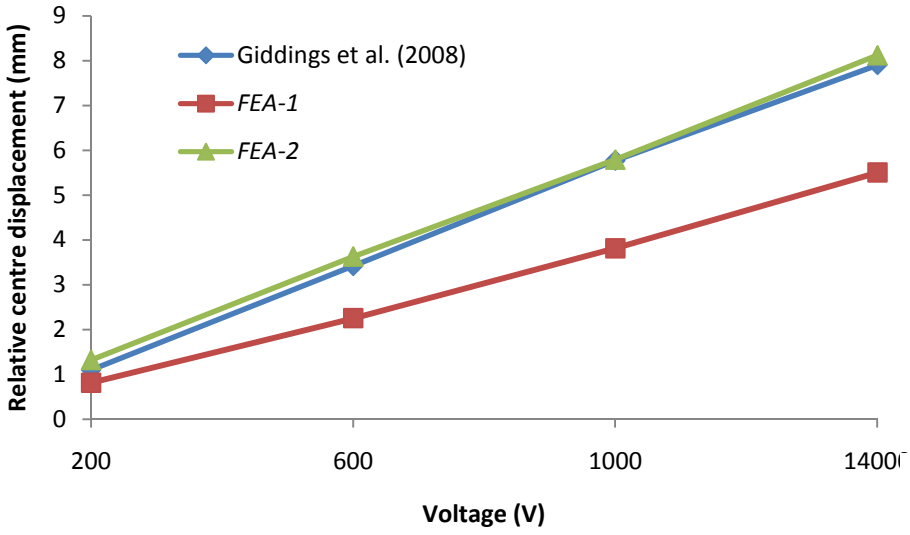


Figure 6.12: z_d values measured at different actuation voltages

The strain coefficient, d_{11}, was modified with an effective value of 600pm/V to accommodate 1800με at 1500V. The free displacements of the laminate using the new value are given by the *FEA-2* plot in Figure 6.12, which were highly accurate in comparison to the *FEA-1* plot. In this case the error between the simulation and the experiment was reduced to 2.8% at 1400V. Portela et al. (2008) used a proportionality factor of 1.5με/V in order to simulate snap-through behaviour in bistable composite using *MFC* actuator. Using this factor the actuation strain is estimated to be 2250με at 1500V. The standard piezoelectric coefficient provided in the manufacture's data list is far too less to be accurately used in the numerical simulation. A detail characterization of the commercially available *MFC* actuator may serve as a useful future work.

6.5 Chapter summary

The developed piezoelectric finite element code, *3DSHAPE-V*, and the piezoelectric material model implemented into *LS-DYNA*'s user defined material subroutine have been successfully validated. From the validation conducted in this chapter the strain induced model has been found to provide the closest match with the experimental strain predictions especially when the substrate was made of orthotropic materials.

The linear model tends to underestimate the strain prediction in the low stiffness direction while the electric field dependent model tends to give a higher strain value in the high

stiffness direction. This is because, the strain coefficient in the linear model is neither dependent on the induced strain nor the applied electric field. Consequently, this would tend to lower the actuation strain. On the contrary, the electric field dependent model gave high strain prediction in the high stiffness direction as it depends exclusively on the applied field for actuation. The strain coefficient increases linearly with the applied field. Hence, as the field increases, it would tend to give a higher estimate of the actuation strain.

The actuation strain in an induced strain model is affected by, both, the applied electric field and the actual strain in the actuator. In reality the actual strain in the actuator will be affected by the material orthotropy, boundary and loading conditions. This is more physically based and accurate than the other two actuation models and these have been proven and validated in this section. The slight discrepancies observed with the induced strain model could be attributed to other factors such as the selection of the piezoelectric coefficients and the loading rates used in the simulation. Hence in subsequent impact investigations the induced strain model will be used.

A validation on the use of *MFC* actuator on bistable composite revealed that the strain coefficient values provided by the manufacture were less than the actual actuation strain capacity of the material. The use of this data in the numerical simulation was found to give a lower estimate of the actual behaviour of the laminate-actuator system. This has also been observed by Portela et al. (2008) in their investigation to use the *MFC* actuator to induce snap through in bistable composites.

The validation provided in this chapter has shown that the induced strain model to be the most appropriate actuation tool for piezoelectric related investigations.

Chapter 7

Effects of piezoelectric actuation on structural deformation: A parametric study

7.1 Chapter introduction

The objective of this chapter is to investigate the effects of piezoelectric actuations on structural deformation. As part of the investigations the effects of the following conditions on piezoelectric actuation capabilities were investigated using the *3DSHAPE-V* code:

1. Boundary conditions
2. Stacking sequences
3. Material properties
4. Actuation voltages
5. Actuator placements
6. Actuator types

The choices for the first three conditions were based on the setups used in low velocity impact related investigations (Aymeric et al., 2008) while the actuator material was limited to the *MFC* type. The outcome of this chapter would constitute a complete characterization on the actuation capabilities of the *MFC* actuator with respect to design parameters listed above.

This was considered important since there were no previous studies that have characterized the performance of the *MFC* actuators with respect to stiff structural components such as the one considered in the present investigation. This would be used as a guideline towards the identification of a favourable laminate-actuator system in terms of laminate geometry, material constitution and actuator parameters such as type and placement to be used in subsequent impact investigations.

7.2 Setups for numerical simulation

This section underlines the numerical setups that have been used in the parametric study. The commonly used boundary conditions in low velocity impact investigations constitute the combinations of simply supported, clamped and free edges. For the purpose of present investigation two types of boundary conditions were considered, i.e., all edges simply supported (*SS*) and all edges fully clamped (*CC*). These support types are schematically illustrated in Figure 7.1 for full and quarter models. For the laminate layup, the following lamination sequences were considered:

1. ($p/0_2/90_2/90_2/0_2/p$) symmetric cross ply layup – (*P0* laminate)
2. ($p/90_2/0_2/0_2/90_2/p$) symmetric cross ply layup – (*P90* laminate)

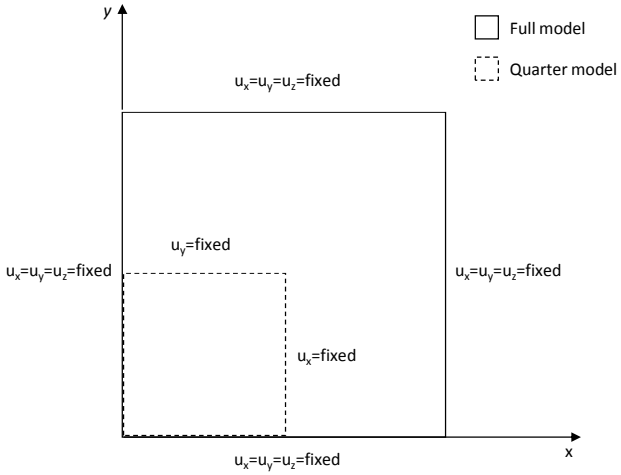
The letter *p* appearing in the lamination sequence indicates the position of the piezoelectric actuators. Two different materials were considered for the composite layers which were HTA/6376C carbon/epoxy and HS160/REM graphite/epoxy.

Although most impact investigations in the literature were on quasi-isotropic laminates, in this study a simple lay-up which consisted of symmetric-cross ply laminate was chosen. A typical quasi-isotropic laminate such as the standard *Boeing* impact coupon is made of $[45/-45/90/0]_s$ lay-up which will consists of at least seven interface layers. In modelling the impact specimen, solid element was used rather than shell element. This is because the shell element was developed based on the plane stress assumption which neglects the contribution of the out-of-plane stress components (Jones, 1999). Although the in-plane stress components are many times larger than the out-of-plane stresses, delamination due to low velocity impact has been found to be mainly instigated by the out-of-plane stresses (Liou, 1997). Hence the shell formulation becomes inadequate for such investigation. Ideally the use of solid element would require the element aspect ratio between the thickness:width:length to be 1:1:1. This would

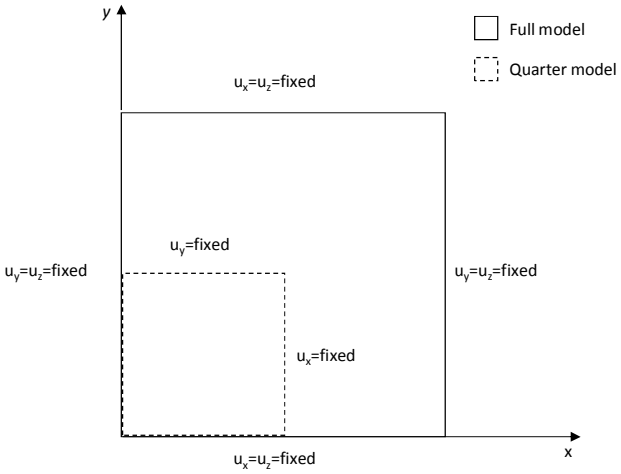
however increase the number of elements in the *FEA* model. The time step in *LS-DYNA* explicit solver is controlled by the shortest distance between two nodes in the *FEA* model. The thickness of a cohesive layer is usually assumed to be one-fifth of a laminate's layer thickness and this would drastically increase the computational time (Iannucci, 2006). Hence, a quasi-isotropic layup was considered to be numerically and computationally intensive. Alternatively, a symmetric cross-ply laminate such as the one used in the present investigation would only require interface elements to be introduced at two interfaces only, i.e., at 0/90 and 90/0 as numerous experimental investigations found no traces of delamination between the plies of same orientation (Aymerich et al., 2008; 2009).

The actuator materials considered in this study were limited to the standard and single crystal *MFC*s. The material properties and geometric data of the composite laminate and the actuator are listed in Tables 7.1 and 7.2 respectively. For the purpose of comparison the thickness of each composite layer of the different materials were assumed to be same and was set to 0.125mm/ply. The thickness of the standard and single crystal *MFC*s was set to 0.3mm which is the actual thickness of the standard *MFC*. The largest available patch size for the standard *MFC* is 85×57mm^2 (www.smart-material.com) and 20×20mm^2 for the single crystal type (Wilkie et al., 2006). However, again for the purpose of comparison the patch size was set to 40×30mm^2 for both the actuators to accommodate the variation in the actuator placement.

The single crystal *MFC* has higher piezoelectric strain constant, but lower elastic modulus. In addition, it also has a very low coercive field, about 300V/mm, which limits its use to applications with low voltage requirements (Wilkie et al., 2006). On the contrary the standard *MFC* has lower piezoelectric strain constants as compared to the single crystal type but has higher elastic modulus and operating voltages.



(a) Clamped (*CC*)



(b) Simply supported (*SS*)

Figure 7.1: Clamped and simply supported boundary conditions

Table 7.1: Material properties of composite laminates

Properties	HTA/6376C (*Mat 1*)[§]	HS160/REM (*Mat 2*) [§§]
Elastic modulus (GPa):		
E_{11}, E_{22}, E_{33}	140,10,10	93.7,7.45,7.45
Shear modulus (GPa):		
G_{12}, G_{23}, G_{13}	5.2,3.9,5.2	3.97,3.97,3.97
Poisson's ratio:		
v_{12}, v_{13}, v_{23}	0.3,0.3,0.5	0.26,0.26,0.26
Dimension (mm)		
length, width	100,100	100,100

§ Data from Iannucci (2006), §§ Data from (Aymeric et al., 2008)

The actuators were symmetrically placed at the top and bottom layers of the laminate. Due to symmetry in geometry, loading and boundary conditions quarter models were used in all the numerical simulations. The different types of actuator placements considered in the parametric study are shown in Figure 7.2 for the quarter model. Figure 7.2 also represents the *FEA* model used in the numerical simulations. Unless specified otherwise, the top and bottom actuators were applied with positive and negative voltages respectively. This mode of actuation will induce a negative moment which allows the plate to bend in an upward direction. In all the analyses no restrictions were imposed on the maximum and minimum applicable voltages on the actuators.

Table 7.2: Material properties of piezoelectric actuators

Properties	Standard *MFC* (*Mat 3*)† †	Single crystal *MFC* (*Mat 4*)‡
Elastic modulus (GPa):		
E_{11}, E_{22}, E_{33}	30.3,15.9,11.47	6.23,11.08,11.08
Shear modulus (GPa):		
G_{12}, G_{23}, G_{13}	5.5,2.14,2.6	2.01,2.01,2.01
Poisson's ratio:		
v_{12}, v_{13}, v_{23}	0.31,0.29,0.33	0.23,0.23,0.23
Piezoelectric strain constant (pm/V):		
d_{11}, d_{12}, d_{13}	460,-210-210	1897,-838,-838
Dimension (mm)		
length, width	40,30	40,30

† † Data from www.smart-materials.com, ‡ Data from Park and Kim, (2008)



Figure 7.2: Actuator placements for quarter model

7.3 Effects of boundary conditions

The effects of piezoelectric actuation on cross-ply laminates with different boundary conditions are presented in Figures 7.3 to 7.22. For the purpose of investigation the following settings were considered:

1. Actuator placement : *TYPE- E*
2. Actuator material : *Mat 3*
3. Composite material : *Mat 1*
4. Laminate thickness : 1mm

7.3.1 Simply supported laminate

This section discusses the effects of simply supported boundary condition on the piezoelectric actuation characteristics. The actuators were actuated with voltages of 0V/0V, 250V/-250V, 500V/-500V and 1000V/-1000V. The first number indicates the voltage applied to the top actuator while the second number indicates the voltage applied to the bottom actuator.

7.3.1.1 *P0* laminate

Figures 7.3 and 7.4 show the centreline displacements of simply supported *P0* laminate about *y*- and *x*-axes respectively. From the figures it can be seen that the displacements of the laminate increased with increasing actuation voltages. A linear relationship could be observed between the displacements and the applied voltages. This was expected since the linear actuation model was used in the development of *3DSHAPE-V* code.

The maximum peak displacement was achieved at 1000V/-1000V. Figure 7.5 compares the curvatures produced about *y*- and *x*-axes at 1000V/-1000V. Although the peak displacement remained the same, a slight mismatch could be seen between the two curvatures produced by the actuation. However, this was noticed to be very minimal.

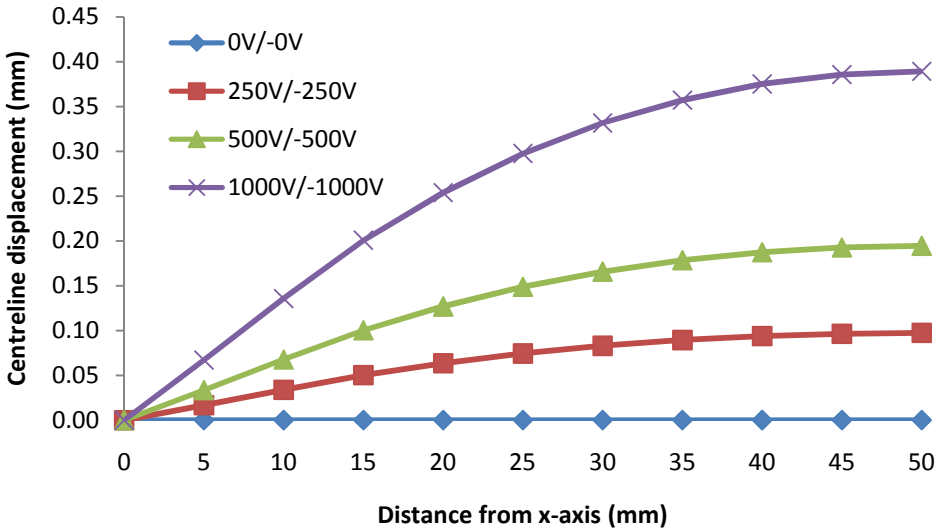


Figure 7.3: Displacements about *y* of *SS* 1mm *P0* laminate

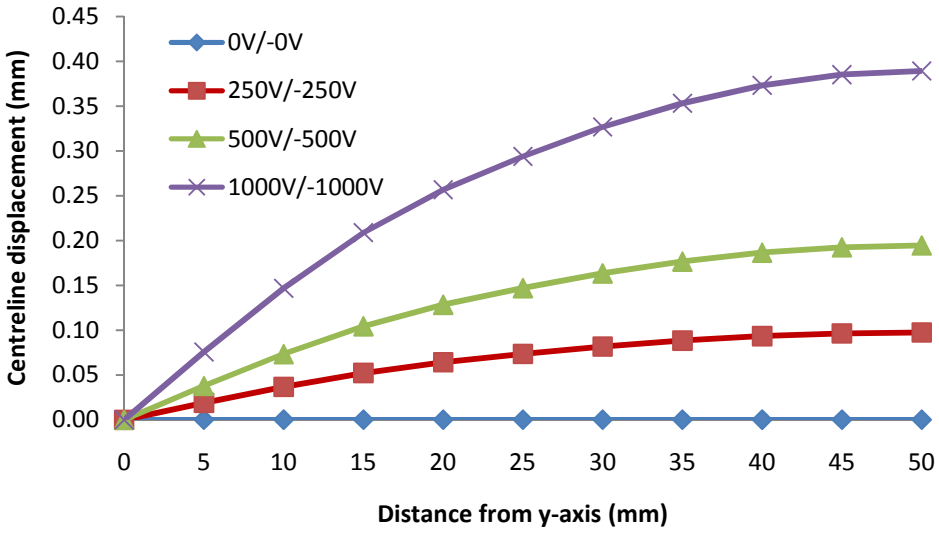


Figure 7.4: Displacements about *x* of *SS* 1mm *P0* laminate

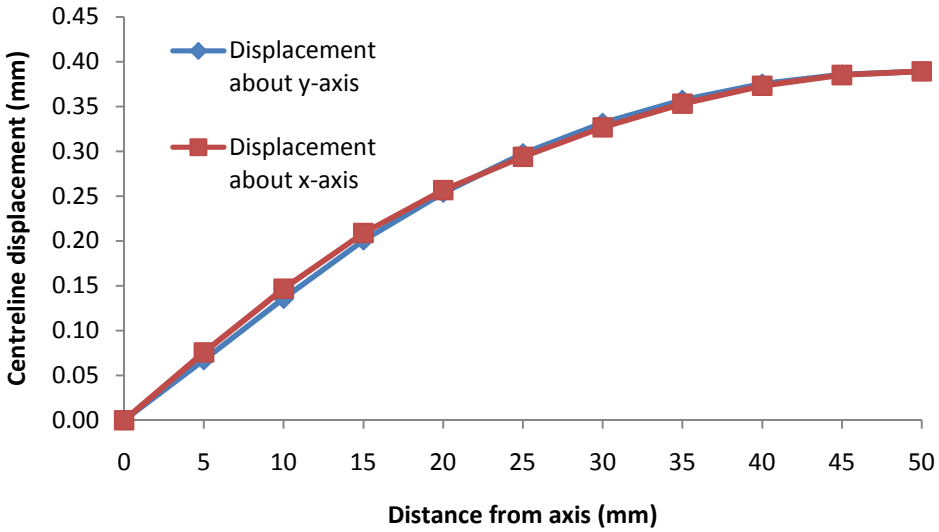


Figure 7.5: Displacements of *SS* 1mm *P0* laminate at 1000V/-1000V

7.3.1.2 *P90* laminate

Figures 7.6 and 7.7 show the centreline displacements of a simply supported *P90* laminate about *y*- and *x*-axes respectively. Similar to the previous case the displacements were found to increase with the actuation voltages with maximum peak displacements achieved at 1000V/-1000V. Figure 7.8 compares the curvatures produced by the actuation with respect to *x*- and *y*-axes at 1000V/-1000V. The mismatch in the curvatures could be seen to be more pronounced in the case of simply supported *P90* laminate. This is because the primary strain direction of the *MFC* is now aligned perpendicular the fibre direction of the outer most composite ply.

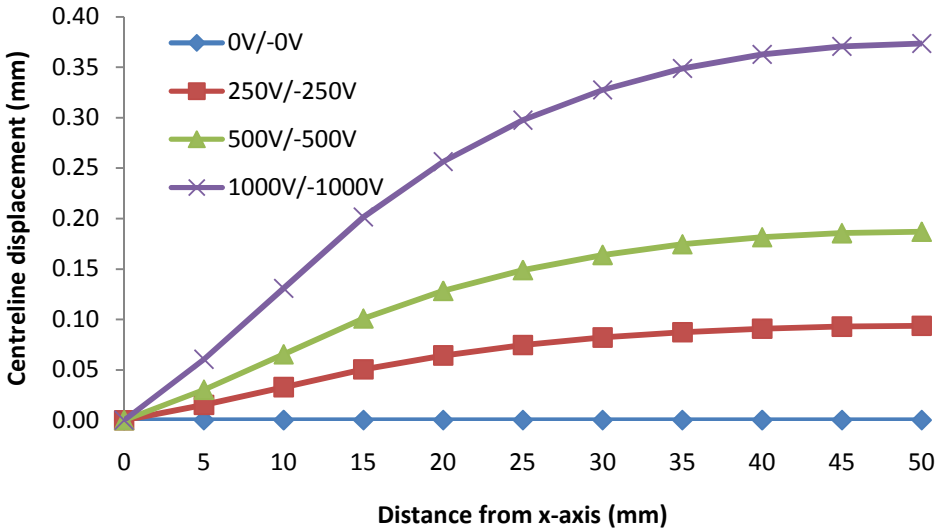


Figure 7.6: Displacements about *y* of *SS* 1mm *P90* laminate

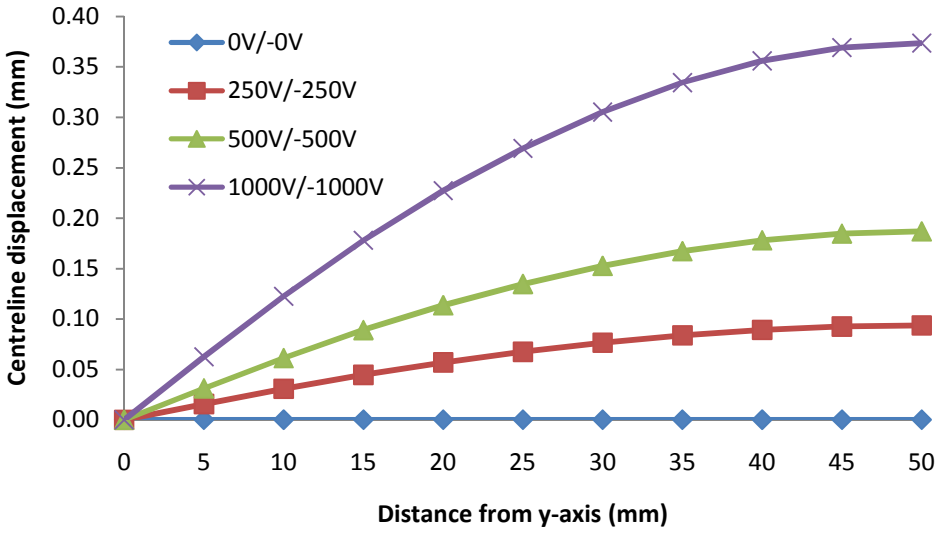


Figure 7.7: Displacements about *x* of *SS* 1mm *P90* laminate

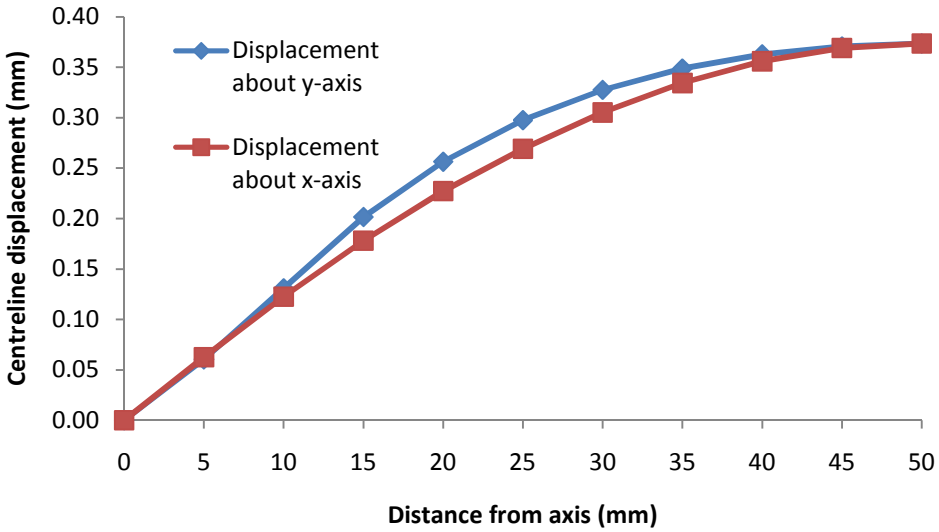


Figure 7.8: Displacements of *SS* 1mm *P90* laminate at 1000V/-1000V

7.3.1.3 *P0* versus *P90* laminate

Figures 7.9 and 7.10 compare the centreline displacements of simply supported *P0* and *P90* laminates about *y*- and *x*-axes respectively. The peak displacement of the *P0* laminate was observed to be slightly higher than the *P90* laminate. In the case of *P0* laminate, the maximum peak displacement was 0.3892mm and this was 0.3736mm with the *P90* laminate, a reduction of 4.0%. This believed to have been caused by the level of material orthotropy in the layer immediately bonded to the actuator. Though this effect may not be seen significant, in the case of the simply supported laminate it was observed that aligning the major axis of the actuator parallel to the fibre direction of the outer ply of the laminate could be used to induce slightly higher bending deformation.

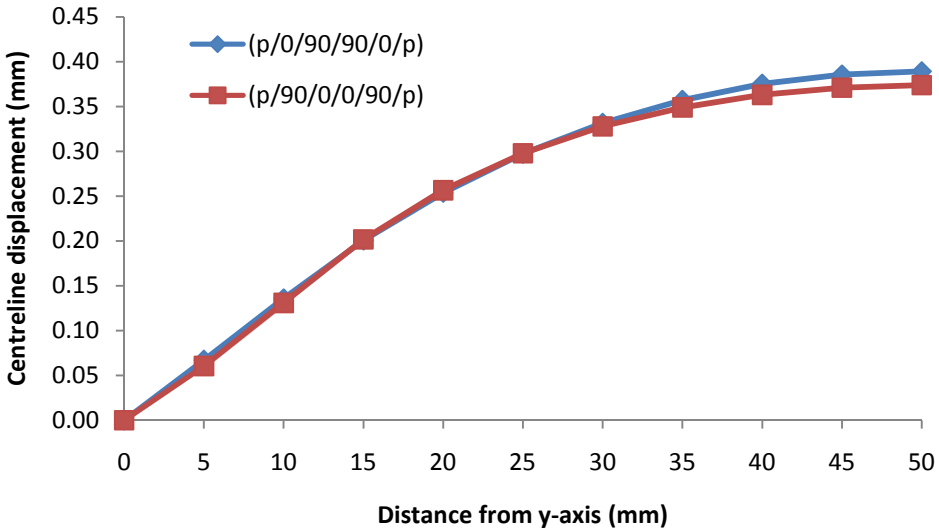


Figure 7.9: Displacements about *y* of *SS* 1mm *P0* and *P90* laminates at ±1000V

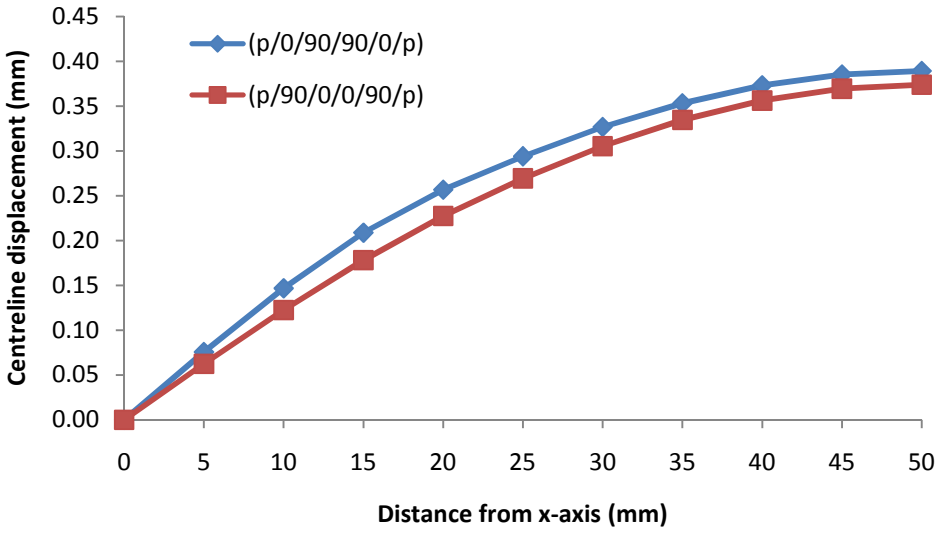


Figure 7.10: Displacements about *x* of *SS* 1mm *P0* and *P90* laminates at ±1000V

7.3.2 Clamped laminate

This section discusses the effects of clamped boundary conditions on the piezoelectric actuation characteristics. Similar to the previous study, the actuators were actuated with voltages of 0V/0V, 250V/-250V, 500V/-500V and 1000V/-1000V.

7.3.2.1 Clamped *P0* laminate

Figures 7.11 and 7.12 show the centreline displacements of the clamped *P0* laminate about *y*- and *x*-axes respectively. As with the previous cases the displacements increased with the actuation voltages in a linear fashion. However, the displacements were much lower as compared to the simply supported *P0* laminate. Unlike in the case of simply supported laminate, clamped support stiffened the laminate by constraining it from deforming freely, hence resulting in lower displacements.

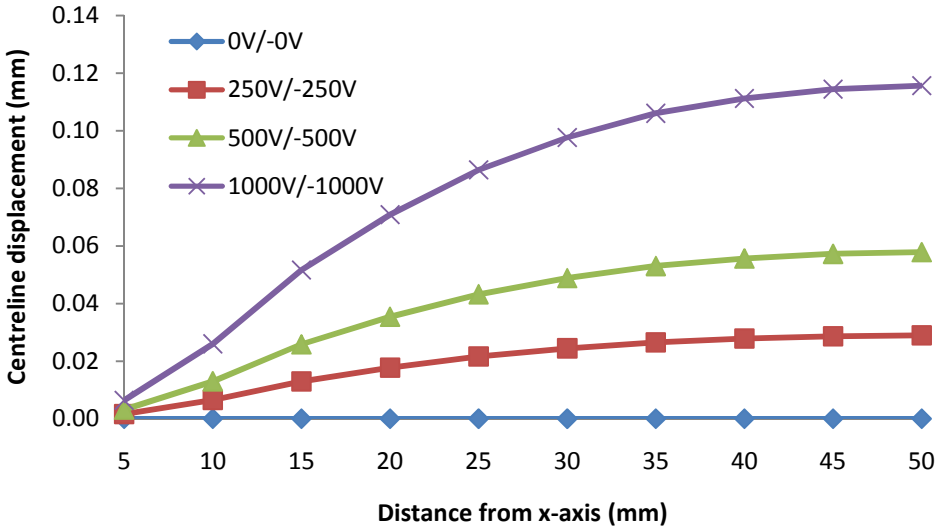


Figure 7.11: Displacements about *y* of *CC* 1mm *P0* laminate

Figure 7.13 shows the curvatures induced by the actuation about *x*- and *y*-axes. A slightly larger mismatch was observed between the two curvatures in comparison to the simply supported *P0* type, which indicated that the mismatch could have been enhanced by the clamped support.

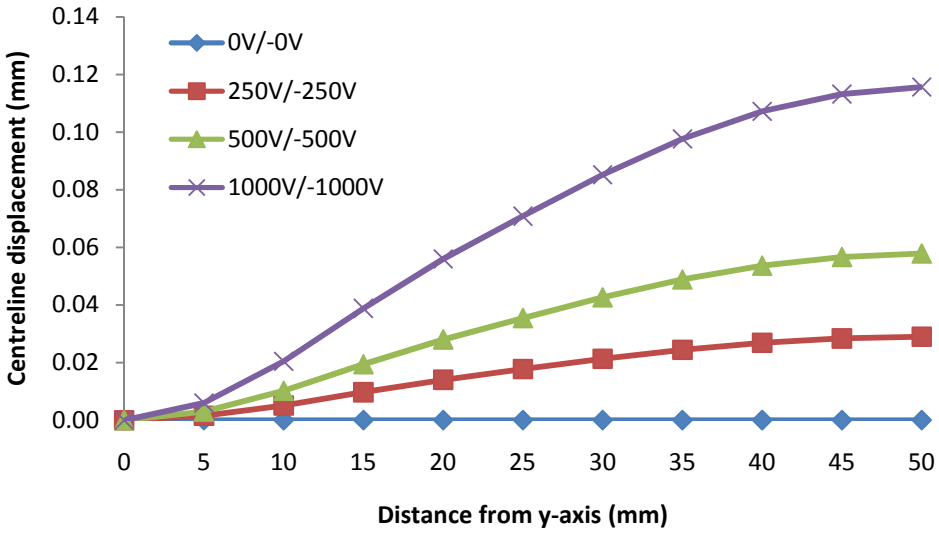


Figure 7.12: Displacements about *x* of *CC* 1mm *P0* laminate

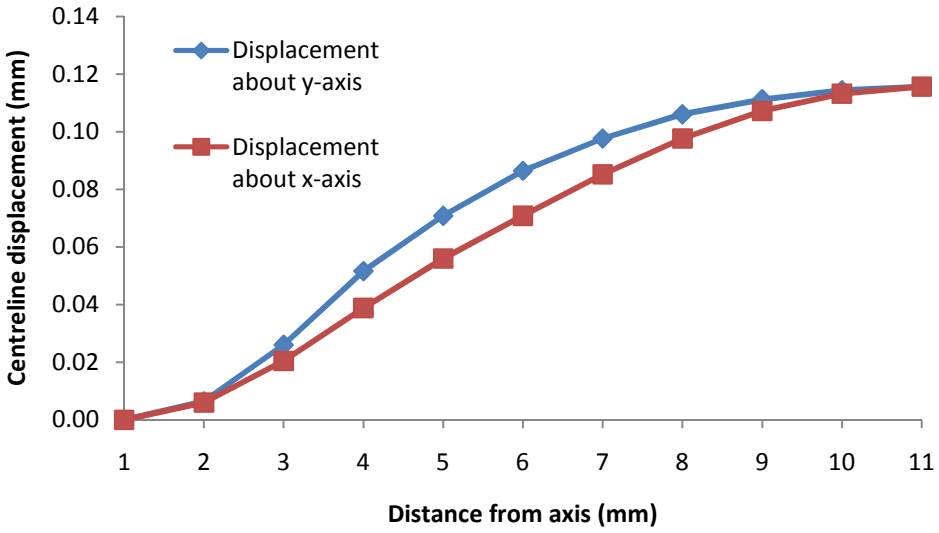


Figure 7.13: Displacements of *CC* 1mm *P0* laminate at ±1000V

7.3.2.2 Clamped *P90* laminate

Figures 7.14 and 7.15 show the displacements of clamped *P90* laminate about *y*- and *x*-axes respectively. Similar to the previous cases the displacements of the laminate increased with the actuation voltages but were lower compared to the simply supported *P90* laminate. It was also observed that the clamped support lowered the displacements near the constrained edges.

The curvatures produced by the actuation had larger mismatch in comparison to the clamped *P0* laminate, Figure 7.16. This was because, in this case, the primary actuation

direction was aligned perpendicular to the fibre direction of the outer most composite ply and the mismatch could have been further enhanced by the clamped support.

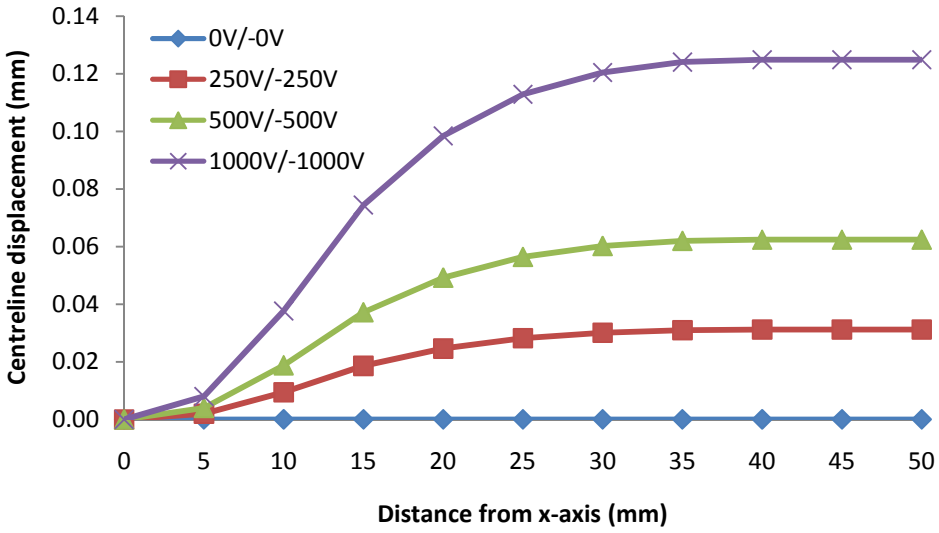


Figure 7.14: Displacement about *y* of *CC* 1 mm *P90* laminate

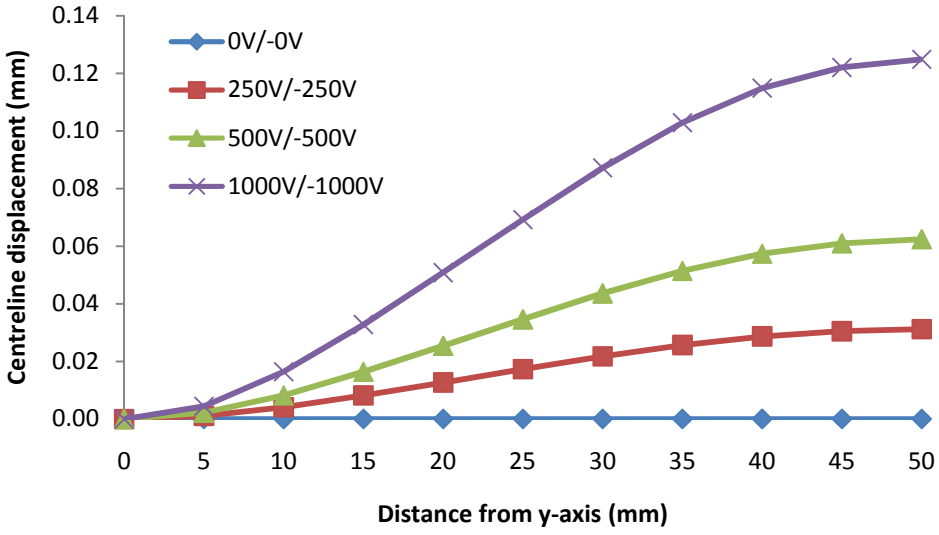


Figure 7.15: Displacement about *x* of *CC* 1mm *P90* laminate

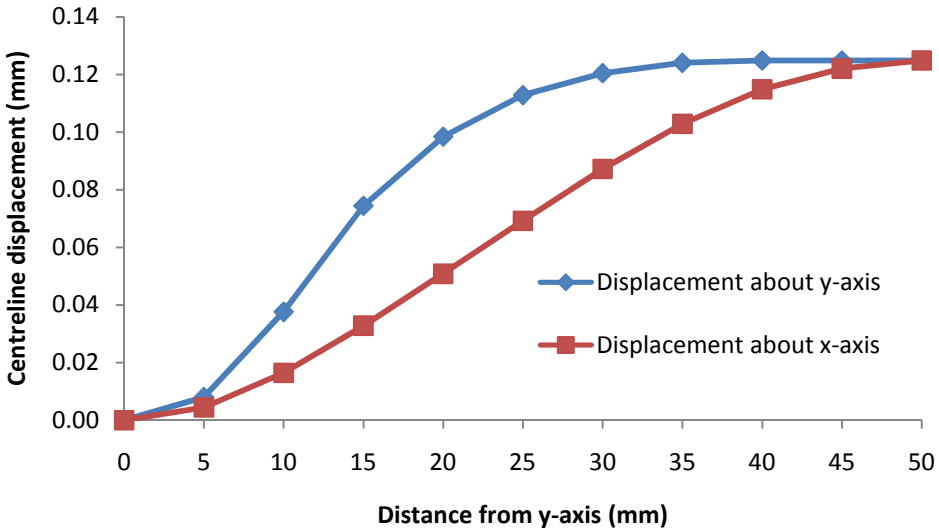


Figure 7.16: Displacement of *CC* 1mm *P90* laminate at ±1000V

7.3.2.3 *P0* versus *P90* laminate

Figures 7.17 and 7.18 compare the centreline displacements of clamped *P0* and *P90* laminates about *y*- and *x*-axes respectively. In the case of clamped support, the displacements of *P0* laminate were observed to be lower than the *P90* type. The maximum peak displacement for the *P0* laminate was 0.1156mm and this was 0.1248mm in the case *P90*, an increase of 8.0%.

Based on the observations in Sections 7.3.1 and 7.3.2 it can be concluded that boundary conditions have major influence on the nature of piezoelectric actuation on composite laminates. In the clamped case, aligning the major axis of the piezoelectric actuator perpendicular to the fibre axis of the outer composite plies produced a higher bending deformation.

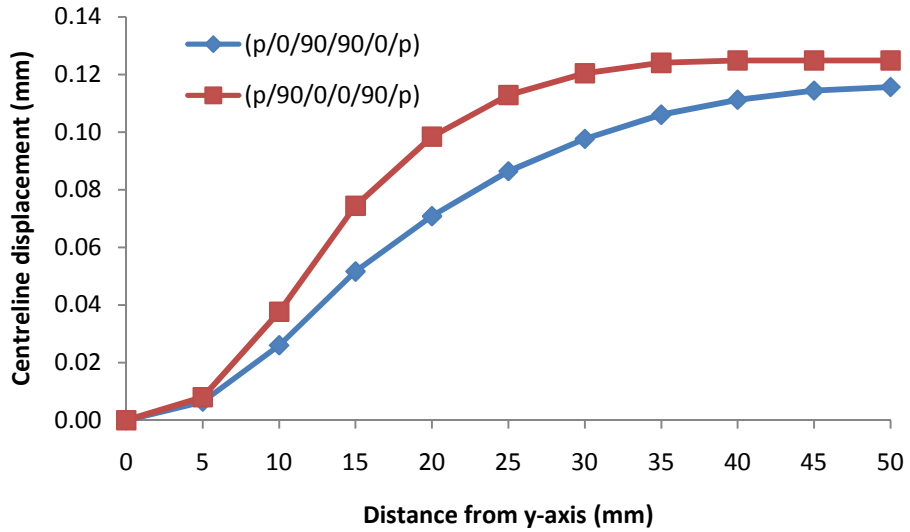


Figure 7.17: Displacements about *y* of *CC* 1mm *P0* and *P90* laminates at ±1000V

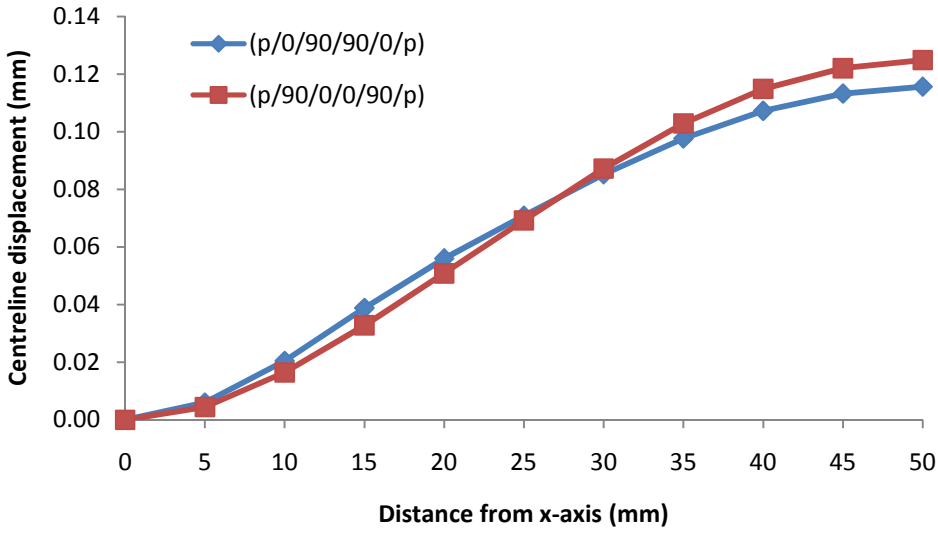


Figure 7.18: Displacements about *x* of *CC* 1mm *P0* and *P90* laminates at ±1000V

7.3.3 Simply supported versus clamped laminates

Figures 7.19 to 7.22 compare the centreline displacements of *P0* and *P90* laminates for different boundary conditions. The clamped support was observed to lower the transverse displacement of the plate considerably. In the case of the simply supported *P0* laminate the peak displacement was 0.3892mm and this was only 0.1156mm for clamped *P0* type, a reduction of almost 70.3%, Figures 7.19 and 7.20. For the simply supported *P90* laminate the peak displacement was 0.3736mm and this was 0.1248mm in the case of clamped *P90*

laminate, Figures 7.21 and 7.22. The reduction in the second case was about 66.5%. This observation indicated that clamped support acts in a disadvantageous way by effectively reducing the piezoelectric effects on the laminate.

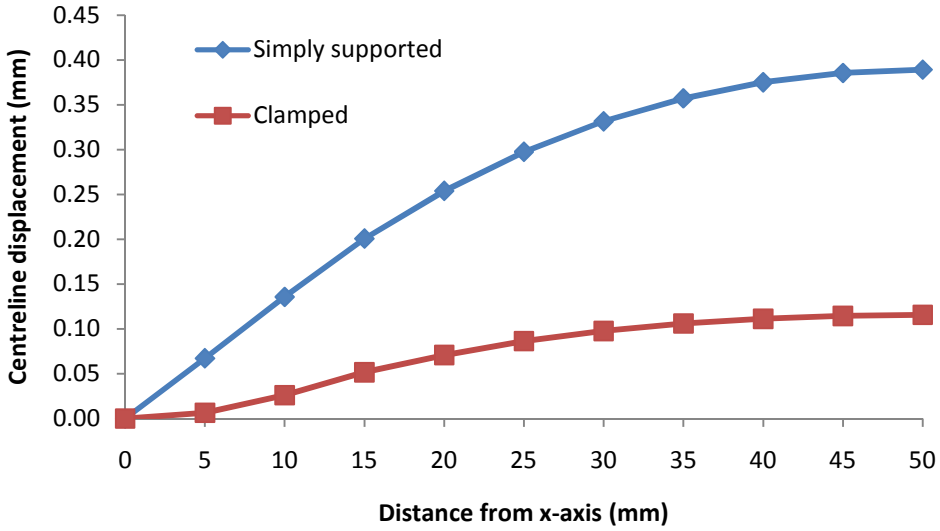


Figure 7.19: Displacements about *y* of *CC* and *SS* 1mm *P0* laminate at ±1000V

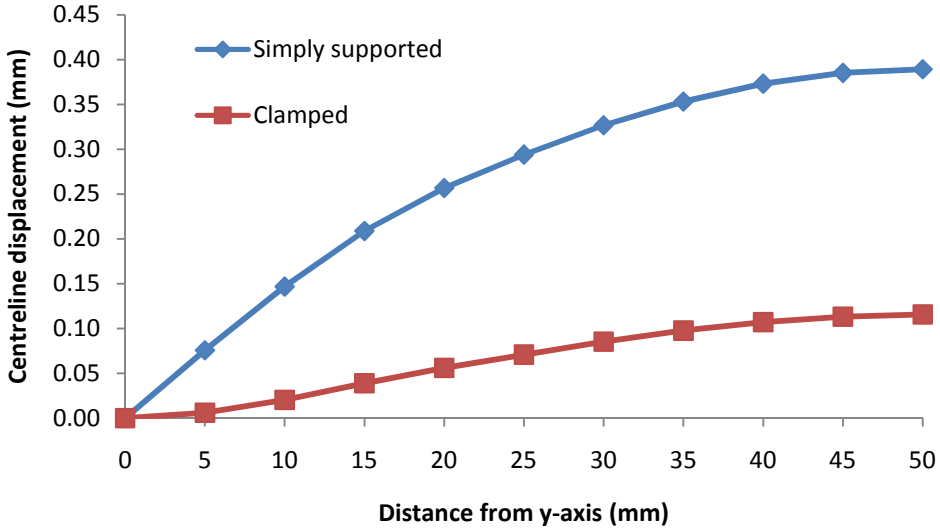


Figure 7.20: Displacements about *x* of *CC* and *SS* 1mm *P0* laminate at ±1000V

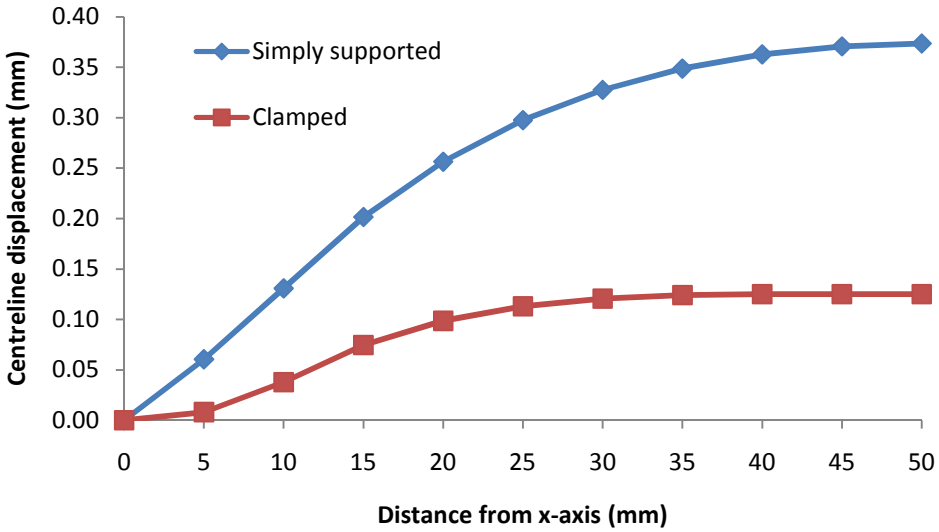


Figure 7.21: Displacements about *y* of *CC* and *SS* 1mm *P90* laminate at ±1000V

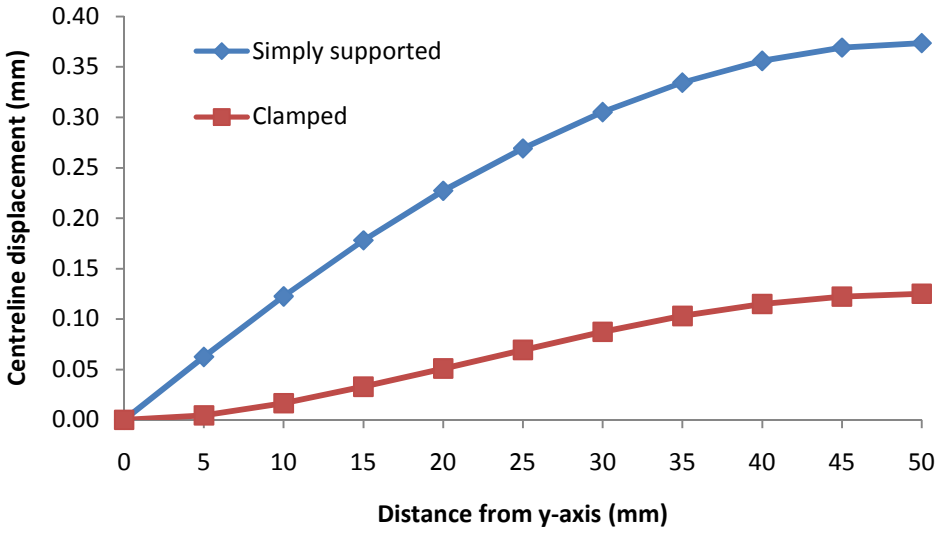


Figure 7.22: Displacements about *x* of *CC* and *SS* 1mm *P90* laminate at ±1000V

7.4 Effects of material properties

The effects of laminate material properties on the piezoelectric actuation capabilities are presented in Figures 7.23 to 7.30. For the purpose of investigation the following settings were considered:

1. Actuator placement : *TYPE E*
2. Actuator material : *Mat 3*

3. Composite material : *Mat 2*
4. Laminate thickness : 1mm

The general behaviour of the laminate using *Mat 2* was found to be the same as using *Mat 1*, Figures 7.23 to 7.28. The displacements were found to increase with increasing actuation voltages and observed to follow a linear relationship, Figures 7.23 to 7.26.

Likewise, the effect of clamped support was observed to be critical especially in the case *P0* laminate. In the case of simply supported *P0* laminate the peak displacement was 0.4648mm and this was reduced to 0.1524mm in the clamped case, a reduction of 67.2%, Figure 7.27. The peak displacement in the case of simply supported *P90* laminate was 0.4480mm and this was 0.1660mm in the case of clamped *P90* laminate, a reduction of 62.9%, Figure 7.28.

However, the effects of piezoelectric actuations were observed to be more pronounced when the laminates were constructed using *Mat 2*. This was because *Mat 2* had a lower elastic modulus and consequently lower bending stiffness as compared to *Mat 1*. Hence for the same actuation voltages, laminates constructed using *Mat 2* showed more susceptibility towards bending deformation and this was evident from Figures 7.29 and 7.30. In the case of simply supported *P0* laminate the increase in peak displacement was 19.4% while this was 31.8% in the case of clamped *P0* laminate, Figures 7.29 and 7.30 respectively.

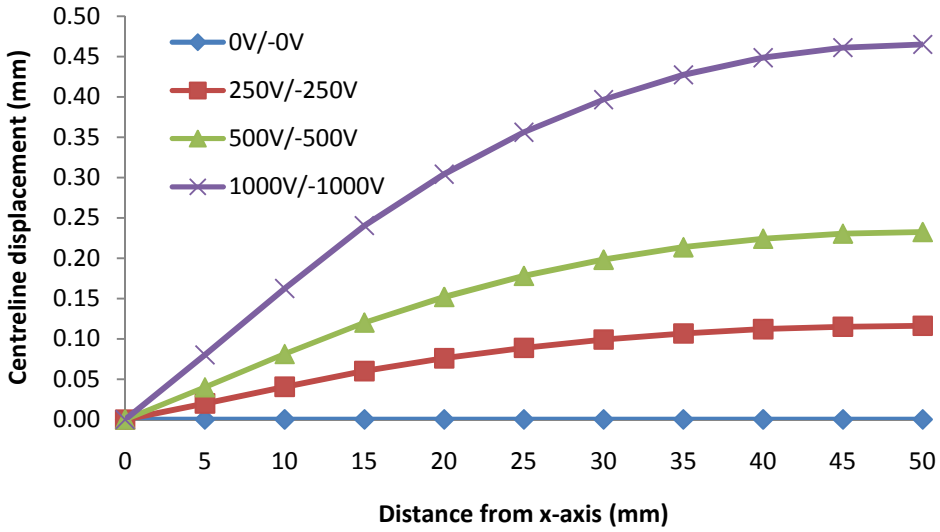


Figure 7.23: Displacements about *y* of *SS* 1mm *P0* laminate

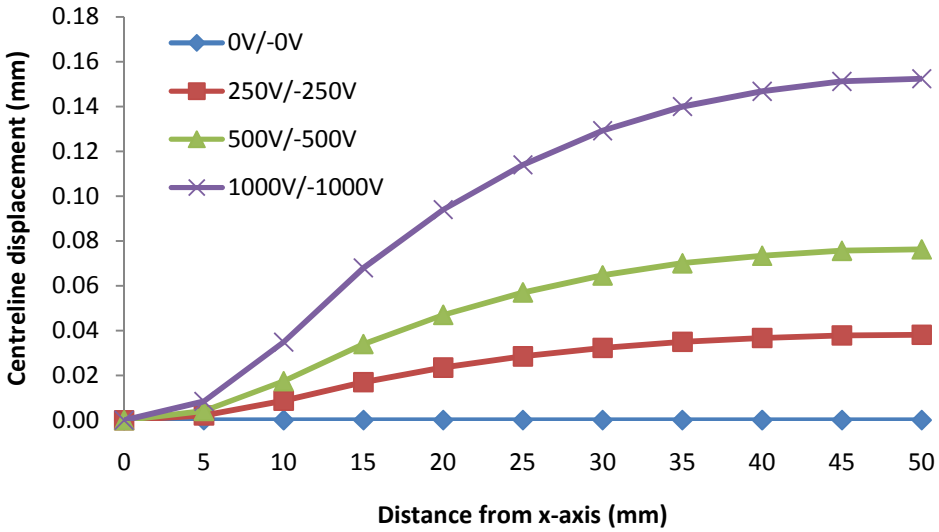


Figure 7.24: Displacements about *y* of *CC* 1mm *P0* laminate

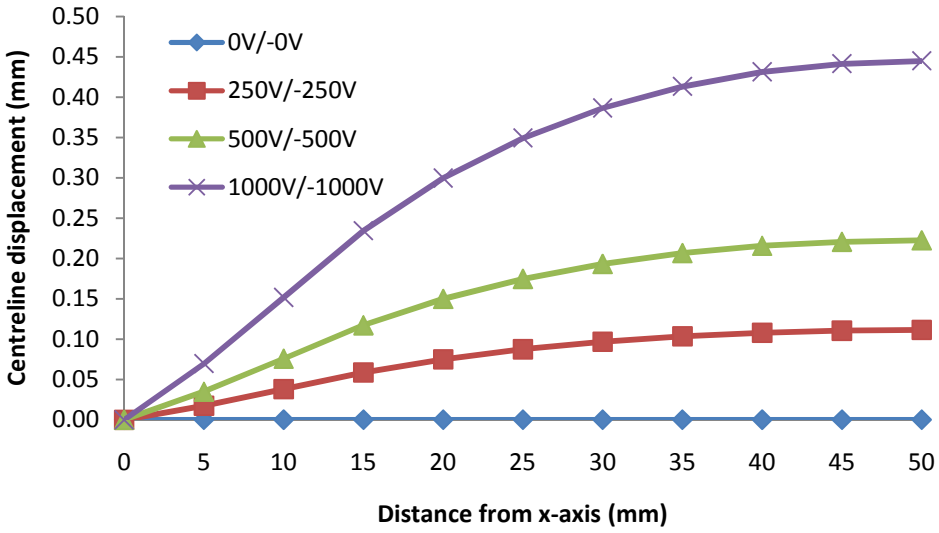


Figure 7.25: Displacements about *y* of *SS* 1mm *P90* laminate

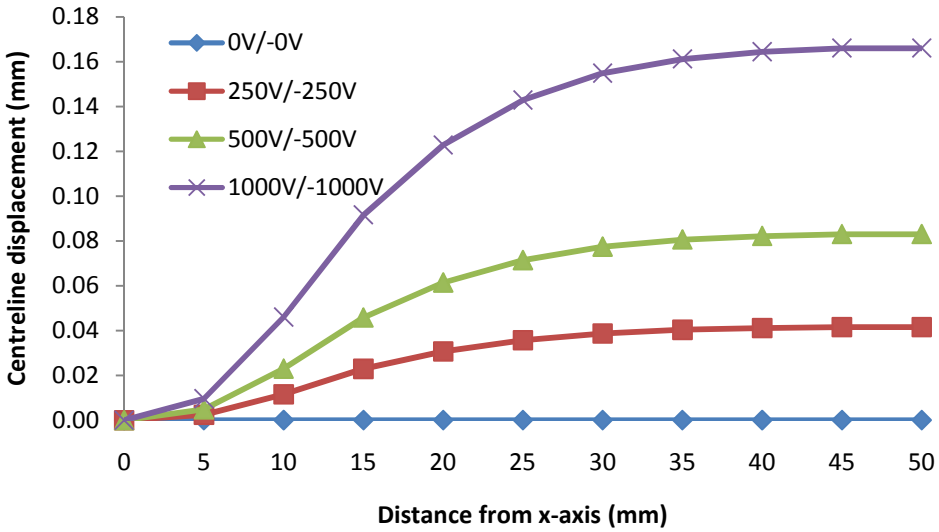


Figure 7.26: Displacements about *y* of *CC* 1mm *P90* laminate

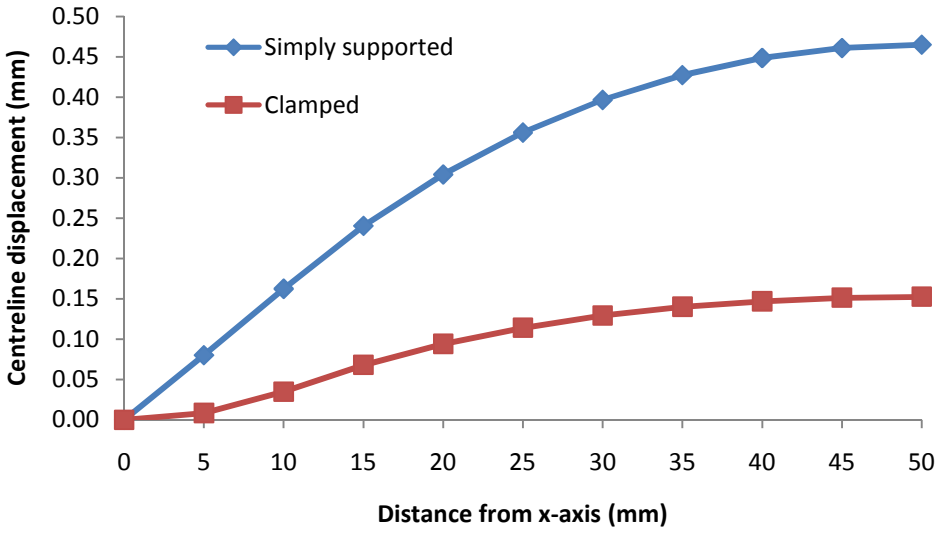


Figure 7.27: Displacements about *y* of *SS* and *CC* 1mm *P0* laminate at ±1000V

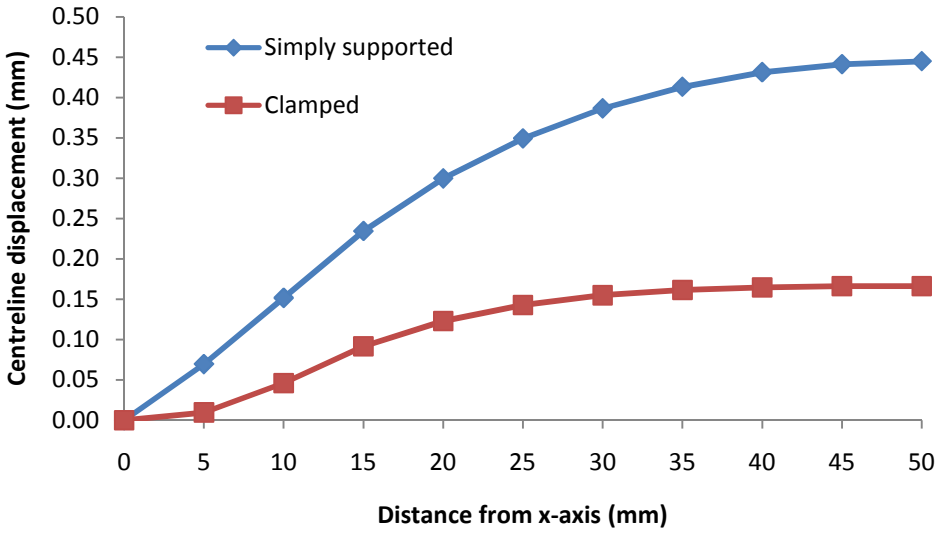


Figure 7.28: Displacements about *y* of *SS* and *CC* 1mm *P90* laminate at ±1000V

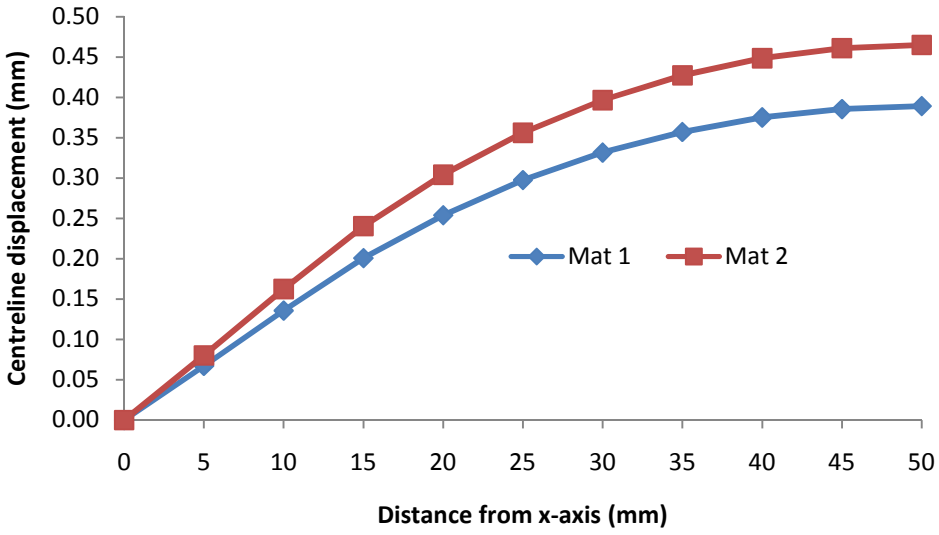


Figure 7.29: Displacements about *y* of *SS* 1mm *P0* laminate at ±1000V

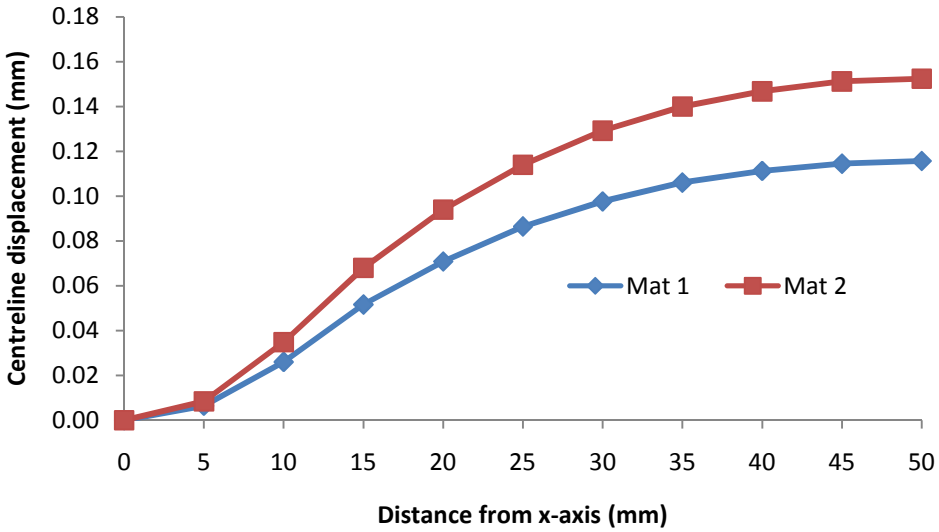


Figure 7.30: Displacements about *y* of *CC* 1mm *P0* laminate at ±1000V

7.5 Effects of laminate thickness

The effects of laminate thickness on the piezoelectric actuation capabilities are presented in Figures 7.31 to 7.33. For the purpose of investigation the following settings were considered:

1. Actuator placement : *TYPE E*
2. Actuator material : *Mat 3*
3. Composite material : *Mat 2*
4. Laminate thickness : 1, 2 and 3mm
5. Lamination : *P0*
6. Actuation voltage : Top actuator 1000V and bottom actuator -1000V

Figures 7.31 and 7.32 show that the increase in laminate thickness almost or completely diminished the piezoelectric effects on the composite laminate. This is because the bending stiffness of a laminate is proportional to the cubic order of the laminate thickness. Hence, a thicker laminate will have higher resistance to bending and thus lowering the effects of piezoelectric actuations on the laminate.

In the case of simply supported laminate, Figure 7.31, the peak displacement of 1mm laminate was 0.4648mm and this was reduced to 0.0210mm in the case of the 3mm laminate, a reduction of 95.7%. In the case of the clamped laminate the reduction was about 96.9%, Figure 7.32. Figure 7.33 compares the centreline displacements of the 2mm *P0* laminate for

the case of clamped and simply supported edges. As with the previous cases, the clamped laminate was found to have adverse effects on the nature of piezoelectric actuation as the peak displacement was reduced by 73.4%.

From these analyses the effects of laminate thickness on piezoelectric actuation characteristics can be seen to be more detrimental than the effects clamped support although both act disadvantageously.

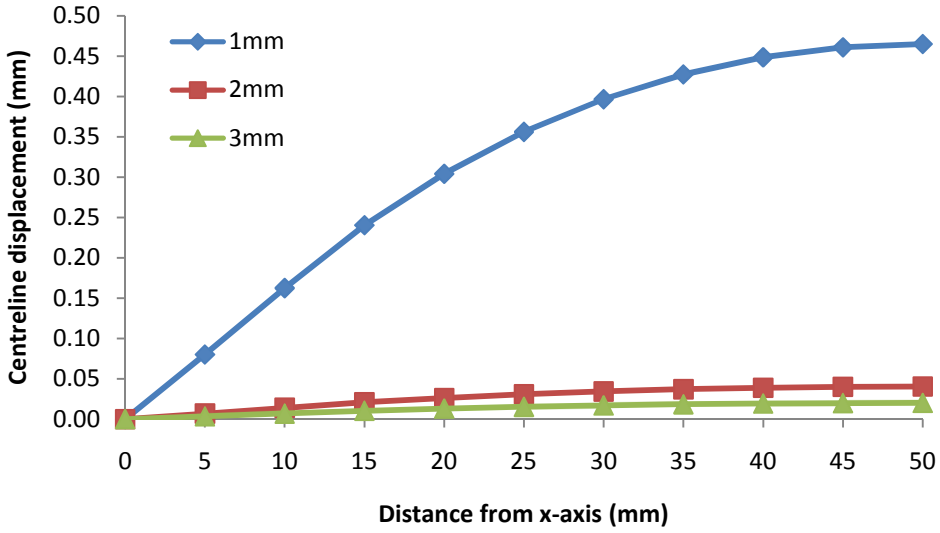


Figure 7.31: Displacements about *y* of *SS P0* laminate at ±1000V

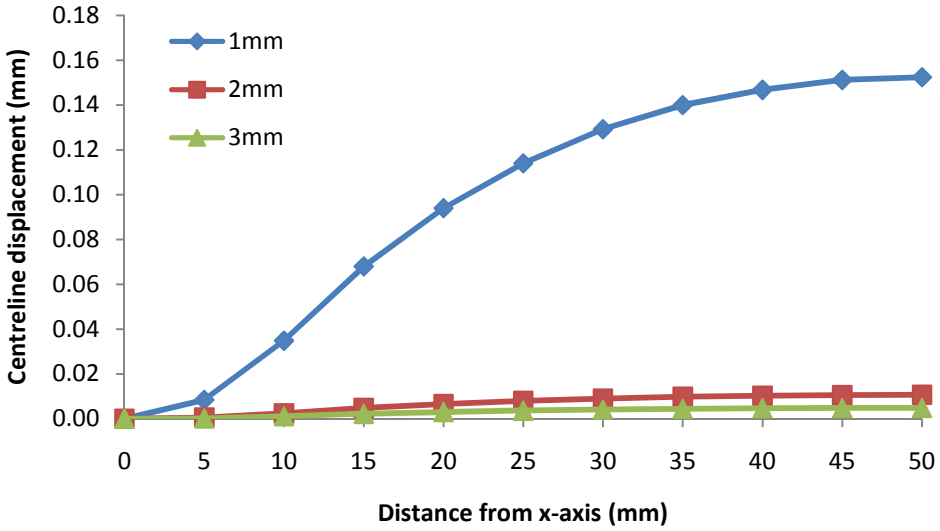


Figure 7.32: Displacements about *y* of *CC P0* laminate at ±1000V

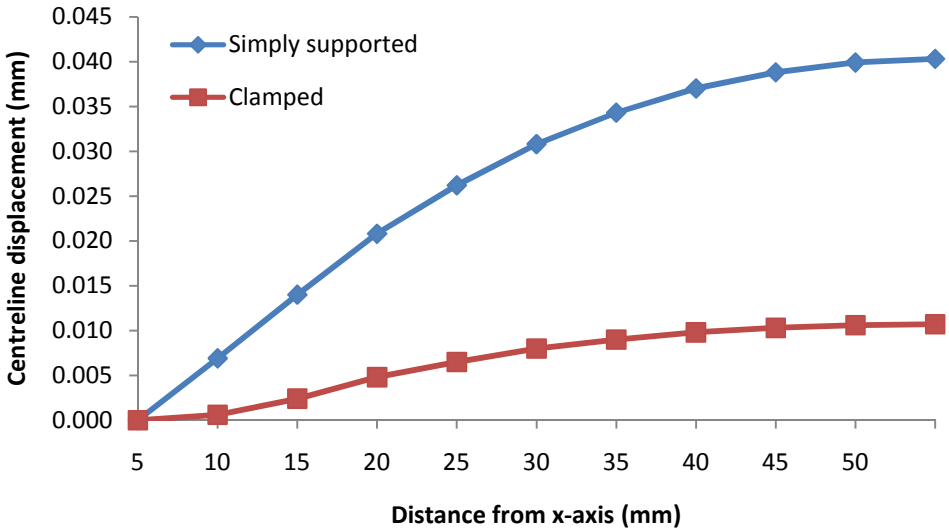


Figure 7.33: Displacements about *y* of 2mm *P0* laminate at ±1000V

7.6 Effects of actuator placements

The effects of actuator placements on the piezoelectric actuation capabilities are presented in Figures 7.34 to 7.38. For the purpose of investigation the following settings were considered:

1. Actuator placement : As shown in Figure 7.2
2. Actuator material : *Mat 3*
3. Composite material : *Mat 2*
4. Laminate thickness : 1mm
5. Lamination : *P0*
6. Actuation voltage : 1000V/-1000V

Figures 7.34 to 7.37 show that the actuator placements significantly affected the displacement pattern of the laminate. From Figures 7.34 to 7.37 it can be seen that actuator placement *TYPE D* gave the highest peak displacement compared to the other placement types for both simply supported and fully clamped laminates. This was due to the anisotropic actuation nature of the actuator. A positive actuation of the top actuator caused it to expand in the fibre direction and contract in all the other directions. On the contrary, under negative actuation, the bottom actuator would undergo expansion in the electrode direction and contraction in the fibre direction. This caused the midsection of the bottom ply to be under compression and its counterpart at the top ply to be under tension. These actions would

increase the peak displacement of the laminate in the midsection. This is not something expected using transversely isotropic actuators such as *G1195* piezoceramics as they generally have isotropic in-plane actuation mode.

Placing the actuators away from the midpoint in the longitudinal direction (*TYPE F* and *TYPE G*) decreased the laminates' peak displacements as in this case the midsection of the top ply would be under compression and its bottom counterpart would be under tension. It was also found that the peak displacements were lowered when the actuators were placed near the boundaries of the laminates (*TYPE A*, *TYPE H* and *TYPE I*). In general, for a simply supported laminate all the actuator placements resulted in upward bending. However, the same was not true for clamped laminates. Only *TYPE A*, *TYPE B*, *TYPE C*, *TYPE D* and *TYPE E* resulted in upward bending of the laminate. For the other placement types the laminate underwent complex deformations and these are illustrated using three-dimensional plots in Figures 7.38 to 7.47. The plots indicated that the actuator placements and boundary conditions significantly influenced the deformation patterns of the laminate. From these analyses it was decided that the actuator placement *TYPE D* was the most suitable actuator placement not only because it gave the maximum displacement but also due to the reason that this type of actuator placement could be used to avoid direct contact of the impactor with the actuator in subsequent impact investigation.

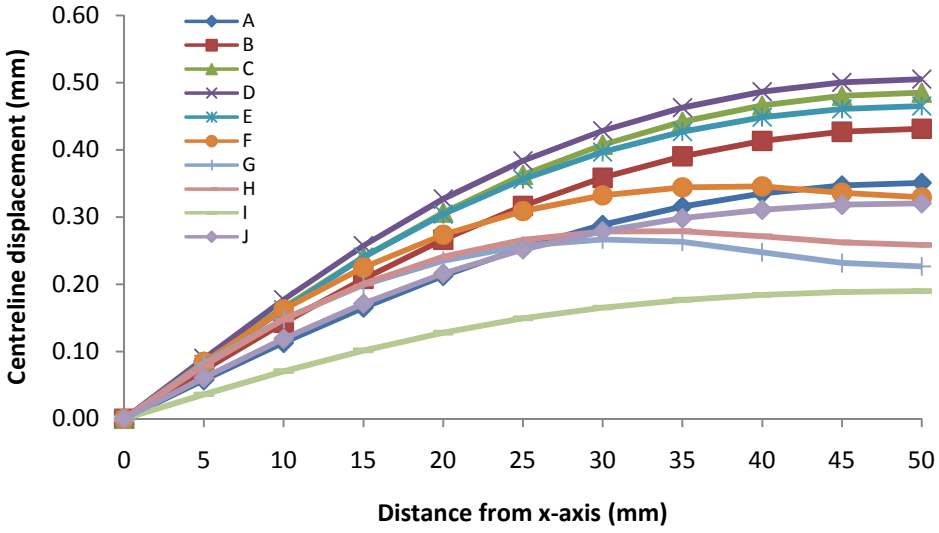


Figure 7.34: Displacements about *y* of *SS* 1mm *P0* laminate at ±1000V

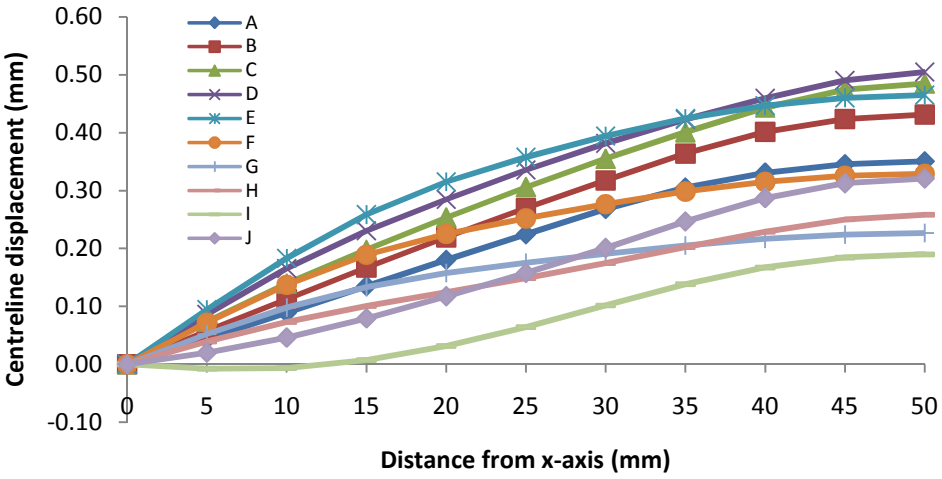


Figure 7.35: Displacements about *x* of *SS* 1mm *P0* laminate at ±1000V

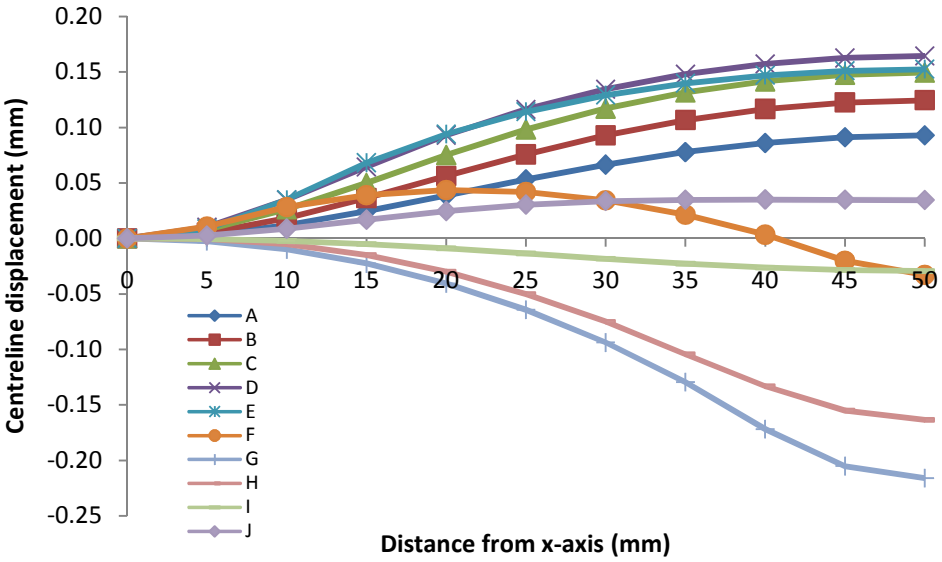


Figure 7.36: Displacements about *y* of *CC* 1mm *P0* laminate at ±1000V

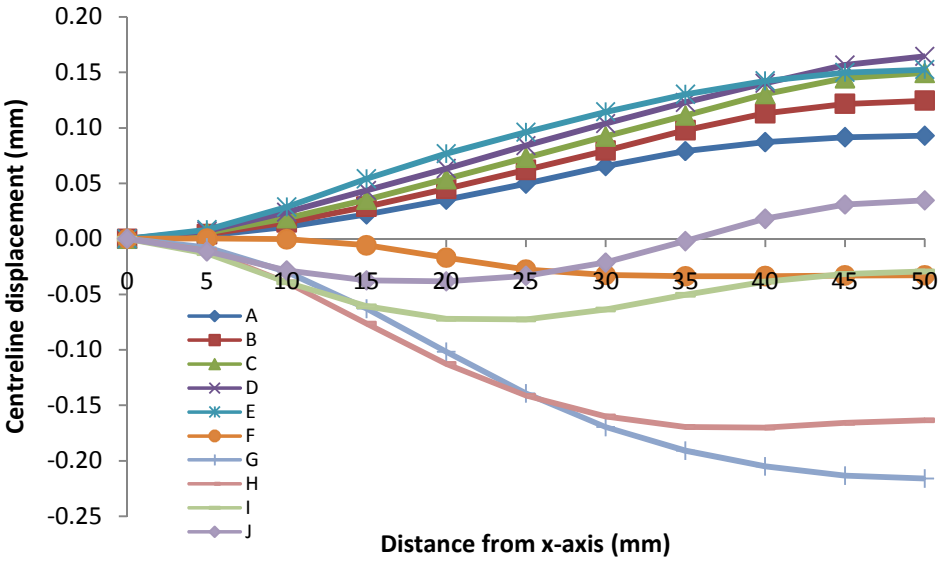
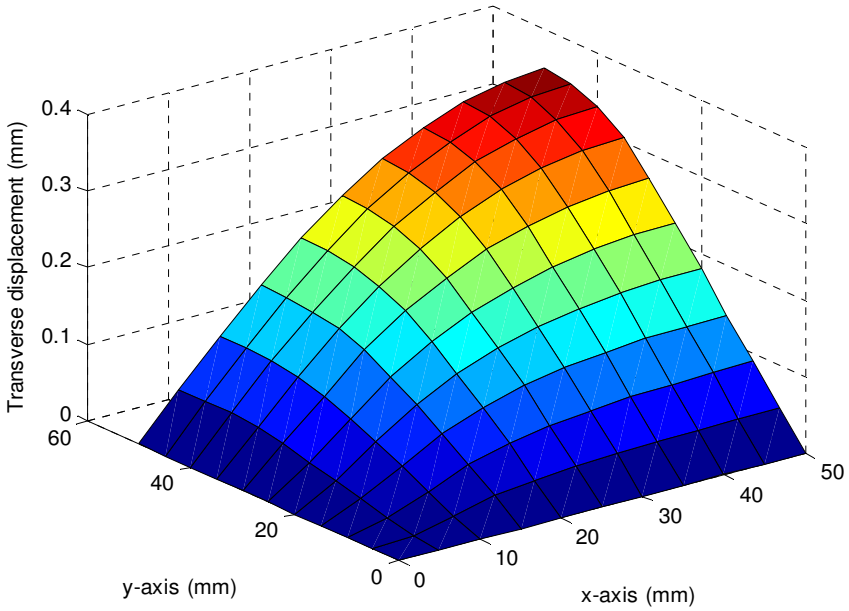
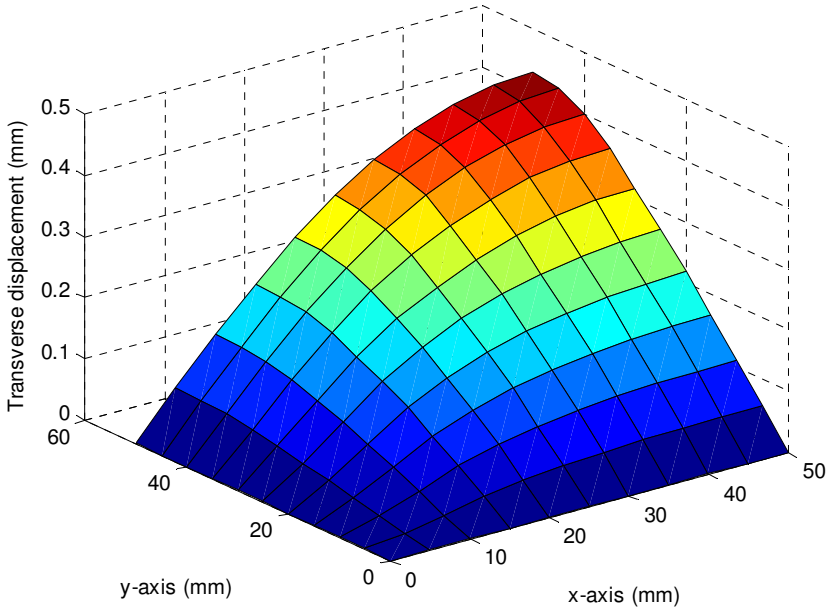


Figure 7.37: Displacements about *x* of *CC* 1mm *P0* laminate at ±1000V

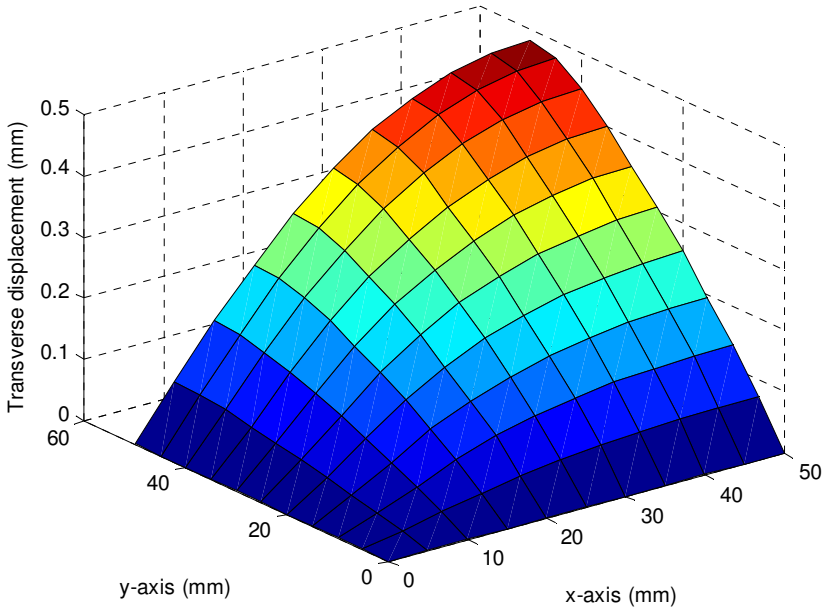


(a) *TYPE-A*

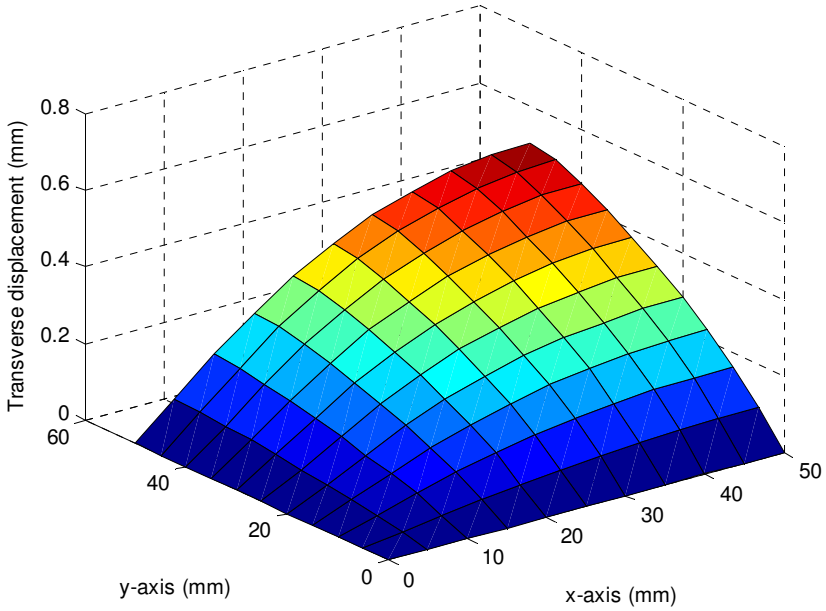


(b) *TYPE-B*

Figure 7.38: Surface plot of *SS* 1mm *P0* laminate at ±1000V - Type *A* & *B*

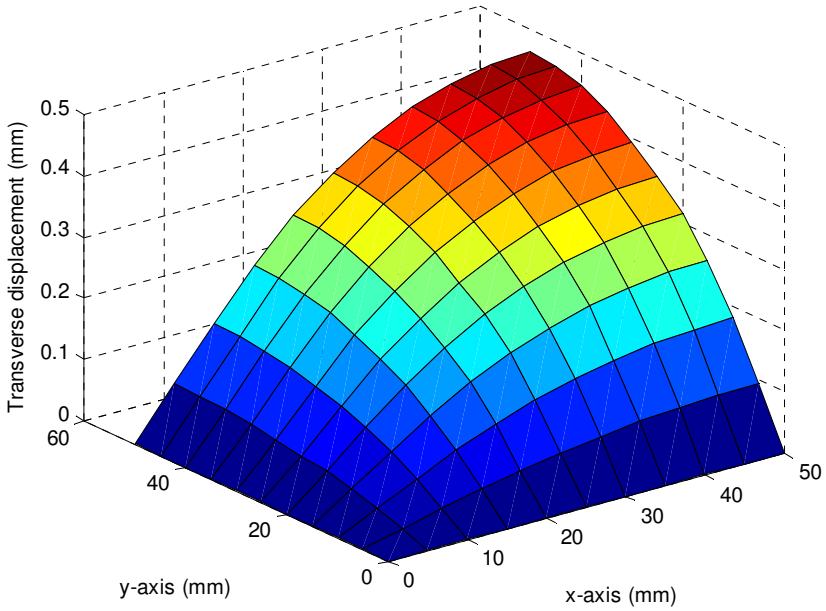


(a) *TYPE-C*

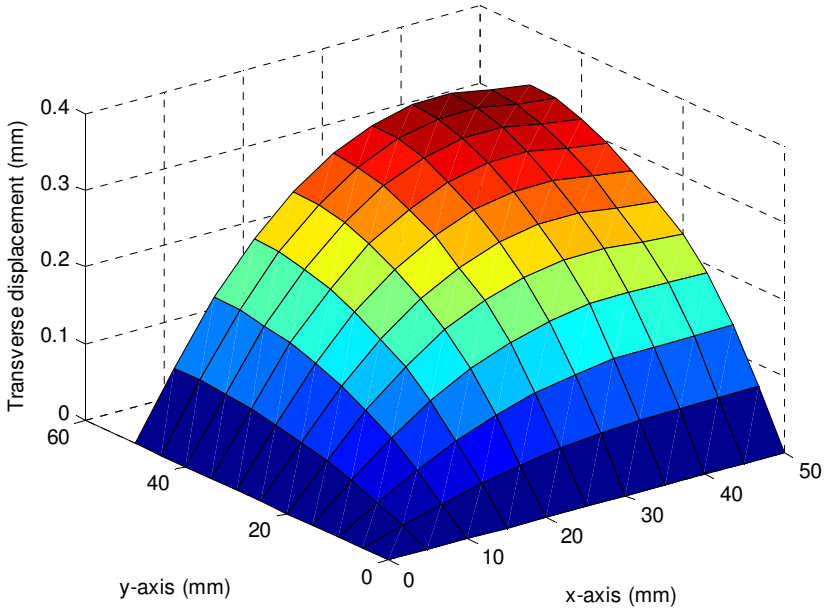


(b) *TYPE-D*

Figure 7.39: Surface plot of *SS* 1mm *P0* laminate at ±1000V - Type *C* & *D*

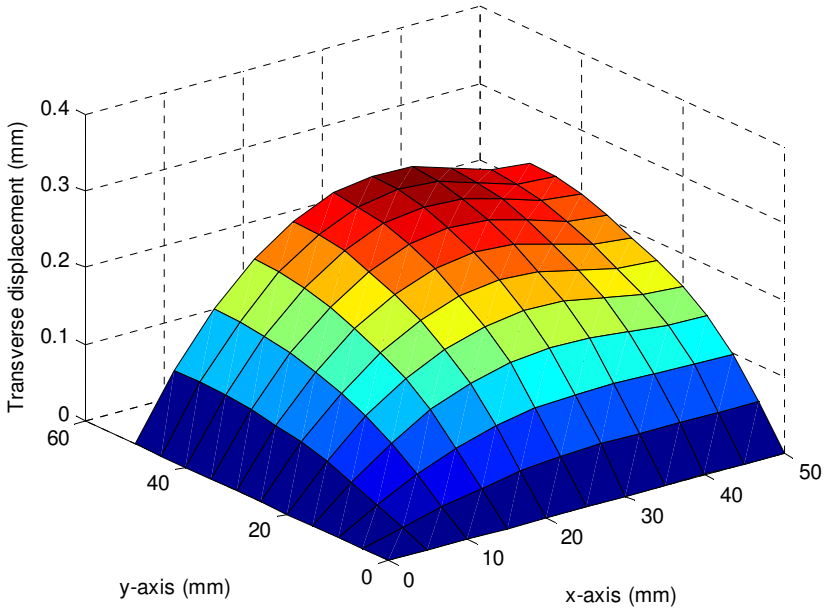


(a) *TYPE-E*

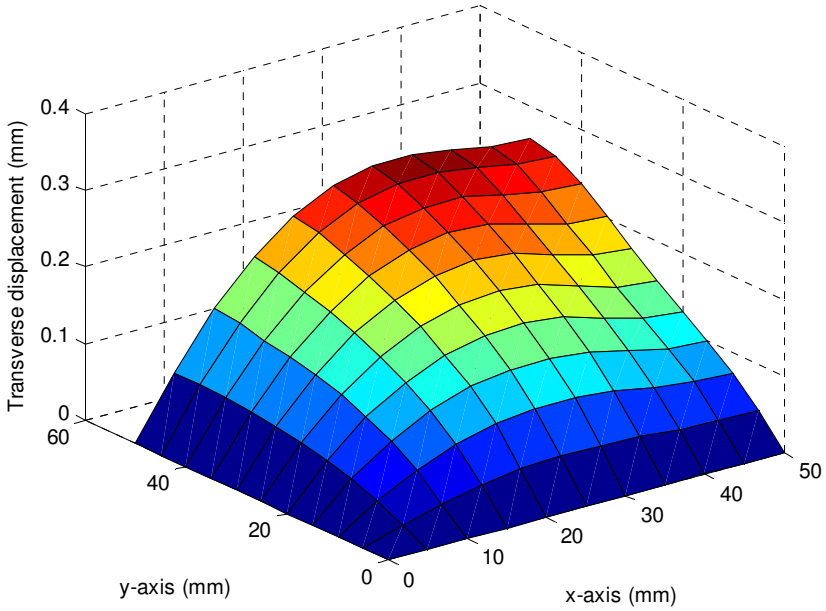


(b) *TYPE-F*

Figure 7.40: Surface plot of *SS* 1mm *P0* laminate at ±1000V - Type *E* & *F*

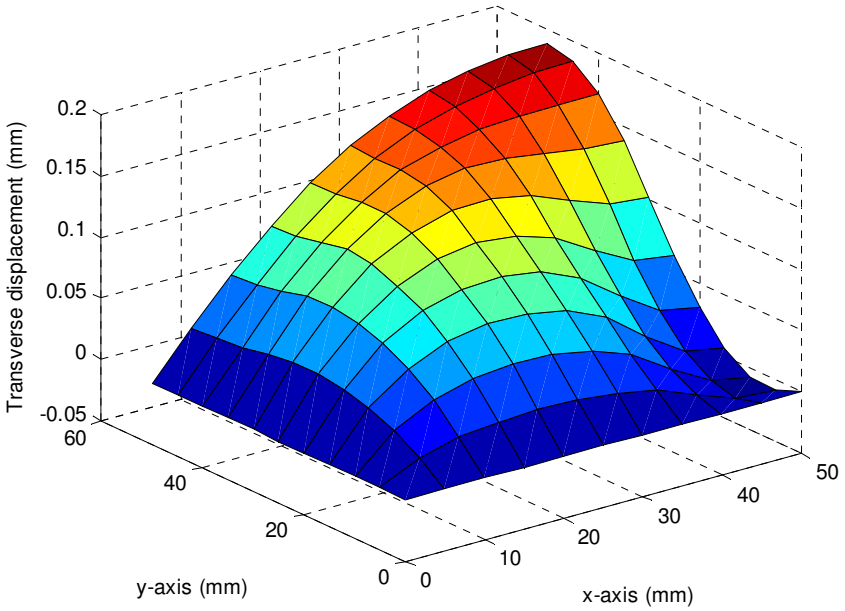


(a) *TYPE-G*

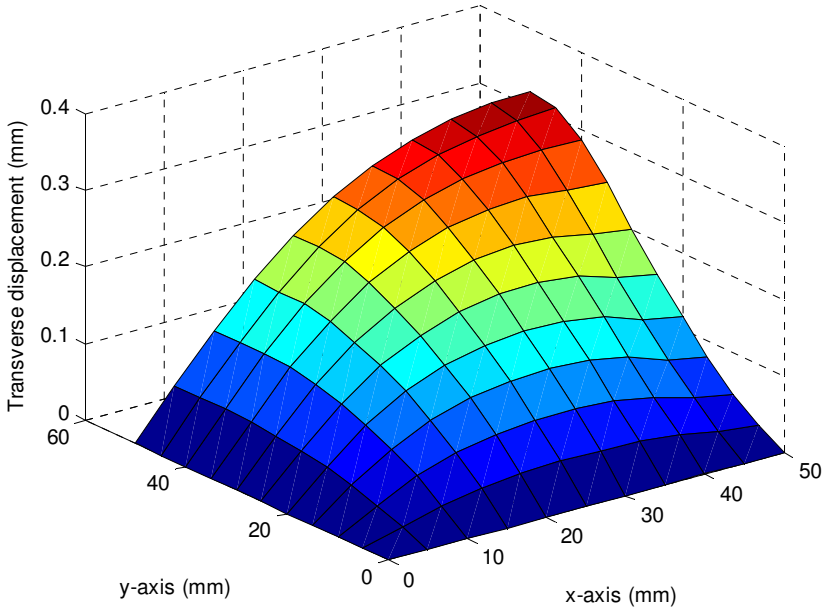


(b) *TYPE-H*

Figure 7.41: Surface plot of *SS* 1mm *P0* laminate at ±1000V - Type *G* & *H*

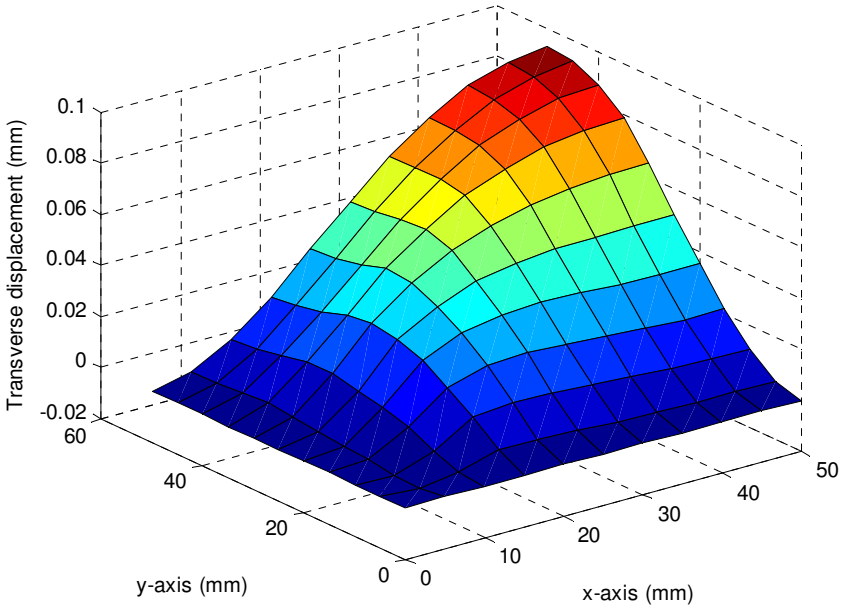


(a) *TYPE-I*

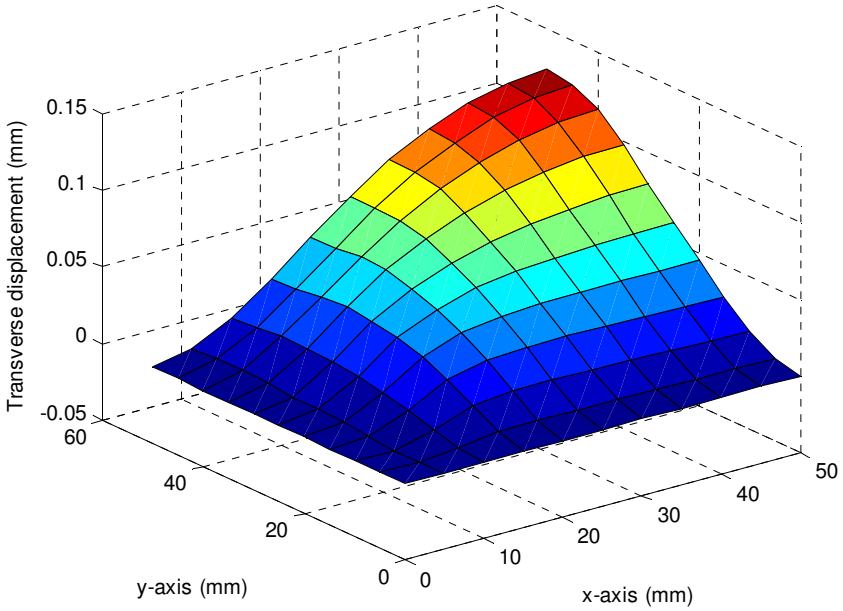


(b) *TYPE-J*

Figure 7.42: Surface plot of *SS* 1mm *P0* laminate at ±1000V - Type *I* & *J*

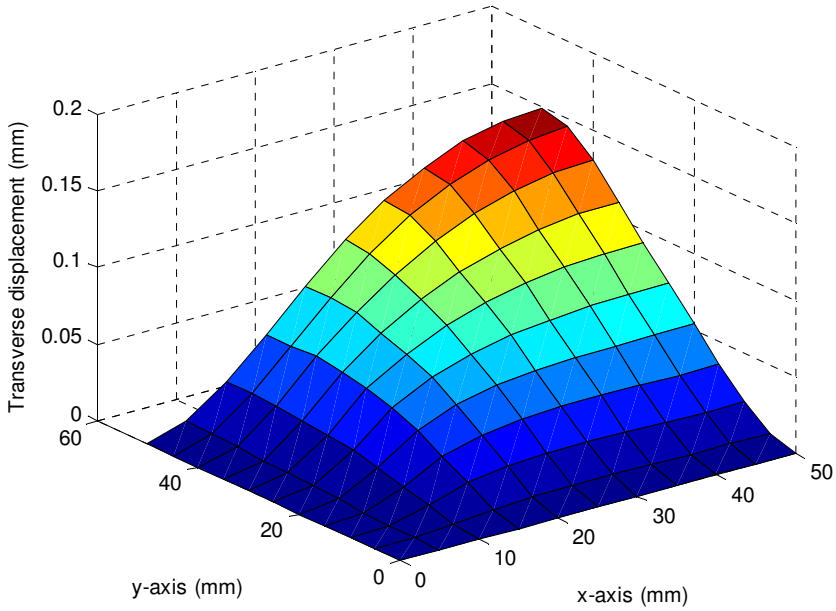


(a) *TYPE-A*

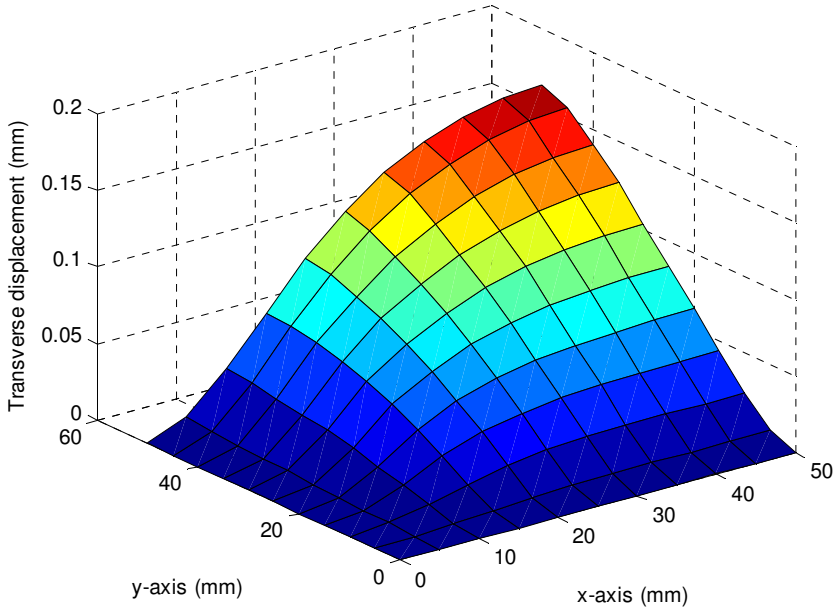


(b) *TYPE-B*

Figure 7.43: Surface plot of *CC* 1mm *P0* laminate at ±1000V - Type *A* & *B*

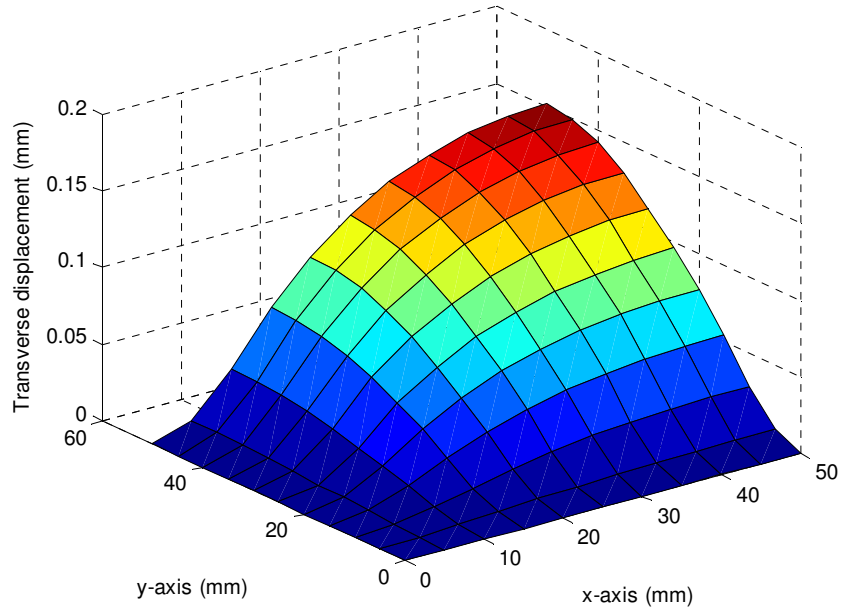


(a) *TYPE-C*

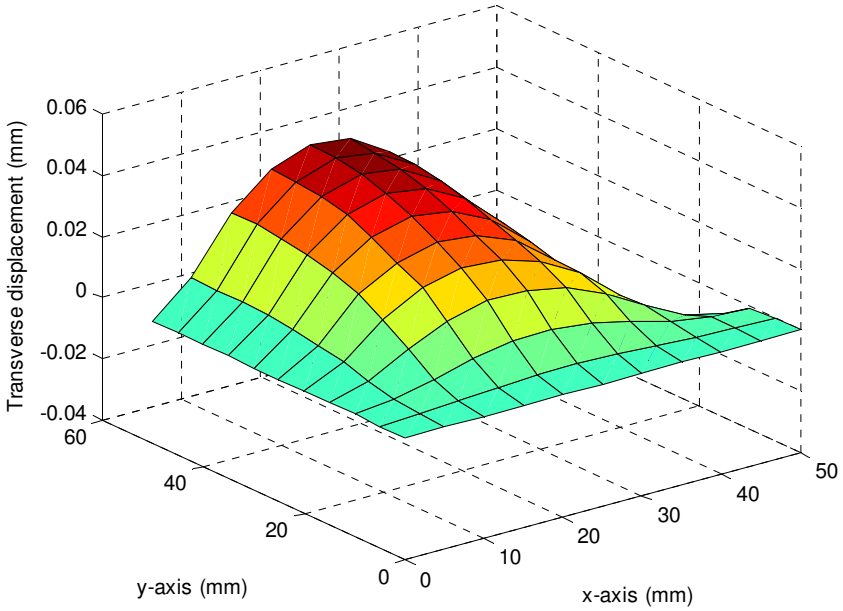


(b) *TYPE-D*

Figure 7.44: Surface plot of *CC* 1mm *P0* laminate at ±1000V - Type *C* & *D*

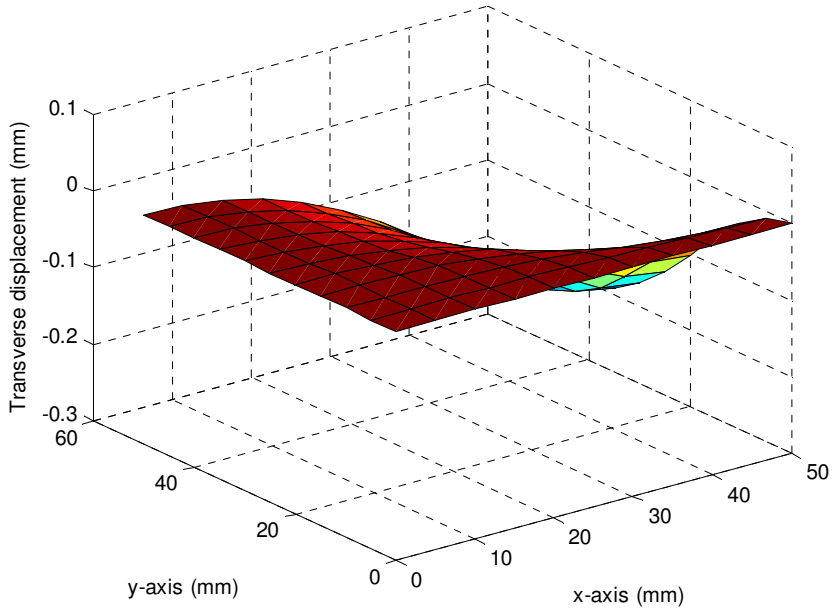


(a) *TYPE-E*

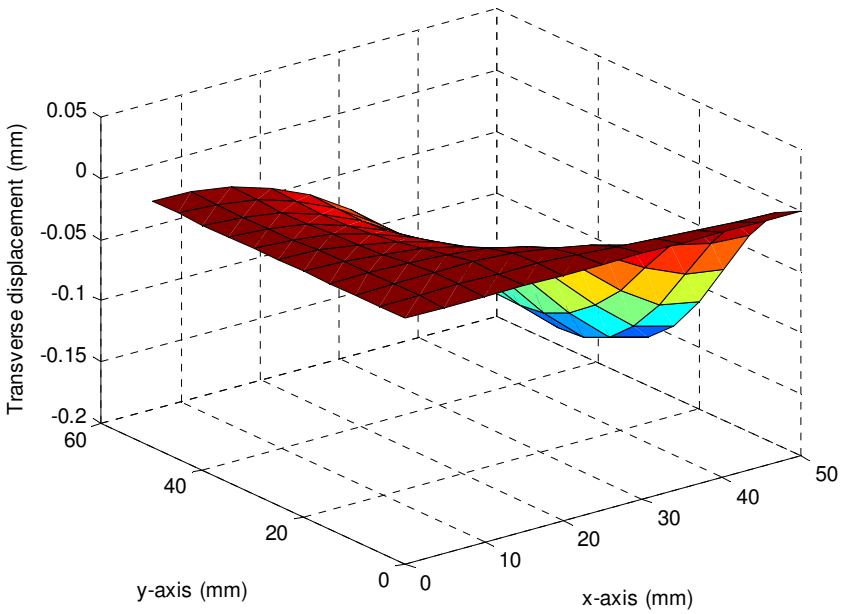


(b) *TYPE-F*

Figure 7.45: Surface plot of *CC* 1mm *P0* laminate at ±1000V - Type *E* & *F*

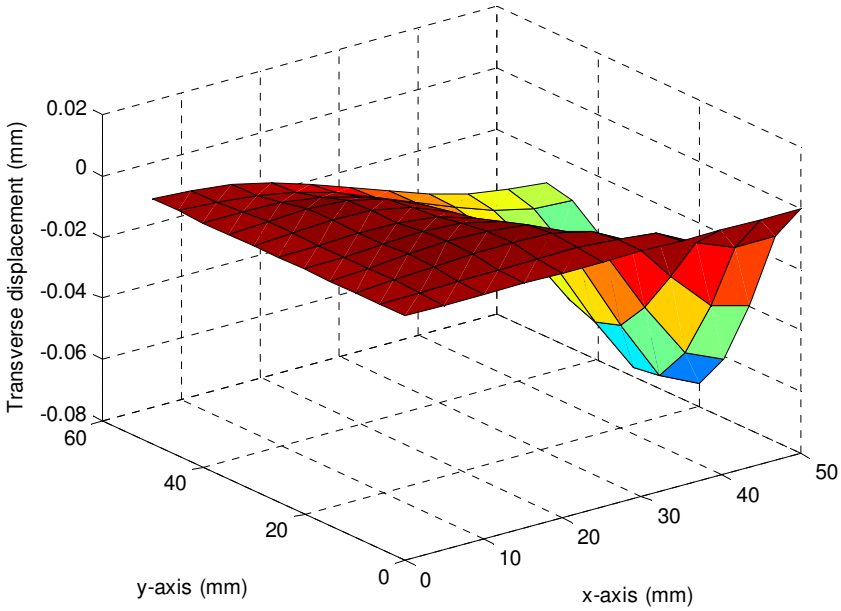


(a) *TYPE-G*

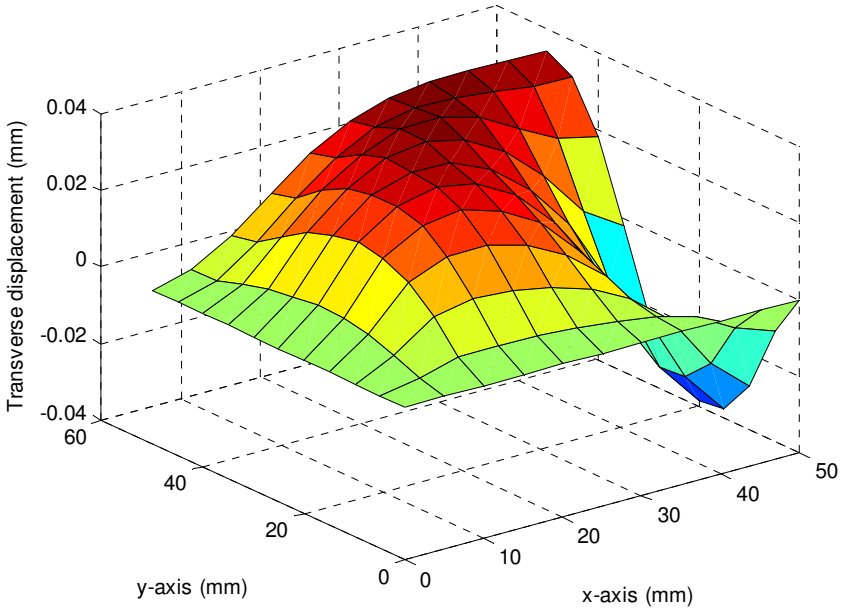


(b) *TYPE-H*

Figure 7.46: Surface plot of *CC* 1mm *P0* laminate at ±1000V - Type *G* & *H*



(a) *TYPE-I*



(b) *TYPE-J*

Figure 7.47: Surface plot of *CC* 1mm *P0* laminate at ±1000V - Type *I* & *J*

7.7 Effects of actuator type

The effects of different actuator materials on structural deformation are presented in Figures 7.48 and 7.49. For the purpose of investigation the following settings were considered:

1. Actuator placement : *TYPE D*
2. Actuator material : *Mat 3* and *Mat 4*
3. Composite material : *Mat 2*
4. Laminate thickness : 1.0mm
5. Lamination : *P0*
6. Actuation voltage : 1000V/-1000V

The voltage on the bottom actuator far exceeded the coercive field strength of single crystal *MFC*. However, the results presented are only for comparison purposes. The standard *MFC* actuator produced a higher deformation than the single crystal *MFC* both under simply supported and clamped conditions, Figures 7.48 and 7.49. This is because, although the single crystal *MFC* possesses larger piezoelectric strain constants, its lower elastic modulus limited its ability to effectively deform the laminate.

In the case of simply supported laminate, the peak displacement achieved using the standard *MFC* was 0.5048mm and this was only 0.4396mm using the single crystal type, a reduction of 6.9%, Figure 7.48. In the case of clamped laminate the difference in the peak displacement was about 19.7%, Figure 7.49. Although the primary strain coefficient of a single crystal *MFC* is four times more than the standard *MFC*, its elastic modulus in the fibre direction is almost five times smaller than the standard type.

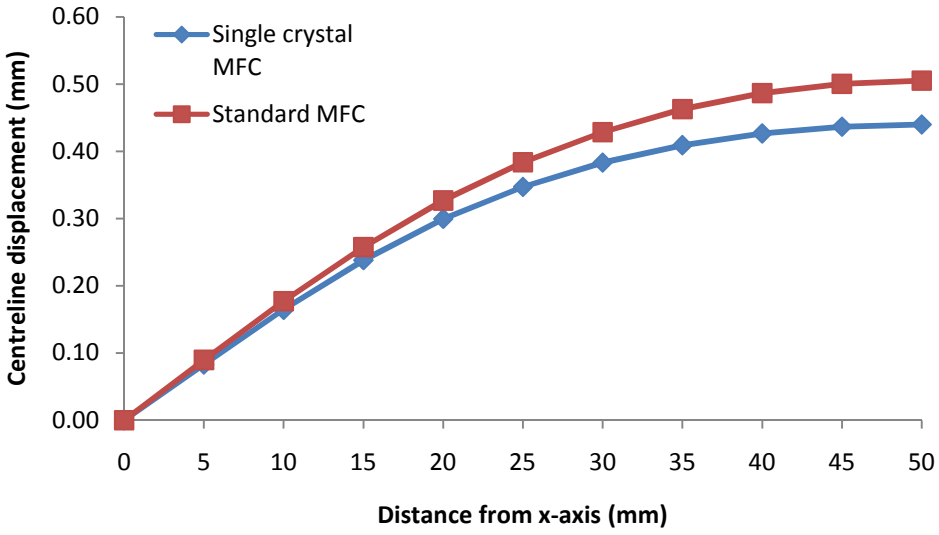


Figure 7.48: Displacement about *y* of *SS* 1mm *P0* laminate using different actuator materials at ±1000V

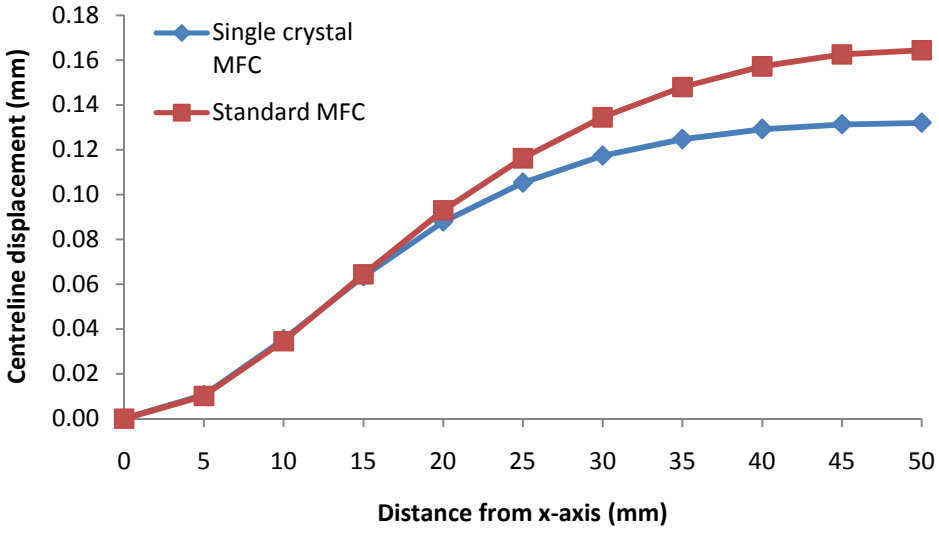


Figure 7.49: Displacement about *y* of *CC* 1mm *P0* laminate using different actuator materials at ±1000V

The blocking force, F_b and free displacement, Δl, produced by the actuator along d_{11} (primary actuation direction of the *MFC*) can be computed using Equations (7.1) and (7.2) respectively (Chopra, 2002):

$$F_b = d_{11} E_{11} b t \frac{\mathcal{V}}{t_{IDE}} \tag{7-1}$$

$$\Delta l = d_{11} l \frac{\mathcal{V}}{t_{IDE}} \tag{7-2}$$

where:

b : Actuator width

l : Actuator length

Based on the above equations, the blocking force versus free displacement plots of the standard and single crystal *MFC*s are shown in Figure 7.50. From the figure it can be seen that the free displacement of the standard *MFC* is lower as compared to the single crystal type. However, the blocking force produced by the standard *MFC* is higher than the single crystal *MFC*. This indicates that the standard *MFC* would produce higher force when constraint and consequently larger displacement as compared to the single crystal *MFC*.

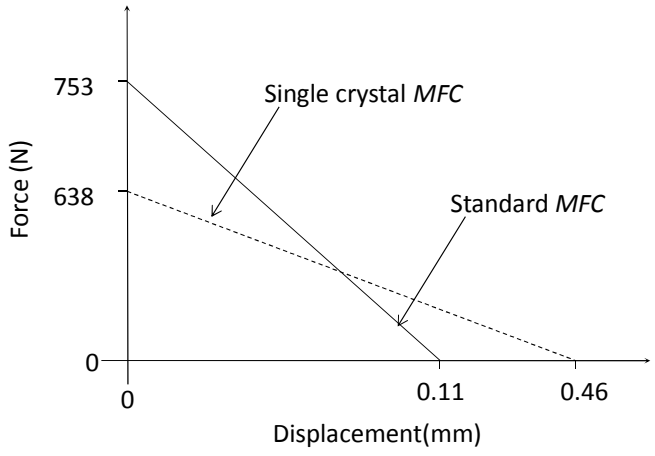


Figure 7.50: Blocking force-free displacement plot at 1500V

Figure 7.51 shows the performance characteristics of the standard *MFC* when bonded to host plate with different elastic modulus. The figure shows that the *MFC* requires larger force

to deform laminates made of carbon fibre as compared to glass fibre. Hence, intuitively glass fibre laminate may serve as a better choice in subsequent impact investigation. However, the choice of the laminate material was restricted to carbon fibre. This was due to several reasons. The carbon fibres are mainly used to construct primary structural components in aerospace applications as compared to glass fibres, Figure 2.3. Carbon fibres offer, both, improved strength and stiffness on weight basis ratio, Figure 2.2. Glass fibres could offer high specific strength but their specific modulus is extremely low. Due to higher strength and low elastic modulus glass fibres have higher failure strain. The *MFC* in this case would then need to resist very high impact force and this may require voltages beyond the ones demonstrated in this study.

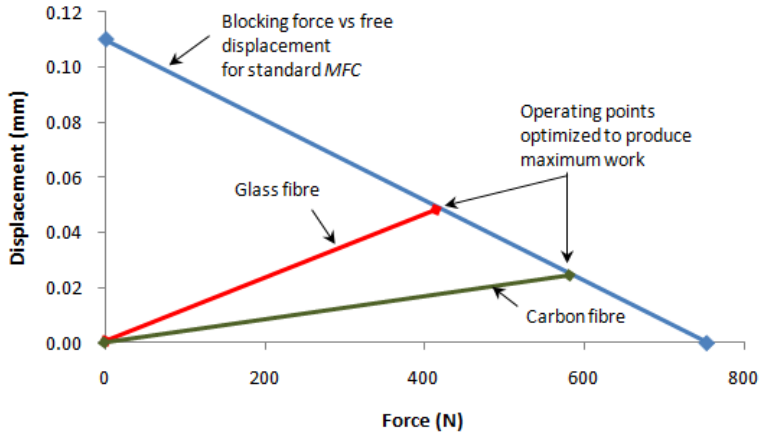


Figure 7.51: Optimized working points for different fibre materials

7.8 Chapter summary

A parametric study was conducted using the static shape control finite element code, *3DSHAPE-V*, to investigate the effects of *MFC* actuation on composite laminates under different design and actuation conditions. This was seen essential as many of the existing works have only characterized the performance of the *MFC* actuator with respect to flexible structures. Since carbon and graphite fibres are mostly used as primary structural components in many aerospace applications and continuously exposed to impact threats it was considered important to characterize the actuation characteristics of the *MFC* with respect to these materials and design conditions.

The investigation considered two cross ply laminates with lamination sequences of $(p/0_2/90_2/90_2/0_2/p)$ and $(p/90_2/0_2/0_2/90_2/p)$ representing some of the common and simple

layups used in impact investigations. The boundary conditions used were simply supported and clamped. The material properties of the composite laminate consisted of high modulus carbon, $E_{1C} / E_{1MFC} = 4.62$, and graphite/epoxy, $E_{1G} / E_{1MFC} = 3.1$, which represented different modulus ratios. The actuator materials consisted of the standard and single crystal *MFC*s.

The displacements of the laminate were found to increase with the actuation voltages in a linear fashion which was expected since the linear piezoelectric actuation model was used in the code development. The lamination sequence, though influenced the deformation of the laminate, was observed not to be significant. It was found that factors such as boundary condition, laminate thickness, actuator placement and actuator type that had profound influences on the piezoelectric actuation characteristics. Since clamped edges are not free to displace, this increased the geometric stiffness of the laminate and considerably lowered to piezoelectric effects.

Likewise, laminate thickness also had adverse effects on the piezoelectric actuation characteristics. Since the bending stiffness is proportional to the cubic order of the laminate thickness, increasing the laminate thickness almost diminished the piezoelectric effects on the laminate and was seen to be more detrimental than the clamped support. Since the *MFC* has anisotropic actuation characteristics, the placement of the actuator was also found to have significant influence on the deformation pattern of the laminate. For the simply supported type all the actuator placements considered in the investigation resulted in an upward bending of the laminate. However, the same was not observed in the case of clamped laminate. As the actuator locations varied, complex deformation patterns were observed. This highlighted the dependence of the piezoelectric actuation on the boundary condition imposed on the laminate.

Lastly, it was found that the material property of the actuator to be an important factor when deformation was the main concern. Though the single crystal *MFC* has larger strain output, its blocking force was lower than the standard *MFC*.

Chapter 8

Interface element formulation and validation

8.1 Chapter introduction

This chapter presents the mathematical formulation of the interface element implemented into the *LS-DYNA* explicit finite element code. The derivation and implementation presented in this chapter are referenced to the work of Iannucci (2006) unless specified otherwise. The damage model was coded into the *LS-DYNA* explicit finite element code through its user defined material subroutine by Iannucci (2006) and for the purpose of the current work the damage model was assigned the material number *umat41v*.

The damage model, *umat41v*, and *MAT 138* were validated using two fracture tests namely the *DCB* and *ENF*. The damage models were also rigorously tested to simulate impact induced delamination in composite laminates. The outcome of this chapter will be the identification of the most appropriate damage model to be used in the subsequent impact investigations.

8.2 Constitutive model

The current interface element was implemented using the single integration solid element. A local coordinate system at the Gauss point of the element is shown in Figure 8.1. The constitutive equation was established by defining three local stresses (σ_{I}, σ_{II} and σ_{III}) and local displacements (u_{I}, u_{II} and u_{III}) at the Gauss point of the element. σ_{I}, σ_{II} and σ_{III} correspond to opening traction (mode I), shear or sliding traction (mode II) and mixed mode traction (mode III) respectively.

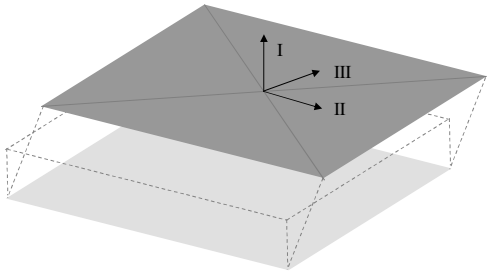


Figure 8.1: Interface element coordinate system

The local stresses and the local displacements are related through the following equation:

$$\begin{Bmatrix} \sigma_I \\ \sigma_{II} \\ \sigma_{III} \end{Bmatrix} = \begin{bmatrix} k_I & 0 & 0 \\ 0 & k_{II} & 0 \\ 0 & 0 & k_{III} \end{bmatrix} \begin{Bmatrix} u_I \\ u_{II} \\ u_{III} \end{Bmatrix} \tag{8-1}$$

where k_{I}, k_{II} and k_{III} are the interface stiffnesses defined as follows:

$$\begin{aligned} k_I &= \frac{E_{33}}{t_c} \\ k_{II} &= \frac{2G_{23}}{t_c} \\ k_{III} &= \frac{2G_{13}}{t_c} \end{aligned} \tag{8-2}$$

where:

E_{33} : Young's modulus in the through thickness direction

G_{23}, G_{13} : out-of-plane shear modulus

t_c : thickness of interface layer

The values for the Young's and shear modulus can be assumed to be equivalent to the properties of a homogenised composite layer or true values of the matrix material. The thickness of the interface layer is usually assumed to be a fraction of the thickness of a single composite ply.

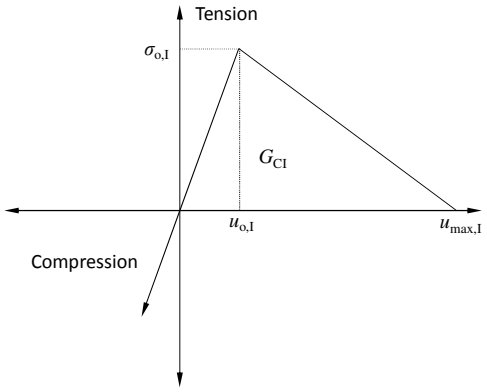


Figure 8.2: Bilinear relationship for mode I delamination

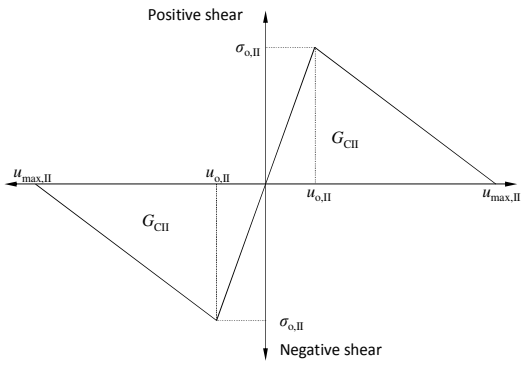


Figure 8.3: Bilinear relationship for mode II delamination

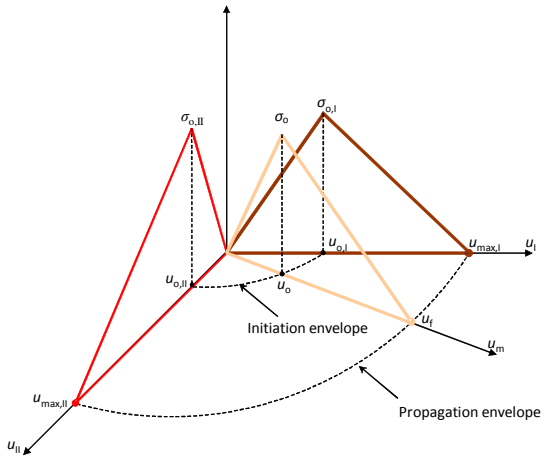


Figure 8.4: Bilinear relationship for mixed mode delamination (*LS-DYNA* keyword user's manual, 2007)

The constitutive relationship describing the traction-relative displacement was based on a simple bilinear softening approach. Figure 8.2 and Figure 8.3 show the bilinear relationship for mode I and II delamination respectively while Figure 8.4 shows the mixed mode delamination law. The element will respond elastically for stress loads that are below the damage onset peak stress value $\sigma_{o,i}$. Damage initiation is assumed once the onset stress value has been reached and the relative displacement corresponding to this stress value is known as the damage onset displacement, $u_{o,i}$. Any loading beyond the damage onset will propagate damage until ultimate failure is reached at which the stress will be zero (Borg et al., 2004). The relative displacement at this point is known as the ultimate failure displacement, $u_{max,i}$.

To indicate the extent of damage three scalar variables, d_I, d_{II} and d_{III} that correspond to the direction of the local stresses and displacements can be used. These variables vary from 0 to 1 to indicate undamaged to fully damaged states. The damage variables are introduced into the constitutive Equation (8-1) as follows:

$$\sigma_i = k_i(1 - d_i)u_i \tag{8-3}$$

where:

i = I, II, III

The above equation can be expressed in the incremental form as:

$$\Delta\sigma_i = k_i(1 - d_i)\Delta u_i - \sigma_i \frac{\Delta d_i}{(1 - d_i)} \tag{8-4}$$

Similarly, the incremental work can be defined as:

$$\Delta W_i = \frac{1}{2}(\sigma_i \Delta u_i - u_i \Delta\sigma_i) \tag{8-5}$$

By substituting Equation (8-4) into Equation (8-5), the incremental work can be alternatively written as:

$$\Delta W_i = \frac{\sigma_i^2}{2k_i(1 - d_i)^2}\Delta d_i \tag{8-6}$$

The ratio between the incremental work and the incremental damage is equivalent to the fracture mechanics energy of the system. This energy can be simply defined as:

$$Y_i = \frac{\sigma_i^2}{2k_i(1 - d_i)^2} \tag{8-7}$$

By substituting Equation (8-3) into Equation (8-7), the strain energy of the interface (undamaged strain energy) can be written as:

$$Y_i = \frac{1}{2}k_i u_i^2 \tag{8-8}$$

Based on Equation (8-8) the relative displacement can be expressed as a function of damage energy release rate as follows:

$$u_i = \sqrt{\frac{2}{k_i}Y_i} \tag{8-9}$$

In the above equation it can be seen that the relative displacement is trivially related to the damage energy release rate. Hence instead of damage evolution being defined as the ratio of

energy release rate over the critical energy value, damage evolution can also be defined using the relative displacement as follows:

$$d_i = \frac{u_{max,i}}{\left(u_{max,i} - u_{o,i}\right)}\left[1 - \frac{u_{o,i}}{u_i}\right] \tag{8-10}$$

By assuming some dimensionless parameters, α_i and β_i, the above equation can be rewritten as:

$$d_i = \frac{\alpha_i}{(\alpha_i - 1)}\left[\frac{\beta_i - 1}{\beta_i}\right] \tag{8-11}$$

where:

$$\alpha_i = \frac{u_{max,i}}{u_{o,i}}$$
$$\beta_i = \frac{u_i}{u_{o,i}} \tag{8-12}$$

The initiation of damage corresponds to $\beta_i = 1$ and damage propagation is assumed when $\alpha_i = \beta_i$. For explicit implementation the incremental of the damage variables can be expressed as:

$$\Delta d_i = \frac{u_{max,i}}{u_{max,i} - u_{o,i}}\left[\frac{u_{o,i}}{u_i^2}\right]\Delta u_i \tag{8-13}$$

For time domain problems, the cumulative damage can then be defined as:

$$d_i^{n+1} = d_i^n + \Delta d_i^{n+1} \tag{8-14}$$

The work dissipated due to damage can also be conveniently expressed in the respective incremental, Equation (8-15), and time domain forms, Equation (8-16), as follow:

$$\Delta W_i = \frac{1}{2} k_i u_i^2 \Delta d_i = \frac{1}{2}\frac{u_{max,i}}{u_{max,i} - u_{o.i}}\sigma_{o,i}\Delta u_i \tag{8-15}$$

$$W_i^{n+1} = W_i^n + \Delta W_i^{n+1} \tag{8-16}$$

where, in Equations (8-14) and (8-16) *n* represent the current time step in explicit calculation.

8.3 Mixed mode formulation

In Section 8.2 the damage formulation was provided for a single loading condition. Under mixed mode loading conditions, the damage may initiate before individual stress limits are reached. For such conditions, the mixed mode damage criteria can be written in the energy form as (Reeder, 1992):

$$1 = \left[\left(\frac{G_I}{G_{CI}}\right)^{\lambda} + \left(\frac{G_{II}}{G_{CII}}\right)^{\lambda} + \left(\frac{G_{III}}{G_{CIII}}\right)^{\lambda}\right] \tag{8-17}$$

The fracture energy, G_i, consumed during the course of damage is:

$$G_i = \int \sigma_i du_i \tag{8-18}$$

Based on Equation (8-18), Equation (8-17) can be converted to strain based equation as follows:

$$1 = \left[\left(\frac{u_I^*}{u_{max,I}}\right)^{2\lambda} + \left(\frac{u_{II}^*}{u_{max,II}}\right)^{2\lambda} + \left(\frac{u_{III}^*}{u_{max,III}}\right)^{2\lambda}\right] \tag{8-19}$$

The effective damage envelope can then be defined as:

$$\beta_e^n = \left[\left(\frac{u_I^n}{u_{o,I}}\right)^{2\lambda} + \left(\frac{u_{II}^n}{u_{o,II}}\right)^{2\lambda} + \left(\frac{u_{III}^n}{u_{o,III}}\right)^{2\lambda}\right]^{\frac{1}{2\lambda}} \tag{8-20}$$

Damage initiation will correspond to $\beta_e^n = 1$ and propagation is assumed when $\beta_e^n = \frac{u_{max,e}}{u_{o,e}}$. As in the case of single loading condition, the effective damage in a mixed mode condition can be defined as:

$$d_e^n = \frac{\alpha_e}{(\alpha_e - 1)}\left[\frac{\beta_e^n - 1}{\beta_e^n}\right] \tag{8-21}$$

where:

$$\beta_e^n = \frac{u_e}{u_{o,e}}$$
$$\alpha_e = \frac{u_{max,e}}{u_{o,e}} \tag{8-22}$$

In the above equations *n* represents the current time step. The above damage formulation is for *umat41v*. The damage formulation of *MAT 138* can be found in *LS-DYNA* keyword user's manual (2007) or in Appendix B.

8.4 Single element validation – mode I

As a first step to the validation process a single element test was considered to illustrate the damage predictive capabilities of *umat41v* and *MAT 138* for mode I delamination. For the purpose of investigation an element of size 0.25×0.25×0.02mm^3 with interface parameters of G_{CI} = 0.52kJ/m^2 and σ_{oI} = 30MPa (Aymeric et al., 2008) was considered. The element was subjected to an opening displacement in the *z*-direction.

The traction-relative displacement curve of the test result is shown in Figure 8.5. As formulated the damage evolution followed a bilinear damage law and was found to correspond to the prescribed material parameters. The traction-separation curve shown in Figure 8.5 was obtained using *umat41v*. The traction-separation curve obtained using *MAT 138* is not shown as a separate figure as the result was exactly identical to the one shown in Figure 8.5.

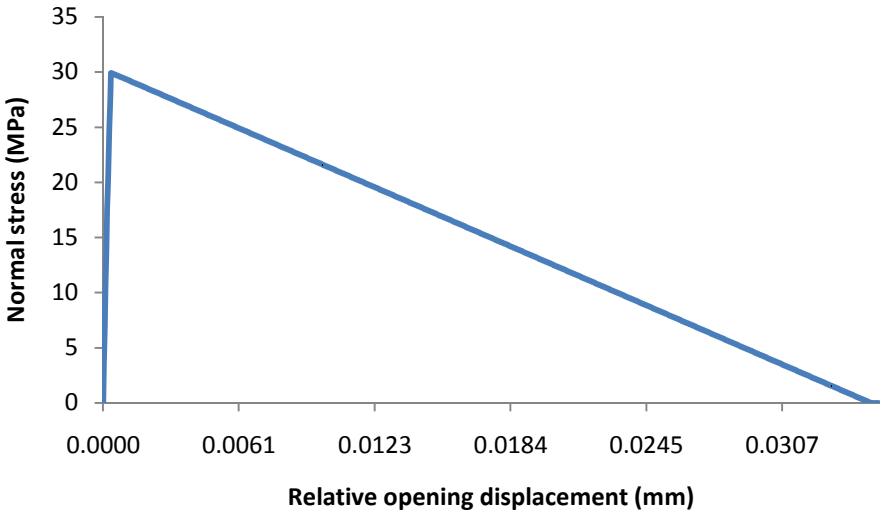


Figure 8.5: Mode I single element validation

8.5 Single element validation – mode II

In this validation a single element test was considered to illustrate the damage predictive capabilities of *umat41v* and *MAT 138* for mode II driven delamination which is of more relevance to the current work. Similar to the mode I test an element with the size of $0.25\times0.25\times0.02\text{mm}^3$ was considered for the purpose of investigation. The following interface parameters were used in the numerical simulation: G_{CII} = 0.97kJ/m^2 and σ_{oII} = 80MPa (Aymeric et al., 2008). The element was subjected to a sliding displacement in the *x*-direction.

Figure 8.6 shows the traction-relative displacement curves obtained using *umat41v* and *MAT 138*. As in the previous case the damage evolution followed a bilinear damage law and corresponded to the prescribed material parameters. However, a small difference was observed with respect to the point of damage initiation. From Figure 8.6 it can be seen that elastic response of *umat41v* to be stiffer in comparison to *MAT 138*. Hence, much earlier damage initiation was detected using *umat41v*. This was associated with the penalty stiffness values assigned to the respective damage models. Nevertheless, both damage models exhibited identical results at failure confirming their adherence to the damage criterion.

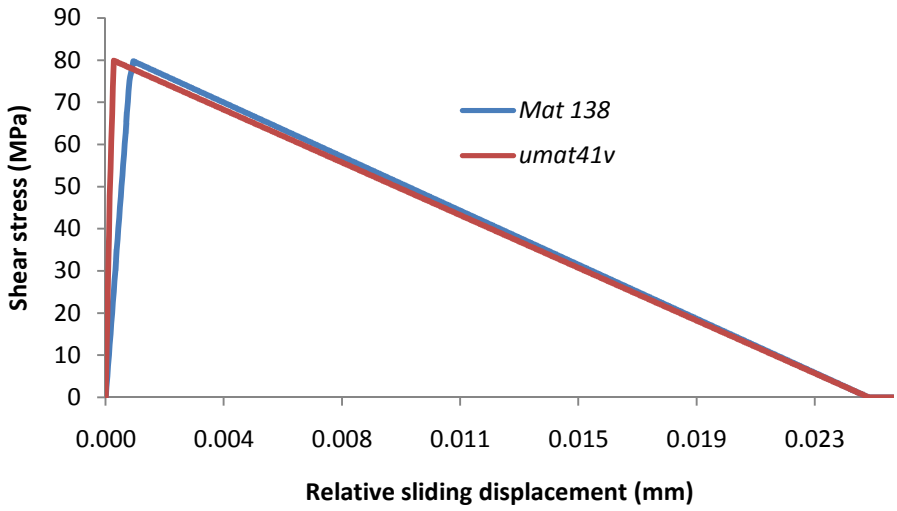


Figure 8.6: Mode II single element validation

8.6 Double cantilever beam test (*DCB*)

An appropriate structural representation for simulating mode I delamination is the *DCB* test. A standard *DCB* test specimen used in the simulation is illustrated in Figure 8.7 (Robinson and Song, 1992). The specimen consisted of two composite arms with an embedded delamination that ran from the beam free end to a specified distance along the beam length. Figure 8.8 shows the finite element model of the test specimen used in the numerical simulation.

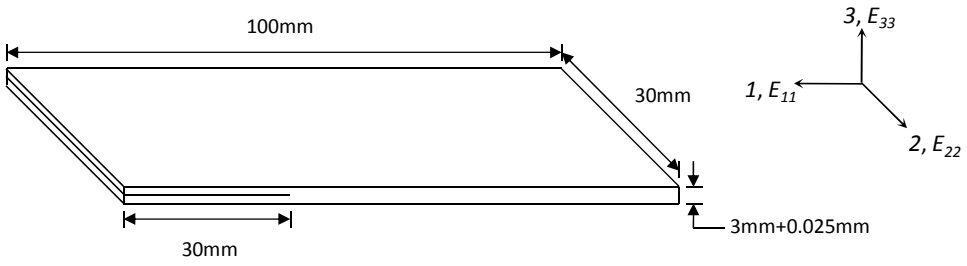


Figure 8.7: *DCB* test specimen (Robinson and Song, 1992)

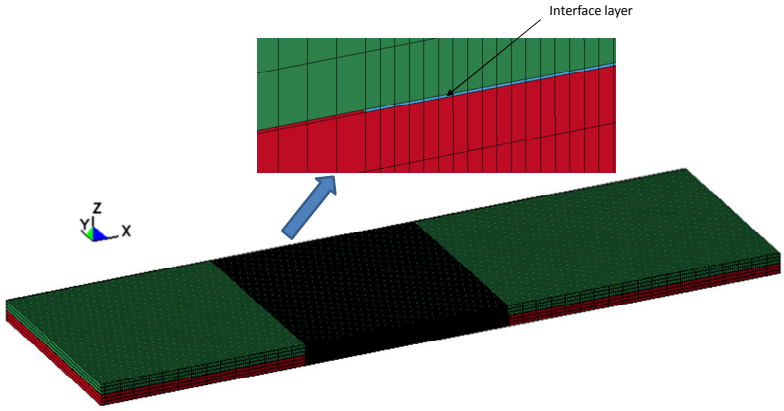


Figure 8.8: Finite element model of *DCB* specimen

Table 8.1: Material and interface properties of *DCB* test

Properties	Graphite/Epoxy§‡	Interface element§†
E_{11}, E_{22}, E_{33} (GPa)	126,7.45,7.45	7.45
G_{12}, G_{23}, G_{13} (GPa)	4.98,4.98,4.98	-
v_{12}, v_{13}, v_{23}	0.263,0.263,0.263	-
ρ (kg/m^3)	1540	1540
$\sigma_{o,I}$, $\sigma_{o,II}$, $\sigma_{o,III}$ (MPa)	-	57,100,100
G_{CI}, G_{CII}, G_{CIII} (N/mm)	-	0.281, 0.900, 0.900

§‡ Data from Robinson and Song (1992), §† Data from Iannucci (2006)

Each arm was modelled using single integration solid element with three elements across the thickness and one across the width. A mesh size of 0.125mm was used in the region starting from the crack end to a distance of 30mm along the length of the beam. Elsewhere the mesh size was 0.25mm. Co-rotational stiffness based hourglass control was used the keep the nonphysical energy modes arising from the use of under integrated element within acceptable range. The material parameters of the beam and the interface layers are given in Table 8.1. The thickness of the interface layer was assumed 0.025mm. The specimen was clamped at the crack-free end.

It has to be noted that the fracture test conducted was quasi-static in nature. Since the problem was solved using explicit method, issues such as damping must be taken into consideration because a failed element could set the system into vibration and affect the

results (Pinho et al., 2006). Introducing appropriate damping could reduce the vibration in the system. However, damping could stiffen the structure and affect its elastic response prior to failure. One way of overcoming this issue would be to use a displacement rate that would keep the kinetic energy of the system to less than 0.001% of the total energy (Iannucci, 2006). This would, however, increase the computational time substantially. In this investigation no damping was used but sufficiently lower opening displacement of 8mm/s was prescribed at the crack tip of the specimen as shown in Figure 8.9.

Figure 8.10 shows the numerical results obtained from *umat41v* and *MAT 138* for the reaction force F_d versus the tip relative opening displacement, w. The drop in the load level indicated delamination had taken place. The numerical models predicted earlier and higher damage load than the one reported in the literature. But these are very marginal and probably caused by factors such as round off errors which are highly probable in quasi-static simulation due to large number of time steps (Pinho et al., 2006). Nevertheless, the results of both damage models were found to accurately match the experimental results reported by Robinson and Song (1992). At the prescribed loading rate, the results showed stability without any noticeable oscillation in the system after failure, although minor fluctuation was noticed with *MAT 138*.

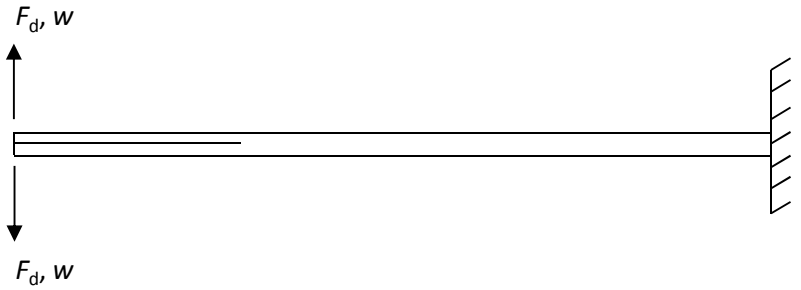


Figure 8.9: Boundary and loading conditions used in *DCB* simulation

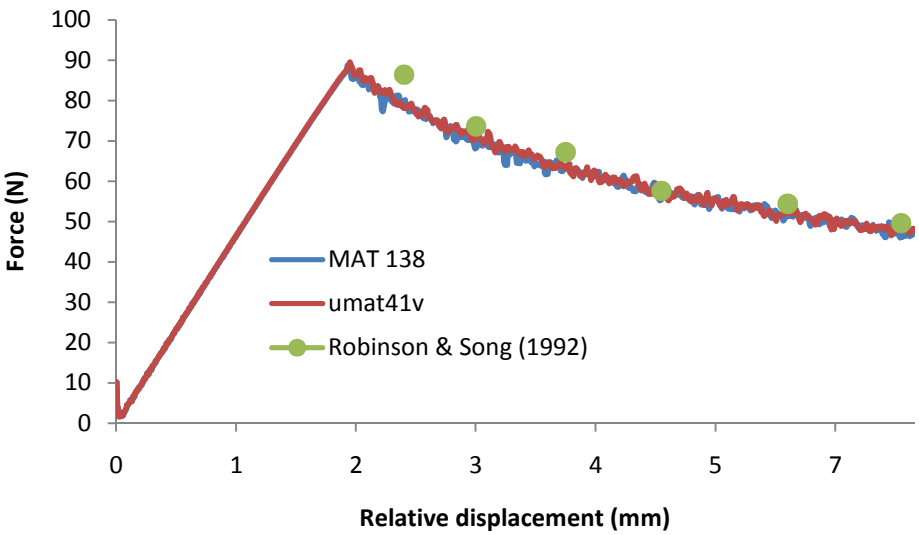


Figure 8.10: Force-relative displacement - *DCB* simulation

8.7 End notched flexure test (*ENF*)

As have been indicated by numerous studies, delamination due to low velocity impact in composite materials is mainly attributed to shear driven delamination. Shear driven delamination can be simulated using an *ENF* test. Figure 8.11 shows the test specimen used for *ENF* simulation in the present study (Goyal et al, 2002).

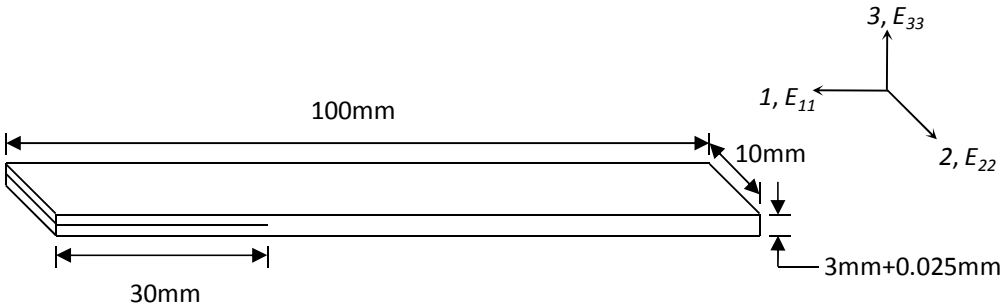


Figure 8.11: *ENF* test specimen (Goyal et al, 2002)

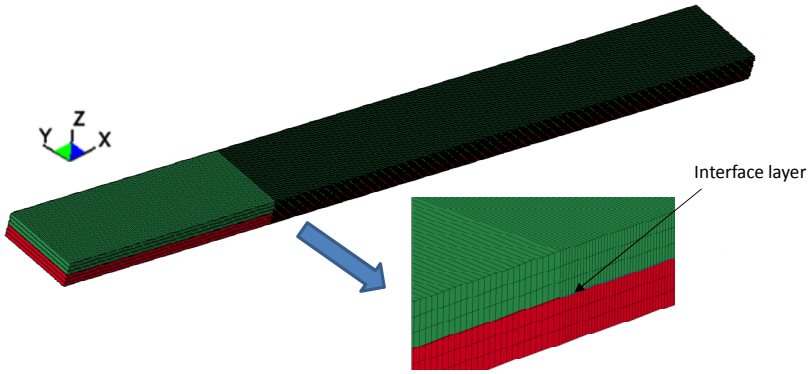


Figure 8.12: Finite element model of *ENF* specimen

Similar to a *DCB* specimen, each arm was modelled using single integration solid element with three elements across the thickness and one along the width. The finite element model used in the simulation is shown in Figure 8.12. A mesh size of 0.125mm was used in the region starting from the crack end to a distance of 70mm along the length of the beam. Elsewhere the mesh size was 0.25mm. A stiffness based co-rotational hourglass control was used to control the nonphysical hourglass energy in the system due to the use of under integrated elements. The material and interface properties are given in Table 8.2. To induce mode II delamination displacement was applied at the centre of the specimen in the negative z-direction. The support and loading conditions are shown in Figure 8.13. To avoid penetration of the arms once the failed elements are deleted *AUTOMATIC-SURFACE-TO-SURFACE* contact logic was defined between the arms.

Table 8.2: Material and interface properties of *ENF* test specimen

Properties	Graphite/Epoxy‡§	Interface element‡§
E_{11}, E_{22}, E_{33} (GPa)	150,11,11	11
G_{12}, G_{23}, G_{13} (GPa)	6.0,3.7,6.0	-
ν_{12}, ν_{13}, ν_{23}	0.25,0.25,0.45	-
ρ (kg/m^3)	1540	1540
$\sigma_{o,I}$, $\sigma_{o,II}$, $\sigma_{o,III}$ (MPa)	-	80,80,60
G_{CI}, G_{CII}, G_{CII} (N/mm)	-	0.352, 1.45, 1.45

‡§ Data obtained from Goyal et al, (2002)

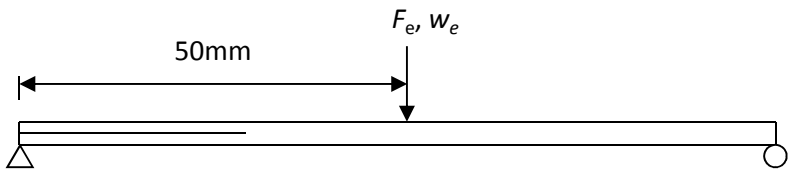


Figure 8.13: Boundary and loading conditions used in *ENF* simulation

Figure 8.14 shows the reaction force versus the bending displacement at the point of load application. The numerical results obtained from the current damage model and *MAT 138* are compared with the analytical solution reported by Mi et al. (1998). The damage load predicted by the numerical models was lower than the analytical prediction. *umat41v* predicted much earlier damage than *MAT 138* and in comparison to the analytical prediction. This is again assumed to have been caused by the assignment of the penalty stiffness values associated with the respective damage models. However, both models predicted damage at almost identical loads and fit the analytical results with good accuracy.

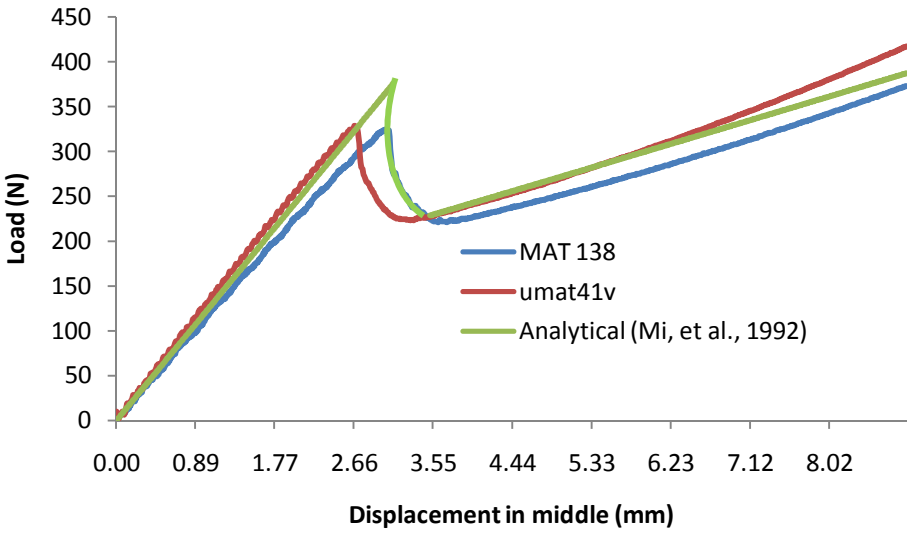


Figure 8.14: Force-relative displacement - *ENF* simulation

8.8 Low velocity impact validation

As one of the objective of this research, the damage models *umat41v* and *MAT138* were tested to simulate low velocity impact induced delamination in composite laminates. This test was considered essential to determine the most appropriate damage model to be used in

subsequent impact investigations as no detail verifications on the performances of these damage models are available in the literature with respect to impact investigation. In Section 8.8.1 the two models were validated for its accuracy in simulating impact induced delamination. Section 8.8.2 tested the numerical stability of the two models with different impact loads. This was crucial as both models were based on the bilinear formulation they could be susceptible to numerical instabilities at high loading rates. The following sections illustrate the drawbacks of *MAT 138* in comparison to the current damage model.

8.8.1 Symmetric cross-ply laminate – thick plate

The first test case was obtained from the work of Aymeric et al. (2008). The test model consisted of a simply supported symmetric cross-ply laminate with a lamination sequence of $(0_2/c/90_2/90_2/c/0_2)$. The letter *c* in the lamination sequence indicates the position of the interface layer. Interface layers were only placed between plies with different orientations as experimental investigation found no traces of delamination at the 90/90 interface (Aymeric et al., 2008). No other failure modes were considered in the investigation apart from delamination. The dimension of the plate was $87.5\times65\times2mm^3$. The impactor was hemispherical steel with a radius of 6.25mm and a mass of 2.3kg.

Table 8.3 lists the material properties of the composite and interface layer used in the numerical simulation. The critical strain energy release rates at the 0/90 interface was assumed to be twice the values at the 90/0 interface to ensure fibre dependent delamination growth (Borg et al., 2004). Due to symmetry in the boundary and loading conditions only a quarter-model was considered. Figure 8.15 shows the finite element model used in the impact simulation.

Table 8.3: Material properties of impact test specimen

Properties	Graphite/Epoxy†§	*MFC*†‡	Interface element†§	Impactor (Rigid)†§
E_{11}, E_{22}, E_{33} (GPa)	93.7, 7.45, 7.45	30.3, 15.9, 11.47	7.45	207
G_{12}, G_{23}, G_{13} (GPa)	3.97, 3.97, 3.97	5.5, 2.14, 2.6	0.86	-
v_{12}, v_{13}, v_{23}	0.261,0.261,0.261	0.31, 0.29, 0.33	-	0.3
ρ (kg/m^3)	1600	4750	1600	-
$\sigma_{o,I}$, $\sigma_{o,II}$, $\sigma_{o,III}$ (MPa)	-	-	30, 80, 80	-
G_{CI}, G_{CII}, G_{CII} (N/mm)	-	-	0.520, 0.970, 0.970	-

†§ Data from Aymeric, Dore and Priolo (2008), †‡ Data obtained from Williams (2004)

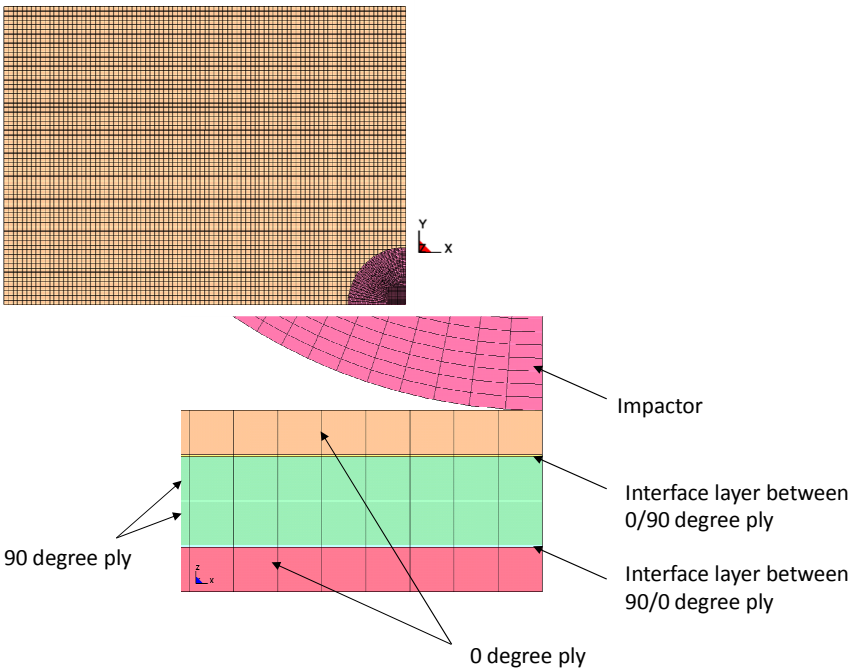
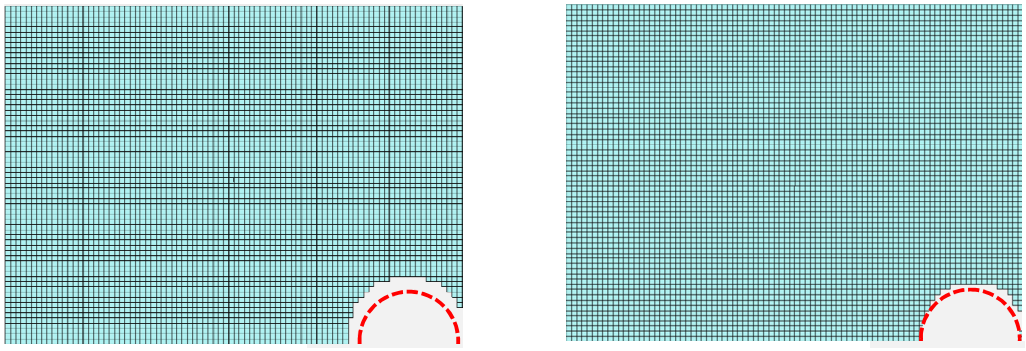


Figure 8.15: Finite element model of ($0_2/c/90_2/90_2/c/0_2$) impact test

Mesh sizes of $0.5\times0.5\times0.5mm^3$ and $0.5\times0.5\times0.02mm^3$ were used to model the composite and interface layers respectively. This resulted in a total of 34125 solid elements for the quarter plate. The composite layer was modelled using single integration solid element while the impactor was modelled using rigid solid element. Stiffness based hourglass control was used to limit the nonphysical energy in the system.

The impact energy was set to 2.1J which corresponded to an impact velocity of 1.35m/s. *AUTOMATIC-SURFACE-TO-SURFACE* contact logic was used between the layers attached to the interface elements to prevent penetration once the failed elements were deleted. The same contact logic was also used to define the impactor-plate interaction. The simulations lasted approximately three hours using *umat41v* and one hour using *MAT 138* with an 8-CPU XEON 64EMT processor.

The extent of delamination from the numerical simulations is shown in Figure 8.16 at 90/0 interface. The dashed red line is the average experimental delamination size reported by Aymeric et al., (2008). From Figure 8.16, it can be seen that the delamination size predicted by *umat41v* was much closer to the experimental results as compared to the one predicted by *MAT 138*.



(a): Predicted delamination using *MAT 138*

(b) Predicted delamination using *umat41v*

Figure 8.16: Predicted delamination at (90/0) interface

Figures 8.17, 8.18 and 8.19 show the kinetic energy, contact force and central nodal displacement plots obtained from the present simulation using *umat41v* and *MAT 138*. From the figures it can be seen that both damage models showed results that were close to each other. However, it can be noticed that the impact response using *umat41v* showed slight stiffening effect. This can be seen from Figure 8.18 and Figure 8.19. The peak contact force

using *umat41v* was slightly higher than *MAT 138*. This was anticipated as the extent of damage using *umat41v* was less compared to *MAT 138*. Since stiffness degradation was higher in the simulation using *MAT 138* as compared to that using *umat4Iv*, consequently this resulted in higher peak displacement using *MAT 138*.

Stiffness degradation will effectively reduce the peak impact force acting on the laminate. The experimental peak impact force was about 1814N compared to 2048N and 2023N using *umat41v* and *MAT 138* respectively. The difference between the experimental and the simulated values could have also been due to other damage formations during the impact. The experimental investigation found traces of matrix cracking during the impact and this was not modelled in the numerical studies. The formation of other damage modes will further degrade the laminate stiffness, hence, lowering the peak contact force. This portion of the study tentatively showed that both models were equally effective in predicting delamination due to impact.

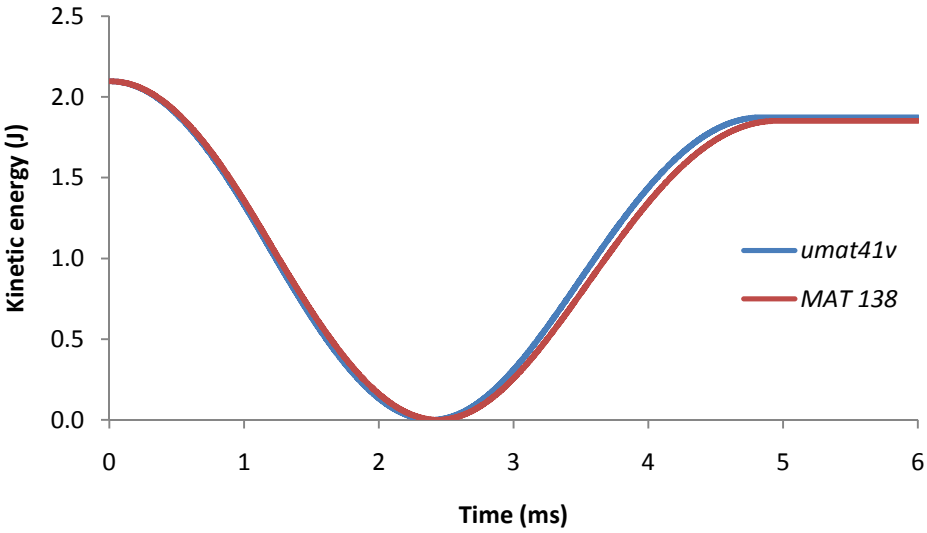


Figure 8.17: Kinetic energy-time plot for 2.1J impact case

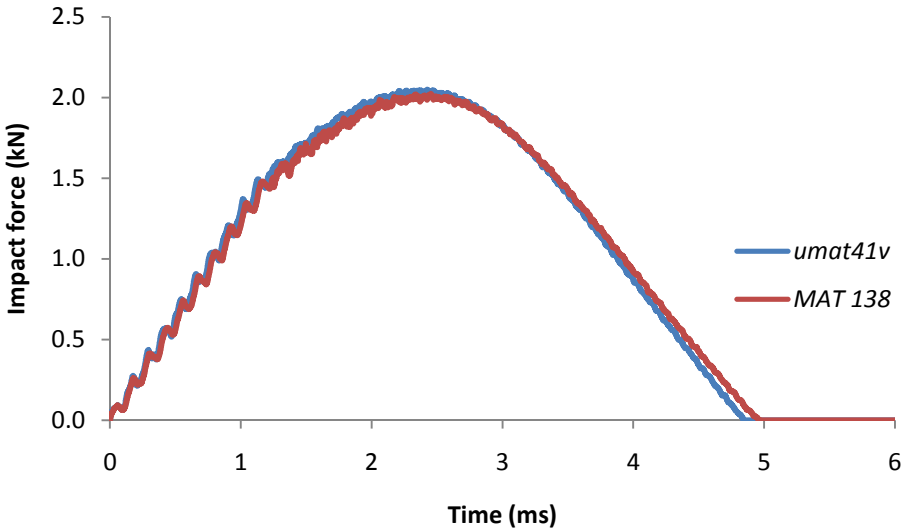


Figure 8.18: Impact force-time plot for 2.1J impact case

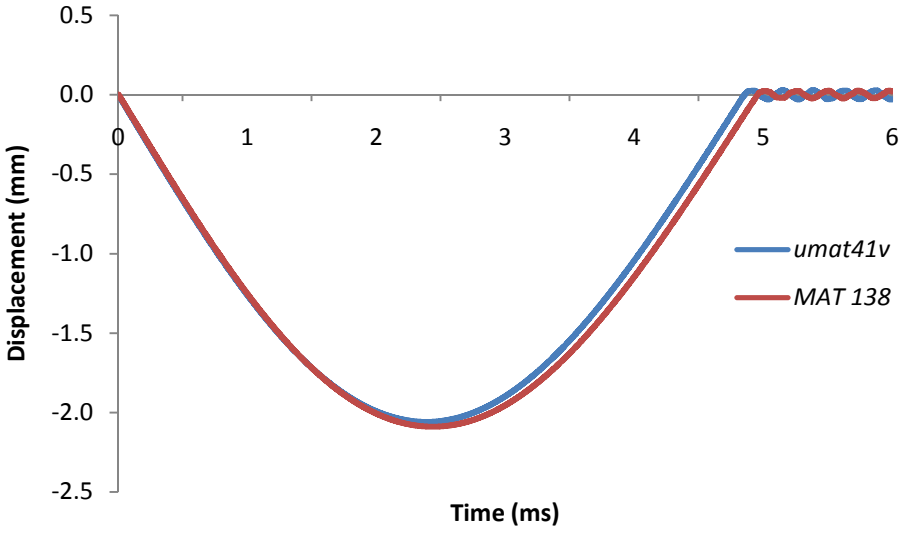


Figure 8.19: Displacement-time plot for 2.1J impact case

8.8.2 Symmetric cross-ply laminate – thin plate

This test model consisted of a simply supported symmetric cross-ply laminate with a lamination sequence of ($p/0_2/c/90_2/90_2/c/0_2/p$). The letters p and c indicate the position of the piezoelectric and interface layers respectively. As with the previous case, interface layers were only placed between composite plies with different orientations and no other failure modes were considered apart from delamination. In addition, no delamination was assumed

between the piezoelectric and the composite layer. The dimension of the composite plate was $87.5\times65\times1mm^3$. Due to symmetry in boundary and loading conditions only a quarter-model was considered. The piezoelectric layer was an *MFC* actuator with an active dimension of $39\times23.5\times0.3mm^3$ for the quarter model. The impactor was hemispherical steel with a radius of 6.25mm and a mass of 2.3kg. Table 8.3 list the material properties of the composite, interface layer and actuator material used in the numerical simulation. The critical strain energy release rates at the 0/90 interface was again assumed to be twice the values at the 90/0 interface to ensure fibre dependent delamination growth.

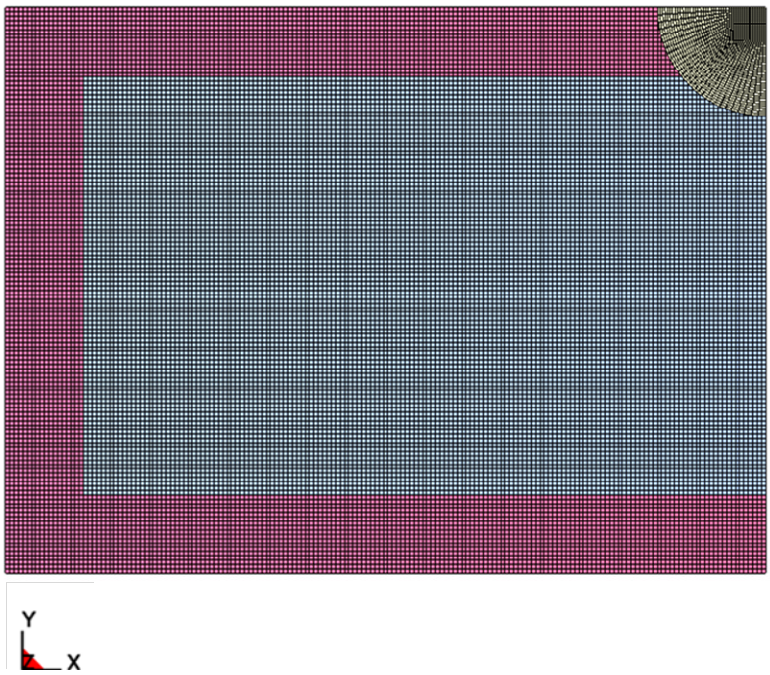


Figure 8.20: Finite element model of impact test specimen – top view

Figure 8.20 and Figure 8.21 show the finite element models used in the impact simulation. Mesh sizes of $0.25\times0.25\times0.25mm^3$, $0.25\times0.25\times0.3mm^3$ and $0.25\times0.25\times0.02mm^3$ were used to model the composite, piezoelectric and interface layers respectively. This resulted in a total of 165828 solid elements for the quarter model. The composite and piezoelectric layers were modelled using single integration solid element while the impactor was modelled using rigid solid element. Stiffness based hourglass control was used to limit the nonphysical energy in the system. The impact energy was set to 7.2J which corresponded to an impact velocity of 2.5m/s. *AUTOMATIC-SURFACE-TO-SURFACE* contact logic was used between the layers attached to the interface elements to prevent penetration once the failed elements are deleted.

The same contact logic was also used to define the impactor-plate interaction. The total simulation time was approximately 18 hours using an 8-CPU XEON 64EMT processor.

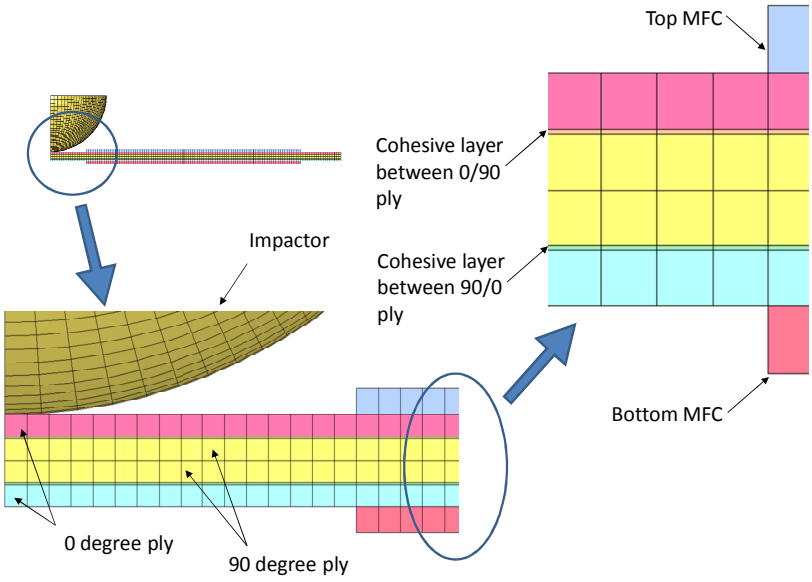
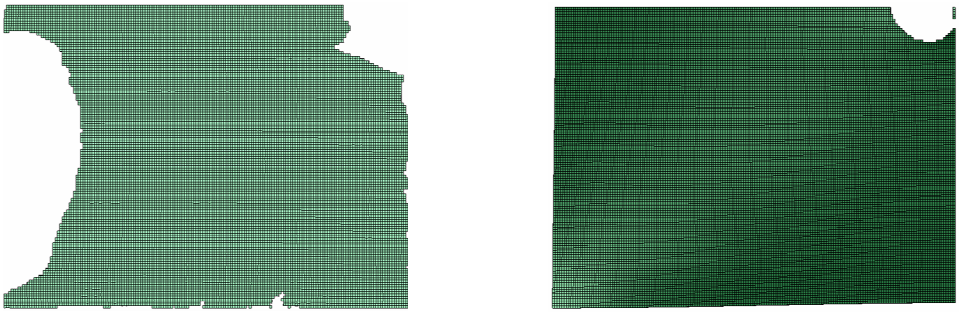
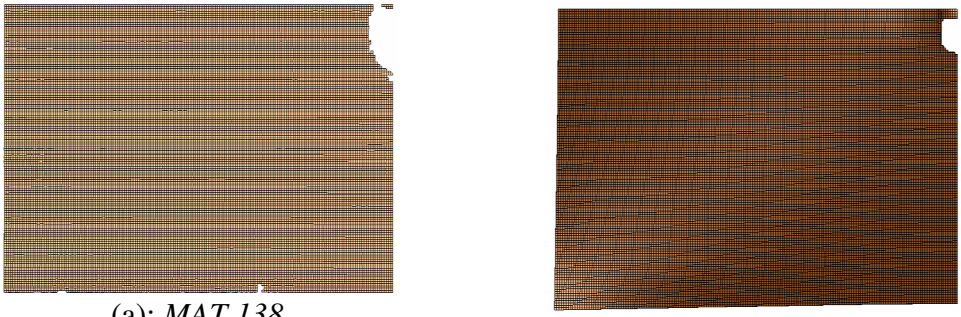


Figure 8.21: Finite element model of impact test specimen – detail view



(a): *MAT 138* (b): *umat41v*

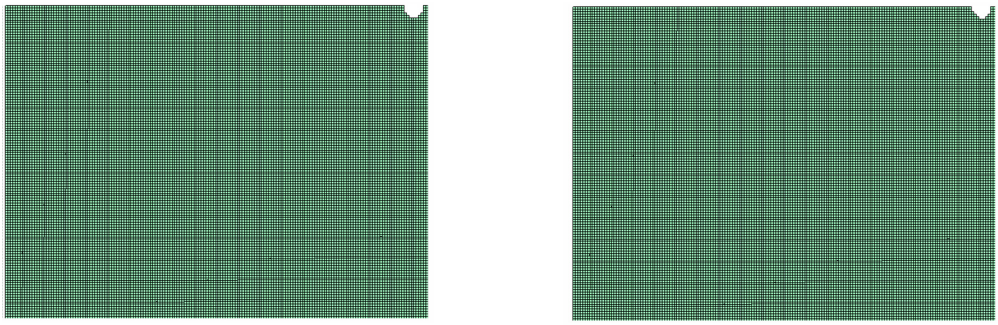
Figure 8.22: Delamination at 90/0 interface –7.2J impact



(a): *MAT 138* (b): *umat41v*

Figure 8.23: Delamination at 0/90 interface –7.2J impact

Figure 8.22 and Figure 8.23 show the delamination pattern at the respective interfaces obtained using *umat41v* and *MAT 138*. The damage simulation using *MAT 138* showed deterioration at both interfaces while simulation using *umat41v* demonstrated a more realistic prediction of the damage. A similar simulation was carried out using a lower impact energy, 1.0J, and it was found that the delamination prediction using *MAT 138* and *umat41v* not only showed a more stable response but predicted the damage close to each other, Figure 8.24. In the 1.0J impact case no delamination was observed in the 0/90 interface.



(a): *MAT 138* (b): *umat41v*

Figure 8.24: Delamination at 90/0 interface –1.0J impact

Figure 8.25 shows the energy plots for the 7.2J impact case using *MAT 138*. From the figure there was a clear sign of energy deterioration in the system as there was substantial presence of hourglass energy. The use of constant stress element is prone to hourglassing. Hourglass normally leads to nonphysical zero energy deformation and produces zero strain and no stress (www.dynasupport.com). It is almost impossible to completely eliminate the presence of hourglass energy with the use of single integration element. However, as a general rule the hourglass energy should be less than 10% of the system's internal energy (www.dynasupport.com). Figure 8.25 shows that the maximum internal energy of the system is about 5.65J and the hourglass energy is about 2.37J. In this case, the hourglass energy is about 41.95% of the system's internal energy. Such large presence of hourglass energy could invalidate the results and this is clearly manifested in Figures 8.22a and 8.23a.

Figure 8.26 shows the variation of the energy levels for the 7.2J impact case using *umat41v*. The energy levels were consistent with the maximum hourglass energy kept below 10% with respect to the peak internal energy. Two approaches were undertaken to improve the simulation using *MAT 138*. In the first approach, different hourglass options were used to control the hourglass energy level. However there was no noticeable improvement in the

solution. The viscous based hourglass option was found to deteriorate the solution even further.

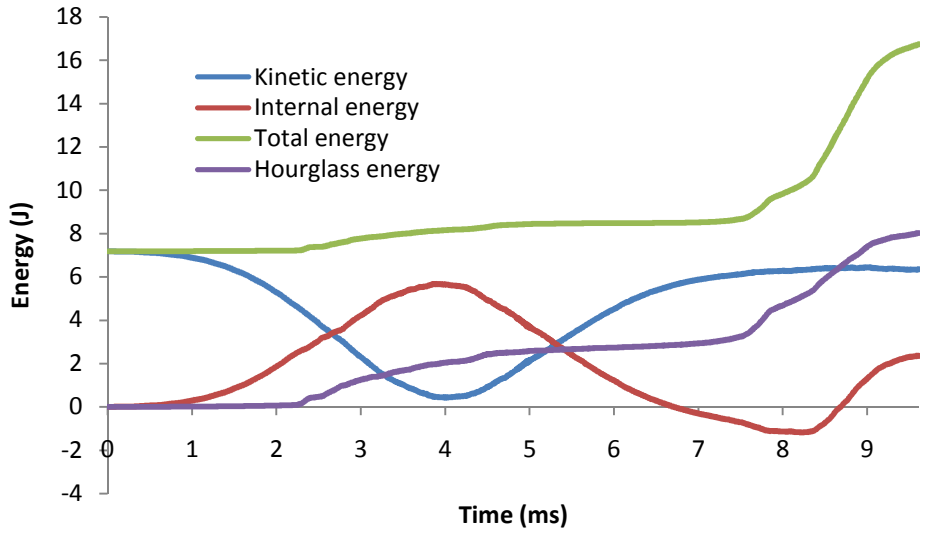


Figure 8.25: Energy vs. time for *MAT 138* – 7.2J impact

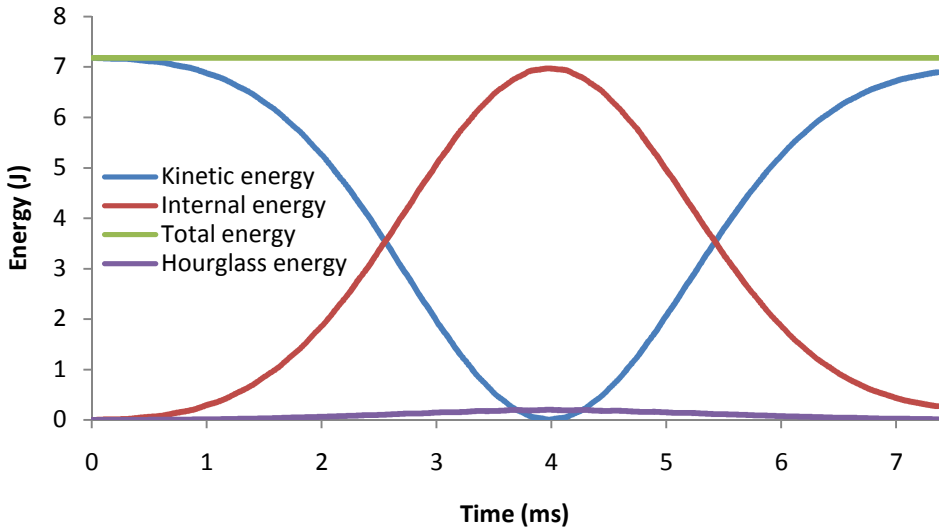
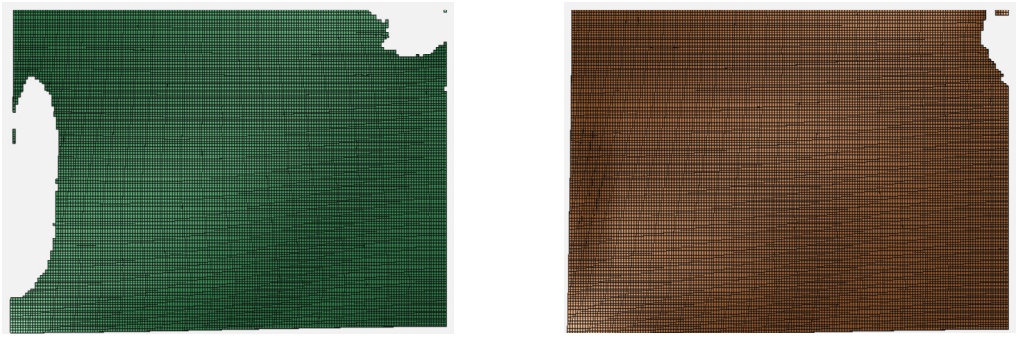


Figure 8.26: Energy vs. time for *umat41v* – 7.2J impact

Secondly, an attempt was made to lower the time step of the impact simulation by a timescale factor of 0.2. However, as can be seen from Figure 8.27 no improvement in the solution was obtained either. The simulation was terminated before the completion time and the delamination plot shown in Figure 8.27 was at 4.4ms. The only possible conclusion was that *MAT 138* could be sensitive the loading rate. At high load rates, the plate could be set into

vibration by the shock waves generated by the failed elements. In addition, as mentioned earlier the under integrated elements are prone to hourglassing making them susceptible to shock waves and hence affecting the results.

The improvement to solution could be achieved by lowering the time step further, but this attempt was not undertaken as the estimated simulation time was close to 60 hours for a timescale factor of 0.067. This was considered to be a pointless attempt as the present damage model took only about 18 hours for the same simulation and the outcomes are more realistic. Another approach to improve the solution would be to introduce damping. However, this was also not undertaken considering the fact that *umat41v* was numerically stable and highly accurate without the need for damping or reduction in the time scale.



(a): Delamination at 90/0 interface (b): Delamination at 0/90 interface

Figure 8.27: Delamination using *MAT 138* – 7.2J impact, time scale factor of 0.2

8.9 Chapter summary

This chapter presented the mathematical formulation of the cohesive element proposed by Iannucci (2006) and a comparison study between the damage predicting capabilities of *LS-DYNA* interface model, *MAT 138*, with the newly implemented damage model, *umat41v*. While both models accurately simulated the damage for the fracture tests, *MAT 138* selectively failed to simulate damage for impact cases when the loading rate was increased. This was not the case with *umat41v* as it predicted the damage accurately regardless of the loading rate. It was postulated that *MAT 138* could be sensitive to loading rate. The damage model *umat41v* has been successfully implemented and verified as an effective numerical tool to predict delamination in composite laminates.

Attempts to improve the solution using *MAT 138* failed to be established even after reducing the computational time step by a scale factor of 0.2. Lowering the time step further would increase the computational time and this is not seen as a practical solution at least for the present work. Hence, from this exercise it was concluded that the current damage model was both numerically stable and computationally efficient for predicting impact induced delamination in composite laminates and will be used in subsequent impact investigations in the later chapters.

Chapter 9

Effects of piezoelectric actuations on the elastic low velocity impact response of composite laminate

9.1 Chapter overview

The objective of this chapter is to investigate the effects of piezoelectric actuations on purely elastic response of composite laminates subjected to low velocity impact. For this purpose, a symmetric cross-ply laminate with surface bonded piezoelectric actuators was considered. Two types of boundary conditions were used, i.e., simply supported (*SS*) and clamped (*CC*).

The different types of piezoelectric control actions used in the investigation were the extension (positive in-phase actuation), compression (negative in-phase actuation), negative bending (out-of-phase actuation: upward bending) and positive bending modes (out-of-phase actuation: downward bending). In-phase actuation refers to the actuator pairs being applied with voltages equal in magnitude and direction. Whereas, out-of-phase actuations refers to actuator pairs being applied with voltages that are equal in magnitude but opposite in direction. In a negative bending mode, actuators bonded to the top surface of the laminate were applied with positive voltages while those attached to the bottom were applied with negative voltages. In a positive bending mode, the top actuators were applied with negative voltages while the bottom ones were applied with positive voltages.

As the main objective of this chapter was to characterize the different piezoelectric control actions on the impact force and displacement histories, only elastic impact was considered.

9.2 Numerical model

The test specimen used in the numerical simulations consisted of a symmetric cross-ply HS160/REM graphite/epoxy laminate with a lamination sequence of ($p/0_2/90_2/90_2/0_2/p$). The letter *p* indicates the position of the piezoelectric layers. The size of the composite laminate was 87.5×65×1mm^3. Due to symmetry in boundary and loading conditions only a quarter-model was considered. The piezoelectric layer was an *MFC* actuator with an active dimension of 42.5×24.5×0.3mm^3 for the quarter model.

The choice of the laminate size was determined based on the parametric study conducted in Chapter 7. A thin laminate was used in the investigation as thick laminate was found to reduce the piezoelectric effects drastically and may not have any effects on the impact force and displacement histories. The position of the actuators was set to *TYPE D* as it has been found to produce the maximum effect with respect to bending. The impactor was hemispherical steel with a radius of 6.25mm and a mass of 2.3kg. Table 8.3 lists the material properties of the composite and actuator material used in the numerical simulation.

Figure 9.1 shows the finite element model of the elastic impact test specimen. Ideally, the use of solid element would require the element aspect ratio between the length:width:thickness to be 1:1:1, hence in this simulation element sizes of 0.25×0.25×0.25mm^3 and 0.25×0.25×0.3mm^3 were used to model the composite and piezoelectric layers respectively. This resulted in a total of 124320 solid elements for the whole structure. The *MFC* was connected to the laminate through node sharing method. This would require the mesh size in the in-plane direction to be the same as the laminate's to which the *MFC* is attached. This obviously increased the number of elements required to mesh the *MFC*. The other option available within the *LSDYNA* code is the use of *TIED* contact option. *TIED* contact can be used to bond two surfaces with different mesh densities (www.dynasupport.com). This would allow the actuator to be meshed more coarsely than the laminate. The *TIED* method requires the projection distance on the slave node to the closet master surface to be zero and *LSDYNA* achieve this by updating the slave node coordinates to lie in the master surface which may sometimes cause element distortion and probably geometry modification (www.dynasupport.com). In addition, master nodes that do not

coincide with the slave nodes could possibly end up in node penetration through the slave surface and to ensure displacement compatibility ideally each slave node should be connected to the master node (www.dynasupport.com). Hence, the node sharing method was used to avoid possible errors that might result with the use of *TIED* option.

The composite and piezoelectric layers were modelled using single integration solid element while the impactor was modelled using rigid solid element. Stiffness based hourglass control was used to limit the nonphysical energy in the system. The impactor-plate interaction was defined using *AUTOMATIC-SURFACE-TO-SURFACE* contact. The average computational times for the impact simulations varied between three to six hours depending on the impact energy levels using an 8-CPU XEON 64EMT processor.

As the main objective of this chapter was to investigate the effects of different piezoelectric control actions on the impact force and displacement histories, no damage model was included in all the numerical simulations presented in this chapter.

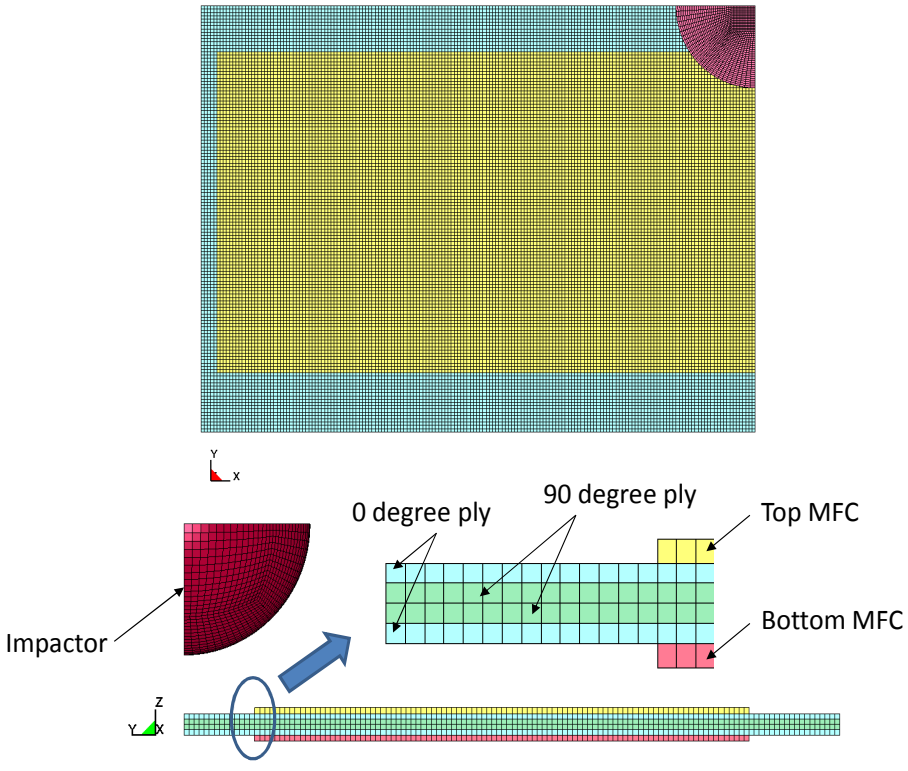


Figure 9.1: Finite element model of elastic impact test specimen

9.3 Impact response of simply supported cross-ply laminate

This section presents the simulation results based on the studies conducted on simply supported cross-ply laminates. Sections 9.3.1 to 9.3.3 examine the effects of different piezoelectric control actions on the impact response. The effects of different electrical loading rates on the impact force and displacement histories are discussed in Section 9.3.4. For the investigations conducted in Sections 9.3.1 to 9.3.3 the impact energies considered were 2.0J and 2.5J and were based on four different types of control actions, i.e., positive in-phase, negative in-phase, negative bending and positive bending actuations. For the investigations conducted in Section 9.3.4 the impact energies considered were 2.0J, 2.5J, 3.0J, 3.5J, 4.0J, 4.5J and 5.0J and were based on negative bending actuation.

9.3.1 Effects of different impact energy levels

This section presents the effect of different impact energy levels on the impact response of simply supported cross-ply laminate under zero piezoelectric actuation. From Figure 9.2, it can be seen that the peak impact forces increased with increasing impact energies. The peak impact force for the 2.5J impact case was 1653N and this was 1388N in the case of 2.0J impact. Correspondingly, the 2.5J impact resulted in higher peak displacement as compared to the 2.0J impact. The peak displacements were 5.169mm and 4.813mm for the 2.5J and 2.0J impact cases respectively, Figure 9.3.

The difference in the peak impact force between the two energy levels was 19.09% and this was only 7.35% for the peak displacement. Since no damage models were included in the analyses, the impact force plots shown in Figure 9.2 can be seen to be symmetric before and after the peak loads indicating no degradation in the laminate stiffness.

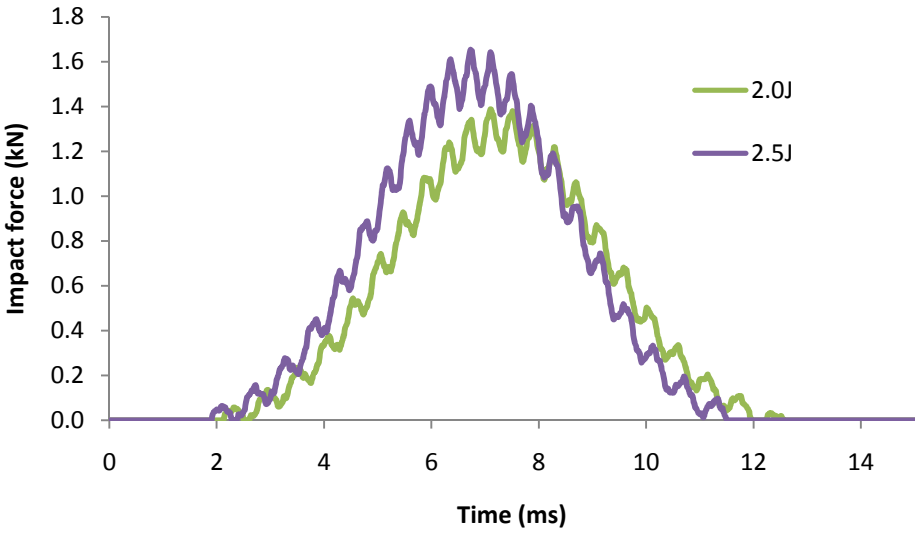


Figure 9.2: Force-time plot for *SS* cross-ply laminate – zero actuation

The oscillations that can be seen in the impact force curves are due the vibration mode excited at the instance of impact. The oscillation can be seen to fluctuate about a mean value of the contact force throughout the impact event. This kind of response is typical in the case of quasi-static impact for which the mass of the impactor is significantly larger than the laminate (Davies and Olsson, 2004). During the impact event the load oscillation increases in amplitude until the maximum load is reached and gradually reduces. In a large mass impact, the impact duration is longer than the time taken for the flexural waves to reach the boundaries of the plate and the impact response is governed by the lowest vibration mode of the laminate (Davies and Olsson, 2004). Figure E.1 shows the first six fundamental modes of the composite plate considered in this section. The lowest mode corresponds to a frequency of 641.4Hz. The excited frequency due to impact was calculated from Figure E.2 and was estimated to be 640Hz (based on the time taken to complete one cycle). Since the excited frequency is very close to the natural frequency of the laminate, there was resonance and this was reflected on the impact force curve.

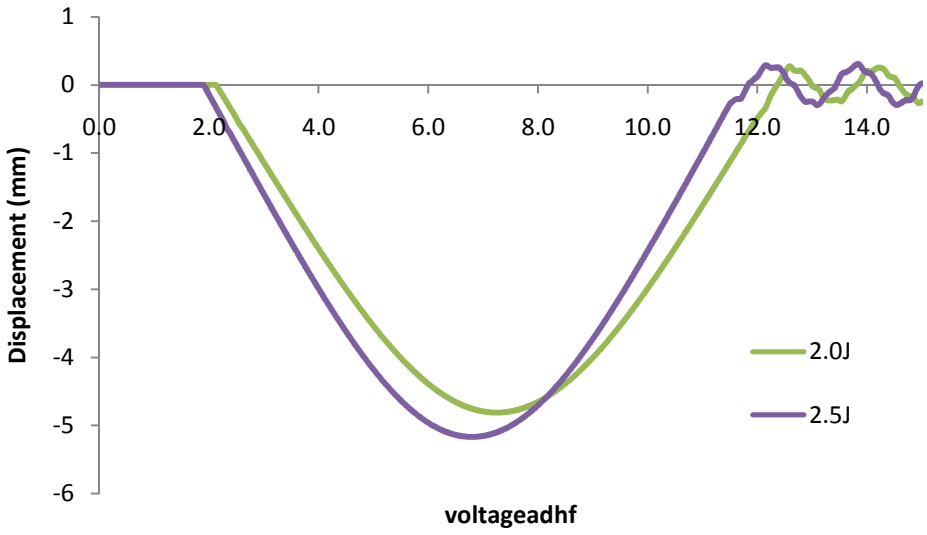


Figure 9.3: Displacement-time plot for *SS* cross-ply laminate – zero actuation

9.3.2 Effects piezoelectric actuations – 2.0J impact

The effects of different piezoelectric control actions on the impact response of a simply supported cross-ply laminate for an impact energy of 2.0J are demonstrated through Figures 9.4 to 9.7. The full impact history curves for the 2.0J impact case under different piezoelectric control actions are provided in Appendix A, Figure A.1. From Figure A.1, it can be seen that the impact force curves did not overlap each other indicating there were changes to the impact force-time history curves as a result of different piezoelectric control actions. A similar trend was also observed with the peak displacement plots, Figure A.2.

Closer views at the region of the peak impact force for the in-phase and out-of-phase actuations are shown separately in Figures 9.4 and 9.5. Figure 9.4 indicated that the in-phase actuations had very minimal effects on the impact force histories as there were no appreciable changes in the plots. Nevertheless, it is worth noting that a positive in-phase actuation increased the net resultant impact force, Figure 9.4, and resulted in higher peak displacement, Figure 9.6. A negative in-phase actuation was found to reduce the peak resultant impact force, Figure 9.4, and gave a lower peak displacement, Figure 9.6. The net peak impact force under zero actuation was 1388N and gave a peak displacement of 4.813mm. Under the positive in-phase actuation the impact force was increased to 1398N with a peak displacement of 4.851mm. The total reduction due to negative in-phase actuation was 11N (0.79%) for the peak impact force and 0.03mm (0.62%) for the peak displacement. Although the in-phase

actuations affected the peak impact force and displacement histories, these were observed to be very small.

An interesting development was observed when out-of-phase voltages were applied to the actuator pair where higher differences in the peak resultant impact force and displacement were noticed. Inducing an upward bending was found to lower the peak resultant impact force by almost 46N, Figure 9.5. This was about 3.31% reduction from the zero actuation case. Consequently, the reduction in the peak impact force lowered the peak displacement to 4.688mm, which was about 2.60% reduction compared to the one achieved with negative in-phase actuation, Figure 9.7.

On the contrary, inducing a downward bending increased the peak resultant impact force to 1451N (4.54%), Figure 9.5, the highest in comparison to all the other cases and correspondingly gave the highest bending deformation which was 4.964mm (3.14%), Figure 9.7. The piezoelectric control actions also affected the contact period. As can be seen from Figure A.2, the laminate under negative bending actuation came into contact with the impactor earlier than the other impact cases, while, the laminate undergoing positive bending actuation was the last to come into contact.

The changes in the impact force and displacement history curves could be explained using Equation (5-43). Neglecting the sensor term, Equation (5-43) can be rewritten as:

$$[M_u]\{\ddot{X}\} + [K_{uu}]\{X\} = \{F_m\} + [K_{ua}]\{\mathcal{V}_a\} \tag{9-1}$$

The last term appearing in Equation (9-1) is the force produced by the piezoelectric actuation and it is simply the product between the voltage and the piezoelectric coupling stiffness. Applying a positive voltage to the top actuator and a negative voltage to the bottom actuator produced a negative moment that deformed the laminate in an upward direction. The net piezoelectric force due to this action acted in the opposite direction to the incoming impact force, which in this case was F_m. The addition of the piezoelectric forces and the impact force reduced the net resultant impact force acting on the laminate. The reduction in the impact force eventually lowered the peak displacement.

The opposite phenomenon occurred when a positive bending actuation was applied. Applying a negative voltage to the top actuator and a positive voltage to the bottom actuator produced a positive moment that deformed the laminate in the downward direction. The net piezoelectric force in this case acted in the same direction of the impact force. This increased

the net resultant force acting on the laminate and consequently produced a higher peak displacement.

Although Equation (3-6) is not directly applicable for the laminate-actuator configuration considered in this section, the in-phase actuation will tend to regulate the contact stiffness at the contact region according to the applied voltages. In this example, a negative in-phase actuation was found to reduce the peak impact force. On the contrary a positive in-phase actuation increased the contact force. However, regulating the contact stiffness was found to be less effective in comparison to applying a counter moment to reduce the impact force.

Hence, in the case of simply supported laminate, inducing a negative moment could be seen to be more effective in reducing the impact force and the displacement compared to the other actuation techniques.

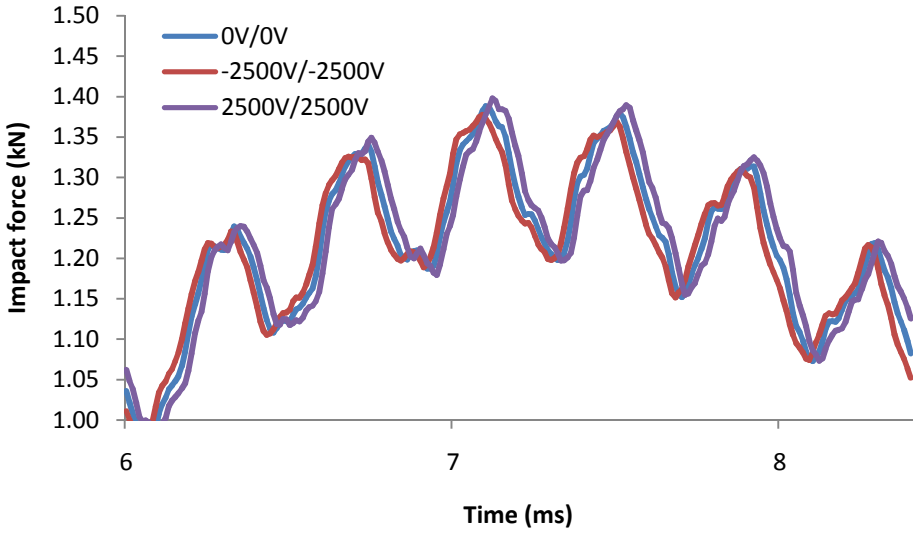


Figure 9.4: Force-time plot for *SS* cross-ply laminate: 2.0J impact – in-phase actuation

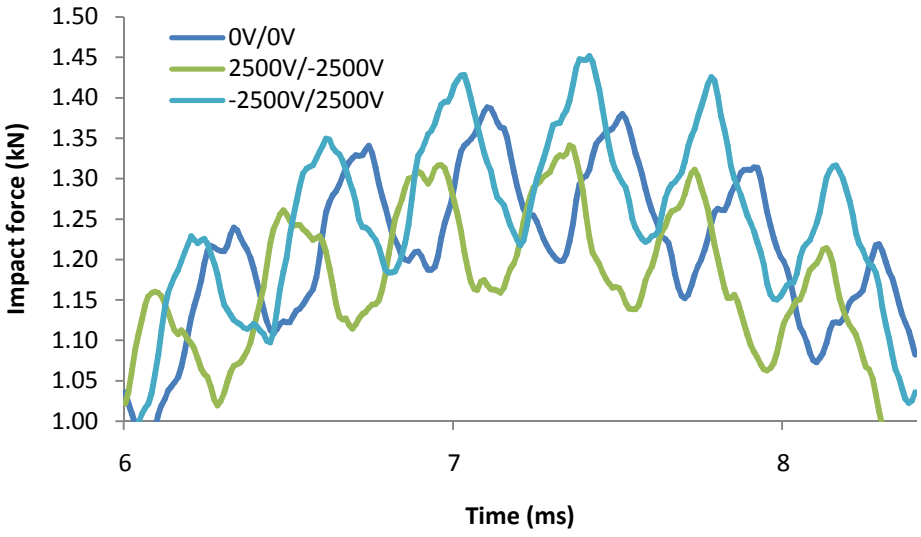


Figure 9.5: Force-time plot for *SS* cross-ply laminate: 2.0J impact – out-of-phase actuation

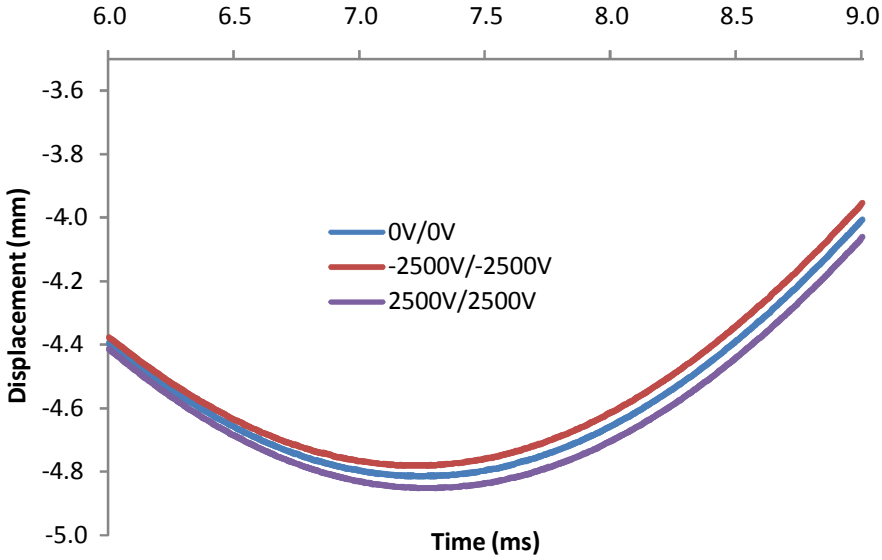


Figure 9.6: Displacement-time plot for *SS* cross-ply laminate: 2.0J impact – in-phase actuation

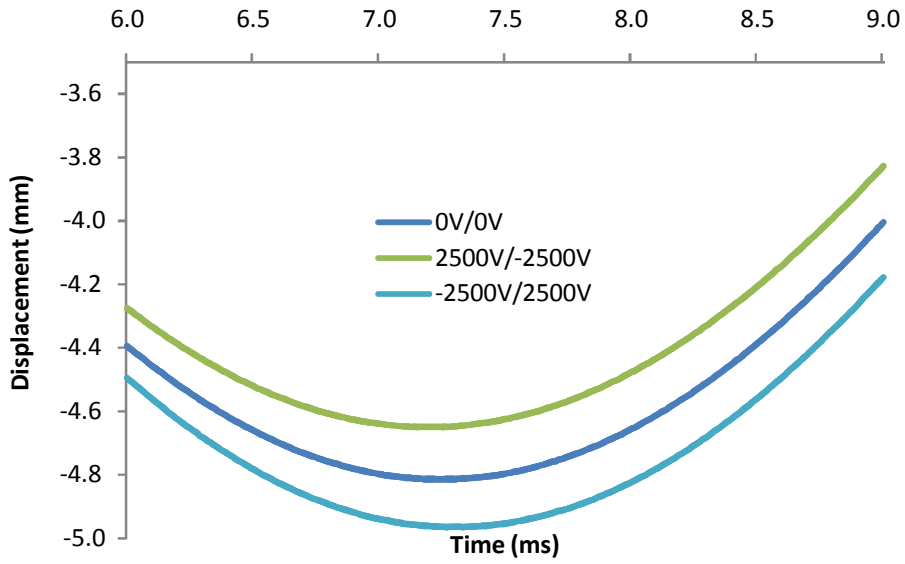


Figure 9.7: Displacement-time plot for *SS* cross-ply laminate: 2.0J impact – out-of-phase actuation

9.3.3 Effects piezoelectric actuations – 2.5J impact

The effects of different piezoelectric control actions on the impact response of simply supported cross-ply laminate for 2.5J impact case are demonstrated through Figures 9.8 to 9.11. The full impact force and displacement history curves are given in Appendix A.

Similar to the previous example, the impact forces and displacements were shown to be affected by the different piezoelectric control actions. Under zero actuation the peak impact force was 1653N and the peak displacement was 5.169mm. As previously observed the in-phase actuations seemed to have very minimal effect on the impact force and displacement histories, Figure 9.8. The peak impact force under positive and negative in-phase actuations were 1658N and 1655N respectively, Figure 9.8. Correspondingly, the peak displacements were 5.205mm for the positive in-phase actuation and 5.136mm for the negative in-phase actuation, Figure 9.10. However, it was observed that the negative in-phase actuation resulted in slightly higher impact force in comparison to zero actuation case contradicting the observation made in Section 9.3.2.

A comparison between the out-of-phase actuations found that the negative bending actuation resulted in the maximum reduction of the impact force, Figure 9.9. However, unlike the observation made in Section 9.3.2, the positive bending actuation resulted in a slightly lower peak impact force in comparison to the zero actuation case instead of giving the

maximum value. The peak impact force under negative bending actuation was 1589N and this was 1649N with the positive bending actuation, Figure 9.9. With respect to peak displacement the lowest was achieved using a negative bending actuation which was 5.019mm and the maximum being with positive bending actuation at 5.311mm, Figure 9.11.

Though some inconsistencies were observed with respect to negative in-phase and positive bending actuations, in the case of simply supported laminate, it can be concluded that the negative bending moment could be used to produce higher differences both in the peak impact force and displacement in comparison to all the other actuation methods.

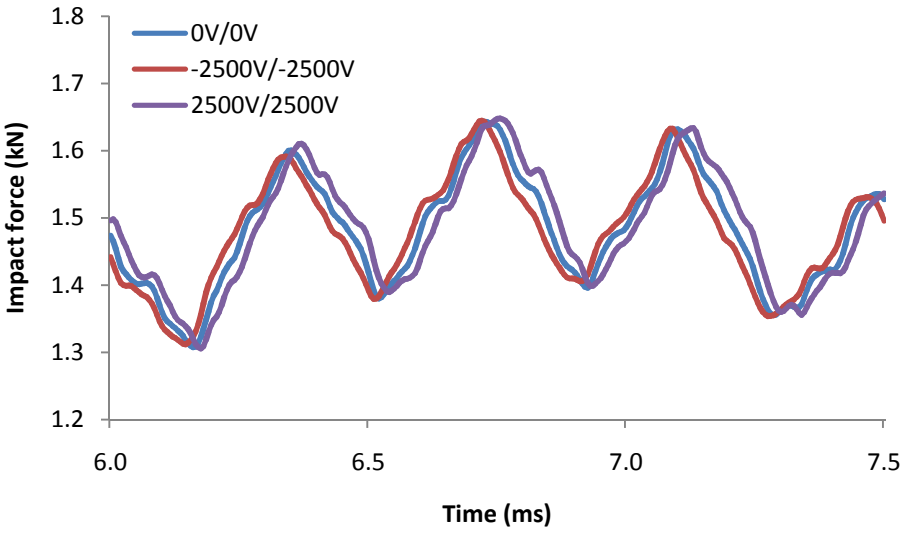


Figure 9.8: Force-time plot for *SS* cross-ply laminate: 2.5J impact – in-phase actuation

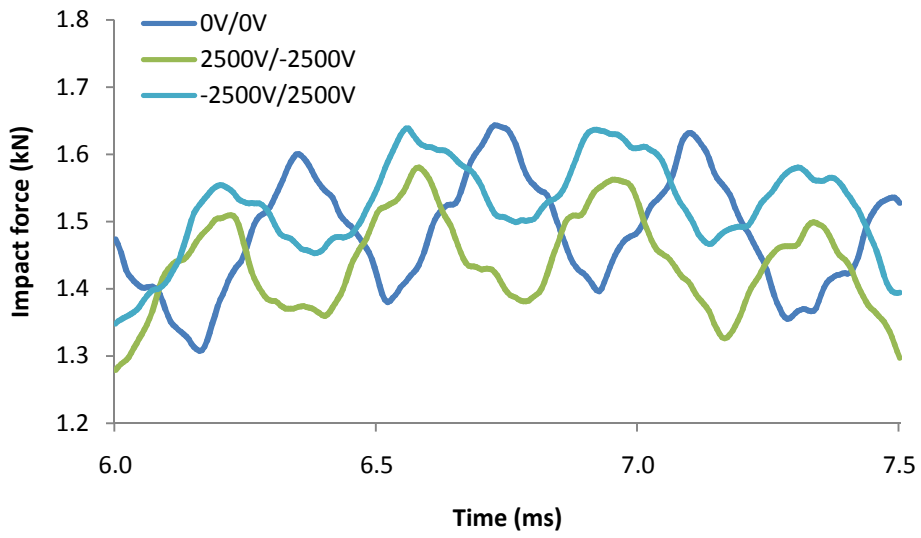


Figure 9.9: Force-time plot for *SS* cross-ply laminate: 2.5J impact – out-of-phase actuation

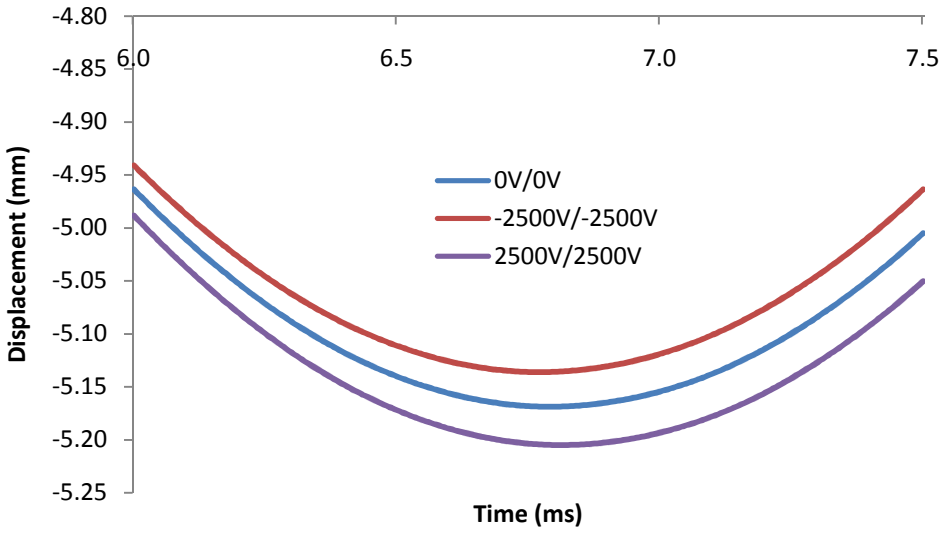


Figure 9.10: Displacement-time plot for *SS* cross-ply laminate: 2.5J impact – in-phase actuation

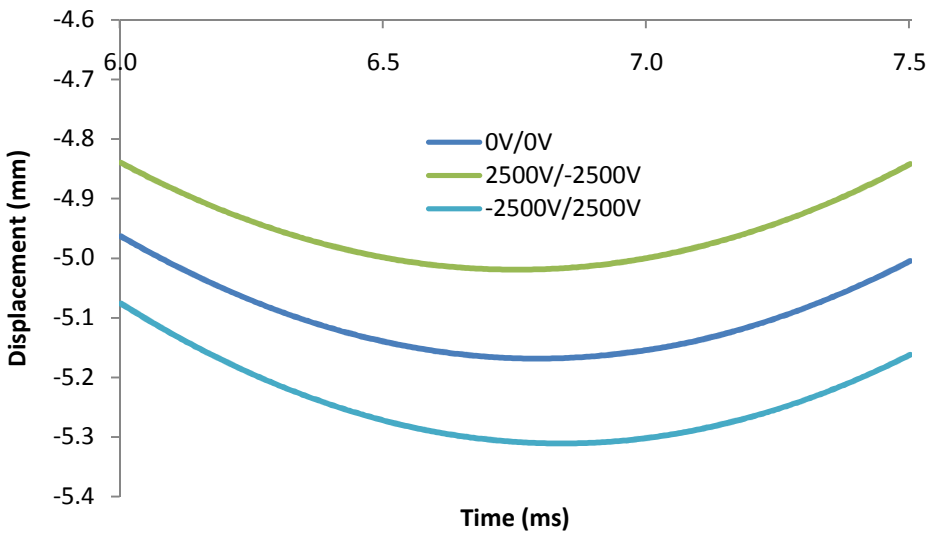


Figure 9.11: Displacement-time plot for *SS* cross-ply laminate: 2.5J impact – out-of-phase actuation

9.3.4 Effects of electrical loading rates on peak impact force and displacement

It was noted in Sections 9.3.2 and 9.3.3 that the reduction in the peak resultant impact force was higher in the case of the 2.5J impact as compared to the 2.0J impact case. On the contrary, it was observed that the difference in the peak displacement was higher for the 2.0J impact case. For the 2.5J impact the reduction in the peak resultant impact force was about 64N (3.82%) and this was 46N (3.39%) in the 2.0J impact case.

As for the displacement, the reduction in the peak displacement for the 2.0J impact was about 0.17mm (3.42%) compared to 0.15mm (2.89%) achieved in the 2.5J impact case. In order to investigate such a development, additional simulations were carried out with different impact energy levels using electrical loading rates of 1ms and 4ms based on the negative bending actuation technique. Figure 9.12 shows the peak resultant impact force-impact energy plots based on the 1ms loading rate.

From Figure 9.12 it can be seen that there were instances for which the peak impact forces under bending actuation were higher compared to when no actuation was applied and this seemed to contradict the findings reported in sections 9.3.2 and 9.3.3. This can be seen to occur at impact energies of 2.0J, 3.5J and 4.0J. For the remaining cases the peak impact forces under the negative bending actuation were shown to be lower in comparison the zero

actuation cases. The peak displacement-impact energy plot is shown in Figure 9.13 for 1ms loading rate. The figure showed that the displacement plots did not confirm to the impact force plots shown in Figure 9.12. By deduction it was anticipated that the displacement would exhibit a similar trend as the impact force plot.

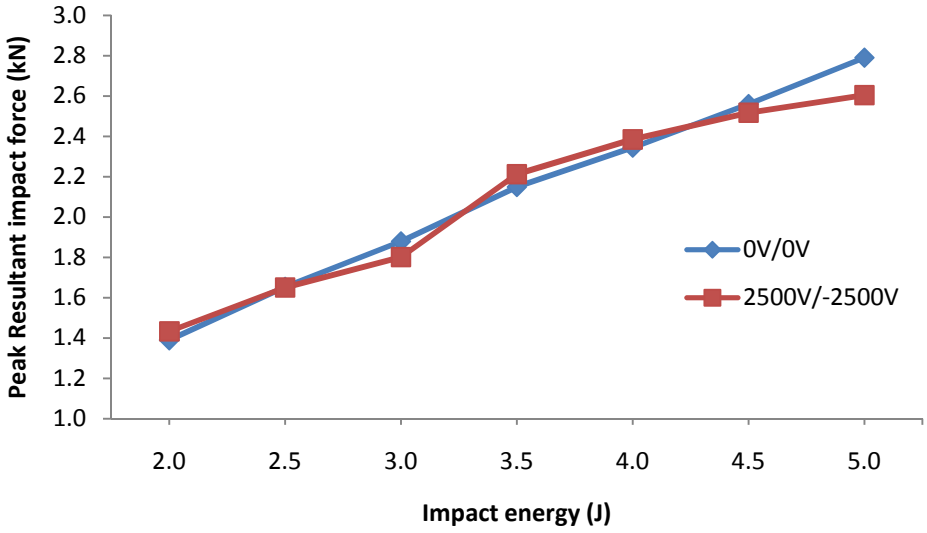


Figure 9.12: Force-impact energy plot for *SS* cross-ply laminate - negative bending actuation, 1ms loading rate

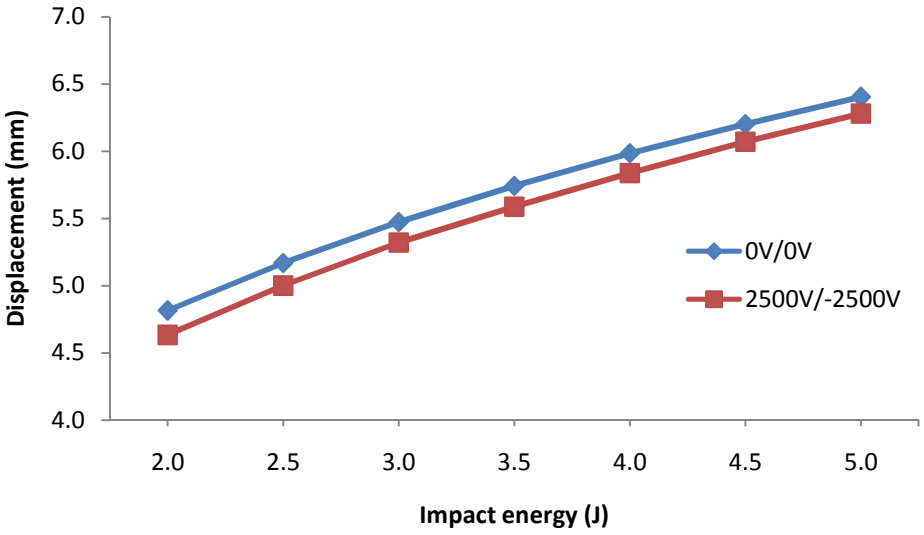


Figure 9.13: Displacement-impact energy plot for *SS* cross-ply laminate - negative bending actuation, 1ms loading rate

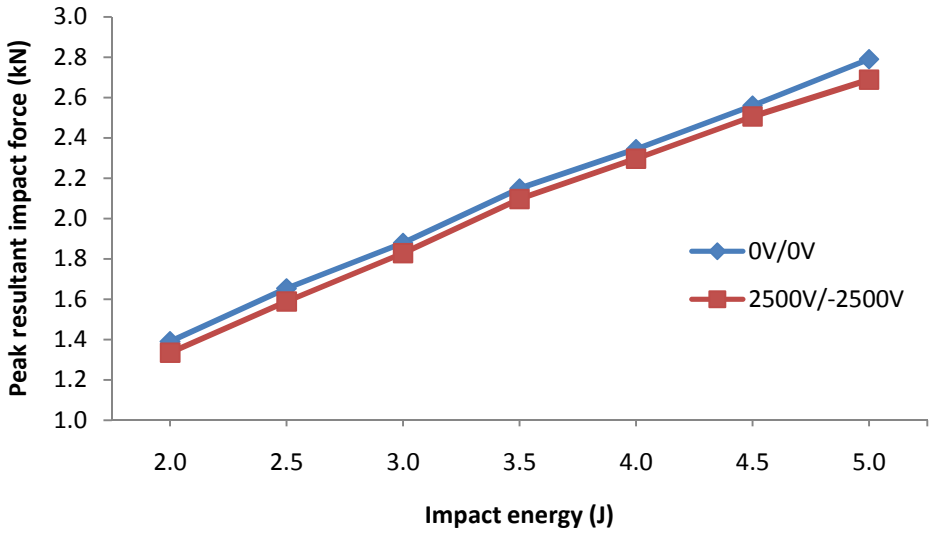


Figure 9.14: Impact force-impact energy plot for *SS* cross-ply laminate - negative bending actuation, 4ms loading rate

In the subsequent investigation the electrical loading rate was increased to 4ms and Figure 9.14 shows the peak resultant impact force-impact energy plots for this case. In this figure, unlike Figure 9.12, the peak resultant impact forces under actuation were lower compared to the peak impact forces when no actuation was applied for all the impact energy levels. The corresponding peak displacement-impact energy plots are shown in Figure 9.15 which agreed to the impact force plots shown in Figure 9.14. These analyses showed that the loading rate had more effect on the impact force as compared to the displacement.

To investigate the effects of the loading rate on the impact force, the displacement plots for impact energies of 2.0J and 2.5J are shown in Figures 9.16 and 9.17 respectively up to few microseconds after the physical contact has taken place for electrical loading rates of 1ms, 2ms and 4ms. The figures showed that the amplitudes of the displacements prior to contact became higher as the loading rate was reduced. Although the average actuation displacement remained the same for all the three cases, the dynamic effect of the lower loading rate was reflected on the impact force during the contact. Shorter loading rate resulted in higher contact displacements hence increased the net resultant impact force.

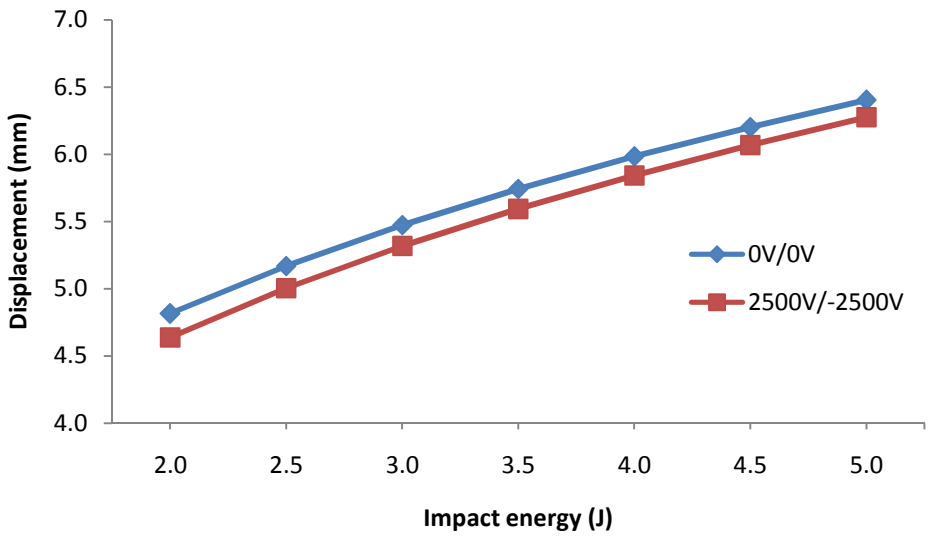


Figure 9.15: Displacement-impact energy plot for *SS* cross-ply laminate - negative bending actuation, 4ms loading rate

However, it was also found that the impact force was not only affected by the amplitude of the displacement prior to contact but also by the instant at which the plate came into contact with the impactor. As an example, Figure 9.18 shows the peak resultant impact forces for the 2.0J and 2.5J impact cases at different loading rates. For the 2.0J impact, the peak resultant impact force was lowest using the 2ms loading rate whereas for the 2.5J impact case the peak resultant impact force was lowest using the 4ms loading rate.

In Figure 9.16, for the 2.0J impact case, the instances of contact for the 1ms and 4ms loading rates occurred during the ascending portion of the displacement, while, for the 2ms loading the contact took place during the descending portion. In Figure 9.17, for the 2.5J impact case, the instances of contact for the 1ms and 2ms actuation cases happened during the ascending portion of the displacement, while, for the 4ms actuation the contact happened during the descending portion. This showed that apart from the loading rate, the instance of contact also affected the peak impact force. It is believed that the instance at which the plate interacts with the impactor could have affected the stress distributions at the contact region and subsequently the impact force.

The effect of electrical loading rate and contact instances could also be the sources for the inconsistencies observed with respect to negative in-phase and positive bending actuations reported in Section 9.3.3. However, a separate investigation into such behaviour was not carried out considering that these types of control actions did not substantially reduce the contact force.

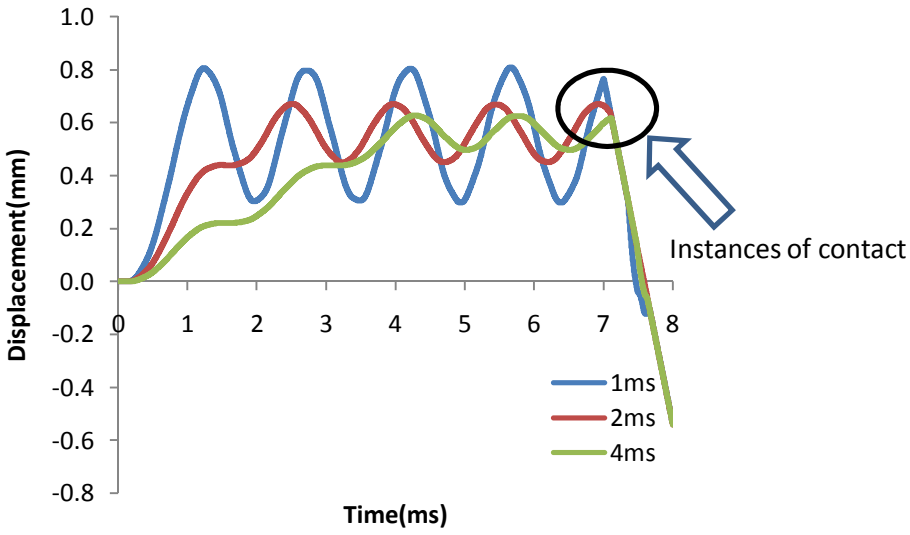


Figure 9.16: Close view of displacement-time plot for *SS* cross-ply laminate - negative bending actuation - 2.0J impact

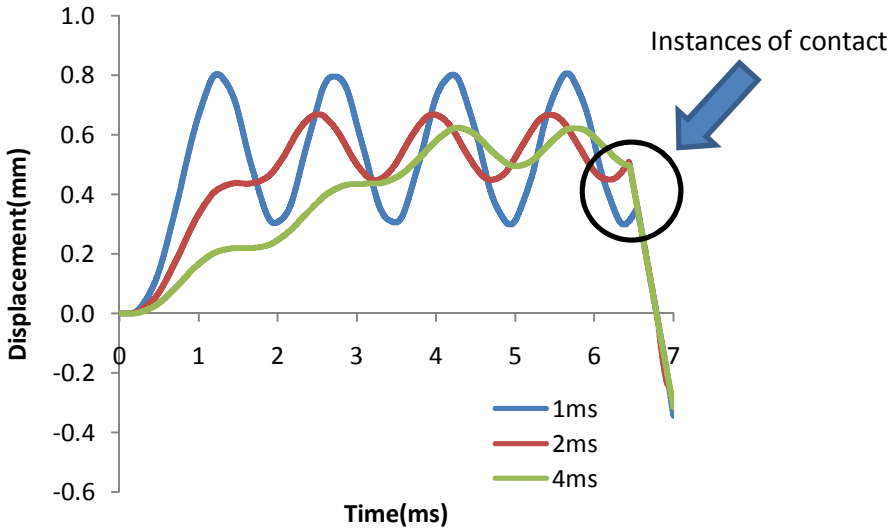


Figure 9.17: Close view of displacement-time plot for *SS* cross-ply laminate - negative bending actuation - 2.5J impact

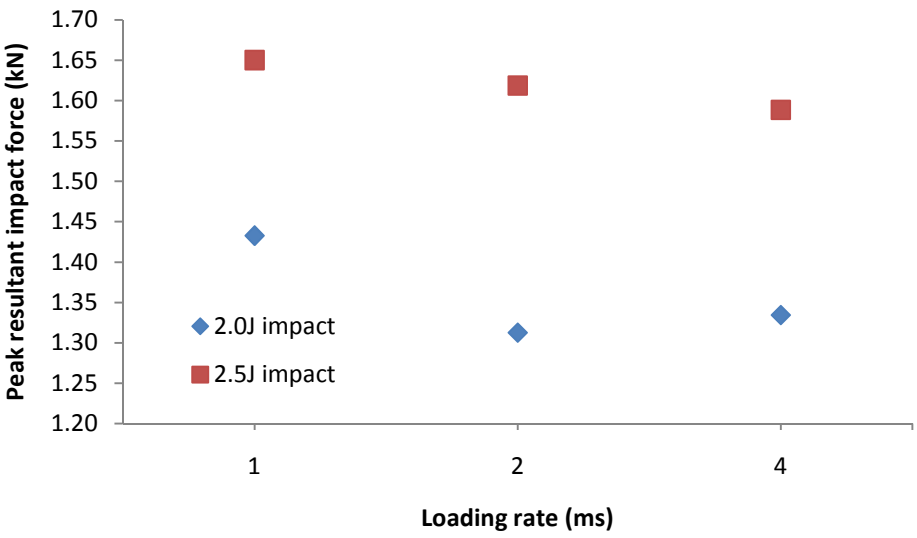


Figure 9.18: Impact force-time plot for *SS* cross-ply laminate - negative bending actuation

9.4 Impact response of clamped cross-ply laminate

The second investigation involved examining the effects of different piezoelectric control actions on the impact response of a clamped cross-ply laminate. Two different impact energy levels were considered, i.e., 1.0J and 2.5J based on four different types of control actions, i.e., positive in-phase actuation, negative in-phase actuation, negative bending actuation and positive bending actuation. As had been shown in Chapter 7, clamped laminates adversely reduced the effect of piezoelectric actuation on them hence extreme cases were selected for the purpose of discussion.

9.4.1 Effects of different impact energy levels

The effects of different impact energy levels on the impact response of clamped cross-ply laminate are presented in Figures 9.19 and 9.20 when no actuation was applied. As in the case of the simply supported laminate, the impact forces were found to increase with increasing impact energy levels, Figure 9.19, and resulted in higher peak displacement, Figure 9.20.

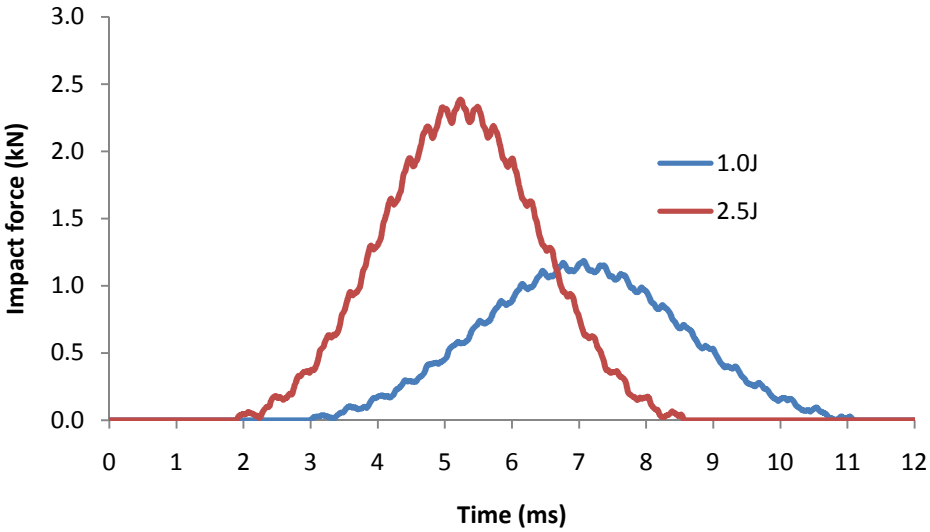


Figure 9.19: Force-time plot for *CC* cross-ply laminate – zero actuation

However, for the same impact energy level clamped laminate resulted in higher peak impact force but lower displacement as compared to the simply supported laminate. This can be seen from the 2.5J impact case. The peak impact force in the case of simply supported laminate was 1653N and this was 2398N in the clamped case, an increase of 45.07%. The displacement under clamped condition was reduced by 31.55% in comparison to the simply supported case. This was due to the membrane effect which stiffened the laminate. Since elastic impact was considered, the impact force before and after the peak load exhibited symmetric behaviour indicating no degradation in the laminate stiffness.

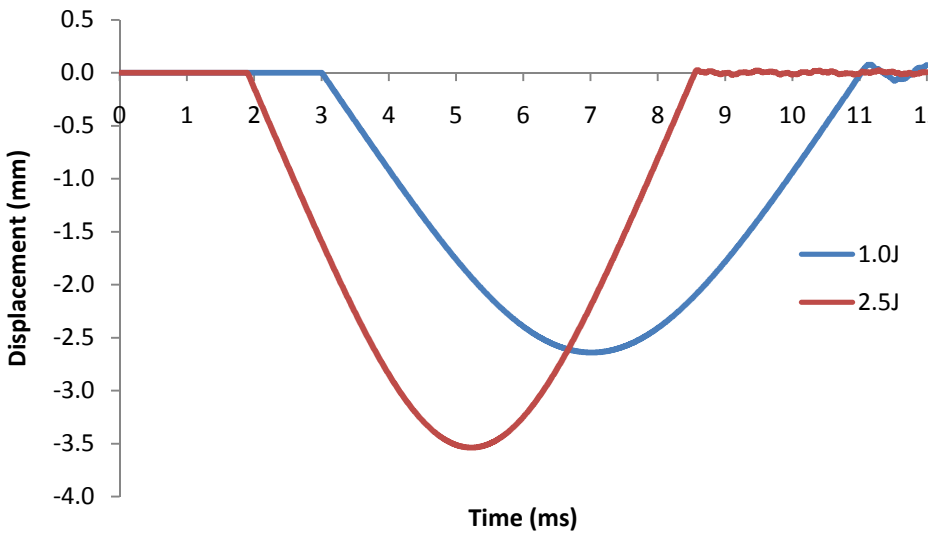


Figure 9.20: Displacement-time plot for *CC* cross-ply laminate – zero actuation

9.4.2 Effects piezoelectric actuations – 1.0J impact

The effects of different piezoelectric control actions on the impact response of clamped cross-ply laminate for the 1.0J impact case are demonstrated through Figures 9.21 to 9.24 for the peak impact forces and displacements. Similar to the responses seen in the simply supported laminates, the peak resultant impact forces of clamped laminate were also found to have been affected by the different piezoelectric control actions. However, unlike in the case of the simply supported laminate, the lowest peak resultant impact force was achieved by applying a negative in-phase actuation voltage, Figure 9.21. In the same figure, a negative bending actuation was also shown to lower the peak resultant impact force. On the other hand, a positive in-phase actuation was found to give the maximum peak resultant impact force followed by positive bending actuation, Figure 9.22.

The displacement plots were found to match the peak impact force curves with minimum plate deformation achieved using negative in-phase actuation and maximum being achieved with positive in-phase actuation, Figures 9.23 and 9.24 respectively. However, neither the force nor the displacement plots showed a significant reduction in either the impact force or the displacement as in the case of simply supported laminate. In the case of zero actuation the peak impact force was 1183N with a peak displacement of 2.643mm. The lowest peak impact force and displacement achieved were 1172N (0.92%) and 2.596mm (1.78%) respectively.

This was expected since the clamped support had already been found to reduce the piezoelectric effects substantially.

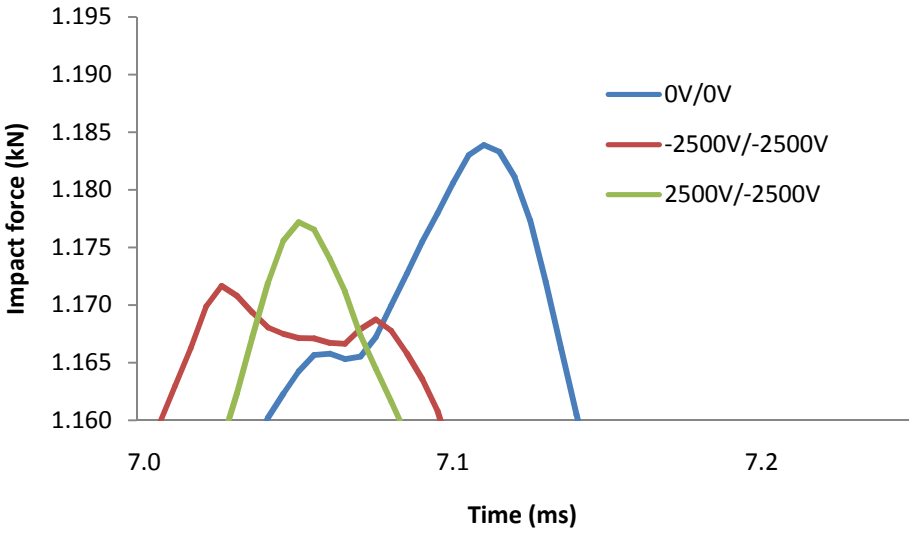


Figure 9.21: Impact force-time plot for *CC* cross-ply laminate: 1.0J impact – negative in-phase and negative bending actuations

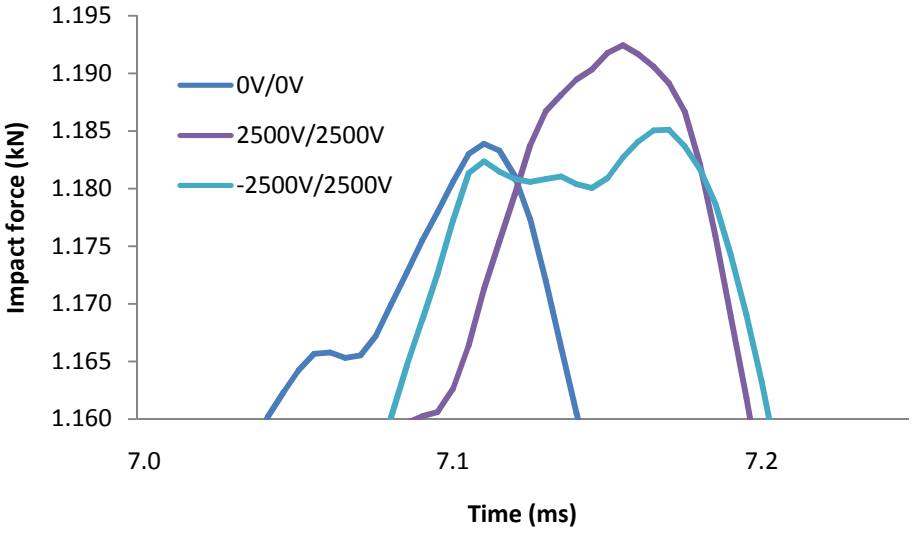


Figure 9.22: Force-time plot for *CC* cross-ply laminate: 1.0J impact – positive in-phase and positive bending actuations

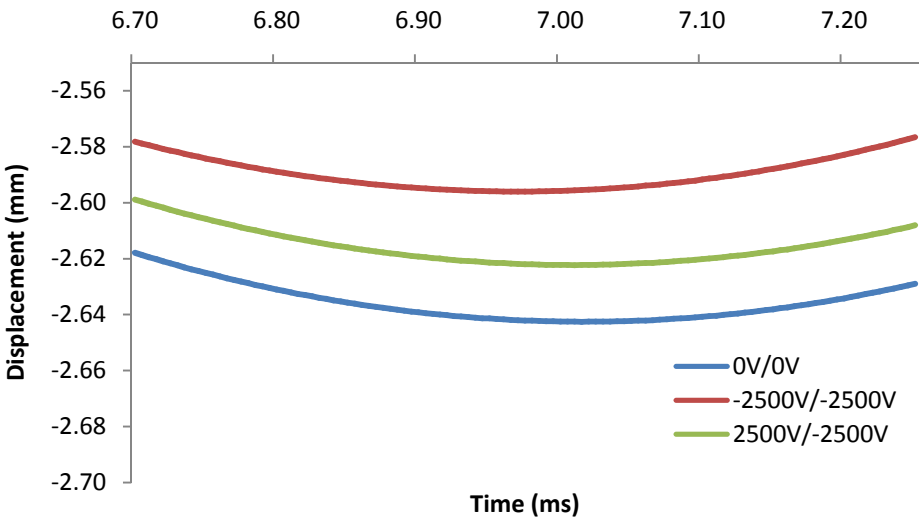


Figure 9.23: Displacement-time plot for *CC* cross-ply laminate: 1.0J impact – negative in-phase and negative bending actuations

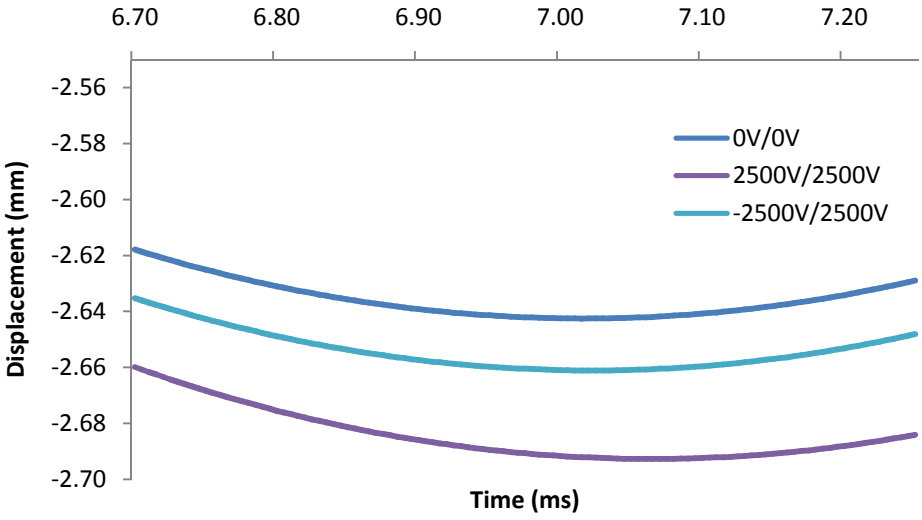


Figure 9.24: Displacement-time plot for *CC* cross-ply laminate: 1.0J impact – positive in-phase and positive bending actuations

9.4.3 Effects of piezoelectric actuations – 2.5J impact

The effects of different piezoelectric control actions on the impact response of the clamped cross-ply laminate for the 2.5J impact case are demonstrated through Figures 9.25 to 9.28 for the peak impact forces and displacements. Similar to the 1.0J impact case the lowest peak resultant impact force was achieved by applying a negative in-phase actuation, Figure 9.25, while, a positive in-phase actuation was found to give the maximum peak resultant impact force, Figure 9.26.

The displacement plots were found to correspond to the peak impact force plots with minimum plate deformation achieved using negative in-phase actuation, Figure 9.27, and maximum being achieved at positive in-phase actuation, Figure 9.28. However, the reductions in the peak resultant impact force and displacement were barely significant. In this particular example the difference in the peak resultant impact force was less than 0.75% and the difference in the peak displacement was just over 1.18%.

Nevertheless, it can be concluded that the negative in-phase actuation could be used to produce higher differences both in the peak impact force and displacement in comparison to all the other actuation methods in the case of clamped laminates.

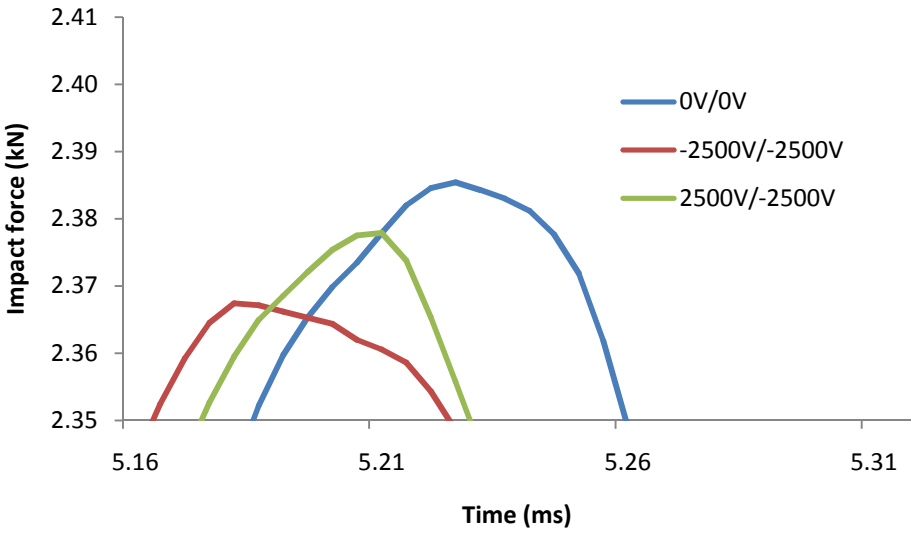


Figure 9.25: Force-time plot for *CC* cross-ply laminate: 2.5J impact – negative in-phase and negative bending actuations

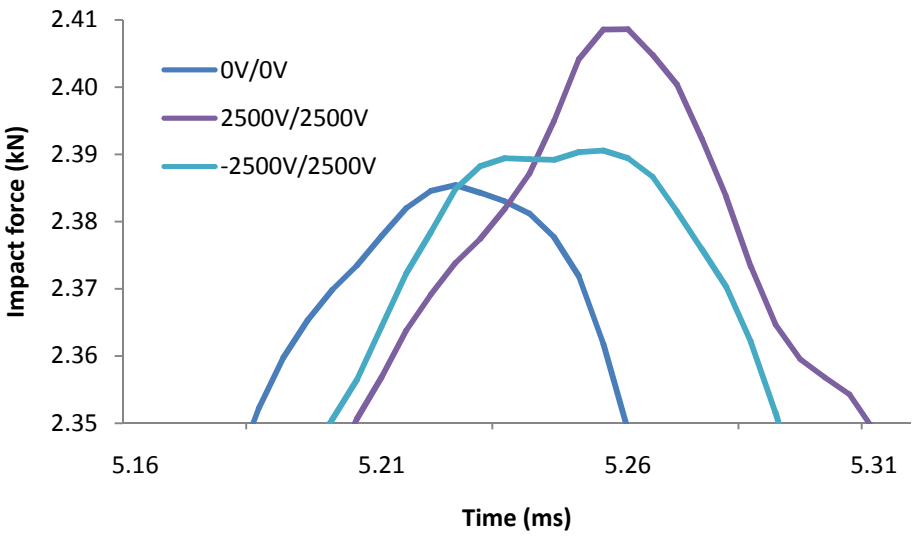


Figure 9.26: Impact force-time plot for *CC* cross-ply laminate: 2.5J impact – positive in-phase and positive bending actuations

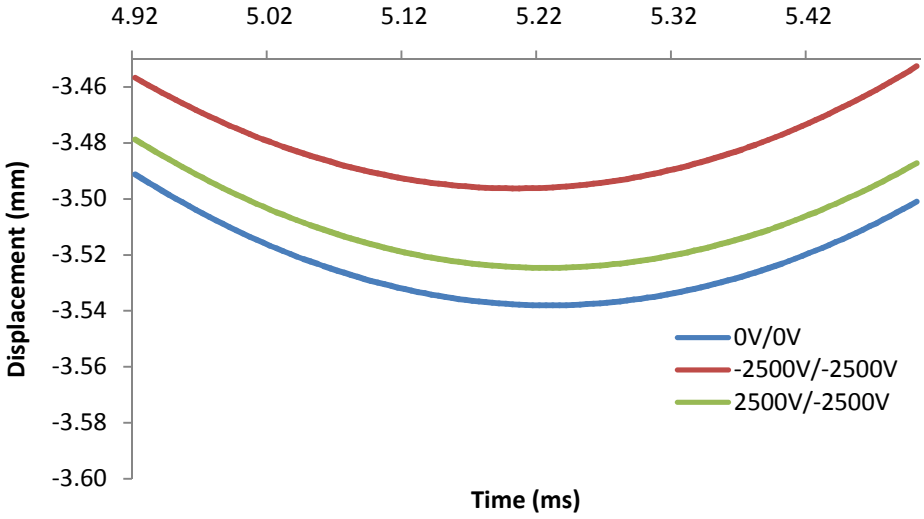


Figure 9.27: Displacement-time plot for *CC* cross-ply laminate: 2.5J impact – negative in-phase and negative bending actuations

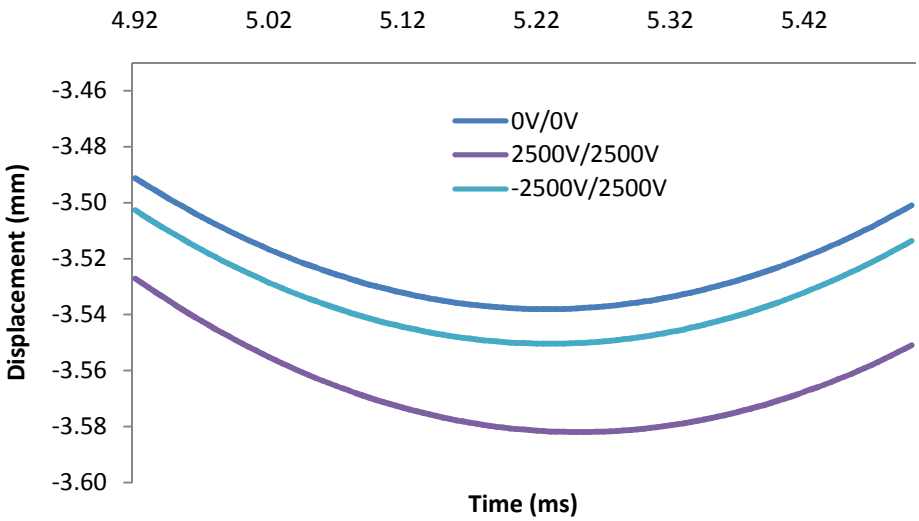


Figure 9.28: Displacement-time plot for *CC* cross-ply laminate: 2.5J impact – positive in-phase and positive bending actuations

9.5 Chapter summary

Some selected impact test cases have been presented in this chapter to highlight the effects of piezoelectric control actions on the impact force and displacement histories. It was found that the piezoelectric control actions can be used to regulate the peak impact force and displacement, however, this was found to be influenced by the boundary conditions. In the case of the simply supported laminate the peak impact force and the displacement could be reduced by inducing a counter moment to the incoming impact load. The counter moment in this case acted by reducing the total impact force acting on the laminate. This consequently reduced the peak displacement as well. In the case of clamped laminates, the same was achieved using a negative in-phase actuation. However, clamped support was found to adversely reduce the effects of piezoelectric control actions on the laminates, hence there were no appreciable changes neither in the impact force nor the displacement histories.

The electrical loading rate was found to affect the peak impact force but not the displacement to the same extent. A shorter loading rate was found to set the plate into vibration with higher amplitude and consequently increased the peak impact force, whereas, a longer loading rate was found to reduce the dynamic effect and consequently the peak impact forces. The instance of contact during actuation was also found to affect the peak contact force.

The findings reported in this chapter are considered essential in order to demonstrate the concept of impact induced delamination control using piezoelectric actuators. This is because delamination initiation and growth depend on the impact load and an effective method to reduce this load could be the key to either reduce or prevent delamination from taking place. Nevertheless, in order to validate the concept no arbitrary laminates can be selected. This is because although the impact forces were seen to have been reduced, these changes were very small. Though Equation (2-8) was developed based on isotropic material condition, assuming the average flexural modulus E_D = 60GPa, G_{CII} = 0.97N/mm and v_{12} = 0.261, the delamination initiation load (threshold load) for the laminate-actuator system considered in the section can be estimated to be 740N. For the 2.5J impact the peak impact forces was 1653N and 2398N for the simply supported and clamped laminates respectively. Even at the maximum voltage used in the simulation the peak impact force could be only reduced to 1589N in the case of simply supported laminate. This was still far beyond the threshold force.

Hence it would be almost impossible to demonstrate the concept of impact induced delamination control using piezoelectric actuators if any arbitrary laminates and impact conditions were to be considered. Based on Equation (2-8) a thick laminate would have a higher delamination threshold force, for example a 2mm thick laminate would increase the threshold force to 2094N. However, it has already been demonstrated in Chapter 7 that thick laminates intensely reduced the piezoelectric effects. Hence the only possible choice to validate the concept is to consider a low impact energy level and a thin laminate.

Chapter 10

Effects of piezoelectric actuations on delamination due to low velocity impact

10.1 Chapter overview

The objective of this chapter is to investigate the potential use of piezoelectric actuator to reduce impact induced delamination based on the technique of force reduction demonstrated in Chapter 9. The investigations presented in this chapter were limited to thin laminates with simply supported edges. Since the investigations were performed on simply supported laminates, the negative bending actuation was used as this has been found to be the most effective method to reduce the impact force for this type of support in comparison to all the other control methods that have been considered previously.

Two impact energy levels have been used in the numerical studies, i.e., 1.0J and 2.0J. This was based on the findings reported in Chapter 9. Since the *MFC* have limited capabilities to reduce the peak impact force no arbitrary impact conditions can be selected as this would render demonstrating the concept of impact induced delamination control using piezoelectric actuators almost impossible. However, it is important to be mentioned that the narrowing to these two energy levels was only made after extensive amount of simulations were carried out using different impact conditions and control actions. The chapter highlights the effects of

negative bending actuation on the size of delamination, peak impact force and displacement as well as on delamination threshold force.

10.2 Numerical model

The test specimen used in the simulation consisted of a simply supported symmetric cross-ply laminate with a lamination sequence of ($p/0_2/c/90_2/90_2/c/0_2/p$). The letters *p* and *c* indicate the position of the piezoelectric and interface layers respectively. Based on the parametric study conducted in Chapter 7, the position of the actuators was set to *TYPE D*. The interface layers were included between plies with different fibre orientations.

For the material constitutive descriptions, the interface layer was modelled using *umat41v* while the composite and piezoelectric layers were modelled using *MAT-ORTHOTROPIC-ELASTIC* and *umat49* respectively. The dimension of the composite plate was $87.5\times65\times1mm^3$. Due to symmetry in boundary and loading conditions only a quarter-model was considered. The piezoelectric layer was an *MFC* actuator with an active dimension of $42.5\times24.5\times0.3mm^3$ for the quarter model.

The impactor was hemispherical steel with a radius of 6.25mm and a mass of 2.3kg. Table 8.3 lists the material properties of the composite and actuator material used in the numerical simulation. Mesh sizes of $0.25\times0.25\times0.25mm^3$, $0.25\times0.25\times0.3mm^3$ and $0.25\times0.25\times0.02mm^3$ were used to model the composite, piezoelectric and cohesive layers respectively. This resulted in a total of 169820 solid elements for the quarter model. Figures 10.1 and 10.2 show the different views of the finite element model used in the impact simulation.

The composite and piezoelectric layers were modelled using single integration solid element while the impactor was modelled using rigid solid element. Stiffness based hourglass control was used to limit the nonphysical energy in the system and *AUTOMATIC-SURFACE-TO-SURFACE* contact to define the impactor-plate interaction.

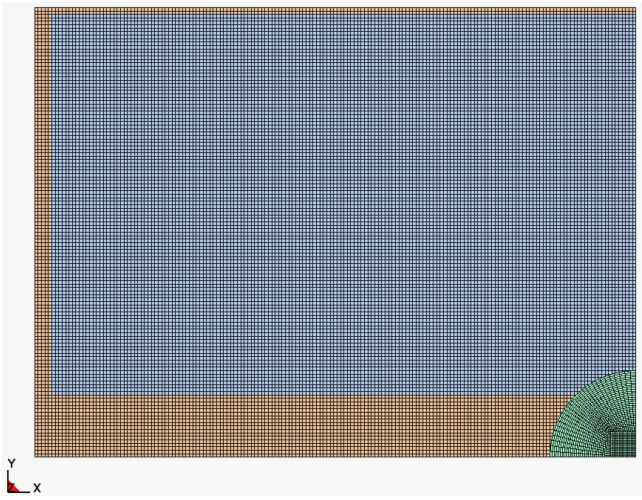


Figure 10.1: Finite element model of impact test specimen – top view

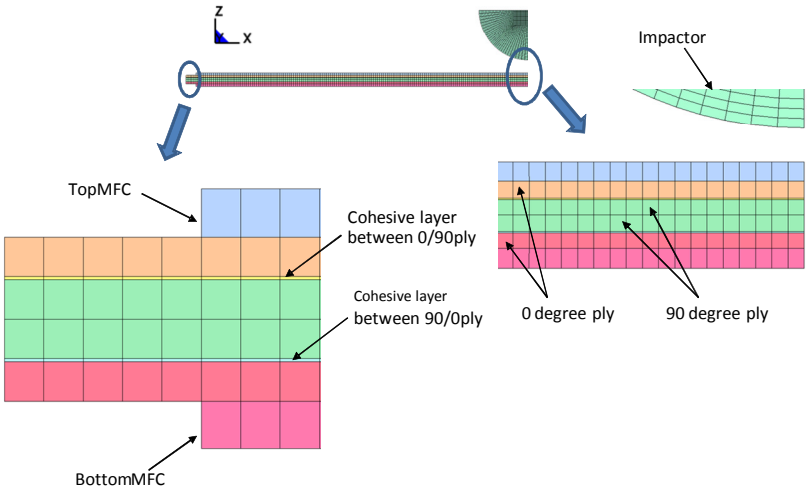
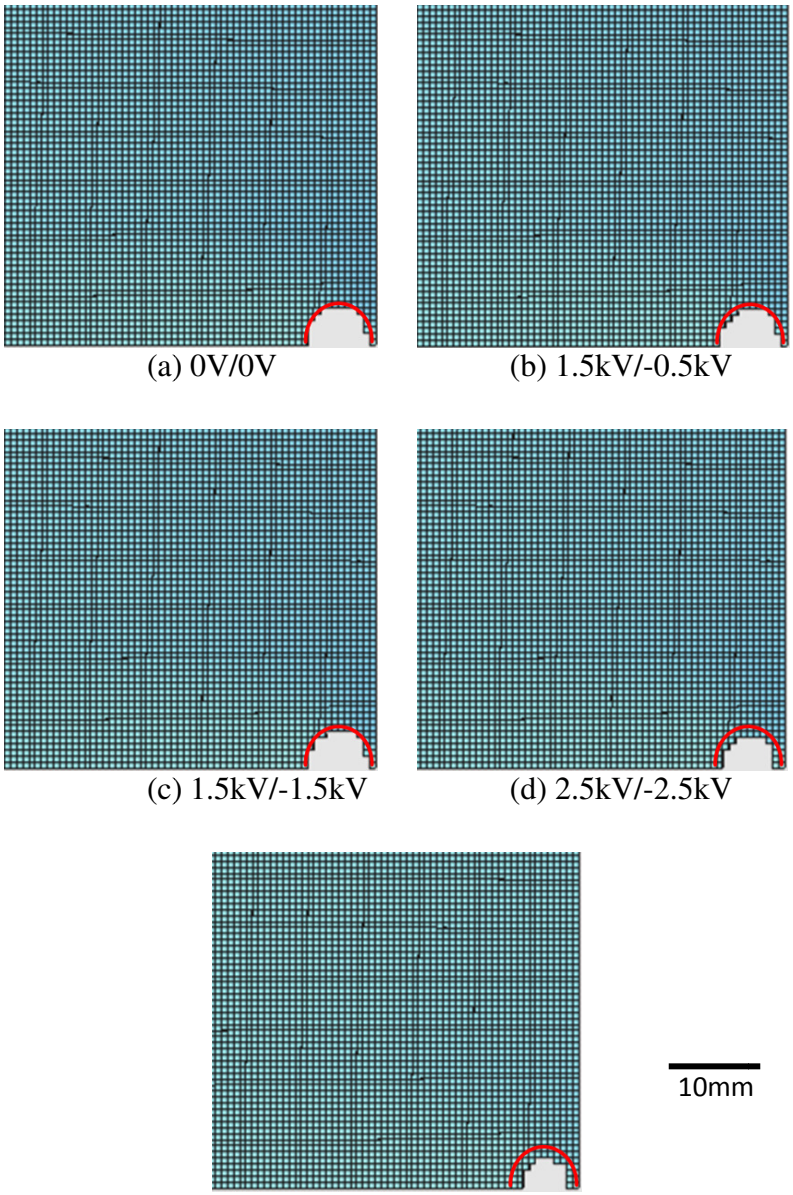


Figure 10.2: Finite element model of impact test specimen – detail view

10.3 Effects of piezoelectric actuations on delamination - 1.0J impact case

This section presents the numerical results obtained from the 1.0J impact test. This impact energy was selected as it resulted in peak impact force close to the delamination threshold load. The extent of delaminations predicted from the numerical simulations are shown in Figures 10.3 at the 90/0 interface for the quarter model. No traces of delamination were found at the 0/90 interface. Figure 10.3a shows the size of the delamination when no voltages were

applied to the actuator pair and represented as semi red circle in subsequent figures for comparison purpose.



(a) 0V/0V (b) 1.5kV/-0.5kV

(c) 1.5kV/-1.5kV (d) 2.5kV/-2.5kV

(e) 3.5kV/-3.5kV

Figure 10.3: Delamination at 90/0 interface for 1.0J impact case

Figure 10.3b shows the effect of negative bending actuation on the delamination size when the voltages to the actuator pair were restricted to its maximum and minimum values of 1.5kV and -0.5kV respectively. From this figure it can be seen that there was almost no reduction in the size of the delaminated area. Neither there was any noticeable change in the delamination size when the actuation voltages were increased to 1.5kV/-1.5kV, Figure 10.3c. However, as the voltages were increased further, in this case to 2.5kV/-2.5kV, the size of the delaminated zone reduced, Figure 10.3d. A further reduction in the delamination size was achieved when the actuation voltages were increased to 3.5kV/-3.5kV, Figure 10.3e.

Figure 10.4 shows the plot of the maximum peak resultant impact force against the actuation voltage. The figure shows that the peak resultant impact forces decreased with increasing actuation voltages. In this case the maximum impact force under zero actuation was 816N and this was reduced to 705N at voltages of 3.5kV/-3.5kV, a reduction of 13.6%.

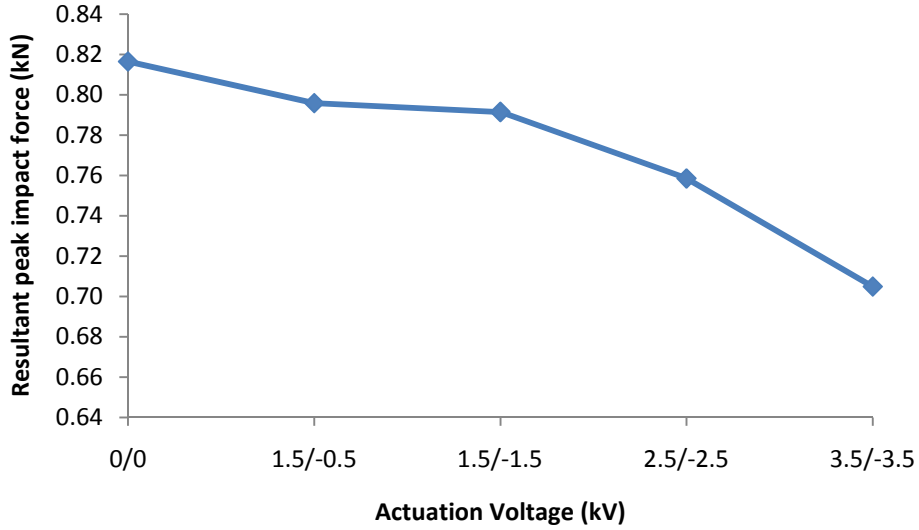


Figure 10.4: Force-actuation voltage plot – 1.0J impact

Corresponding to the reduction in the peak impact forces, Figure 10.5 shows that the peak displacements also reduced. In this particular example, at a maximum actuation voltage the reduction in displacement was about 0.49mm or 13.2%.

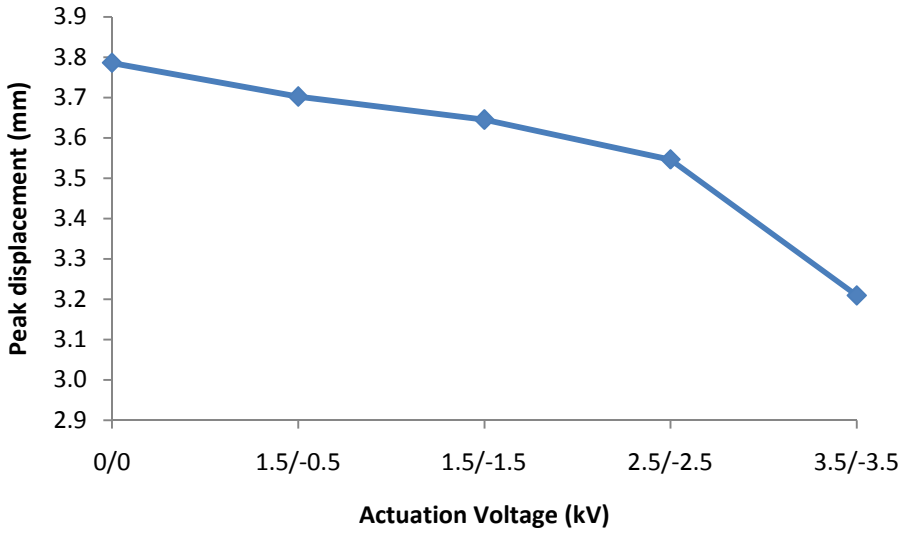


Figure 10.5: Peak displacement-actuation voltage plot – 1.0J impact

Figure 10.6 shows the delamination threshold forces at different actuation voltages. For each actuation case, the delamination threshold force was determined based on the force that corresponded to the first failed element. The analytical threshold force was previously calculated to be 740N. From Figure 10.6 the threshold force for delamination under zero actuation was estimated to be 650N. This could be considered to be a good match considering the simplifications assumed in the derivations of the analytical equation in addition to material parameters used in the equation to calculate the delamination threshold force.

The threshold forces were observed to drop as the actuation voltages were increased. This indicated that the delamination would initiate at much lower force as compared to when there was no actuation. However, the drop in the threshold forces was not as significant as the reduction in the peak impact forces. The reduction in the delamination threshold force was only 1.2% at maximum actuation voltage compared to the reduction of peak impact force at about 13.6%.

Figure 10.7 compares the delamination threshold force with the peak impact force and maximum force for complete delamination to occur. The maximum force for complete delamination to occur was determined based on the zero actuation case. In Figure 10.7 it can be seen that as the actuation voltages were increased, the peak impact forces were shifted closer to the threshold force levels. This explains the reduction in the delamination size for the 2.5kV/-2.5kV and 3.5kV/-3.5kV actuation cases. The peak impact forces for the 1.5kV/-0.5kV and 1.5kV/-1.5kV actuation cases remained close to the maximum delamination force

and hence this explains why there were no obvious reductions in the delamination size for these two actuation cases.

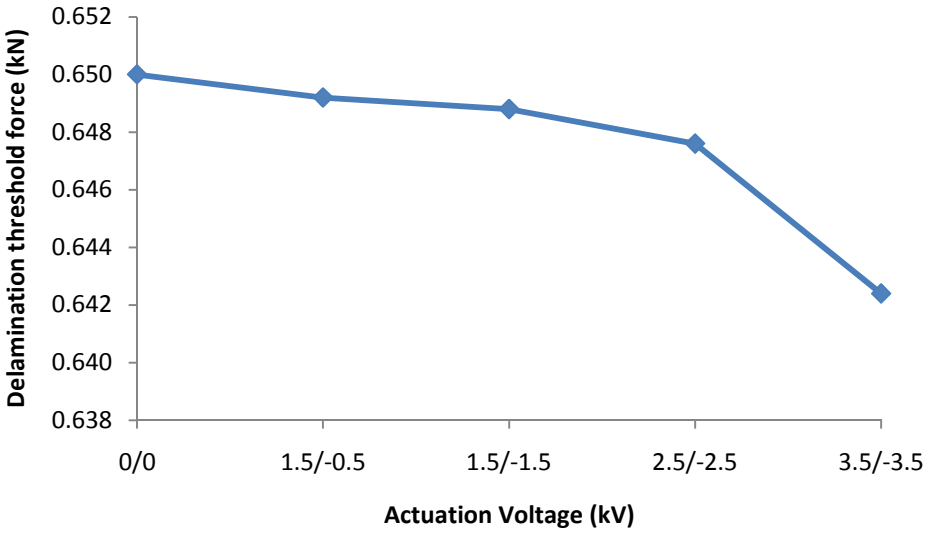


Figure 10.6: Delamination threshold force-actuation voltage plot – 1.0J impact

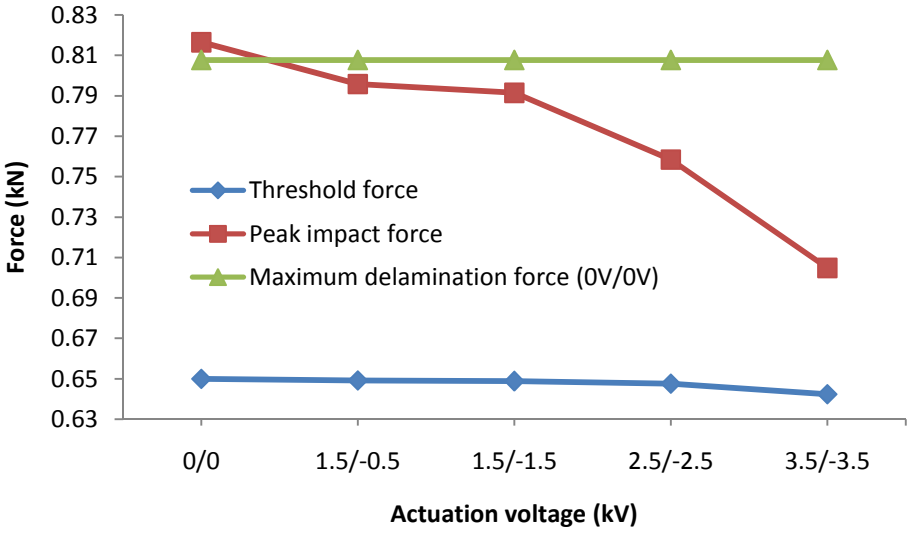


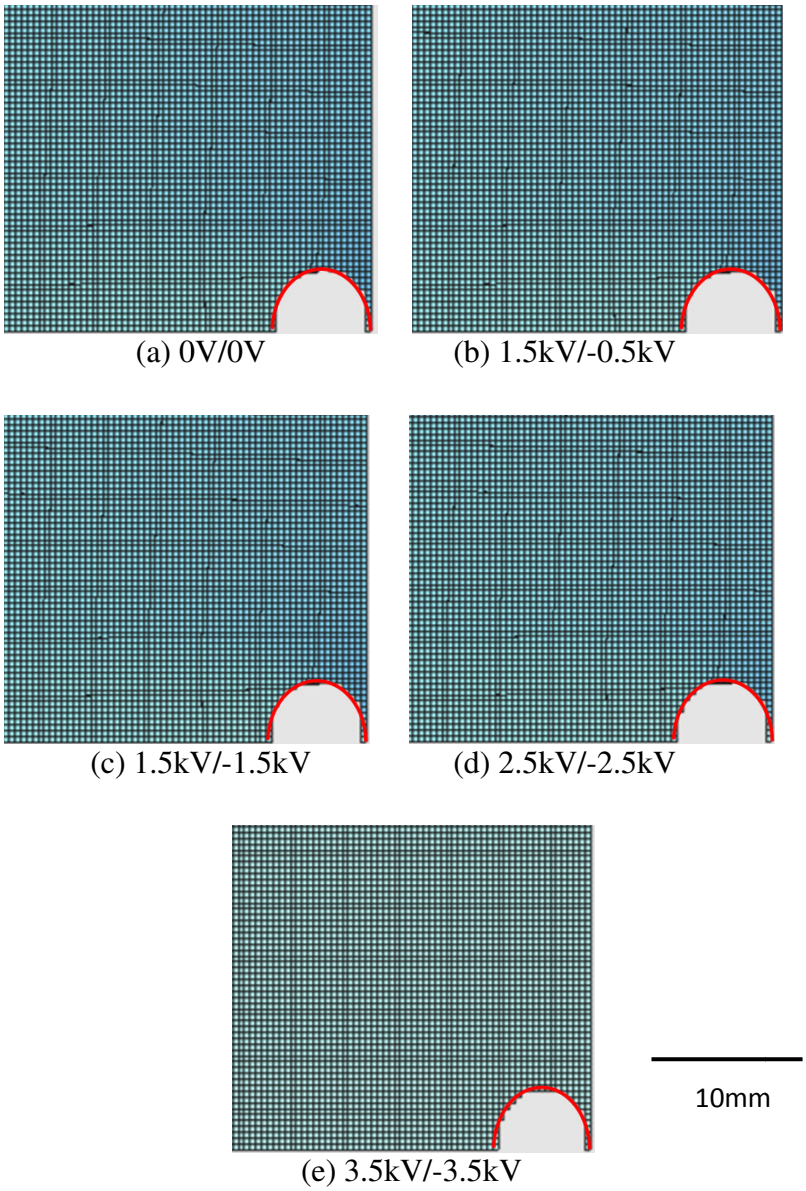
Figure 10.7: Force-actuation voltage plot – 1.0J impact

10.4 Effects of piezoelectric actuations on delamination - 2.0J impact case

This section presents the numerical results obtained from the 2.0J impact test. This energy level resulted in a peak impact force that was almost two times more than the delamination threshold force. The extent of delamination from the numerical simulations is shown in Figures 10.8 at the 90/0 ply interface for the quarter model. No traces of delamination were found at the 0/90 ply interface. Unlike in the case of 1.0J impact there was no reduction in the size of the delaminated zone even when the voltages were increased to 3.5kV/-3.5kV.

Figures 10.9 and 10.10 show the resultant peak impact forces and peak displacements for the 2.0J impact case respectively. As can be seen from the figures, both, the peak impact forces and the displacements decreased with increasing actuation voltages. The difference in the peak impact force at an actuation of 3.5kV/-3.5kV was about 7.9% whereas the reduction in the displacement was about 15.2%.

Figure 10.11 shows a comparison between the delamination threshold force, peak impact force and maximum force for complete delamination to occur. In this figure it can be seen that the peak impact forces under actuation reduced with increasing actuation voltages but this could be seen to be very marginal. In comparison to the threshold force, the peak impact force under actuation remained much closer to the maximum delamination force. Hence, this explained why there were no noticeable improvements in the size of the delamination. As was previously observed the delamination threshold force reduced with increasing actuation voltages. At maximum actuation the reduction was about 0.92%. This again could be seen to be very small in comparison with the drop in the peak impact force at about 7.9%.



(a) 0V/0V (b) 1.5kV/-0.5kV

(c) 1.5kV/-1.5kV (d) 2.5kV/-2.5kV

(e) 3.5kV/-3.5kV

Figure 10.8: Delamination at 90/0 interface for 2.0J impact

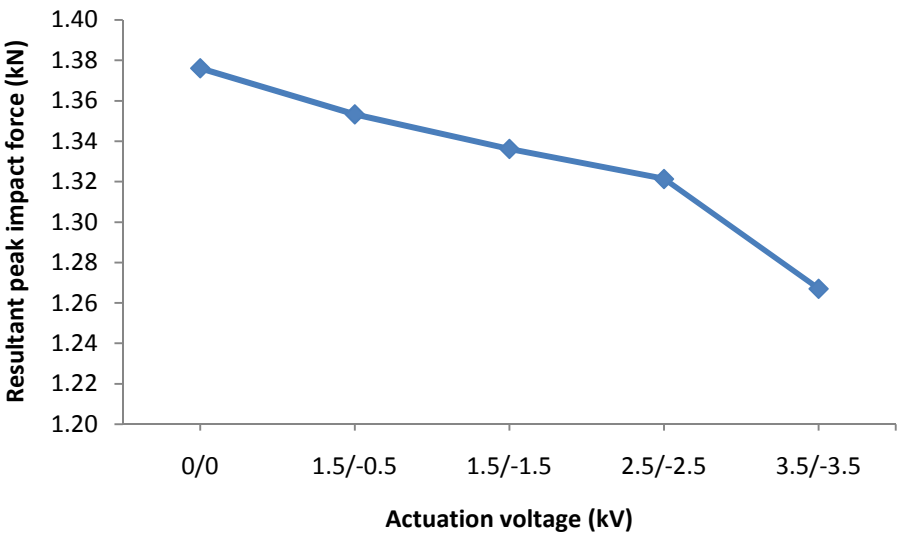


Figure 10.9: Force-actuation voltage plot – 2.0J impact

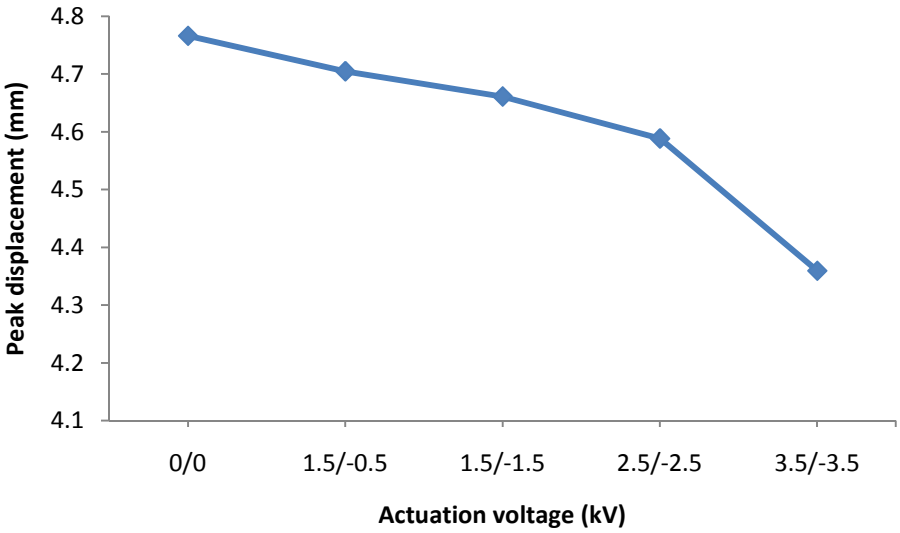


Figure 10.10: Displacement-actuation voltage plot – 2.0J impact

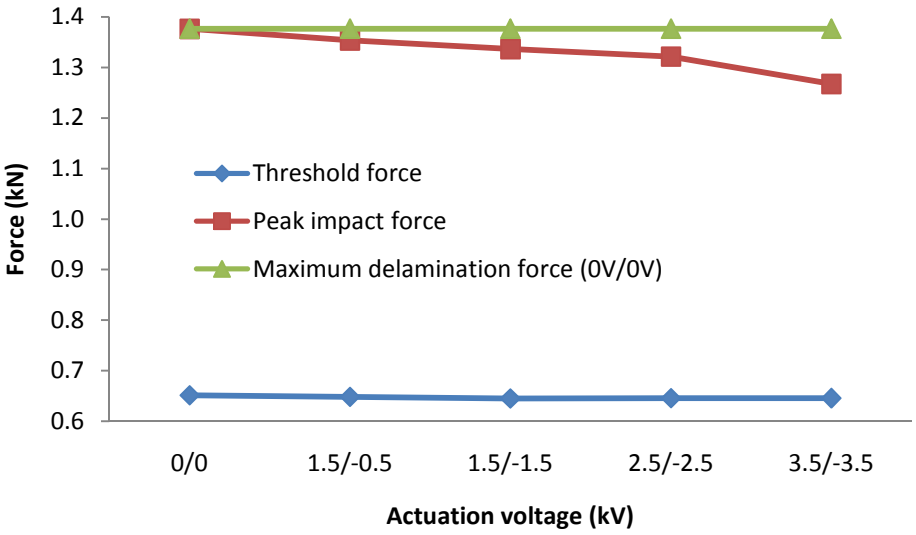


Figure 10.11: Force-actuation voltage plot – 2.0J impact

10.5 Chapter summary

This chapter presented two test cases on the effects of piezoelectric actuations on the delamination induced by low velocity impact on a simply supported cross-ply laminate. The two cases were selected such that the impact energies corresponded to delamination initiation and propagation.

It was found that piezoelectric actuators could be used to regulate the peak impact force and displacement by appropriate actuation when subjected to relative low energy impact loads. In the case of a 1.0J impact, a negative bending actuation was shown to reduce the peak impact force and displacement and correspondingly reduced the size of the delaminated zone. In the 1.0J impact case the peak impact force was 816N which was about 25.5% higher than the delamination threshold force. Applying a negative bending with an actuation voltage of 3.5kV/-3.5kV reduced the peak impact force to 705N bringing it closer to the delamination threshold force which was about 650N.

However, for high a higher impact energy level, the effectiveness of the actuator to reduce the delamination size was found to decrease. Although the peak load could be reduced, it remained high compared to the delamination threshold force. As demonstrated in Chapter 9, the peak impact force and displacement will increase with increasing impact energy. Since the proposed method for reducing the impact load is effectively a shape control problem, to counter the large displacement due to high impact load, the laminate must undergo substantial

deformation in the counter direction of the impact load in order to reduce the net impact force acting on the laminate. However, this was not achievable even after increasing the actuation voltages to 3.5kV/-3.5kV for the 2.0J impact case. At maximum actuation, the peak impact force was about 1267N compared to the delamination force at 645N.

The analyses conducted in this section found that the size of delamination could be reduced if the peak impact force acting on a laminate could be brought closer to the threshold value which actually limited the propagation of the damage. Consequently, delamination could be prevented if the peak impact force could be kept below the threshold value. However, the study demonstrated that even in the case of very low impact energy, with the existing actuator material the voltages required to reduce the impact force were substantially high. This requires actuators with improved properties both mechanically and electrically. However, the *MFC* has relatively lower mechanical properties in comparison to other ceramic actuators such as the *G1195*. The primary elastic modulus of the *MFC* is 30.3GPa which is half that of *G1195*. Although the *MFC* has very high strain output, its ability to effectively deform the laminate is limited by its low mechanical properties.

Hence, though it has been numerically proven that the piezoelectric actuators could be used to reduce impact load and consequently delamination, it remains technically impossible for the actual implementation and validation due limitations with the existing actuator materials. However, assuming powerful piezoelectric actuators are possible in near future, the integration of these materials, with structural devices could be seen as a promising option to limit damages in composite laminates subjected to low velocity impact.

Chapter 11

Summary, conclusions and future work

11.1 Summary

The main objective of the present work was to numerically investigate the possible use of piezoelectric actuator as a tool to either reduce or prevent delamination in composite laminates induced by low velocity impact. To achieve this objective a sequence of approach was adopted.

Firstly, since the study was numerically based, the identification of an appropriate damage model to predict delamination was seen essential. For this purpose a literature review on impact dynamics and the commonly used failure models to predict delamination in laminated composite was conducted. From the review it was found that the most commonly used failure models consisted of stress based method, fracture mechanics and cohesive based damage models.

The stress based methods were found to offer a relative simple prediction of delamination. However, since the stress based methods were developed for static problems, their use in dynamic analysis was found to be numerically unstable and mesh dependent for accurate delamination prediction. The fracture mechanics approach was found to be effective to predict delamination growth and not its initiation as it required an initial flaw in the analysis. Cohesive based damage model was found to combine the advantages of stress based methods

and fracture mechanics approach into a single comprehensive damage model. Most of the recent works have relied on the use of cohesive based damage model for accurate prediction of delamination. The cohesive based damage model is available in *LS-DYNA* but was found to be sensitive to loading rate, hence was not suitable for the use in the present research work. A cohesive based damage model has been formulated and implemented into *LS-DYNA* by Iannucci (2006). As part of the research objectives this model was tested and found to offer accurate prediction of damage and hence used in further impact investigation in subsequent chapters.

Secondly, it was noted that *LS-DYNA* lacked the piezoelectric material module to simulate the piezoelectric effects. The closest substitute was the orthotropic thermal material due to one-to-one relationship between voltage and temperature. The thermal strain is then equivalent to the piezoelectric strain with a linear variation with the applied temperature. Though this model could have been readily used to achieve the objective of this research, a review into piezoelectric modelling found that the linear approach was limited to applications with low operating requirements.

The linear model could not account for the effects encountered at high operating fields and under combined loading conditions. A simplified higher order model was proposed by Crawley and Lazarus (1991). A series of validations found that the induced strain model to be the most appropriate actuation model as it accounted for the nonlinear effects at high fields and under combined loading conditions. This model was implemented into *LS-DYNA* explicit finite element code to be used along with the damage model that had already been implemented into the same code.

However, the initial strategy was to develop an independent finite element code based on the linear inverse shape control piezoelectric actuation model and dynamically link the code to *LS-DYNA*. But this was found to be a formidable task due to issues such storage and memory as the number of finite element mesh used in impact investigation could be very large and this could not be handled by the code. However, the code was completed for possible future use.

The *MFC* was found to be the most appropriate actuator for impact related investigation due to its high flexibility and improved actuation characteristics. However, a review into its application with respect to structural control revealed that it was mainly used to control flexible structures and in applications such as vibration and bistable composite. Hence there was a need to characterize the performance of this actuator with respect to shape control of composite laminates that were commonly used in impact investigations. Although the

proposed piezoelectric material module had already been implemented into *LS-DYNA* at this stage of the research work, it was found that this would be a computationally demanding endeavour using an explicit code.

Hence, the static code that was developed at the earlier stage of the research was used to investigate the actuation characteristics of the *MFC* on composite laminate considering various design and actuation parameters. This study was deemed essential which otherwise would be almost impossible to identify a suitable laminate-actuator configuration with appreciable presence of piezoelectric effects to be used in subsequent impact investigation. Some of the important observations were that the piezoelectric effects almost or completely diminished in the case of clamped and thick laminates. Hence, the investigation into this sort of laminate system would not have yielded any useful results.

Based on the findings reported in the earlier investigations a suitable laminate-actuator system was selected and used to investigate the effects of piezoelectric actuation on purely elastic composite impact. This was done to identify an appropriate actuation technique that could be used to reduce the impact force acting on a composite laminate. From this study it was found that for the case of simply supported laminate the peak impact force could be reduced by applying a negative bending actuation. In the case of clamped laminate the same was achieved using negative in-phase actuation. However, as had been observed earlier the piezoelectric effect on clamped laminate was seen to be not as prominent as in the case of simply supported laminate. These findings were later used to demonstrate the damage control capabilities of the *MFC* on a simply supported laminate-actuator system subjected to impact. It was found that the *MFC* could indeed be used to reduce the delamination but there were shortfalls to this approach.

The actuator could only reduce the delamination at substantially large actuation voltages. Furthermore when the impact energies were increased the actuator did not have any effect on the delamination size. This was expected since the *MFC*, although superior in terms of actuation capabilities, has very low elastic modulus compared to other ceramics actuators. In this investigation, the *MFC* was used to increase the curvature of the laminate against the incoming impact force which is effectively a shape control problem. In order for an actuator to effectively deform a structure, apart from being superior electrically it must also have improved mechanical properties. The elastic modulus of the *MFC* in the longitudinal direction is almost half of the ceramic actuator such as *G1195*. The low modulus of the *MFC* could not effectively deform the structure. This highlights that for the practically implementation of the proposed technique powerful actuators are needed. Research activities are underway at the

Department of Aeronautics, Imperial College London to fabricate *MFC* actuators. If the mechanical properties of the actuator could be improved along with its electrical properties, the practical implementation of the proposed method of delamination control may be feasible.

11.2 Conclusions and future work

This research has achieved its intended objective in demonstrating the capabilities of piezoelectric actuator as a potential tool for reducing delamination in composite laminates subjected to low velocity impact. However, only limited cases could be presented and there are several major shortfalls to the practical implementation of this approach. The biggest drawback is that it cannot be experimentally tested to actually validate the method works. The numerical study proved the concept but could be experimentally proven.

The issue that hinder the experimental investigation is the actuation voltage. The *MFC* has a maximum operating voltage of 1500V/-500V. However, it was found that it took a voltage of 3500V/-3500V to reduce the delamination even in the case of 1.0J impact. The *MFC* will not be able to sustain the resulting high electric fields. At high coercive field the *MFC* will depolarize and loose its piezoelectric effect. The followings are some recommendations for future work:

1. Although it might be difficult to experimentally verify the concept of impact induced delamination control using piezoelectric actuators with the existing actuator materials, a further study into design optimization both electrically and structurally could possibly yield some insight towards realizing this concept. In this study the actuators were assumed to be symmetrically surface bonded to the laminate. However, they could also be used as distributed patches. Distributed actuators would normally give more control authority as compared to a single continuous patch (Chee, 2000). This coupled with design optimization technique could possibly be used to identify a more realistic laminate-actuator system with less voltage requirement. In this case the inverse shape control method could be useful. Since impact is a dynamic event, the shape of the structures will continuously change throughout the impact event. The inverse shape control approach could be used to determine the voltages sequentially throughout the impact event to counter the impact load more effectively as compared to the open loop control method demonstrated in this work.

2. The control strategy adopted in this study can be considered to be very basic. It would be almost impossible to deform the structure with an equal effect to the incoming impact load using the present control approach. Saravanos and Christoforou (2002a) have demonstrated that an active control approach could be used to reduce the net impact load acting on the laminate considerably. Hence a proper control strategy such as active closed loop control could also help realizing this concept.
3. The actuator itself might need to be powerful enough to produce effective deformation but as the same time flexible enough not to get damaged. Research activities are on going to produce better actuators both mechanically and electrically. One such kind is the carbon nanotube actuators (Riemenschneider et al., 2009). They exhibit excellent mechanical and electrical properties and have the potential to become actuator materials of future. However, the commercialization of such technology for practical applications may not be immediate. The other alternative would be to use shape memory alloys. Shape memory alloys have the capacity to produce larger deformation as compared to piezoelectric actuators. Hence this could be an existing actuator material that could be possibly used to validate the concept. Birman et al. (1996) have investigated the possible use of shape memory alloy fibres to optimize the design of composite plates subjected to low velocity impact. The fibres were embedded in the martensitic phase into the composite laminates. During impact the shape memory fibres undergone stress transformation phase and generated tensile stresses which helped to improve the impact resistance of the laminate by effectively absorbing the impact energy and reducing the plate's deflection. In another similar investigation Khalili et al. (2007) demonstrated the use of shape memory fibres to improve the impact resistance of composite plates using a spring mass model. They have shown that during the stress recovery process, the shape memory fibres not only reduced the maximum impact force and deflection of the laminate but also damped the plate more uniformly and rapidly after the impact. They also found that placing the shape memory fibres at the mid-plane of the laminate could be used to control the overall behaviour of the laminate as compared to placing the fibres at the top and bottom of the laminate.
4. Other issues that might also be given consideration would include extending the technique to real structural components and not just to simple laboratory pieces.

5. In the investigation conducted, the impact location was assumed to be known. This may not be true as in most practical applications the locations of the impact are not known prior to the physical contact. Although there are methods to identify the location and magnitude of the impact, these are achieved only after the physical contact has taken place. However, it might be useful to include sensing technology such as optical and proximity sensor that could possibly be used to identify the location of impact prior to contact.
6. The complete characterization of the commercially available *MFC* could also serve as a useful future work. It has been found in Chapter 6 that the material data provided by the manufactures were far less than the actual actuation capacity of the actuator.

Finally, the piezoelectric material module that has been implemented into *LS-DYNA* is not solely meant for impact investigation. It could be extended to analyze any design problems integrated with piezoelectric actuators with a physically based actuation model.

Appendix A

A.1 Figures from impact simulation

This section contains part of the impact force and displacement history figures reported in Chapter 9.

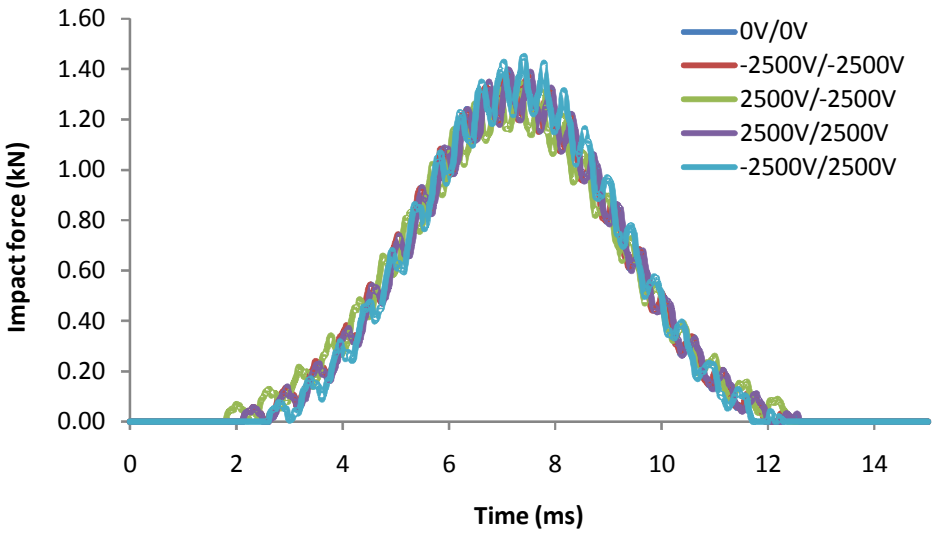


Figure A. 1: Impact force-time plot for simply supported cross-ply laminate - 2.0J impact case

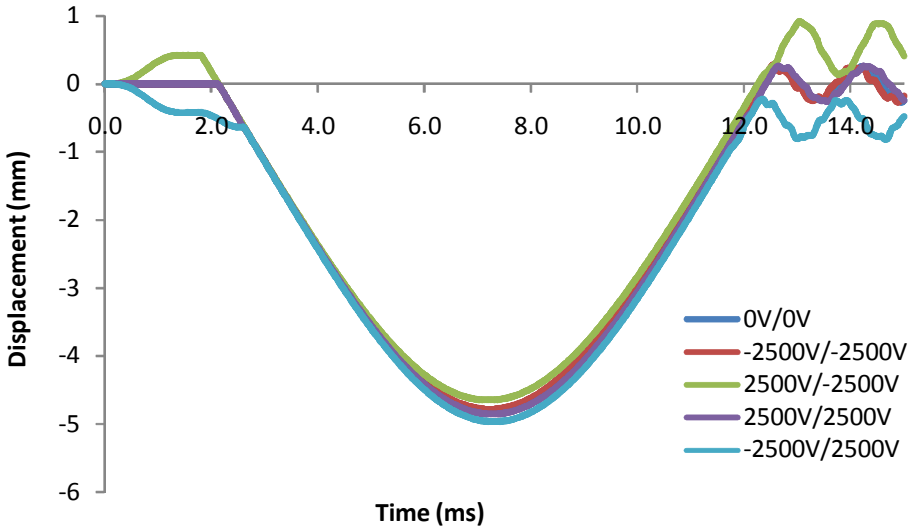


Figure A. 2: Displacement-time plot for simply supported cross-ply laminate: 2.0J impact case

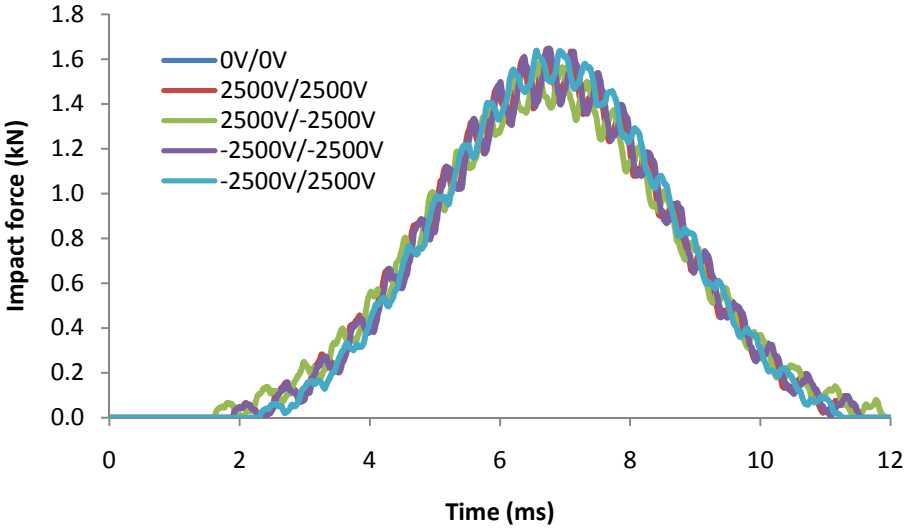


Figure A. 3: Impact force-time plot for simply supported cross-ply laminate - 2.5J impact case

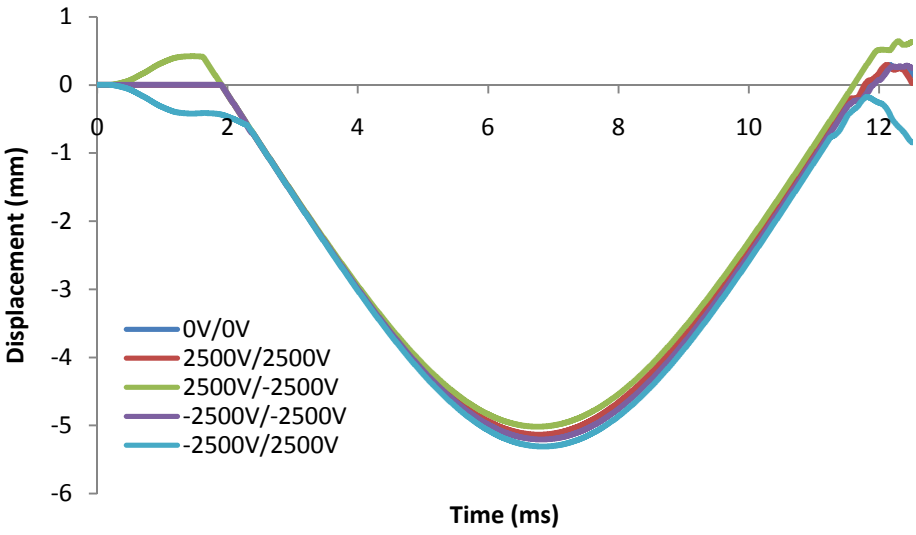


Figure A. 4: Displacement-time plot for simply supported cross-ply laminate: 2.5J impact case

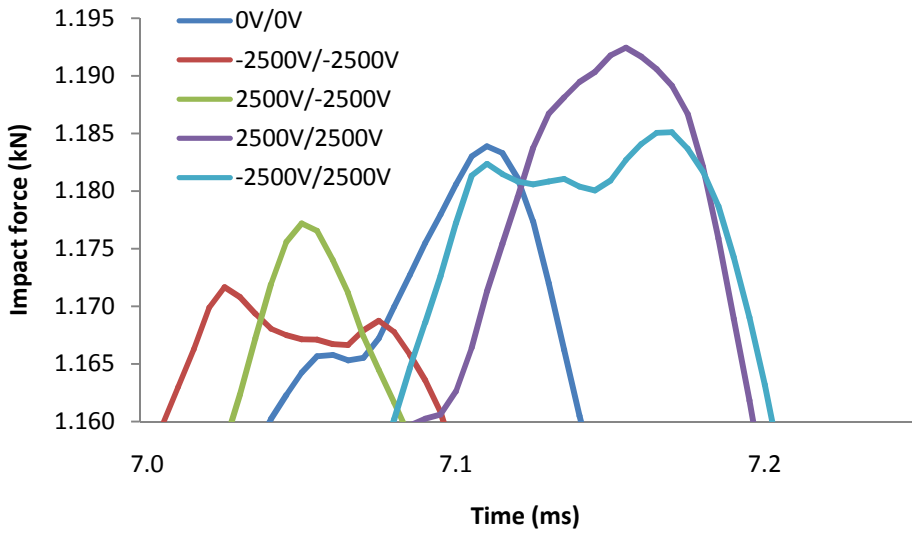


Figure A. 5: Peak resultant impact force-time plot for clamped cross-ply laminate: 1.0J impact case

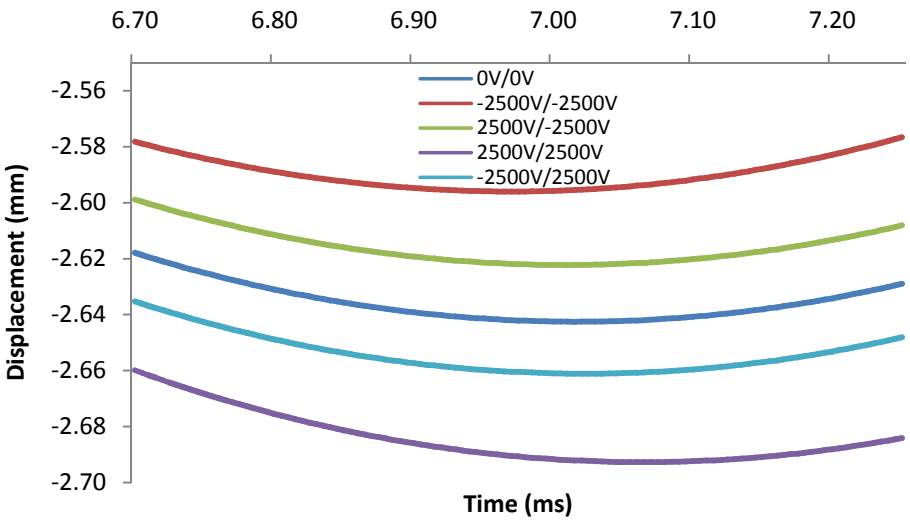


Figure A. 6: Displacement-time plot for clamped cross-ply laminate: 1.0J impact case

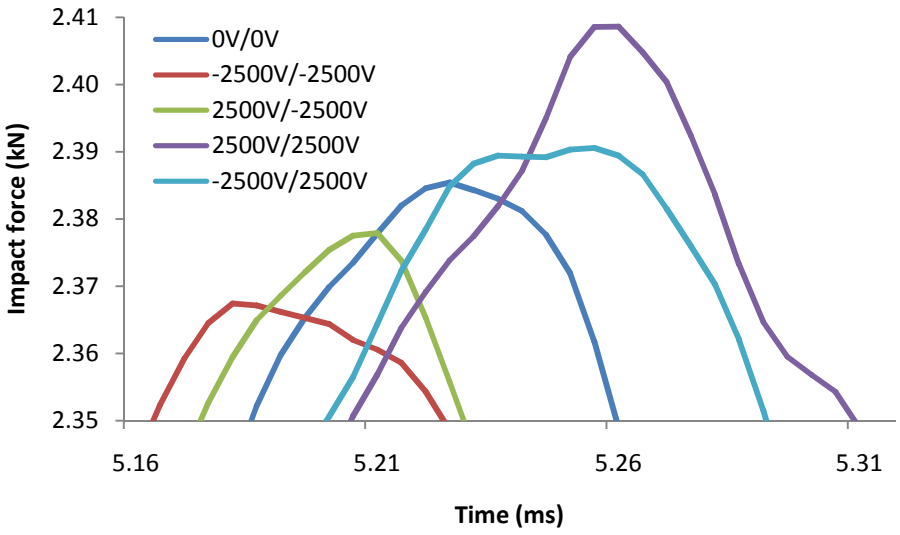


Figure A. 7: Peak resultant impact force-time plot for clamped cross-ply laminate: 2.5J impact case

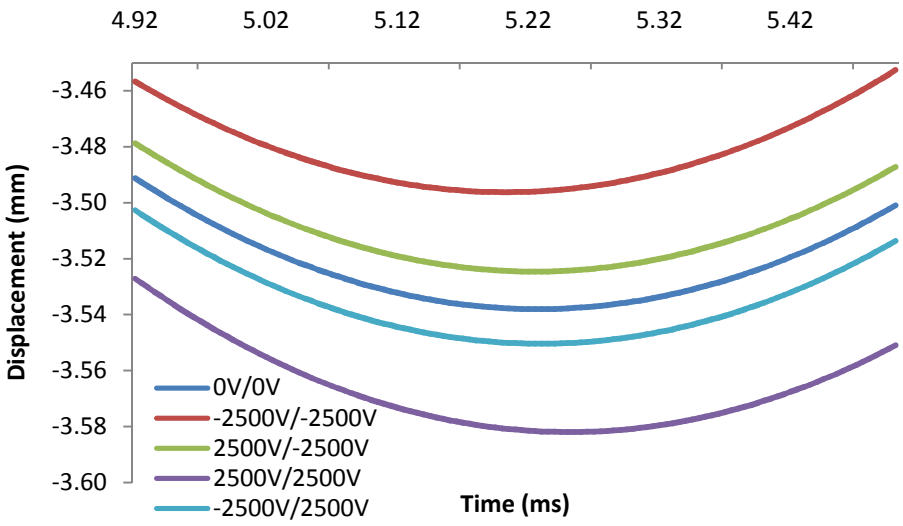


Figure A. 8: Displacement-time plot for clamped cross-ply laminate: 2.5J impact case

Appendix B

B.1 MAT 138

This section contains the mathematical formulation of *MAT 138* (*LS-DYNA* Keyword User's Manual, 2007). The formulation is based on bilinear traction-separation law with quadratic mixed mode delamination criterion. The total mixed mode relative displacement is given as:

$$\delta_m = \sqrt{\delta_I^2 + \delta_{II}^2} \tag{B1.1}$$

where:

$\delta_I = \delta_3$: separation in normal direction (mode I)

$\delta_{II} = \sqrt{\delta_1^2 + \delta_2^2}$: separation in tangential direction (mode II)

The mixed mode damage initiation displacement δ^0 is given as:

$$\delta^0 = \delta_I^0 \delta_{II}^0 \sqrt{\frac{1+\beta^2}{(\delta_{II}^0)^2 + (\beta\delta_I^0)^2}} \tag{B1.2}$$

where $\delta_I^0 = T/EN$ and $\delta_{II}^0 = S/ET$ are the single mode damage initiation separation and $\beta = \delta_{II}/\delta_I$ is the 'mode mixity'. T and S are the peak tractions in normal and tangential directions respectively while *EN* and *ET* are the respective normal and in-plane stiffness of the cohesive element. The ultimate mixed mode displacement δ^F for the power law is (XMU>0) is:

$$\delta^F = \frac{2(1+\beta)^2}{\delta^0}\left[\left(\frac{EN}{GIC}\right)^{XM} + \left(\frac{ET.\beta^2}{GIIC}\right)\right]^{-\frac{1}{XMU}} \quad \text{(B1.3)}$$

And alternatively for the Benzeggagh-Kenane law (XMU<0):

$$\delta^F = \frac{2}{\delta^0\left(\frac{1}{1+\beta^2}EN + \frac{\beta^2}{1+\beta^2}ET\right)}\left[GIC + (GIIC - GIC)\left(\frac{\beta^2.ET}{EN+\beta^2.ET}\right)^{|XMU|}\right] \quad \text{(B1.4)}$$

Appendix C

C.1 Derivation of delamination threshold load equation

This section contains the derivation of the delamination threshold load as outline by Davies et al. (1997). The delamination threshold load equation was derived through a series simplifications and assumptions. Firstly, a quasi-isotropic laminate was assumed to be perfectly isotropic and the delamination is perfectly circular and confined to a single plane, Figure C.1 (Davies et al., 1997). Hence, the energy release rate around the boundary of a single circular delamination was evaluated using isotropic plate theory. The undamaged deflection of a delamination free plate was estimated as:

$$\delta_u = \frac{3Pa^2(1-v^2)}{4\pi(2t)^3} \tag{C1.1}$$

If there is a fraction-free delamination of radius *a*, then the damaged deflection is given as:

$$\delta_d = \frac{3Pa^2(1-v^2)4\pi t^3}{2} \tag{C1.2}$$

The work done to drive the crack is given as:

$$W = \frac{1}{2}P(\delta_u - \delta_d) = \frac{9Pa^2(1-v^2)}{64\pi E_D t^3} \tag{C1.3}$$

Since the crack length increases with *a*, by equating:

$$G.2\pi a\delta_a = \frac{\partial W}{\partial a}\delta_a \tag{C1.4}$$

It was found that:

$$G = \frac{9P^2(1-v^2)}{64\pi^2 E_D t^3} \tag{C1.5}$$

By inverting the above equation, the delamination threshold load can be expressed as:

$$P_c^2 = \frac{8\pi^2 E_D (2t)^3}{9(1-v^2)} G_{IIC} \tag{C1.6}$$

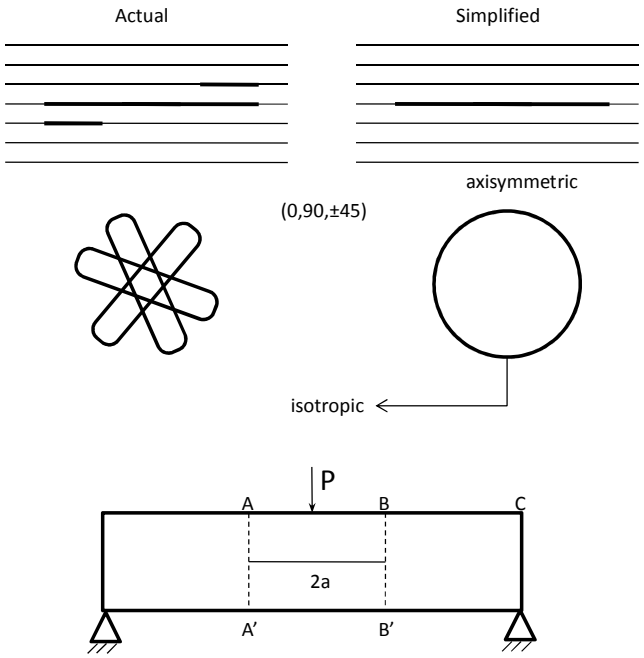


Figure C.1: Simplified model of a quasi-isotropic laminate with internal delamination (Davies et al., 1997)

Appendix D

D.1 Numerical models

The numerical models used in the fracture tests and impact simulations are detailed in Table C.1:

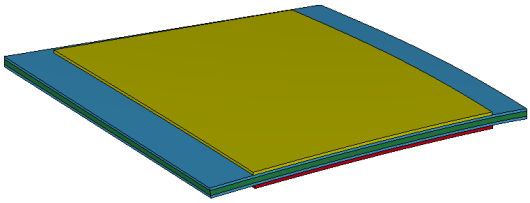
Table C.1: Finite element details of numerical simulations

Type of simulation	Finite element details
DCB	3120 solid elements (arm) 400 solid elements (interface) 8336 nodes
ENF	4080 solid elements (arm) 560 solid elements (interface) 10896 nodes
Impact simulation Section 8.8.1	22750 solid elements (laminate) 11375 solid elements (interface) 40656 nodes
Impact simulation Section 8.8.2	91000 solid elements (laminate) 45500 solid elements (interface) 29328 solid elements (*MFC*) 191222 nodes
Impact simulation Chapter 9	91000 solid elements (laminate) 33320 solid elements (*MFC*) 149138 nodes
Impact simulation Chapter 10	91000 solid elements (laminate) 45500 solid elements (interface) 33320 solid elements (*MFC*) 195250 nodes

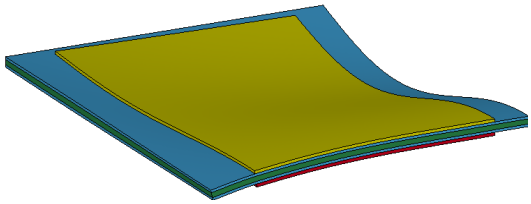
Appendix E

E.1 Modal analysis

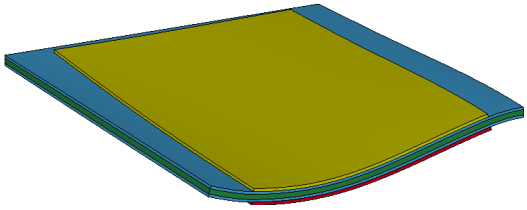
Figure E.1 shows the first six fundamental modes of the composite plate used in the impact investigation in Section 9.2.



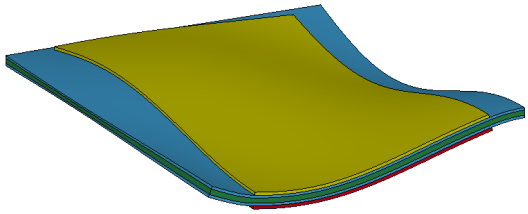
(a) mode 1 – 641.4Hz



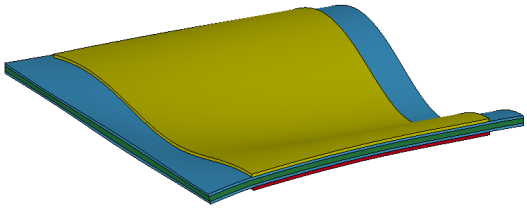
(b) mode 2 – 3558.4Hz



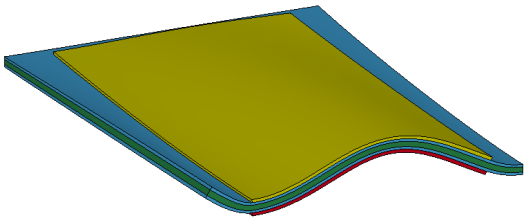
(c) mode 3 – 3584.6Hz



(d) mode 4 – 5825.9Hz



(e) mode 5 – 9239.8Hz



(f) mode 6 – 9544.2Hz

Figure E.1: The first six modes of the *SS* elastic impact specimen

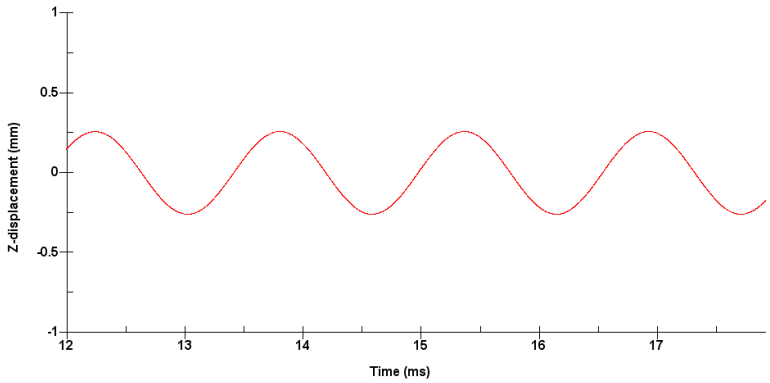


Figure E.2: Displacement-time plot for *SS* cross-ply laminate: 2.0J impact

Bibliography

Abaqus Analysis User Manual-version 6.8

Abrate, S. (1998). *Impact on composite structures.* Cambridge University Press.

Abrate, S. (1991). Impact on laminated composite materials. *Applied mechanics review,* 44 (4), 155-190.

Abrate, S. (1994). Impact on laminated composites: recent advances. *Applied mechanics review,* 47 (11), 517-554.

Abrate, S. (2001). Modeling of impacts on composite structures. *Composite structures,* 51, 129-138.

Aeronautics Department, Imperial College London.

Agarwal, B. D., and Broutman, L. J. (1990). *Analysis and performance of fiber composites.* John Wiley and Sons.

Ajit, A., Ang, K. K., and Wang, C. M. (2001). Shape control of coupled nonlinear piezoelectric beams. *Smart materials and structures,* 10, 914-924.

Ajit, A., Ang, K. K., and Wang, C. M. (2003). Shape control of statically indeterminate laminated beams with piezoelectric actuators. *Mechanics of advanced materials and structures,* 10(2), 145-160.

Alfano, G. (2006). On the influence of the shape of the interface law on the application of cohesive zone model. *Composite science and technology,* 66(6),723-730

Allik, H., and Hughes, T. J. (1970). Finite element method for piezoelectric vibration. *International journal of numerical methods in engineering*, 2, 151-158.

Amaro, A. M., Reis, P. N., Magalhaes, A. G., and de Moura, M. F. (2009). The influence of the boundary conditions on low-velocity impact composite damage. *The authors. Journal Compilation. Blackwell Publishing Ltd.*

Anderson, E. H. (1989). *Piezoceramic induced strain actuation of one- and two-dimensional structures.* Masters Thesis, Massachusetts Institute of Technology.

Armas, C. A. L. (2008). *Evaluation of constitutive laws for the computer simulation of fatigue-driven delamination in composite materials.* PhD Thesis, Imperial College London.

Aslan, Z., Karakuzu, R., and Okutan, B. (2003). The response of laminated composite plates under low-velocity impact loading. *Composite structures*, 59, 119-127.

Aymerich, F., Dore, F., and Priolo, P. (2008). Prediction of impact-induced delamination in cross-ply composite laminates using cohesive interface elements. *Composites science and technology*, 68, 2383-2390.

Aymerich, F., Dore, F., and Priolo, P. (2009). Simulation of multiple delaminations in impacted cross-ply laminates using a finite element model based on cohesive interface elements. *Composites science and technology*, 69, 1699-1709.

Bailey, T., and Hubbard, J. E. (1985). Distributed piezoelectric polymer active vibration control of a cantilever beam. *AIAA journal of guidance and control*, 8 (5), 605-611.

Bascom, W. D., Bitner, J. L., Moulton, R. J., and Siebert, A. R. (1980). The interlaminar fracture of organic-matrix woven reinforcement composites. *Composites*, 11, 9-18.

Benjeddou, A. (2000). Advances in piezoelectric finite element modelling of adaptive structural elements: a survey. *Computers and structures*, 76(1-3), 347-363.

Bent, A. A. (1997). *Active fiber composites for structural actuation.* PhD thesis, Massachusetts Institute of Technology.

Bent, A. A., and Hagood, N. W. (1997). Piezoelectric fiber composites with interdigitated electrodes. *Journal of intelligent material systems and structures*, 8 (11), 903-919.

Birman, V., Chandrashekhara, K., and Sukhendu, S. (1996). An approach to optimization of shape memory alloy hybrid composite plates subjected to low-velocity impact. *Composite; Part B*, 27B, 439-446.

Borg, R., Nilsson, L., and Simonsson, K. (2004). Simulation of low velocity impact on fiber laminates using cohesive based delamination model. *Composites science and technology*, 64, 279-288.

Bowen, C. R., Nelson, L. J., Stevens, R., and Cain, M. G. (2006). Optimisation of interdigitated electrodes for piezoelectric actuators and active fiber composites. *Journal of electroceramics*, 16 (4), 263-269.

Bowen, C. R., Salo, A. I., Butler, R., Chang, E., and Kim, H. A. (2007). Bi-stable composites with piezoelectric actuators for shape change. *Key engineering materials,* 334-335, 1109-1112.

Cantwell, W. J., and Morton, J. (1992). The significance of damage and defects and their deflection in composite materials: a review. *The journal of strain analysis for engineering design*, 27 (1).

Chandrashekhara, K., and Agarwal, A. N. (1993). Active vibration control of laminated composite plates using piezoelectric devices: A finite element approach. *Journal of intelligent material systems and structures*, 4, 496-508.

Chandrashenkhara, K., and Bhatia, K. (1993). Enhancement of buckling loads of laminated plates using piezoelectric devices. *Composite materials and structures, ASME,* AD-37/AMD-179, 163-173.

Chang, F. K., and Chang, K. Y. (1987). A progressive damage model for laminated composites containing stress concentrations. *Journal of composite materials*, 21, 834-855.

Chatopadhyay, A., Gu, H., and Liu, Q. (1999). Modeling of smart composite box beams with nonlinear induced strain. *Composites Part B*, 30, 603-612.

Chatopadhyay, A., and Seeley, C. E. (1997). A higher order theory for modelling composite laminates with induced strain actuators. *Composites Part B*, 28B, 243-252.

Chee, C. (2000). *Static shape control of laminated composite plate smart structures using piezoelectric actuators.* PhD thesis, University of Sydney Australia.

Chee, C. Y., Tong, L., and Steven, G. P. (1999). A mixed model for composite beams with piezoelectric actuators and sensors. *Smart materials and structures*, 8, 417-432.

Chee, C. Y., Tong, L., and Steven, P. (1998). A review on the modelling of piezoelectric sensors and actuators incorporated in intelligent structures. *Journal of intelligent material systems and structures*, 9, 3-19.

Cho, C., and Zhao, G. (2002). Effects of geometric and material factors on mechanical response of laminated composites due to low velocity impact. *Journal of composite materials*, 36 (12), 1403-1428.

Choi, H. Y., and Chang, F. K. (1992). A model for predicting damage in graphite/epoxy laminated composite resulting from low velocity point impact. *Journal of composite materials*, 26(21), 2134-2169.

Chopra, I. (2002). Review of state of art of smart structures and integrated systems. *AIAA journal*, 40 (11).

Chun, L., and Lam, K. Y. (1998). Dynamic response of fully-clamped laminated composite plates subjected to low-velocity impact of a mass. *International journal of solids and structures*, 35(11), 963-979.

Clyne, T. W., and Withers, P. J. (1993). *An introduction to metal matrix composites.* Cambridge University Press.

Crawley, E. F., and Anderson, E. H. (1990). Detailed models of piezoceramic actuation of beams. *Journal of intelligent material systems and structures*,1 (1), 4-25.

Crawley, E. F., and Lazarus, K. B. (1991). Induced strain actuation of isotropic and anisotropic plates. *AIAA journal*, 29 (6), 944-951.

Damjanovic, D. (2005). *Hysteresis in piezoelectric and ferroelectric materials*. The science of hysteresis, 3(1), Mayergoyz and G. Bertotti, Elsevier.

Daniel, I. M., and Ishai, O. (2006). *Engineering mechanics of composite materials.* Oxford University Press.

Davies, G. A., and Olsson, R. (2004). Impact on composite structures. *The aeronautical journal*, 541-563.

Davies, G. A., and Zhang X. (1995). Impact damage prediction in carbon composite structures. *International journal of impact engineering*, 16, 149-170.

Davies, G. A., Robinson, P., Robson, J., and Eady, D. (1997). Shear driven delamination propagation in two dimensions. *Composites part A*, 28A, 757-765.

de Freitas, M., Silva, A., and Reis, L. (2000). Numerical evaluation of failure mechanisms on composite specimens subjected to impact loading. *Composites part B*, 31 (3), 199-207.

Deo, R. B., Starnes, J. H., and Holzwarth, R. C. (2001). Low cost composite materials and structures for aircraft applications. *RTO-MP.069(11)*, Loen Norway.

Ducharne, B., Guyomar, D., and Sebald, G. (2007). Low frequency modelling of hysteresis behaviour and dielectric permittivity in ferroelectric ceramics under electric field. *Journal of physics D: Applied physics*, 40, 551-555.

Farooq, U., and Gregory, K. (2009). Finite element simulation of low velocity impact damage morphology in quasi isotropic composite panels under variable shape impactor. *European journal of scientific research*, 25 (4), 636-648.

Finn, S. R., and Springer, G. S. (1992). Delamination in composite plates under transverse static loads – experimental results. *Journal of reinforced plastics and composites*, 11, 1196-1238.

Gandhi, M. V., and Thompson, B. S. (1992). *Smart materials and structures.* London, UK: Chapman & Hall.

Giddings, P., Bowen, C. R., Butler, R., and Kim, H. A. (2008). Characterisation of actuation properties of piezoelectric bi-stable carbon-fibre laminates. *Composites part A*, 39, 697-703.

Goyal, V. K., Davila, C. G., Johnson, E. R., and Jaunky, N. (2002). An irreversible constitutive law for modeling the delamination process using interface elements. *AIAA* , 1-12.

Greenhalgh, E., and Hiley, M. (2003). The assessment of novel materials and processes for the impact tolerant design of composite aerospace structures. *Composites part A*, 34 (2), 151-161.

Ha, S. K., Keilers, C., and Chang, F. K. (1992). Finite element analysis of composite structures containing distributed piezoceramic sensors and actuators. *AIAA journal*, 30 (3), 772-780.

Hagood, N., Kindel, R., Ghandi, K., and Gaudenzi, P. (1993). Improving transverse actuation of piezoceramics using interdigitated surface electrodes. *Smart structures and intelligent systems,* SPIE, 341-352.

Hall, D. A. (2001). Review nonlinearity in piezoelectric ceramics. *Journal of materials science*, 36, 4575-4601.

Her, S. C., and Liang, Y. C. (2004). The finite element analysis of composite laminates and shell structures subjected to low velocity impact. *Composite structures*, 66, 277-285.

Hou, J. P., Petrinic, N., Ruiz, C., and Hallett, S. R. (2000). Prediction of impact damage in composite plates. *Composites science and technology*, 60, 273-281.

Hurlebaus, S., and Gaul, L. (2006). Smart structure dynamics. *Mechanical systems and signal processing*, 20, 255-281.

Iannucci, L. (2006). Dynamic delamination modelling using interface elements. *Computers and structures*, 84, 1029-1048.

Iannucci, L., and Willows, M. L. (2006). An energy based damage mechanics approach to modelling impact onto woven composite materials - part 1: numerical models. *Composites part A*, 37, 2041-2056.

Ibrahim, I. A., Mohamed, F. A., and Laverina, E. J. (1991). Particulate reinforced metal matrix composites - a review. *Journal of materials science*, 26, 1137-1156.

Introduction, piezoelectric ceramics (2001). Morgan Electro Ceramics.

Irwin, G. R. (1958). Fracture. *In Handbuch der Physik*, VI Flugge, 558-590.

Jones, R. M. (1999). *Mechanics of composite materials.* Taylor and Francis.

Jordan, T. L., and Ounaies, Z. (2001). *Piezoelectric ceramics characterization.* NASA Langley Research Center Hampton Virginia: NASA/CR-2001-211225.

Joshi, S. P. (1992). Non-linear constitutive relations for piezoceramic materials. *Smart materials and structures*, 1, 80-83.

Kasano, H. (1999). Recent advances in high-velocity impact perforation of fiber composite laminates. *The Japan society of mechanical engineers*, 42(2).

Khalili, S. M. R., Shokuhfar, A., Ghasemi, F. A., and Malekzadeh, K. (2007). Dynamic response of smart hybrid composite plate subjected to low velocity impact. *Journal of composite materials*, 41, 2347-2370.

Kim, J. K., and Sham, M. L. (2000). Impact and delamination failure of woven-fabric composites. *Composites science and technology*, 60, 745-761.

Kim, J., Varadan, V. V., and Varadan, V. K. (1997). Finite element modelling of structures including piezoelectric active devices. *International journal for numerical methods in engineering*, 40, 817-832.

Koconis, D. B., Kollar, L. P., and Springer, G. S. (1994a). Shape control of composite plates and shells with embedded actuators. I. Voltages specified. *Journal of composite materials*, 28 (5), 415-458.

Koconis, D. B., Kollar, L. P., and Springer, G. S. (1994b). Shape control of composite plates and shells with embedded actuators. II. Desired shape specified. *Journal of composite materials*, 28(3), 262-285.

Krueger, R. (2002). The virtual crack closure technique: History, approach and application. *NASA report.*TM 211628.

Lazarus, K. B., and Napolitano, K. L. (1993). Smart structures, an overview. *Wright-Patterson AFB. OH, WL-TR-93-3101*.

Lee, S., Choo, B. C., Park, H. C., Goo, N. S., and Yoon, K. J. (2004). Piezoelectric actuator-sensor analysis using a three-dimensional assumed strain solid element. *Journal of intelligent material systems and structures*, 15, 329-338.

Liou, W. J. (1997). Impact analysis of laminated composite plates with statical indentation laws. *Computers and structures*, 62(5), 817-829.

Liou, W. J., Tseng, C. I., and Chao, L. P. (1996). Stress analysis of laminated E-glass epoxy composite plates subject to impact dynamic loading. *Computers and structures*, 61 (1), 1-11.

Liu, D. (1988). Impact induced delamination: a view of bending stiffness mismatching. *Journal of composite materials*, 22, 674-692.

LS-DYNA theory manual (2006). Livermore software technology corporation.

LS-DYNA keyword user's manual (2007). Livermore software technology corporation.

Mackerle, J. (2003). Smart materials and structures - a finite element approach - an addendum: a bibliography (1997-2002). *Modelling and simulation in materials science and engineering*, 11, 707-744.

Mi, Y., Crisfield, M. A., Hellweg, H. B., and Davies, G. A. (1998). Progressive delamination using interface elements. *Journal of composite materials*, 32(14), 1246-1272.

Mitrevski, T., Marshall, I. H., Thomson, R., Jones, R., and Whittingham, B. (2005). The effect of impactor on the impact response of composite laminates. *Composite structures*, 67, 139-148.

Nelson, L. J. (2002). Smart piezoelectric fibre composites. *Materials science and technology*, 18, 1245-1256.

Olabi, A. G., and Grunwald, H. (2008). Design and application of magnetostrictive materials. *Materials and design*, 29, 469-483.

Olsson, R. (2001). Analytical prediction of large mass impact damage in composite laminates. *Composites part A*, 32, 1207-1215.

Olsson, R. (2003). Closed form prediction of peak load and delamination onset under small mass impact. *Composite structures*, 59(3), 341-349.

Olsson, R. (2000). Mass criterion for wave controlled impact response of composite plates. *Composites part A*, 31, 879-884.

Orifici, A. C., Herszberg, I., and Thomson, R. S. (2008). Review of methodologies for composite material modelling incorporating failure. *Composite structures*, 86 (1-3), 194-210.

Park, C. H., Saouab, A., Breard, J., Han, W. S., Vautrin, A., and Lee, W. I. (2009). An integrated optimisation for the weight, the structural performance and the cost of composite structures. *Composites science and technology*, 69(7-8), 1101-1107.

Park, G., and Inman, D. J. (2007). Structural health monitoring using piezoelectric impedance measurements. *Philosophical transactions of the royal society A*, 365, 373-392.

Park, J. S., and Kim, J. H. (2008). Design and aeroelastic analysis of active twist rotor blades incorporating single crystal macro fibre composite actuators. *Composites: Part B*, 39, 1011-1025.

Pinho, S. T., Iannucci, L., and Robinson, P. (2006). Formulation and implementation of decohesion elements in an explicit finite element code. *Composites part A*, 37, 778-789.

Portela, P., Camanho, P., Weaver, P., and Bond, I. (2008). Analysis of morphing, multistable structures actuated by piezoelectric patches. *Computers and structures*,86 (3-5), 347-356.

Prasad, S. E., Waechter, D. F., Blacow, R. G., King, H. W., and Yaman, Y. (2005). Application of piezoelectrics to smart structures. *II ECCOMAS Thematic conference on smart structures and materials.* Lisbon, Portugal – July 18-21.

Rawal, S. P. (2001). Metal-matrix composites for space applications. *Journal of the minerals, metals, and materials society*, 53 (4), 14-17.

Reddy, J. N. (2004). *Mechanics of laminated composite plates and shells: theory and analysis.* CRC Press.

Reeder, J. R. (1992). Evaluation of mixed-mode delamination failure criteria. *NASA report.*TM 104210.

Richardson, M. O., and Wisheart, M. J. (1996). Review of low-velocity impact properties of composite materials. *Composites part A*, 27A, 1123-1131.

Riemenschneider, J., Opitz, S., Sinapius, M., and Monner, H. P. (2009). Modeling of carbon nanotube actuators: Part II – Mechanical properties, electro mechanical coupling and validation of the model. *Journal of intelligent material systems and structures*, 20,253-263.

Robinson, P., and Davies, G. A. (1992). Impactor mass and specimen geometry effects on low velocity impact of laminated composites. *International journal of impact engineering*, 12 (2), 189-207.

Rosato, D. V., and Grove, C. S. (1996). *Filament winding: its development, manufacture, application and design.* John Wiley and Sons.

Robinson, P., and Song, D. Q. (1992). A modified DCB specimen for mode I testing of multidirectional laminates. *Journal of composite material*, 26, 554-557.

Rybicki, E. F., and Kanninen, M. F. (1977). A finite element calculation of stress intensity factors by a modified crack closure integral. *Engineering fracture mechanics*, 9, 931-938.

Samal, M. K., Seshu, P., Parashar, S. K., von Wagner, U., Hagedorn, P., Dutta, B. K., et al. (2006). Nonlinear behaviour of piezoceramics under weak electric fields. Part-I: 3-D finite element formulation. *International journal of solids and structures*, 43, 1422-1436.

Samanta, B., Ray, M. C., and Bhattacharyya, R. (1996). Finite element model for active control of intelligent structures. *AIAA journal*, 34 (9), 1885-1893.

Saravanos, D. A., and Christoforou, A. P. (2002a). Impact response of adaptive piezoelectric laminated plates. *AIAA journal, 40* (10), 2087-2095.

Saravanos, D. A., and Christoforou, A. P. (2002b). Low-energy impact of adaptive cylindrical piezoelectric-composite shells. *International journal of solids and structures*, 39, 2257-2279.

Schoeppner, G. A., and Abrate, S. (2000). Delamination threshold loads for low velocity impact on composite laminates. *Composites part A*, 31, 903-915.

Schultz, M. R. (2003). Use of piezoelectric actuator to effect snap-through behavior of unsymmetric composite laminates. PhD thesis, Virginia Polytechnic Institute and State University.

Shah, D. K., Chan, W. S., and Joshi, S. P. (1994a). Delamination detection and suppression in a composite laminate using piezoceramic layers. *Smart materials and structures*, 3, 293-301.

Shah, D. K., Joshi, S. P., and Chan, W. S. (1994b). Stress concentration reduction in a plate with a hole using piezoceramic layers. *Smart materials and structures*, 3, 302-308.

Shaik Dawood, M. S. I., Iannucci, L., and Greenhalgh, E. S. (2008). Three-dimensional static shape control analysis of composite plates using distributed piezoelectric actuators. *Smart materials and structures*, 17(2).

Sirohi, J., and Chopra, I. (2000). Fundamental understanding of piezoelectric strain sensors. *Journal of intelligent material systems and structures*, 11(4), 246-257.

Smith, R. C., and Ounaies, Z. (1999). *A domain wall model for hysteresis in piezoelectric materials.* NASA Langley Research Center Hampton Virginia: NASA/CR-1999-209832.

Sodano, H. A., Park, G., and Inman, D. J. (2004). An investigation into the performance of macro-fiber composites for sensing and structural vibration applications. *Mechanical systems and signal processing*, 18 (3), 683-697.

Soutis, C. S. (2005). Fiber reinforced composite in aircraft construction. *Progress in aerospace sciences*, 41, 143-151.

Srinivasan, A. V., and McFarland, D. M. (2001). *Smart structures: Analysis and design.* Cambridge University Press.

Suemasu, H., and Majima, O. (1996). Multiple delaminations and their severity in circular axisymmetric plates subjected to transverse loading. *Journal of composite materials*, 30 (4), 441-453.

Suleman, A., and Venkayya, V. B. (1994). Flutter control of an adaptive laminated composite panel with piezoelectric layers. *Wright Patterson AFB.* OH, WL-TR-95-3038.

Sun, D., and Tong, L. (2004). Adhesive element modelling and weighted static shape control of composite plates with piezoelectric actuator patches. *International journal for numerical methods in engineering*, 60, 1911-1932.

Sun, D., and Tong, L. (2005). Design optimization of piezoelectric actuator patterns for static shape control of smart plates. *Smart materials and structures*, 14, 1353-1362.

Tawfik, S. A. (2008). Stability and morphing characteristics of bistable composite laminates. PhD Thesis*,* Georgia Institute of Technology.

Thornburgh, R. P., and Chattopadhyay, A. (2001). Nonlinear actuation of smart composites using a coupled piezoelectric-mechanical model. *Smart materials and structures*, 10, 743-749.

Tseng, K. K., and Wang, L. (2004). Structural health monitoring using piezoelectric material. *ANSYS proceedings paper*, 152.

Tzou, H. S. (1993). *Piezoelectric shells distributed sensing and control of continua*. KAP, Norwell, MA.

Tzou, H. S., and Tseng, C. I. (1990). Distributed piezoelectric sensor/actuator design for dynamic measurement/control of distributed parameter systems: a piezoelectric finite element approach. *Journal of sound and vibration*, 138, 17-34.

Wang, Q. M., Zhang, Q., Xu, B., Liu, R., and Cross, L. E. (1999). Nonlinear piezoelectric behavior of ceramic bending mode actuators under strong electric fields. *Journal of applied physics*, 86 (6), 3352-3360.

Wilkie, W. K., Inman, D. J., Lloyd, J. M., and High, J. W. (2006). Anisotropic laminar piezocomposite actuator incorporating machined PMN-PT single crystal fibers. *Journal of intelligent material systems and structures*, 17, 15-28.

Williams, R. B., Park, G., Inman, D. J., and Wilkie, W. J. (2002). An overview of composite actuators with piezoceramic fibers. *Proceedings of 20th international modal analysis conference*, Los Angeles CA, 4-7.

Williams, K. V., and Vaziri, R. (2001). Application of a damage mechanics model for predicting the impact response of composite materials. *Composite structures*, 79(10), 997-1011.

Williams, R. B. (2004). *Nonlinear mechanical and actuation characterization of piezoceramic fiber composites.* PhD thesis, Virginia Polytechnic Institute and State University.

www.dynasuuport.com.

www.piceramic.com.

www.smart-material.com.

Yan, C., Lifeng, W., and Jianyue, R. (2008). Multi-functional SiC/Al composites for aerospace applications. *Chinese journal of aeronautics*, 21, 578-584.

Yao, L. Q., Zhang, J. G., Lu, L., and Lai, M. O. (2004). Nonlinear extension and bending of piezoelectric laminated plate under large applied field actuation. *Smart materials and structures*, 13, 404-414.

Ye, L. (1988) Role of Matrix Resin in Delamination Onset and Growth in composite Laminates, *Composite science and technology*, 33, 257-277

Yin, L., and Shen, Y. (1997). Strain sensing of composite plates subjected to low velocity impact with distributed piezoelectric sensors: A mixed finite element approach. *Journal of sound and vibration*, 9 (1), 17-31.

Zhang, X., Davies, G.A.O., and Hitching, D. (1999). Impact damage with compressive preload and post-impact compression of carbon composite plates. *International journal of impact engineering*, 22, 485-509.

Zhang, Y., Niu, H., Xie, S., and Zhang, X. (2008). Numerical and experimental investigation of active vibration control in a cylindrical shell partially covered by a laminated PVDF actuator. *Smart materials and structures*, 17.

Zou, Z., Reid, S.R., and Li, S., (2003). A continuum damage model for delaminations in laminated composites. *Journal of mechanics and physics of solids*, 51, 333-356

Zou, Z., Reid, S.R., Li, S., and Soden, P.D., (2002). Application of a delamination model to laminated composite structures. *Composite structures*, 56, 375-389